Dissertation
submitted to the
Combined Faculty of Mathematics, Engineering and Natural Sciences
of Heidelberg University, Germany
for the degree of
Doctor of Natural Sciences

Put forward by

Junia Aletta Beatrix Göller
born in Unna (Germany)

Oral examination: 25.07.2025

Stars in the Making:
Probing Star Formation and its Effects in Simulated Galaxies

Referees:

Prof. Ralf S. Klessen

Prof. James A. Hinton

To the giantesses on whose shoulders I stand.

Stars in the Making: Probing Star Formation and its Effects in Simulated Galaxies

Up to today, the formation of stars in the broader galactic context remains poorly understood. The role of the external forces – such as ram-pressure stripping – and internal properties of galaxies – including the gravitational potential and large-scale gas dynamics – are a topic of active debate. In this thesis, we study star formation across two contrasting galactic environments: jellyfish galaxies and the Milky Way. These example systems allow us to investigate both the extragalactic and intragalactic mechanisms affecting star formation.

In the first part of this thesis we use the magnetohydrodynamical cosmological simulation TNG50 to probe a sample of jellyfish galaxies for their star formation, asking if gas compression from ram-pressure increases the star formation rate (SFR) in such galaxies, as some observations suggest. We find no such enhancement in the general population, but instead for the majority of jellyfish see a phase of enhanced SFR in their individual evolution.

In the second part we introduce the Rhea simulation suite, a set of elaborate hydrodynamical simulations conducted by us to model the Milky Way galaxy. We study the importance of the galactic gravitational potential for star formation, and find the bar to have the strongest influence, as it changes the location and properties of star-forming regions. A spiral arm potential merely reorganizes gas in the galaxy and thus increases SFR in its potential wells.

We also find the extend of the star-forming disk to divide the galactic stellar disk into a region dominated by in-situ formed stars, and an outer migrator-dominated region. This duality, in our simulations, affects the stellar density distribution and thus the stellar galactic rotation curve. If no distinction is made between the two regions, the resulting velocity curve can mimic a cut-off in the galactic mass distribution.

Sterne in ihrer Entstehung: Untersuchung der Sternentstehung und ihrer Effekte in simulierten Galaxien

Die Entstehung von Sternen ist im galaktischen Kontext bis heute nur unzureichend verstanden. So wird über die Rolle von externen Kräften - wie etwa der Staudruckablösung - und der der Galaxie eigenen Eigenschaften - wie ihr Gravitationspotenzial und großskalige Gasdynamik - noch immer debattiert. In dieser Arbeit untersuchen wir Sternentstehung in zwei sehr unterschiedlichen galaktischen Umgebungen: simulierten Quallengalaxien und der Milchstraße. Diese Beispielsysteme erlauben es uns sowohl die extragalaktischen als auch die intragalaktischen Prozesse zu studieren, die Sternentstehung beeinflussen.

Im ersten Teil dieser Arbeit nutzen wir die magnetohydrodynamische Simulation TNG50 um Quallengalaxien auf ihre Sternentstehung hin zu untersuchen. Die Frage ist, ob die Gasverdichtung durch Staudruck die Sternentstehungsrate (SER) in diesen Galaxien erhöht, wie manche Beobachtungen indizieren. Wir finden in der allgemeinen Population keine solch erhöhte Sternentstehung, die Entwicklung der einzelnen Galaxien beinhaltet jedoch bei den meisten von ihnen eine Phase erhöhter SER.

Im zweiten Teil führen wir die Rhea Simulationen ein, ein Set von aufwendigen hydrodynamischen Simulationen, die wir durchgeführt haben um die Milchstraße zu modellieren. Hier untersuchen wir die Wichtigkeit des galaktischen Gravitationspotenzials für die Sternentstehung. Das Balkenpotenzial hat den größten Einfluss, da es den Ort und die Eigenschaften von Sternentstehungsgebieten verändert. Das Potenzial von Spiralarmen sorgt lediglich für eine Umverteilung von Gas und erhöht dadurch die SER in seinen Gravitationssenken.

Wir sehen außerdem, dass die Ausdehnung der sternenbildenden Scheibe die stellare Scheibe in zwei Bereiche unterteilt, einen dominiert durch in-situ geformte Sterne, und einen der von migrierenden Sternen dominiert wird. In unseren Simulationen beeinflusst diese Dualität die stellare Dichteverteilung und dadurch die stellare Rotationskurve. Wird kein Unterschied zwischen den zwei Regionen gemacht, ahmt die resultierende Rotationskurve den Effekt eines Abbruchs der galaktischen Massenverteilung nach.

Contents

1 Introduction

1.1 About this Thesis

Stars are the building blocks of every galaxy. They emit the light on which most observations depend, they are responsible for numerous feedback processes that shape their host galaxies and the surrounding interstellar medium (ISM). In their vicinity, planets form; in their cores, light elements undergo nuclear fusion, which are later expelled and redistributed through feedback mechanisms such as supernovae, enriching the ISM and building the foundation of our chemically rich universe. Our understanding of the star-formation cycle – from the gravitational collapse of molecular clouds to the various forms of stellar feedback through stellar evolution – is becoming increasingly detailed, particularly within our own Galaxy (e.g., Girichidis et al., 2020). Nevertheless, many questions about the formation of stars remain unanswered. For instance, the cause of the long depletion time observed in both our Galaxy (e.g., Zuckerman & Palmer, 1974) and molecular clouds (e.g., Krumholz & Tan, 2007; Evans et al., 2009) compared to characteristic free-fall times. This discrepancy brings the exact conditions under which stars are formed into the focus of ongoing research. As stars usually form deeply embedded within giant molecular clouds, direct observations of the process are inherently challenging and tracers of dense star-forming gas are especially hard to detect in external galaxies (e.g., Stuber et al., 2023). For most sites of star formation (SF), information remains sparse, especially the temporal evolution of star-forming sites and the exact gas distribution (independent of observational tracers) are difficult to extract from observations. These properties, on the other hand, are straightforward to obtain from numerical simulations.

Therefore, great efforts have gone into simulating SF, from the small scale of individual clouds (e.g., Attwood et al., 2009; Bertram et al., 2012; Grudić et al., 2021; Hunter et al., 2023) up to whole galaxies (e.g., Benincasa et al., 2016; Tress

et al., 2020a; Jeffreson et al., 2024) and even cosmological boxes of several Mpc in sidelength (e.g., Furlong et al., 2015; Hwang et al., 2019; Motwani et al., 2022; Rhee et al., 2024). These simulations enable detailed studies of the physical properties within star-forming gas – such as temperature, density, and magnetic field – while also addressing the bigger picture: *Where* do stars form? *What* is the environment they form in? *How* does this environment alter/suppress/support SF? And does this affect our observations?

In this thesis we focus on the connection between the galactic environment and SF. We examine the statistics of SF in different environments and, from there, study the physical processes shaping the ISM and ultimately the sites of SF. To do so, we choose two very distinct types of galaxies, jellyfish galaxies and the Milky Way, to study SF in vastly different galactic systems.

In the state-of-the-art cosmological magnetohydrodynamical simulation TNG50 from the IllustrisTNG simulation suite (Pillepich et al., 2019; Nelson et al., 2019b), we analyze SF in the rather extreme environments of jellyfish galaxies, including both their stellar bodies and ram-pressure stripped tails (see Chapter 3). As jellyfish galaxies exist only in the context of galaxy clusters, we extract them from a full cosmological box of 51.7 comoving Mpc in sidelength, where they emerge self-consistently. In contrast to observational studies – which often see enhanced star formation rates (SFRs) in jellyfish galaxies, likely driven by gas compression from ram-pressure stripping – we find that, on average, the SFR in TNG50 jellyfish galaxies is reduced relative to non-jellyfish galaxies of comparable mass. However, when studying the development of SFR over time, many jellyfish galaxies show a peak in SFR coinciding with the first pericenter passage of the galaxy in the galaxy cluster. Tails of jellyfish galaxies show star formation activity despite being stripped from the galactic body, however, SFR is greatly reduced.

To model the Milky Way's galactic environment, we conduct a set of elaborate (magneto-)hydrodynamical simulations, the Rhea simulations (which we present in Section 2.3.8). For that, we implement a probabilistic treatment of star formation within the Arepo-framework, controlled by the local SFR and free-fall time of gas. We model the Milky Way-like galaxy in our simulations as an isolated galaxy and impose different gravitational potentials on the galactic disk. We study the influence of different galactic potentials on the SFR, as well as where stars are formed (see Chapter 4). We find little difference in SFR between a barred + spiral arm potential

and a simple axisymmetric one, however, gas flows in the bar prevent the galactic center from quenching over time. Formation of stable star-forming spiral arms only occurs in simulations including a spiral arm potential, in those simulations slightly more stars ($\sim$ 62 %) are formed within spiral arms than in the interarm region. Axisymmetric potentials only build short-lived spiral structures. SF in the galactic center with a barred potential is about as clustered as in an axisymmetric potential, but sites of star formation are smaller and more short-lived.

Moreover, in all our Milky Way-like simulations we find that the star-forming disk is smaller in radius than the stellar disk (see Chapter 5). This results in large orbital eccentricities of star particles with a mean galactocentric distance $\gtrsim$ 20 kpc and a broken exponential density distribution of stars. We find that this impacts the measured stellar rotation curve in the outer parts of the galaxy, which results in a lowered rotation curve, if not properly accounted for. We propose this as a plausible alternative explanation for the observed Keplerian decline in the rotation curve from Gaia DR3 data (Jiao et al., 2023).

Together, our results demonstrate that both extra- and intragalactic environments can have a significant impact on SF in galaxies. The extragalactic influence of a galaxy cluster can change the location of SF and the SFR in galaxies by stripping them of their gas, triggering bursts of star formation and enabling SF in the gaseous wakes of the galaxies. The intragalactic gravitational potential affects the location of SF and also the properties of star-forming areas. Especially the presence of a bar in the Galactic potential proves important for an adequate representation of SF in the Galactic center. SF also influences the interpretation of observational features not directly connected to it, such as the stellar galactic rotation curve. We discuss the consequences of such findings in detail in Chapter 6.

1.2 Structure Formation

We begin this thesis with a review of the cosmological principles, to set the stage for the formation of structures on the smaller scales of galaxies and molecular clouds.

1.2.1 Cosmic Structures

Building Blocks of the Universe

In the most generally accepted cosmological model, the ΛCDM-model, the Universe is made up by a cosmic fluid, which consists of radiation (or relativistic matter), baryonic matter, dark matter (DM) and dark energy (DE). From current measurements, radiation and baryonic matter together make up only ~ 5 %, whereas DM accounts for about 27 % and dark energy for the remaining cosmic fluid (Planck Collaboration et al., 2020). Because DM and DE do not interact electromagnetically, they cannot be observed directly by current telescopes (however, it is possible to observe DM indirectly, for example via gravitational lensing). Nonetheless they are important for today's appearance of our universe. DM forms the basic structure of filaments and sheets, in which galaxies and galaxy clusters are embedded, while DE drives the expansion of the Universe.

The cosmic fluid, following the rules of the ΛCDM-model, dictates a hierarchical, bottom-up formation of structures. Cold dark matter (CDM, as given in the name ΛCDM) condenses via gravitational interaction to DM halos and decouples from the cosmic expansion, with small structures forming first and then merging together, forming larger structures. Baryonic matter falls into the growing gravitational wells where it forms more smaller-scale structures, such as galaxies. Galactic rotation curves and velocity dispersions of galaxy clusters indicate that DM halos still enclose those baryonic structures. The cosmic expansion, driven by DE, counteracts the structure formation, by lowering the matter density and consequently weakening gravity.

Cosmic Expansion

The scale factor a is a measure of cosmic expansion, it is the ratio of the Universe's size at a specific time to today's size. Today's value therefore is $a_0 = 1$, and it gets smaller when going back in the Universe's history. It therefore translates to redshift

z via

$$a = \frac{1}{1+z}, \tag{1.1}$$

where z from an observational perspective is defined as

$$z = \frac{\lambda_{\text{obs}} - \lambda_{\text{em}}}{\lambda_{\text{em}}}, \tag{1.2}$$

where λ_{obs} is the observed wavelength and λ_{em} is the emitted wavelength.

To describe the cosmic expansion, the Hubble parameter H is commonly used, which connects to the scale parameter via

$$H^2 = \left(\frac{\dot{a}}{a}\right)^2 = \frac{8\pi G}{3}\rho - \frac{Kc^2}{a^2} + \frac{\Lambda c^2}{3}, \tag{1.3}$$

where a dotted quantity denotes a time derivative, c is the speed of light, G is the gravitational constant and $\rho = \rho(t)$ is density, K denotes the curvature of the universe and Λ is the cosmological constant, a measure closely connected to DE. Cosmological measures are sometimes given with a factor $h = H_0/100\,\text{km}\,\text{s}^{-1}\,\text{Mpc}^{-1}$, which is used to account for the uncertainty of the Hubble parameter, as its exact value is unclear up to this day and differs depending on the used measures (see e.g., Bonamente et al., 2006; Komatsu et al., 2009; Riess et al., 2009; Suyu et al., 2010; Freedman et al., 2012; Riess et al., 2022).

Equation 1.3 is also the first Friedmann equation and directly translates to

$$H^2(a) = H_0^2\left[\Omega_{r0}a^{-4} + \Omega_{m0}a^{-3} + \Omega_{\Lambda 0} + \Omega_{K0}a^{-2}\right], \tag{1.4}$$

where the subscript 0 denotes present day values, r is radiation, and baryonic and dark matter are denoted by m. This equation ties the Hubble parameter to the ingredients of the cosmic fluid. Here, Ω is a dimensionless quantity defined by

$$\Omega = \frac{\rho}{\rho_{\text{crit}}} \tag{1.5}$$

and for curvature and cosmological constant is

$$\Omega_{\Lambda 0} = \frac{\Lambda c^2}{3H_0^2}, \quad \Omega_{K0} = -\frac{Kc^2}{H_0^2}. \tag{1.6}$$

Ω_{r0} and Ω_{m0} are defined by

$$\Omega_{X0} = \frac{8\pi G \rho_{X0}}{3H_0^2} \tag{1.7}$$

(where X denotes for r or m). Here, ρ_{crit} is the critical density at which the Universe is Euclidean if $K = 0$ and $\Lambda = 0$. The parameters H_0, Ω_{m0}, Ω_{r0} and $\Omega_{\Lambda 0}$ can for example be derived from observations of the cosmic microwave background (CMB), as done by Planck (Planck Collaboration et al., 2020), which report values of $H_0 = (67.4 \pm 0.5)$ km s^{-1} Mpc^{-1}, $\Omega_{m0} = 0.315 \pm 0.007$, $\Omega_{K0} = 0.001 \pm 0.002$ and $\Omega_{\Lambda 0} = 0.6847 \pm 0.0073$. This is consistent with a flat, expanding Universe.

Together with the second Friedmann equation

$$\frac{\ddot{a}}{a} = -\frac{4\pi G}{3}\left(\rho + \frac{3P}{c^2}\right) + \frac{\Lambda c^2}{3} \tag{1.8}$$

(where $P = P(t)$ is pressure) one can derive the adiabatic equation

$$\frac{\mathrm{d}}{\mathrm{d}t}\left(a^3 \rho c^2\right) = -P \frac{\mathrm{d}}{\mathrm{d}t}\left(a^3\right). \tag{1.9}$$

This equation can be broken down to a basic principle: Energy is conserved. The left hand-side represents a change in internal energy, which equals a pressure work on the right hand-side. From thermodynamics we know that this is only true in the absence of a heat flow. This indicates the fundamental property of isotropy, which would be violated by a heat flow. An isotropic Universe is the first fundamental assumption of cosmology, meaning that cosmological laws are independent from direction. The second basis is uniformity, i.e., the Universe looks the same everywhere. Otherwise the universality of the laws of physics could not be taken for granted. Observations and complementary simulations back this assumptions (see e.g., Springel et al., 2006). On large scales ($\gg$Mpc), galaxies are evenly distributed on the sky.

The critical density is used in the definition of a virial radius R_{vir} and virial mass M_{vir}, which is used as a measure of mass for a gravitationally bound system. The virial radius is defined as the radius within which the mean density is some factor f times the critical density of the Universe at this time, i.e.

$$\overline{\rho}\,(R < R_{\mathrm{vir}}) = f \rho_{\mathrm{crit}}. \tag{1.10}$$

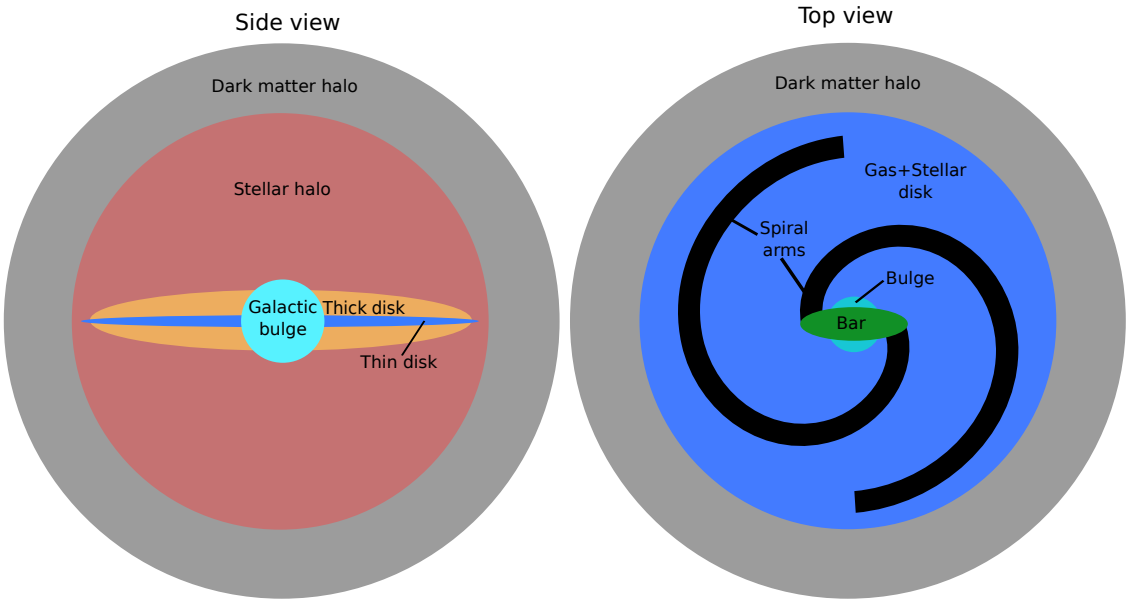

Figure 1.1: Schematic overview over the general structure of spiral galaxies such as the Milky Way as seen from the side (left) and top (right). A DM halo envelops the disk structure and the stellar halo. The stellar disk consists of the thick and thin stellar disk, with different scale heights, the center of the galaxy can be dominated by a galactic bulge and bar. Several spiral arms (usually two or more) are present in the stellar and gaseous structure.

The virial mass is then the mass within this radius. The factor f is often set to 200, an alternative notation of virial values therefore is with an index '200', '200c' or similar.

1.2.2 Galaxies

As mentioned in the previous section, DM halos are sites of galaxy formation. Recent observations make clear that galaxies formed very early on in the cosmic history, with the earliest currently known galaxy, JADES-GS-z14-0 found by the James Webb Space Telescope (JWST), being at a redshift of $z = 14.32^{+0.08}_{-0.20}$. This means that earliest galaxies already existed about 300 Myr after the Big Bang (Carniani et al., 2024). Following the formation of first stars and galaxies in the early Universe (see e.g., Bromm et al., 2009), galaxies further evolved and drove the reionization and metal enrichment of the Universe (see e.g., review from Madau & Dickinson,

2014).

Collapse within DM Halos

In the most simplified picture of galaxy formation, baryonic matter is collected in the gravitational wells of DM halos (see Fig. 1.1). DM particles can move freely within the halo, as they only interact via gravity, whereas baryonic gas undergoes different physical interactions that transform its potential energy into heat during collapse. This heat then has to be radiated away so the thermal pressure does not prevent gravitational collapse, making the process of collapse controlled by two timescales: The cooling time and the free-fall time.

The cooling time of gas at the halo virial temperature T_{vir} is

$$t_{\mathrm{cool}} = \frac{3k_B T_{\mathrm{vir}}}{2n\Lambda(T)}, \tag{1.11}$$

where k_B is the Boltzmann constant, n is the number density of gas particles and $\Lambda(T)$ is the cooling function. It is a formal description of cooling by different physical processes, such as bremsstrahlung, ionization/recombination, Compton scattering and electron scattering. Since the importance of those processes depends on gas metallicity, $\Lambda(T)$ differs for regions with different metallicity. The parameter t_{cool} describes the time a gas cloud needs to radiate away a significant fraction of its heat.

The free-fall time

$$t_{\mathrm{ff}} = \sqrt{\frac{3\pi}{32G\rho}} \tag{1.12}$$

is the time a gas cloud needs for collapse if it can collapse freely, i.e., no counteracting forces forbid its collapse. This is the case if $t_{\mathrm{cool}} < t_{\mathrm{ff}}$. In that case, the gas can radiate away its heat faster than it collapses, allowing for a free-fall collapse (Rees & Ostriker, 1977; Carroll & Ostlie, 2017; Schneider, 2015).

If on the other hand $t_{\mathrm{cool}} \gg t_{\mathrm{ff}}$, cloud temperature rises adiabatically as it collapses. This increases internal pressure which halts the collapse and the cloud ends in virial equilibrium (Carroll & Ostlie, 2017; Schneider, 2015).

The ability of gas to collapse to protogalactic structures therefore depends on its temperature and density. If the properties allow for collapse, protogalactic structures

form, which may already form stars. However, those structures undergo further collisions, tidal interactions and mergers with each other, resulting in more massive structures or the disruption of smaller ones (Carroll & Ostlie, 2017).

Spiral and Elliptical Galaxies

In a more or less unperturbed case, gas then settles with its angular momentum conserved, arranging it in a disk. This disk-like structure simplifies further cooling and star formation as it limits the gas to a restricted volume (Schneider, 2015). In these galaxies, elaborate structures such as galactic bulges, bars and spiral arms emerge (see Fig. 1.1). As the first stars in young galaxies are metal poor and massive, they have a short lifetime, at the end of which they explode as supernovae, heating the gas and increasing the turbulence, which, in turn, slows down star formation (Carroll & Ostlie, 2017).

Elliptical galaxies (also called early-type galaxies) are thought to form from major mergers of those gas-rich disk galaxies (or late-type galaxies) (Toomre, 1977; Barnes, 1989; Schneider, 2015). Those mergers destroy the stellar disk and change the galactic structure completely, as they perturb the gas, increase velocity dispersions, trigger star bursts and also the activity of active galactic nuclei (Schneider, 2015; Hani et al., 2020; La Marca et al., 2024). The interaction heats or even ejects the gas, causing the low SFRs observed in today's elliptical galaxies (Schneider, 2015).

Emergence of Spiral Arms

Close interactions between galaxies can also be a reason for the emergence of spiral arms in galaxies (Dobbs et al., 2010; Tress et al., 2020a, see Fig. 1.2), which we see in observations of gas and stars and emerge in simulations (see Fig. 1.1 for a general picture). In general, dynamically cold (i.e., with a low velocity dispersion σ) disks are likely to form spiral structures, because any disturbance can induce it (Goldreich & Lynden-Bell, 1965). As a dynamically hot disk (i.e., when the kinetic energy is dominated by random motion) is less prone to develop spiral structures, the presence of gas is of utter importance. Because it can produce new dynamically cold stars it keeps conditions such that spiral arms can arise (Sellwood & Carlberg, 1984). Spiral arms are sites of ongoing star formation, as seen in Fig. 1.2, but it is debated if spiral arms increase the star formation efficiency (SFE), or if they merely

Figure 1.2: M51 as seen by the Hubble Space Telescope (HST). Two spiral arms are induced by the close interaction with NGC 5195. Ongoing star formation in the spiral arms is indicated by red and blue regions. Credit: NASA, ESA, S. Beckwith (STScI) and the Hubble Heritage Team (STScI/AURA)

collect dense gas which would form stars anyway. Findings in support for both theories were presented (e.g., Seigar & James, 2002; Foyle et al., 2010; Querejeta et al., 2021), while numerical simulations tend to find no enhanced SFE (Dobbs et al., 2011b; Kim et al., 2020).

In isolated galaxies, a theory for the formation of spiral structures is the self-propagating star formation model (Mueller & Arnett, 1976; Gerola & Seiden, 1978), which assumes spiral arms to arise because of star formation and stellar feedback. A star-forming region gets stretched into an arc by shear forces, and stellar feedback from massive stars shapes the surrounding ISM by compressing it, inducing new star formation. This leads to a propagation of star formation throughout the disk, that forms spiral arms. In this model, spiral arms are transient features, that appear and disappear in a disk galaxy. Another theory of the origin of spiral arms is the density wave theory (Lin & Shu, 1964; Shu, 2016), which suggests that spiral arms

Figure 1.3: Bar of NGC 1512 as seen by the James Webb Space Telescope (JWST, upper left) and HST (lower right). Dust lanes feeding the central ring structure are clearly visible (orange in JWST, brown in HST). The central ring contains stars (blue) and gas. Credit: NASA, ESA, CSA, STScI, Janice Lee (STScI), Thomas Williams (Oxford), PHANGS Team

are quasistatic density waves, i.e., overdense regions that move at a different speed than the rotation speed of the disk, the global pattern speed Ω_p. Matter approaching the overdense region will increase its velocity, but decrease it when overtaking it, making the overdensity a self-sustaining long-lived feature.

Formation of the Galactic Bar

Density waves can also lead to the formation of bars in galaxies (see Fig. 1.1), when a cavity wave undergoes a swing amplification when reflected between the galactic center and the co-rotation radius of the bar (Tress, 2021). Galaxies with massive bulges then often lack bars, because as the central mass of the galaxy increases, an inner Lindblad resonance (ILR, a Lindblad resonance is a resonance between the orbits of individual stars and large-scale density perturbations where $m(\Omega_\mathrm{p} - \Omega) = \pm\kappa$ is fulfilled, with Ω the angular frequency of the star and κ the epicyclic frequency in a perturbation with an m-fold symmetry; for a bar structure $m = 2$, Binney & Tremaine, 2008) develops and the wave can no longer travel all

the way to the center, cutting the feedback-loop (Tress, 2021). Another possible explanation for the formation of bars is that eccentric orbits in the galactic center align along a common major axis (Lynden-Bell, 1979). Within the bar, several families of stellar orbits develop. Orbits of the x1 family are elongated along the major axis of the bar and rotate in the same direction. Near the center, orbits of the x2 family are elongated perpendicular to the bar. The co-rotation radius (where $\Omega_\mathrm{p} = \Omega$) strongly limits the bar, usually they extend to about 80 % of the galactocentric distance of the co-rotation (Elmegreen et al., 1996). Within the bar, often ring-like structures can be found, as seen in Fig. 1.3, fed by dust lanes reaching from the tip to the center of the bar. The analogue of such a structure in the Milky Way is the central molecular zone (CMZ). Even though a majority of spiral galaxies are found to have bars (the barred fraction of spiral galaxies is reported to be between 55 % (Aguerri et al., 2009) and 72 % (Eskridge & Frogel, 1999)), they are non-longlived features, that can be destroyed and reappear several times during a galaxies existence and also its appearance can change drastically (Bournaud & Combes, 2002; Bournaud et al., 2005; Łokas, 2019).

1.2.3 Cloud and Star Formation

Star Formation in Galactic Context

Galaxies are sites of ongoing star formation, although not all to the same extent. In general, elliptical galaxies show a much lower star formation activity than spiral galaxies, placing them in the red sequence and blue cloud respectively on the galactic color-magnitude diagram (Bell et al., 2004). Depending on their stellar mass M_*, star-forming galaxies form a sequence in SFR, the star-forming main sequence (SFMS), which can be described by SFR $\propto M_*^m$. The exponent m differs greatly with redshift and usually is reported to lay between 0.6 and 1 (Speagle et al., 2014).

The physical processes at play in galactic star formation, however, are poorly understood. From a most naive understanding, one would expect a constant correlation between the surface density of SFR (Σ_SFR) and gas (Σ_gas) of the form $\Sigma_\mathrm{SFR} \propto \Sigma_\mathrm{gas}^{1.5}$ from Equation 1.12 and

$$\mathrm{SFR} = \epsilon \frac{M_\mathrm{gas}}{t_\mathrm{ff}}. \tag{1.13}$$

Here, ϵ denotes the SFE per free-fall time. We will explain it in more detail later on. The Kennicutt-Schmidt-relation, which connects the surface density of gas to SFR (Schmidt, 1959; Kennicutt, 1998), actually falls remarkably close to this value. Kennicutt (1998), in his study of 97 galaxies, finds a correlation of

$$\Sigma_{\mathrm{SFR}} = (2.5 \pm 0.7) \times 10^{-4} \left(\frac{\Sigma_{\mathrm{gas}}}{\mathrm{M}_\odot\,\mathrm{pc}^{-2}} \right)^{1.4\pm0.15} \mathrm{M}_\odot\,\mathrm{yr}^{-1}\,\mathrm{kpc}^{-2}. \tag{1.14}$$

Correlations between Σ_{SFR} and Σ_{gas} are found over a wide range of galaxy classes, from normal spiral to starburst galaxies. However, the exact form of this relation is frequently discussed and modified (see e.g., Bigiel et al., 2008).

Giant Molecular Clouds - The Sites of Star Formation

Star formation in galaxies occurs exclusively in giant molecular clouds (GMCs). Those are structures with a typical size of 20 to 200 pc and a mass of $10^2 - 10^7$ $\mathrm{M}_\odot$ (Blitz, 1993; Oka et al., 2001; Roman-Duval et al., 2010; Schulz, 2012; Demachi et al., 2024), which consist of molecular hydrogen (H_2), at a temperature of 10-50 K (Oka et al., 2001; Roman-Duval et al., 2010; Schulz, 2012) and a density of about $10^2 - 10^3$ cm^{-3} (Blitz, 1993; Carroll & Ostlie, 2017; Girichidis et al., 2020). Even though the cold neutral medium (see Section 1.3.2 for explanation) together with molecular gas makes up up to 50 % of the ISM (Pringle et al., 2001; Ferrière, 2001), its volume filling factor is less than 1 % (Berkhuijsen, 1999; Ferrière, 2001), as it is arranged in cold, dense structures where it is protected from destruction.

Despite of the ISM being dominated by hydrogen (see Section 1.3.2), the formation of molecular hydrogen is very inefficient. As direct formation in the gas phase is strongly suppressed (Latter & Black, 1991), most H_2 is formed by adsorption of H atoms on the surface of dust grains, where they can merge (Gould & Salpeter, 1963; Hollenbach & Salpeter, 1971). The characteristic time for such formation of molecular hydrogen is 10^8 yr (Gould & Salpeter, 1963). In addition to inefficient formation, the lifetime of unshielded H_2 in the ISM is low, just on the order of $\sim 10^{10}$ s (Stecher & Williams, 1967). The main process responsible for destruction of H_2 is photodissociation, when the molecule is excited by a Lyman-Werner-photon (11.2-13.6 eV) and in about 15 % of the cases decays into the vibrational continuum (Draine & Bertoldi, 1996). Because this is a line-based and not a continuum-based

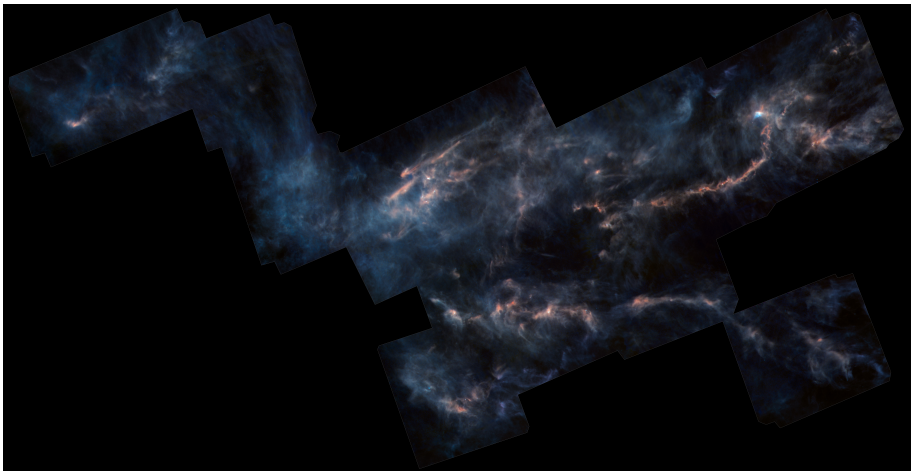

Figure 1.4: Taurus Molecular Cloud as seen by ESA's Herschel observatory. Filaments and dense clumps are clearly visible in the clouds structure. In the upper left, the pre-stellar core Lynds 1544 can be seen. Credit: ESA/Herschel/NASA/JPL-Caltech; acknowledgement: R. Hurt (JPL-Caltech)

process, self-shielding is efficient, such that H_2 molecules on the surface of a molecular cloud absorb most of the Lyman-Werner photons, and only a small fraction can reach further into the cloud. Therefore, the rate of photodissociation in molecular clouds is much lower than in optically thin gas (Girichidis et al., 2020). The process becomes important once the column density of H_2 reaches $N_{H_2} \sim 10^{14}$ cm^{-2} (Draine & Bertoldi, 1996; Girichidis et al., 2020). The total hydrogen column density N_H where self-shielding becomes important, then depends on the interstellar radiation field G_0 (ISRF, expressed in Habing units, Habing 1968) and the gas density n (Girichidis et al., 2020):

$$N_H = 10^{20} G_0 n^{-1} \,\mathrm{cm}^{-2}. \tag{1.15}$$

Because of this self-shielding, GMCs have relatively sharp boundaries, where the transition from atomic to molecular hydrogen takes place. Outside of these boundaries H_2 gets photodissociated, leading to a shell of atomic hydrogen surrounding a GMC. Inside, GMCs show a highly filamentary structure, as can be seen in Fig. 1.4, and they can further be substructured into clumps and cores. Clumps are coherent overdense regions within the GMC, with a mass of $50 - 500$ M$_\odot$, sizes up to

a few pc, a mean density of $10^3 - 10^4$ cm^{-3} and a temperature of 10-20 K (Bergin & Tafalla, 2007; Loren, 1989; Williams et al., 1994). They follow a distribution of $\mathrm{d}N/\mathrm{d}M \sim M^{-\alpha}$, with α between 1.4 and 1.8 (Bergin & Tafalla, 2007; Blitz, 1993; Kramer et al., 1998). Cores are even smaller, with masses of just a few $M_\odot$, sizes of $0.03 - 0.2$ pc, a high density of $10^4 - 10^5$ cm^{-3} and temperatures of 8-12 K (Bergin & Tafalla, 2007; Jijina et al., 1999; Caselli et al., 2002; Motte et al., 1998). They are interpreted as sites of ongoing star formation.

GMCs are not in equilibrium with their surrounding gas (Burkert, 2006). They are sometimes found to be gravitationally bound (Lada et al., 2024), indicating that gravitational instabilities aid in their emergence, however, most GMCs are found to be unbound (Dobbs et al., 2011a). As the galaxy is a rotating system, the Coriolis force supports gas against collapse, meaning that the Jeans criterion (which we will describe later during this section) is not the only criterion that has to be met for gas to collapse. Instead, the Toomre parameter Q (Toomre, 1964) can be used as a metric if a rotationally supported gas disk is stable against perturbations. This is the case if

$$Q = \frac{c_s \kappa}{\pi G \Sigma} > 1, \tag{1.16}$$

where c_s is the sound speed, Σ is the surface density of the disk and κ is the aforementioned epicyclic frequency. If $Q < 1$ the disk is unstable, perturbations of the size of GMCs need a Q of the order of 0.1 to be prone to collapse. This is only possible in cold gas, where the sound speed is sufficiently low. GMCs therefore can be formed by Toomre instabilities driven by thermal instabilities (Smith, 2018).

In general, conditions have to be produced that enable high column densities, which are needed to shield the GMC from the ISRF. Any process producing such environmental conditions is feasible to trigger GMC formation. GMCs could also form from inelastic collision of small atomic clouds (Oort, 1954; Field & Saslaw, 1965), which continues up to the point where mass and density are high enough for self shielding and self-gravity begins to dominate the cloud. Density waves in spiral arm could increase collision rates as densities are higher there (Tress, 2021). However, the time needed to form massive GMCs in this model is too long compared to GMC lifetimes (which are around 10-20 Myr, Kawamura et al. 2009; Meidt et al. 2015; Corbelli et al. 2017; Chevance et al. 2020). Another possible trigger of

GMC formation is turbulence, as GMCs can form where large-scale turbulent flows converge (Mac Low & Klessen, 2004; Ballesteros-Paredes et al., 2007). Turbulent flows can also add to accretion onto the GMC, which boosts and sustains turbulence in the cloud (Klessen & Hennebelle, 2010; Goldbaum et al., 2011). In a magnetized medium that is already near gravitational instability, Parker instabilities (Parker, 1966) can cause gravitational instabilities.

As mentioned before, GMCs have a lifetime of the order of 10 Myr, which is about an order of magnitude larger than their free-fall time from Equation 1.12 with the given properties. This already indicates the existence of a force stabilizing the clouds against collapse. If we now have a look at the SFE ϵ, the picture becomes even clearer. From Equation 1.13 and the depletion time

$$t_{\mathrm{depl}} = \frac{M}{\mathrm{SFR}}, \tag{1.17}$$

which gives the timescale in which a GMC would consume its gas by star formation, ϵ can be defined as

$$\epsilon = \frac{t_{\mathrm{ff}}}{t_{\mathrm{depl}}}. \tag{1.18}$$

In their study of molecular gas in M51, Leroy et al. (2017) find a depletion time of the order of Gyr, together with the low free-fall times, results in a SFE of just ~ 0.1 %. What causes this low efficiency of star formation in the cold, dense gas of GMCs?

In general, for a cloud to collapse, its self-gravity has to overcome all other present forces, like turbulence, thermal or magnetic pressure. The Jeans criterion, which can be derived from the virial theorem, gives a first estimate, if a system is dominated by gravity. It can be expressed as the Jeans mass

$$M_J \simeq \left(\frac{5k_BT}{G\mu m_{\mathrm{H}}}\right)^{\frac{3}{2}} \left(\frac{3}{4\pi\rho}\right)^{\frac{1}{2}} \tag{1.19}$$

(μ is the mean molecular weight and m_{H} the proton mass) or the Jeans length

$$\lambda_J = \left(\frac{15k_BT}{4\pi G\mu m_{\mathrm{H}}\rho}\right)^{\frac{1}{2}}, \tag{1.20}$$

and a cloud is unstable if its mass exceed the Jeans mass or its radius exceeds the Jeans length (Carroll & Ostlie, 2017). This treatment, however, neglects many forces opposing collapse. If one, for example, takes into account a magnetic field B within the cloud, and an external pressure of P_0 acting on the cloud, the virial equation can be written as (Smith, 2018; Spitzer, 1968)

$$4\pi R^3 P_0 = 3\frac{Mk_BT}{\mu m_\mathrm{H}} - \frac{1}{R}\left(\frac{3}{5}GM^2 - \frac{1}{3}R^4B^2\right). \tag{1.21}$$

The terms in parentheses lets us then express a critical mass above which gravity overcomes magnetic stabilization (Smith, 2018):

$$M_\mathrm{crit} = \frac{1}{3}\left(\frac{5}{G}\right)^{\frac{3}{2}}\frac{B^3}{(4\pi\rho)^2} \approx \left(4\times10^6\,\mathrm{M}_\odot\right)\left(\frac{n}{1\,\mathrm{cm}^{-3}}\right)^{-2}\left(\frac{B}{3\,\mu\mathrm{G}}\right)^3. \tag{1.22}$$

At a typical magnetic field strength of the MW of 3 μG and a typical ISM density of ~ 1 cm^{-3}, this critical mass is already higher than masses of many GMCs. A magnetic field therefore stabilizes the ISM against gravitational cloud formation. Gas stabilized in this way by a magnetic field is referred to as subcritical, whereas clouds that are massive enough to collapse despite their magnetic field are supercritical. As the magnetic flux is conserved, M_crit does not change under compression, i.e., a subcritical cloud has to either gain mass or dissipate its magnetic field. A suitable mechanism for that in the molecular gas of GMCs would be ambipolar diffusion. However, from observations we know most GMCs to be supercritical or only slightly subcritical (Crutcher, 1999; Bourke et al., 2001; Crutcher et al., 2010).

Moreover, turbulence can stabilize a GMC against collapse. Sources of turbulence are plenty, and while it can also induce overdense, gravitationally dominated regions within the cloud, in total it can have a stabilizing effect (e.g., Krumholz & Tan, 2007).

Another reason for low SFE can be stellar feedback. As the cloud collapses it produces stars. Their presence can alter the cloud in numerous ways, by heating and ionizing the gas, dispersing it by radiation pressure and stellar winds (Tasker et al., 2015; Chevance et al., 2022) or finally supernovae. If this feedback is efficient, it can stop star formation (Tasker et al., 2015) and disperse the cloud soon after the formation of first stars (Chevance et al., 2022). The cloud thus would get destroyed

before it can use up more of its gas in star formation.

Finally, GMCs also can be destroyed by external causes, like shear forces from galactic rotation or other dynamical influences (Jeffreson & Kruijssen, 2018).

The Stages of Star Formation

The collapse and formation of a star has three stages: prestellar core, protostellar collapse and pre-main-sequence contraction, which we now describe in accordance with Bodenheimer (2011) and Carroll & Ostlie (2017).

As mentioned previously, overdense regions form as the GMC cools and contracts. When they become unstable due to one of the aforementioned reasons, they begin to collapse. As the matter is optically thin, this is an isothermal process at first, meaning that density of the gas rises, while temperature does not. This implies that the local Jeans mass decreases (see Equation 1.19). Therefore, local collapse points develop and the cloud fragments. This is thought to be the reason why stars often form in clusters. When the gas becomes optically thick due to high density, it transitions to an adiabatic collapse. From that moment onward, the temperature of the gas increases. Finally, the collapse is stopped when the gas pressure becomes high enough to withstand the gravitational forces. Since clouds do not have uniform density but a density gradient, they experience inside-out-collapse, i.e., while the inner region might already be stopped in its collapse by internal pressure, surrounding gas still collapses onto it. When it hits the halted region, a shock forms, heating the gas further. The temperature therefore keeps rising until it is sufficient to split hydrogen molecules. As this process absorbs the energy from contraction, a second collapse sets in, which continues until a new hydrostatic equilibrium is reached. At this point, the temperature of the protostar already is at the order of several thousand Kelvin and it is deeply embedded into a shell of matter still accreting onto the core. Most of the protostar's energy actually still comes from this accretion. Because of angular momentum conservation, the matter of the shell organizes into a rotating disk around the protostar. Coupling within the disk enables transport of angular momentum, which makes further infall possible that otherwise would be forbidden. Transition to a pre-main-sequence star is marked by the moment when most energy is no longer coming from accretion, but from contraction of the star. The central temperature further increases and

fusion of deuterium and lithium starts, until finally temperatures sufficient for the PP chain and CNO cycle are reached, at which point the star transitions to the main sequence.

The final mass of the formed star depends on many factors, the initial mass of the gas cloud being just one of them. Different initial mass functions (IMF) try to determine the statistics of the masses of formed stars, with the most prominent ones being those of Salpeter (1955), Kroupa (2002) and Chabrier (2003a). IMFs describe the number of stars per unit volume in given mass interval and usually take the form of a power law:

$$\xi(m) = \frac{\mathrm{d}N}{\mathrm{d}m} = \xi_0 m^{-\alpha}. \tag{1.23}$$

For α, Salpeter (1955) proposed 2.35 for stars of masses $0.4 - 10\ \mathrm{M}_\odot$. Kroupa (2002) refined that IMF at the low mass end by making it a broken power law with $\alpha = 0.3$ for masses between 0.01 and 0.08 $\mathrm{M}_\odot$ and $\alpha = 1.3$ between 0.08 and 0.5 $\mathrm{M}_\odot$. Chabrier (2003a) deviates from a pure power law formulation and gives

$$\xi(\log m) = \frac{\mathrm{d}N}{\mathrm{d}\log m} = \begin{cases} A \exp\left[-\frac{(\log m - \log m_c)^2}{2\sigma^2}\right] & m \leq 1.0\,\mathrm{M}_\odot \\ 4.43 \times 10^{-2} m^{-1.3} & m > 1.0\,\mathrm{M}_\odot \end{cases}, \tag{1.24}$$

with $A = 0.158$, $m_c = 0.079$ and $\sigma = 0.69$ for individual stars and $A = 0.086$, $m_c = 0.22$ and $\sigma = 0.57$ for stellar systems (binaries). In general, the slope of the stellar IMF is less steep than for clumps in GMCs, which we quoted before.

1.3 The Galactic Environment

1.3.1 Galaxy Clusters and the Intracluster Medium

In the deep potential wells at the intersections of dark matter filaments, massive, gravitationally bound structures form, called galaxy clusters or groups (Schneider, 2015). Those structures can have thousands of member galaxies and therefore are the most massive bound structures known today, ranging in mass from 10^{12} to 10^{15} $M_\odot$ (Carroll & Ostlie, 2017; Schneider, 2015). Structures that massive should form late in cosmic time however, protoclusters are found at redshifts as high as $z \sim 8$ (Trenti et al., 2012).

Historically, agglomerations of galaxies were divided into 'groups' and 'clusters' by number: Groups have less than 50 members in a sphere of less than $1.4-1.5h^{-1}$ Mpc across (Carroll & Ostlie, 2017; Schneider, 2015), whereas clusters have more than 50 members and a larger physical size (Schneider, 2015).

The MW itself is part of a group, called the Local Group, together with M31 and M33 and about 50 more galaxies, most of them faint dwarf galaxies (Schneider, 2015). The mass of the Local Group is believed to be between $2 - 5 \times 10^{12}$ $M_\odot$ (Peñarrubia et al., 2014; van der Marel et al., 2012), about the combined mass of M31 and the MW, the two most massive members of the group. Those massive spiral galaxies with their satellite galaxies build two lobes that form the group, moving towards each other at a relative velocity of about 109.3 ± 4.4 km s^{-1} (van der Marel et al., 2012). The Local Group then is part of the Virgo Supercluster (which has a mass of about $10^{15}h^{-1}$ $M_\odot$, Einasto et al., 2007).

Even though for historical reasons literature differentiates between 'groups' and 'clusters' of galaxies, we will omit this distinction and adopt the term 'cluster' as a collective term.

Properties of Field and Cluster Galaxies

Properties of galaxies differ between those located within a cluster and those outside of them (we will call those galaxies 'field galaxies' from here on). Cluster galaxies tend to have a lower SFR (Bower & Balogh, 2004), redder color (Kennicutt, 1983) and are more HI deficient compared to field galaxies (Giovanelli & Haynes, 1985; Boselli & Gavazzi, 2006; Roediger, 2009). However, one of the most prominent dif-

ferences is the spiral fraction: Clusters are dominated by elliptical galaxies, whereas luminous field galaxies are predominantly spirals (Dressler, 1980). This effect is named the morphology-density-relation.

A second effect was found by Butcher & Oemler (1984), a correlation between cluster color and redshift. At the present epoch, the fraction of blue galaxies in clusters is about 0.03 and increases with redshift (Butcher & Oemler, 1984), until it reaches the same fraction as found in field galaxies at a redshift of $z \gtrsim 1.3$ (Schneider, 2015). In literature this is named the Butcher-Oemler effect.

Both effects can be explained by clusters not being static but evolving objects, with field galaxies getting caught by the gravitational potential of the cluster and subsequently falling into it, losing large parts of their interstellar gas in the process (Schneider, 2015). This suppresses further star formation in the infalling galaxy, which gradually gets transformed into an S0 or early-type galaxy. The lost ISM becomes part of the intracluster medium (ICM).

The Intracluster Medium

The ICM envelopes all galaxies of a cluster and consists of two components: a diffuse distribution of stars which do not belong to any galaxy (Carroll & Ostlie, 2017), and a hot diffuse ionized gas at temperatures between $10^7 - 10^8$ K (Schneider, 2015). This gas makes up about 15 % of the total cluster mass, even though baryonic matter is responsible for just a minority of cluster mass, as about 80 % is made up by DM (Schneider, 2015). It has a density between 10^{-3} and 10^{-1} cm^{-3} (which is up to 7 orders of magnitude higher than the mean cosmic baryonic density, Peterson & Fabian, 2006). Due to bremsstrahlung, the gas in the ICM is a strong X-ray emitter with characteristic luminosities of $L_X \sim 10^{43} - 10^{45}$ erg s^{-1}, making clusters the second brightest extragalactic X-ray emitters right after active galactic nuclei (Schneider, 2015). An example is depicted in Fig. 1.5, where we show the X-ray emission in the Coma cluster. There one can also see an increase of intensity towards the cluster center, which is typical for X-ray emission by the ICM.

1.3.2 The Interstellar Medium

The ICM, at least partially, is gas stripped from the interior of galaxies, i.e., is made up of former ISM. The ISM is a medium that permeates a galaxy, in the Milky

Figure 1.5: The Coma cluster as seen in optical by SDSS overlayed with X-ray emission as seen by XMM-Newton's European Photon Imaging Camera (EPIC). The clusters shows strong, extended X-ray emission that increases towards the cluster center. Credit: ESA/XMM-Newton/SDSS/J. Sanders et al. 2019

Way it makes up about 10-15 % of the galactic disk mass (Ferrière, 2001) and has a mass of about 1.2×10^{10} $M_\odot$ (Kalberla & Kerp, 2009). It mainly consists of gas, made up by number of 90.8 % hydrogen, 9.1 % helium and 0.12 % metals (by mass the fraction is 70.4 %, 28.1 % and 1.5 % respectively, Ferrière, 2001). About 200 different molecules have been detected in the ISM (Endres et al., 2016).

ISM Phases

While the ISM spans a wide range in temperature ($10^1 - 10^8$ K) and density ($10^{-2} - 10^2$ cm^{-3} and even higher densities in GMCs), it mostly resides in distinct thermal phases. Those can be most simply derived if thermal equilibrium and pressure balance is assumed, as proposed by Field et al. (1969). This results in two stable solutions covering a wide range of pressures. The first is called the cold neutral medium (CNM), which has a temperature of $50-100$ K and a density of $20-50$ cm^{-3},

the second the warm neutral medium (WNM), with temperatures of 6×10^3 to 10^4 K and densities of $0.2 - 0.5$ cm^{-3}. Gas at an intermediate temperature will, depending on its density, be cooled until it becomes part of the CNM, or heated until it reaches the WNM (Girichidis et al., 2020). McKee & Ostriker (1977) expanded this model by a third component, the hot ionized medium (HIM). This is created by supernovae and winds from massive stars, that heat and ionize their surrounding gas, creating bubbles of low density gas (10^{-2} cm^{-3}) at temperatures of $T \sim 10^6$ K (Girichidis et al., 2020). The cooling function Λ already mentioned in Section 1.2.2 is such that cooling times of gas at these temperatures and densities are substantial, such that, even though the gas will cool eventually, it builds a third phase of the ISM. Photoionization and also collisional ionization in the warm medium creates a fourth phase, the warm ionized medium (WIM), at the same density as the WNM and temperatures of $T \sim 8 \times 10^3$ K (Girichidis et al., 2020). At high densities, the CNM transitions to form molecular clouds at the properties mentioned in Section 1.2.3.

Interstellar Dust

About 0.5-1 % of ISM mass consists of dust grains (Ferrière, 2001) and is usually cold, at the order of tens of K (Hocuk et al., 2017). Those grains mainly consist of graphite (Mathis et al., 1977; Draine & Lee, 1984; Ferrière, 2001), silicate (Knacke & Thomson, 1973; Draine & Lee, 1984; Ferrière, 2001) and macroscopic molecules called polycyclic aromatic hydrocarbons (PAH) (Leger & Puget, 1984; Duley & Williams, 1981; Ferrière, 2001) and have sizes ranging from 50 nm to 0.25 μm (Mathis et al., 1977; Girichidis et al., 2020). The distribution of size a follows a power law of the form $N(a) \propto a^{-q}$ and $3.3 < q < 3.6$ (Mathis et al., 1977) and is usually quoted as $q = 3.5$ (Ferrière, 2001; Girichidis et al., 2020). Metals get depleted from the interstellar gas by getting locked-up in dust grains (Ferrière, 2001). The dust is mainly formed in the atmospheres of asymptotic giant branch (AGB) stars (Waters, 2004), but can also form in SN explosions (Douvion et al., 2001; Dunne et al., 2003). Dust grains have an important impact on the ISM chemistry, by being the main site of H_2 formation (see Section 1.2.3), and play a role in the ISM temperature balance (see Section 1.3.2).

The Magnetic Field

Dust grains are also important for the observation of galactic magnetic fields, as one of the main phenomena tied to magnetic fields is dust polarization. As the dust grains are not spherical but elongated, they align with their longer axis perpendicular to the magnetic field, resulting into polarization of light passing them[1]. Because a large fraction of the ISM is ionized, galactic magnetic fields are often treated in ideal MHD, as the field is expected to be "frozen-in" into the medium, i.e., coupled to the gas flow. Equipartition between energy density in magnetic fields and gas is expected (Chandrasekhar & Fermi, 1953; Groves et al., 2003), which results in a theoretical correlation of $B \propto \sqrt{\rho_{\mathrm{gas}}}$. Generally, a correlation of $B \propto \rho_{\mathrm{gas}}^{\alpha}$ is assumed, where α observationally is found to be between 0.3 and 0.5 (Niklas & Beck, 1997; Manna & Roy, 2023; Heesen et al., 2023). Simulations find similar results (e.g., Kim et al., 2001). Because of this, they counteract collapse of gas under gravity, as we described in Section 1.2.3. The origin of galactic magnetic fields is not fully understood, however, they are thought to develop from initial seed fields via small- and large-scale dynamos (Beck & Wielebinski, 2013). On a galactic scale the fields are mostly parallel to the galactic disk and trace structures such as spiral arms. Even though they are very weak - usually just a few μG in the ISM of spiral galaxies - they are important for the energy budget of the ISM (Han, 2017).

Cosmic Rays

In terms of energy, another important component are cosmic rays (CR). Those are high-energy particles (mostly protons, Girichidis et al., 2020), spanning an energy range from less than 10^7 eV to at least 3×10^{20} eV (Carroll & Ostlie, 2017), with their energy spectrum following a power law of the form (Aartsen et al., 2013)

$$\frac{\mathrm{d}N}{\mathrm{d}\ln E \mathrm{d}A\mathrm{d}\Omega\mathrm{d}t} \propto \left(\frac{E}{1\,\mathrm{GeV}}\right)^{-\gamma+1}, \tag{1.25}$$

where γ ranges between 2.6 and 3.4, depending on the energy range. As those are charged particles, they couple to the magnetic field lines and vice versa, resulting in streaming instabilities which heat the ISM (Girichidis et al., 2020). Several processes

[1] This is an overly simplified description of the phenomenon, for an in-depth review see e.g., Lazarian, 2007; Han, 2017

are discussed for CR production, such as shocks in SN and stellar winds (Ferrière, 2001; Girichidis et al., 2020).

Kinetic energy, cosmic rays and magnetic fields contribute about equally to the energy budget of the ISM (Boulares & Cox, 1990; Ferrière, 2001).

Cooling and Heating Processes in the ISM

We already mentioned the cooling function Λ to be important for the thermal phases of the ISM, and now want to describe in a bit more detail the processes of heating and cooling present in the ISM. The most basic physical process leading to heating or cooling of gas is adiabatic contraction or expansion, which we already mentioned in Section 1.2.3. Apart from that, mostly radiative processes are of importance, which - in a very crude simplification - are based on the fact that particle collisions can excite internal excited states of particles, which can deexcite by the emission of a photon and, vice versa, photons can excite internal degrees of freedom and by collision this energy is transferred into kinetic energy.

At low temperatures < 20 K and high densities $\sim 10^3$ cm^{-3}, cooling is dominated by rotationally excited states of CO. At $T \sim 20$ K and higher, C^+ also becomes important at low densities (with rising gas density, it is bound increasingly in CO), and cooling from fine structure lines of atomic neutral C is more efficient than CO cooling (Girichidis et al., 2020). At densities $\gg 10^3$ cm^{-3}, the relative population of the lowest rotational levels of CO quickly reach the local thermodynamical equilibrium and CO molecules tend to freeze out on dust grains (Girichidis et al., 2020). At about 100 K, cooling by transitions between fine structure energy levels begins to fully dominate cooling, with the main actors being C^+, C, O and at higher temperatures (because they do not have fine structure in their ground state) H and H_2 (Girichidis et al., 2020). At $T > 10^4$ K, most cooling is via dipole-allowed electronic transitions. Between $10^4 - 10^5$ K, H and He dominate here and, when these elements are fully ionized, atomic line transitions of heavier elements take over, mostly C, O, Ne and Fe (Girichidis et al., 2020; Tress, 2021). When even metals are fully ionized, at temperature $> 10^7$ K, cooling via bremsstrahlung dominates (Draine, 2011). In the presence of dust, dust cooling is another important cooling component: Dust grains are efficient radiators, and if the dust temperature is lower than the gas temperature, energy will flow from gas to dust and being radiated away (Girichidis et al.,

2020).

In terms of heating, various stellar processes like stellar winds, jets and SN can heat the ISM (Tress, 2021). Another source is photoelectric heating, where UV photons hit dust grains, freeing electrons from them which in subsequent collisions heat the gas (Girichidis et al., 2020). Moreover, UV photons can photo-dissociate H_2 (see Section 1.2.3). The resulting hydrogen atoms have a kinetic energy higher than that of the surrounding gas particles, i.e., are heated (Girichidis et al., 2020). However, as mentioned, the absorption of a photon only lead to dissociation in about 15 % of the cases. If that does not happen, the H_2 molecule often decays into a bound rovibrational state and via collisional de-excitation transfers the photon energy to kinetic energy (Girichidis et al., 2020; Tress, 2021). Other sources of heating can also be cosmic rays and high-energy radiation like X-rays (Girichidis et al., 2020), and finally turbulence (Minter & Spangler, 1997; Tress, 2021).

1.3.3 Stellar Feedback

Feedback from stars plays an important role in the destruction of molecular clouds and in self-regulating star formation (see Section 1.2.3), as well as in shaping the chemical and thermal composition of the ISM (see Section 1.3.2).

Pre-Supernova Feedback

Stellar feedback is dominated by massive O and B type stars, even though these make up just a minor fraction of the stellar population (Ferrière, 2001; Abbott, 1982). Primarily, they affect their surrounding ISM by radiation, via the dissociation of H_2 (see Section 1.2.3 and 1.3.2) and other molecules, and ionization and heating of the surrounding gas, creating the WIM (Ferrière, 2001). Their strong ionizing radiation produces HII regions, i.e., hot ($T \sim 8000$ K, Ferrière, 2001) expanding regions of high thermal pressure where hydrogen is fully ionized. Strömgren (1939) derived the radius R_S of an HII region in photoionization equilibrium around a star with a photon flux S within a uniform density medium with the recombination rate αn_H^2 to be (Carroll & Ostlie, 2017)

$$R_S \simeq \left(\frac{3S}{4\pi\alpha n_H^2} \right)^{\frac{1}{3}}, \tag{1.26}$$

Figure 1.6: Southern region of the Carina nebula as seen by the infrared array camera of NASA's Spitzer Space Telescope. Located above the picture frame is Eta Carinae, a massive star, that with its radiation and winds destroys the gas cloud, leaving just the pillar-like structures seen here in pink. Credit: NASA/JPL-Caltech/N. Smith (University of Colorado at Boulder)

which depending on the density can range from 0.1 pc to 100 pc. After the formation of an O or B star, the expansion of the HII region surrounding it to a size of order R_S is rapid. However, even after reaching a photoionization equilibrium, the ionized gas is overpressured compared to its surroundings. A low-density cavity surrounded by a denser shell forms.

Stellar winds are the second important form of feedback from stars, and can be produced by stars of all masses during their lifetime, even though by different processes (Girichidis et al., 2020; Ferrière, 2001). Together with SN, they enrich the ISM with metals forged in the cores of stars and, in clusters of stars, partake in the formation of superbubbles and galactic outflows (Ferrière, 2001). Moreover, they drive turbulence in the ISM with their outflow velocities from 10s to 1000s km s^{-1} (Castor et al., 1975; Girichidis et al., 2020) and outflow rates of $\dot{M} < 10^{-10}$ $M_\odot$ yr^{-1}

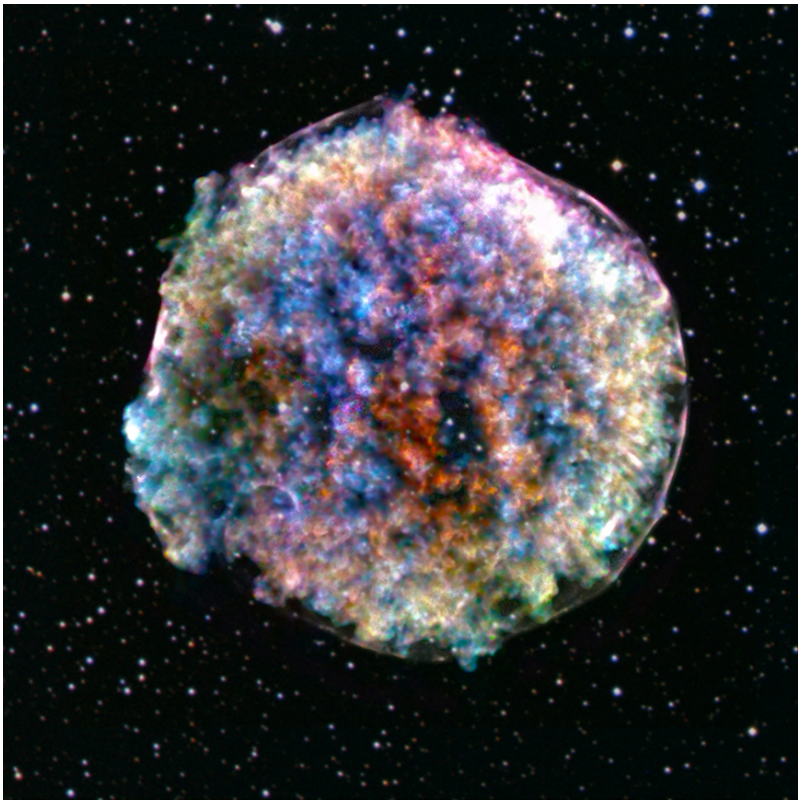

Figure 1.7: SN remnant SN1572, also called Tycho's supernova, as seen in X-ray (the different colors correspond to X-rays of different energies) by NASA's Chandra X-ray Observatory and optical from the Digitized Sky Survey. Even though this is a Type Ia SN, it impressively shows the structure of a SN remnant, with the outer shock front and the hot inner gas emitting strongly in the X-ray spectrum. Credit: X-ray: NASA/CXC/RIKEN & GSFC/T. Sato et al; Optical: DSS

(Girichidis et al., 2020) to 10^{-6} $M_\odot$ yr^{-1} (e.g. Castor et al., 1975; Höfner et al., 2003; Sandin & Höfner, 2004) and even 10^{-4} $M_\odot$ yr^{-1} (Carroll & Ostlie, 2017). They also carve a cavity into the ISM surrounding the star and create a shell of shocked dense gas. In Fig. 1.6 we depict the effect the massive star Eta Carinae (above the picture frame) has on the gas and dust in its vicinity, dispersing the cloud with its strong UV radiation and stellar winds.

Effects of Supernovae

Most stars with masses $\gtrsim 8$ $M_\odot$ end their life in a supernova (SN) event. Typically, these SN release about 10^{51} erg (up to several times 10^{52} erg in the case of very massive stars, Girichidis et al., 2020) of thermal energy (which is only 0.01 % of the total energy, the majority is released as neutrinos, Carroll & Ostlie, 2017) and eject some mass, of which the amount depends on its initial mass in a non-trivial correlation (see Limongi & Chieffi, 2010a,b, for more information).

The most common SN type is a core-collapse SN (there are other types of SN, such as Type Ia, electron-capture and pair-instability, however, we will concentrate on core-collapse SN, using the term SN only for this type of SN unless indicated otherwise). This type of SN emerges, when a massive star uses up its hydrogen in its core, resulting in burning of heavier elements. The star then develops an onion-like shell structure, with lighter elements being burned further out, and heavier elements nearer to the core. When finally iron is formed by fusion, no heavier elements can be formed by an exothermic reaction and fusion comes to a halt. In this high temperature environment, now photodisintegration of the formed heavy elements sets in, and free electrons are captured by the formed protons in an inverse β-decay, forming neutrons. This robs the core of its stabilizing pressure and results in a rapid collapse. Because of Pauli's exclusion principle, neutron degeneracy pressure eventually brings this collapse to a halt. This sends a pressure wave through the still infalling matter from the outer core, which steepens into a shock once it becomes supersonic. This shock heats the infalling outer iron core, leading to further photodisintegration, that robs the shock of its energy, making it nearly stationary. The region of the shock becomes so dense that neutrinos can not freely pass it, and therefore build up behind it. This additional pressure, together with the heating of the gas, finally results in the shock front moving outwards again. It drives the envelope of the star until it becomes optically thin and the energy is released from the dying star (Carroll & Ostlie, 2017).

The stellar ejecta have a velocity of 5×10^3 to 10^4 km s^{-1}, which is much higher than the sound speed of the ISM and therefore forms a shock front (Reynolds, 2008). In Fig. 1.7 we show Tycho's SN, where this hot shock front can be seen clearly in X-rays. The expansion velocity of this SN, for example, is estimated to be 4700 ± 100 km s^{-1} (Hayato et al., 2010). Initially, the SN remnant has a phase of

free expansion, when it cools and expands adiabatically behind the shock front, with a velocity profile of $v \propto r$. After a few days, a reverse shock forms, reheating the interior ejecta (Reynolds, 2008). When the mass swept up at the shock front is about equal to the ejected mass, all of the ejecta is shocked and the SN remnant further develops in a self-similar matter (Reynolds, 2008). This follows the solution of an adiabatic point explosion on a medium of negligible pressure, which was developed by Sedov (1959) and Taylor (1950). This phase therefore is called the Sedov-Taylor phase. This phase ends, when the shock slows down enough for substantial radiative cooling to take place. The shell therefore cools, while the interior is still hot enough to provide substantial pressure, such that the bubble expands driven by this pressure. This is the so called snowplow phase. Finally, when also the interior cooled, the shell will still expand driven by momentum-conservation. (Reynolds, 2008).

The effect of SN on the ISM is connected to prior activity of the exploding star as for example stellar winds. Those decrease the density of the surrounding medium prior to the SN explosion, which strengthens the effect of the SN feedback (e.g., Fichtner et al., 2024).

As most stars are formed in clusters (see Section 1.2.3), massive O and B stars with strong winds and SN often reside close together, which enables their feedback to act collectively and form superbubbles (Ferrière, 2001). Whereas a SN remnant of an individual SN reaches a radius of about 50 pc, a superbubble can grow to radii of $200 - 300$ pc (Ferrière, 2001). This is, because in a superbubble energy is injected continuously, first from stellar winds, then from subsequent SN of the stars of the cluster (Ferrière, 2001). Even though SN dominate the energy input of superbubbles, winds make up between 12 % (Ferriere, 1995) and 17 % (Abbott, 1982) and therefore, also because of preprocessing of the ISM, play a significant role in the formation of a superbubble. The solar system itself is placed inside a superbubble, called the Local Bubble, which was created about 14 Myr ago and has a current radius of about 170 pc (Zucker et al., 2022; O'Neill et al., 2024).

Other forms of stellar feedback include radiation pressure and stellar jets, which are collimated outflows leaving the star at high velocity. Non-ionizing radiation of stars can penetrate deeply into the ISM, constituting the main part of the ISRF (Mathis et al., 1983). The ISRF influences the thermal and chemical set-up of the ISM via heating and photo-dissociation of H_2.

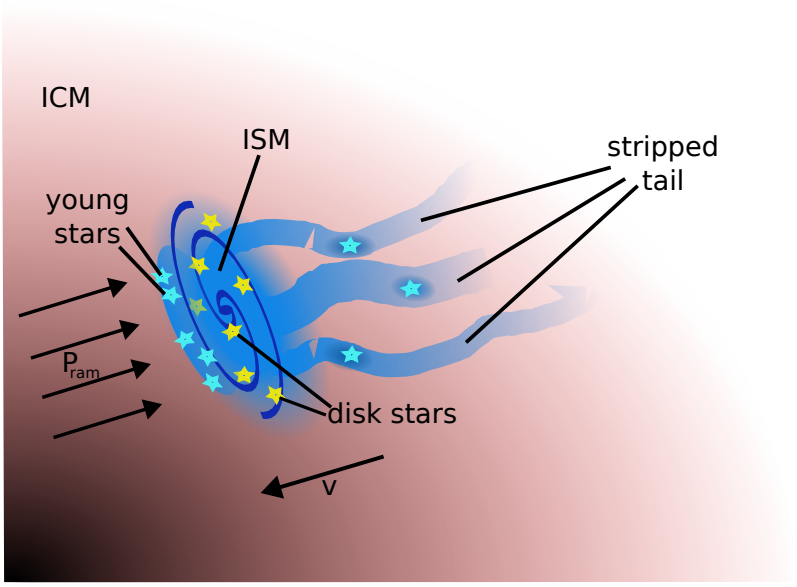

Figure 1.8: Schematic depiction of a jellyfish galaxy. A galaxy moves through the ICM, which results in ram-pressure exerted onto it. This compresses gas in the front of the galaxy, probably leading to star formation there, and also presses gas of the ISM out of the disk, producing stripped gas tails behind the galactic disk. In these tails sporadically stars can form.

1.3.4 Jellyfish Galaxies

As we already saw in Section 1.3.1, the environment of a galaxy influences its appearance and its SFR. It is unclear, what processes exactly cause galaxies in clusters to lose their gas and alter their star formation, but several theories were proposed. Multiple encounters with other galaxies at high velocity could rob galaxies of their gas, which is called harassment and was proposed by Moore et al. (1996). The infall of a field galaxy into a galactic cluster could also strip it of its circumgalactic medium, which subsequently prevents replenishment of the galaxy with gas, causing it to use up its gas in star formation and subsequently quench, which is termed starvation and was originally proposed by Larson et al. (1980). A third promising mechanism was proposed by Gunn & Gott (1972) and is referred to by ram-pressure stripping (RPS).

Ram-Pressure Stripping

RPS occurs, when a field galaxy falls into a galaxy cluster, where the increased pressure from the ICM drags the galactic gas out of the galaxy (schematically depicted in Fig. 1.8). That stripped gas can build long gaseous tails trailing the galaxy. An impressive example is ESO 137-001, which we see in Fig. 1.9 (right). This galaxy has a gaseous tail of ∼80 kpc in length, with ongoing star formation (Sun et al., 2010; Jáchym et al., 2019). A galaxy like this, because of its appearance, is called a jellyfish galaxy.

The strength of ram-pressure depends on the density of the ICM ρ_{ICM} and the velocity of the galaxy relative to the ICM v_{gal} and has the form (Roediger, 2009)

$$p_{\mathrm{ram}} = \rho_{\mathrm{ICM}} v_{\mathrm{gal}}^2. \tag{1.27}$$

The gravitational force of the infalling galaxy on its gas counteracts this pressure and is given by

$$f_{\mathrm{grav}}(r) = \max(a_Z(r)) \cdot \Sigma(r), \tag{1.28}$$

where a_Z is the gravitational acceleration perpendicular to the galactic disk, Σ the surface density and r the radial distance from the galactic center (Roediger, 2009). Generally, f_{grav} decreases when the galactocentric distance rises. The distance where $p_{\mathrm{ram}} = f_{\mathrm{grav}}$ is called the stripping radius, outside of this radius gas gets stripped from the galaxy as $p_{\mathrm{ram}} > f_{\mathrm{grav}}$, inside it stays bound to the galactic disk because $p_{\mathrm{ram}} < f_{\mathrm{grav}}$ (Roediger, 2009).

Here we assume a face-on movement of the galaxy through the ICM, however, from simulations we know galactic inclination to have little effect on the gas loss (e.g., Marcolini et al., 2003; Roediger & Brüggen, 2006). RPS profiles change with redshift and of course RPS is influenced by the cluster properties (Tecce et al., 2011; Vega-Martínez et al., 2022). Typically, jellyfish galaxies are late-type galaxies, probably because of the gas deficiency of early-type galaxies, however, instances of RPS in ellipticals were reported in the past (e.g., Sheen et al., 2017).

Figure 1.9: Two spectacular examples of jellyfish galaxies. Left: D100 in the Coma cluster, optical from HST, overlayed with Hα data from Subaru Suprime-Cam in red. A long and narrow (60 kpc×1.5 kpc) straight tail is visible. Credit: NASA, ESA, Hubble, Subaru-Teleskop, W. Cramer (Yale) et al., M. Yagi, J. DePasquale, also presented in Cramer et al. (2019). Right: Again ESO 137-001, as seen by HST in the optical bandwidth, overlayed with Hα emission in pink (from VLT/MUSE) and CO(2-1) emission in orange (from ALMA). Credit: ALMA (ESO/NAOJ/NRAO), P. Jachym (Czech Academy of Sciences) et al., also presented in Jáchym et al. (2019).

The Appearance of Jellyfish Galaxies

In Fig. 1.8 we present a schematic depiction of the general appearance of a jellyfish galaxy, the most extreme case of ram-pressure stripping. Fig. 1.9 shows two typical examples of those galaxies. The stellar disk is unperturbed, as RPS does not act on the stars, whereas the gas trails the galaxy in a long tail. This tail can have a filamentary and disrupted structure, as seen on the right of Fig. 1.9, which is seen in many jellyfish galaxies and differs from feature which would be expected from tidal interaction (Yoshida et al., 2008), stressing the origin from RPS. The smooth and straight appearance of the tail on the left indicates the presence of a magnetic field that prevents turbulence (Cramer et al., 2019; Ramos-Martínez et al., 2018).

If within the stellar disk a gaseous disk remains, its extent is smaller than that of the stellar disk, because Equation 1.28 depends on the galactocentric distance. RPS also acts more strongly on atomic than on molecular gas, as molecular gas is concentrated more towards the disk and is more strongly bound (Schneider, 2015).

Jellyfish Galaxies in Observation and Simulation

Jellyfish galaxies have been observed from the radio (Roberts et al., 2021a) up to the X-ray (Sun et al., 2010) spectrum and upon various redshifts (e.g., in Gas Stripping Phenomena in galaxies with MUSE (GASP), Poggianti et al., 2017; in the LOFAR Two-metre Sky Survey (LoTSS), Roberts et al., 2021a; in the Massive Cluster Survey (MACS) Ebeling et al., 2014). Even though one would expect the stripping to quench the galaxies eventually, it is unclear how fast this happens and how the galactic SFR behaves prior to quenching. Jellyfish galaxies are clearly not quenched, star formation is observed in the galactic disks (Roediger, 2009; Vulcani et al., 2018) as well as in the tails (Roediger, 2009; Vulcani et al., 2018; Cramer et al., 2019; Jáchym et al., 2019), where it appears in bright Hα[2] regions called 'fireballs' (Yoshida et al., 2008; Jáchym et al., 2019). In some observations, the SFR of jellyfish galaxies is even found to be enhanced compared to the SFMS (Vulcani et al., 2018; Ramatsoku et al., 2020; Vulcani et al., 2020; Lee et al., 2022), which relates the galaxy mass to SFR. Other observations find no such enhancement (Mun et al., 2021) or even suggest a reduced SFR (Yoon et al., 2017). However, most observations use Hα emission as a tracer of young stars and therefore ongoing star formation, but especially in ram-pressure stripped tails conditions are very different from galactic disks and Hα therefore might not be linked to star formation in the same way (Boselli et al., 2016; Fossati et al., 2016). SFR, especially in tails, could be overestimated (Cramer et al., 2019). An enhanced SFR would place jellyfish galaxies as a promising candidate for a connecting phase between field galaxies and cluster galaxies, because the strong Balmer absorption line features which are frequently observed in cluster galaxies can only be explained by a sudden, not a gradual, decline of SFR and, in the most extreme cases, even only with burst in star formation preceding the quenching (Abadi et al., 1999).

[2] Hα denotes the first line of the Balmer series ($n = 3$ to $n = 2$) with a wavelength of about 656 nm. Since the energy needed to excite an electron to $n = 3$ is close to the ionization energy of hydrogen, Hα emission is used to trace ionized hydrogen.

As the number of observed jellyfish galaxies is still limited and because of the mentioned difficulties in extracting essential properties such as SFR, efforts have been made to simulate jellyfish galaxies and the complex processes within. However, the results of this efforts vary. Whereas Kronberger et al. (2008) and Kapferer et al. (2009) find enhanced SFR in ram-pressure stripped galaxies (by up to a factor of 3 and more than a magnitude, respectively), Tonnesen & Bryan (2012) find no such effect. Roediger et al. (2014) finds SF in jellyfish disks and tails, however, SFR is enhanced only in disk regions where gas will be stripped soon and Steinhauser et al. (2016) finds enhanced SFR in galaxies experiencing only mild RPS. Troncoso Iribarren et al. (2016) and Troncoso-Iribarren et al. (2020) finally, in one of the rare studies in a full cosmological simulation (the aforementioned simulations were mostly wind-tunnel simulations, for the difference please consult Chapter 1.4), finds enhanced SF in the leading half of infalling galaxies compared to the trailing half and compared to normal star-forming galaxies.

1.3.5 The Milky Way

Finally, we want to have a closer look at our cosmic home, the Milky Way (MW) Galaxy (in the following we adopt 'Galaxy' when referring to the Milky Way, whereas 'galaxy' is used for any generic galaxy). Even though the MW builds the immediate environment of the solar system, our peculiar location within the Galactic disk makes its observation a challenging task. Here I will review our knowledge about the properties of the Galaxy.

The MW is a barred spiral galaxy, which probably would be classified as an SBc (Hodge, 1983) if viewed from the outside, similar to M31 (see Fig. 1.10). The general structure is as depicted already in Fig. 1.1. It has a virial mass of $1.3 \pm 0.3 \times 10^{12}$ $M_\odot$ within a virial radius of 282 ± 30 kpc. DM heavily dominates the mass, the stellar component contains only $5 \pm 1 \times 10^{10}$ $M_\odot$ and the total baryonic mass fraction is 0.07 ± 0.01 (Bland-Hawthorn & Gerhard, 2016). Therefore, the MW disk has a largely flat rotation curve, with a circular rotation velocity at the suns radius of 238 ± 15 km s^{-1} (Bland-Hawthorn & Gerhard, 2016). Observations suggest a galactic SFR of $1-3$ $M_\odot$ yr^{-1} (Murray & Rahman, 2010; Chomiuk & Povich, 2011; Licquia & Newman, 2015; Bland-Hawthorn & Gerhard, 2016; Elia et al., 2022).

Figure 1.10: M31, a galaxy similar to the MW in mass and star formation activity. Credit: Jan Beckmann and Julian Zoller, distant-luminosity.com/M31.html. With their kind permission for publication.

The Galactic Center

In the center of the Galaxy, a supermassive black hole resides, called Sagittarius A* (Sgr A*), with a mass of about 4.3×10^6 $M_\odot$ (e.g., Gravity Collaboration et al., 2023) according to latest measurements. The exact distance of the sun to the galactic center was revised numerous times (e.g., Eisenhauer et al., 2003; Reid et al., 2009; Chatzopoulos et al., 2015) and is currently estimated to be about 8.2 kpc (e.g., Bland-Hawthorn & Gerhard, 2016). Sgr A* is embedded in the nuclear stellar cluster (NSC), which has a radius of about 12 pc and a mass of $(1.8 \pm 0.3) \times 10^7$ $M_\odot$ (Bland-Hawthorn & Gerhard, 2016) to 6.1×10^7 $M_\odot$ (Chatzopoulos et al., 2015), which, in turn, is surrounded by a nuclear stellar disk (NSC) with a mass of $(1.4 \pm 0.6) \times 10^9$ $M_\odot$ (Launhardt et al., 2002; Bland-Hawthorn & Gerhard, 2016) and a radius between 150 pc (Schönrich et al., 2015) and 230 pc (Launhardt et al., 2002). This structure

probably formed from the CMZ (Schönrich et al., 2015; Tress, 2021), which we already mentioned in Section 1.2.2. Both the NSC and NSD are part of the Galactic bulge, a structure of high scale height of about 180 pc (Bland-Hawthorn & Gerhard, 2016) build from predominately old stars (Ortolani et al., 1995). The MW bulge has a so called boxy/peanut structure (Bland-Hawthorn & Gerhard, 2016). The bulge forms the inner part of the Galactic bar (see Section 1.2.2), which has a total half-length of 5.0 ± 0.2 kpc and is inclined to the line of sight (LOS) from earth by 28°-33° (Wegg et al., 2015). The structure's pattern speed is 43 ± 9 km s^{-1} kpc^{-1}, which places the corotation radius between 4.5 and 7.0 kpc (Bland-Hawthorn & Gerhard, 2016).

The Galactic Disk

The galactic stellar disk consists of a thin and thick component. These components at solar radius have a scale height of about 270 pc and 810 pc respectively (when fitted with a sech^2 function), and a respective scale length of ~ 2.6 kpc and ~ 2.0 kpc (with substantial uncertainties, Bland-Hawthorn & Gerhard, 2016). The thin disk is dominant, contributing about 85 % of stars in the galactic plane (Allende Prieto, 2010) and being about an order of magnitude more massive than the thick disk (Bland-Hawthorn & Gerhard, 2016). The components are differentiated by age of the stars, with stars of the thick disk being older and more metal poor than in the thin disk (Kordopatis et al., 2011). Several theories were proposed on how two components developed, e.g., accretion of stars from disrupted satellite galaxies (Abadi et al., 2003; Steinmetz, 2012), heating of the thin disk by mergers (Quinn et al., 1993; Kazantzidis et al., 2008; Villalobos & Helmi, 2008; Steinmetz, 2012) or in situ star formation triggered by a gas rich merger (Brook et al., 2005; Bournaud et al., 2007; Steinmetz, 2012). Accretion from and mergers with satellite galaxies are most likely also responsible for stellar streams surrounding the galaxy (Bland-Hawthorn & Gerhard, 2016), like e.g., the Sagittarius Stream (Lynden-Bell & Lynden-Bell, 1995; Newberg et al., 2002; Majewski et al., 2003) and the Helmi Stream (Helmi et al., 1999).

The MW also contains a gaseous HI disk, with a scale length of $3.15 - 4$ kpc and an exponential scale height at solar radius of 3.9 kpc (Kalberla & Dedes, 2008). The HI disk builds a continuous structure out to $r \sim 35$ kpc, but HI can be traced to up

to 60 kpc (Kalberla & Dedes, 2008). The galactic disk is found to have between 2 and 4 spiral arms (more studies lean towards a 4-arm structure), depending on the used tracer and the definition of a spiral arm (e.g., Drimmel, 2000; Benjamin, 2009; Hou & Han, 2014; Shen & Zheng, 2020; Xu et al., 2023; Alinder et al., 2024), which are present as overdensities in stars as well as gas. Moreover, the outer MW disk is warped in both gas (May et al., 1993; Kalberla et al., 2007; Kalberla & Dedes, 2008) and stars (Carney & Seitzer, 1993).

The DM and Stellar Halo

The Galactic disk is surrounded by a halo of stars and DM. Stars of the stellar halo, even though stellar density is low, containing only about 1 % of stellar mass of the MW, can be traced up to a radius of $r \sim 50$ kpc and organize in a spheroidal structure (Bland-Hawthorn & Gerhard, 2016). It consists of old and metal-poor stars with high velocity dispersion and little rotation (Bland-Hawthorn & Gerhard, 2016), spawning questions about its formation. It was originally proposed that the halo builds during the initial collapse of the Galaxy (Searle & Zinn, 1978, see Section 1.2.2), but nowadays is assumed to have build up from stars from tidally disrupted satellite galaxies accreted by the MW (e.g., Ibata et al., 1997; Belokurov, 2013; Helmi, 2008; Bland-Hawthorn & Gerhard, 2016). Some stars might also have formed in the stellar disk and subsequently be ejected (Abadi et al., 2006), or formed from gas from infalling satellite galaxies (e.g., Cooper et al., 2015; Font et al., 2011; McCarthy et al., 2012; Tissera et al., 2013; Pillepich et al., 2015; Bland-Hawthorn & Gerhard, 2016). The whole galactic system is embedded in a DM halo (again, see Section 1.2.2). The density profile of this halo is usually described by a Plummer or Navarro-Frenk-White profile, which, in the case of the MW, has a scale length of ~ 25 kpc (Bland-Hawthorn & Gerhard, 2016).

As mentioned in Section 1.3.1, the MW is part of the Local Group and multiple smaller galaxies are bound to it and might be accreted in the future. At least 61 small galaxies in the MW's vicinity are known (Drlica-Wagner et al., 2020), the most noticeable of them are the Small and Large Magellanic Clouds (SMC & LMC). However, it could be that the LMC is not actually bound to the MW (Besla et al., 2007). Even though the MW accreted several small satellite galaxies during its lifetime, it probably did not have a major merger within the last $\sim$ 10 Gyr,

which gives it a rather quiet history (Hammer et al., 2007; Stewart et al., 2008; Bland-Hawthorn & Gerhard, 2016).

The Milky Way in Observation and Simulation

As our home galaxy, the Milky Way was covered by numerous observational surveys, spanning a wide range of wavelengths. The molecular gas (e.g., sampled by CO) for example was targeted by SEDIGISM (Schuller et al., 2017), CHIMPS (Rigby et al., 2016) and FQS (Benedettini et al., 2020); the atomic gas (e.g., sampled by HI emission) by THOR (Beuther et al., 2016) and VGPS (Stil et al., 2006); and the ionized medium in the hot phase by eROSITA (Predehl et al., 2021), and twenty years prior by ROSAT (Voges et al., 1999). The WIM, among others, was sampled by the WHAM sky survey (Haffner et al., 2003). Galactic dust was studied e.g., in ATLASGAL (Schuller et al., 2009) and Hi-GAL (Molinari et al., 2010). Stellar surveys are e.g., Gaia (Gaia Collaboration et al., 2023) in the optical, and GLIMPSE (Benjamin et al., 2005) and MIPSGAL (Carey et al., 2009) in the infrared; star-forming regions within the MW were the target of GLOSTAR (Brunthaler et al., 2021). All these efforts have contributed significantly to the picture of the MW that we described above.

Because of the aforementioned peculiar point of view from inside the MWs disk, interpretation of observational findings are often difficult. To help with this, numerous simulations complement observations. In a full cosmological treatment MW analogues were studied e.g., in in Illustris (Elias et al., 2018), IllustrisTNG (Pillepich et al., 2021), Simba (Li et al., 2021), EAGLE (Ortega-Martinez et al., 2022) and FIREbox (Gensior et al., 2023). In those simulations one can follow the entire formation process of the MW, but their resolution is not high enough to study galactic details like individual sites of star formation. This low resolution is increased in so-called 'zoom-in' simulations. There, promising structures from low-resolution simulations are selected and get re-simulated with a higher resolution. In terms of the MW, one has to name here APOSTLE (Fattahi et al., 2016), Latte (Wetzel et al., 2016), Auriga (Grand et al., 2017), NIHAO (Buck et al., 2020) and VINTERGATAN (Agertz et al., 2021). These simulations are suited to study individual galactic components, but are usually still too low in resolution in space and time to follow small-scale processes like the formation of molecular clouds, and may also

lack the proper treatment of physics governing those small-scale processes.

For those processes one usually simulates the Galaxy in a box, isolated from most external influences and running for a much shorter time-scale than in cosmological simulations. Pettitt et al. (2014) used this approach in the smoothed particle hydrodynamics (SPH) code Phantom to simulate a MW-like 13 kpc disk galaxy with a modular potential including the bulge, halos, disk and spiral arms. They already take into account ISM cooling and some chemical processes in the gas, but ignore star formation, feedback and magnetic fields. With this, they tried to recreate morphological features of the MW. Renaud et al. (2013) (using the adaptive mesh refinement (AMR) code Ramses) managed to form non-axisymmetric features in his simulation of a 28 kpc gaseous disk, using a dynamic potential which includes the dark matter halo, spheroid and bulge, thin and thick disk, but their simulation time only spans a few cloud lifetimes. With the moving-mesh code Arepo, Jeffreson et al. (2020) studied the impact of different galactic potentials (which, however, ignore the Galactic bar) on molecular clouds in the gaseous Galactic disk. They take into account star formation, stellar feedback, and non-equilibrium chemistry of hydrogen, carbon, and oxygen. These simulations all ignored the Galactic magnetic field, which is not the case for Wibking & Krumholz (2023) and Konstantinou et al. (2024), that treat the MW in full MHD to study features of the magnetic field. Wibking & Krumholz (2023) (using Gizmo) includes gaseous chemistry, star formation, and feedback from photoionization and supernovae, but their simulated galaxies lack a Galactic bar. Konstantinou et al. (2024) as well include chemistry, star formation and supernovae in their simulation, but they too have no Galactic bar.

The Galactic bar was studied in detail by Tress et al. (2020b) and Sormani et al. (2020a) (again using Arepo), which take it one step further and do not simulate the full Galaxy but only its center (up to 5 kpc) with a refined bar potential. Such they can study the CMZ at sub-pc resolution, which, with current computational resources, is hard to reach when simulating the full Galaxy. Furthermore, similar to the aforementioned zoom-in simulations, one can use the same technique in isolated galaxy by simulating only parts of it at high resolution, as done for example by 'The Cloud Factory' (Smith et al., 2020).

1.4 Numerical Simulations

1.4.1 Simulation Methods

We now already mentioned a number of simulations. Simulations by now are an essential part of modern astrophysics, so in this section we will go into more detail about how astrophysical simulations are conducted.

The Equations of Magnetohydrodynamics

In many situations the ISM can be modeled as an inviscid, compressible fluid that follows the laws of hydrodynamics (HD). Together with a magnetic field B (which we treat in ideal magnetohydrodynamics here, i.e., in the limit of a perfectly conducting fluid, ignoring magnetic diffusion and the magnetic field is frozen into the medium), the laws of magnetohydrodynamics (MHD) read as follows (see e.g., Shu (1992) for a complete derivation, Pakmor & Springel, 2013 gives a derivation of the cosmological form):

$$\text{mass conservation}: \quad \frac{\partial \rho}{\partial t} + \nabla \cdot (\rho \boldsymbol{v}) = 0 \tag{1.29}$$

$$\text{Euler equation}: \quad \frac{\partial (\rho \boldsymbol{v})}{\partial t} + \nabla \cdot \left(\rho \boldsymbol{v}\boldsymbol{v}^{\mathrm{T}} + P\mathbf{I} - \frac{\boldsymbol{B}\boldsymbol{B}^{\mathrm{T}}}{4\pi} \right) = -\rho \nabla \Phi \tag{1.30}$$

$$\text{energy conservation}: \quad \frac{\partial e}{\partial t} + \nabla \cdot \left[(e+P)\boldsymbol{v} - \frac{\boldsymbol{B}(\boldsymbol{v}\cdot\boldsymbol{B})}{4\pi} \right] = - \rho(\boldsymbol{v}\cdot\nabla\Phi) + \mathcal{H} - \Lambda \tag{1.31}$$

$$\text{induction equation}: \quad \frac{\partial \boldsymbol{B}}{\partial t} + \nabla \cdot \left(\boldsymbol{B}\boldsymbol{v}^{\mathrm{T}} - \boldsymbol{v}\boldsymbol{B}^{\mathrm{T}} \right) = 0 \tag{1.32}$$

$$\text{divergence constraint}: \quad \nabla \cdot \boldsymbol{B} = 0. \tag{1.33}$$

As before, ρ is the mass density, $\boldsymbol{v}$ is the velocity vector, P is the pressure, Φ is the gravitational potential, Λ denotes cooling and $\mathcal{H}$ heating (for the corresponding processes please see Section 1.3.2), and I is the identity matrix. The total energy per unit volume is

$$e = e_{\mathrm{th}} + \frac{\rho \boldsymbol{v}^2}{2} + \frac{\boldsymbol{B}^2}{8\pi}, \tag{1.34}$$

and the total pressure is

$$P = P_{\mathrm{th}} + \frac{\boldsymbol{B}^2}{8\pi}. \tag{1.35}$$

To close this system of equations, an additional closure function of the form

$$P_{\mathrm{th}} = P_{\mathrm{th}}\left(\rho, T\right) \tag{1.36}$$

is needed, one often uses

$$P_{\mathrm{th}} = \left(\gamma - 1\right) e_{\mathrm{th}}, \tag{1.37}$$

where γ is the adiabatic index. Equation 1.29 ensures the conservation and smooth flow of mass in the system, the Euler Equation 1.30 makes sure momentum is conserved and only changed by forces of pressure, gravity or the magnetic field, and Equation 1.31 allows for energy to be changed only by processes of heating or cooling, a change in the gravitational potential or by influences of the magnetic field. The induction equation (Equation 1.32) describes the development of the magnetic field. When solving for these equations, special care has to be taken for compliance with Equation 1.33, i.e., the absence of magnetic divergence. Otherwise, solutions become unphysical. Several divergence cleaning methods have been proposed, widely used are Powell (Powell et al., 1999) and Dedner cleaning (Dedner et al., 2002).

Particle- and Grid-Based Methods

In order to solve these partial differential equations numerically, the continuous space and time has to be discretized. How this is done depends on the adopted view of the problem. Shall the fluid dynamic be solved in an Eulerian or Lagrangian fashion?

If a Lagrangian view is adopted, a particle based method is chosen. In this method the fluid is approximated by randomly distributed point-like mass elements that follow the flow dynamic. In each timestep, forces acting on each mass element can be computed and the properties and positions of the elements are updated. In the very well-known method of Smoothed Particle Hydrodynamics (SPH, Lucy, 1977; Gingold & Monaghan, 1977), to contain the continuous nature of the fluid, each

particle has an differentiable adaptive smoothing kernel, often a Gaussian is used (Monaghan, 1992). This method has the clear advantage of adaptive resolution, i.e., the resolution is highest in regions of high density (Springel, 2010a), which probably are also regions of interest. However, if the scientific interest lays in low-density regions, such as the CGM, it is not straight-forward to define a different resolution criterion. Also, SPH is known to suppress fluid instabilities (Springel, 2010b). SPH is used in several noticeable astrophysical simulation codes, e.g., GADGET (Springel, 2005) and GASOLINE (Wadsley et al., 2004).

The Eulerian view is usually treated in grid-based methods. In those methods, the simulation domain is divided into subdomains by a grid. This grid can be structured or unstructured, and, depending on the problem geometry, the partial differential equations are most often solved by a formalism that can be classified as one of the following methods (Ferziger et al., 2020; Knabner & Angermann, 2000):

- Finite Difference Method (FDM): At each grid point the partial differentials are approximated by finite differences, transforming them into a system of linear algebraic equations.
- Finite Volume Method (FVM): Here, the grid cells are the central elements, the grid defines the border of the so called control volume. In the center of mass of each grid cell/control volume the so called node lies, i.e., the point where the fluid values shall be found. Fluid properties are integrated over the cell volume. The discontinuities at the cell borders builds a Riemann problem, a Riemann solver is used to calculate the flux across cell boundaries.
- Finite Element Method (FEM): This method again works with the grid cells, which are called elements here. However, before integration, here the differential equations are multiplied by weight functions. By integration by parts, a so called weak formulation is reached. The desired fluid quantity is approximated via basis functions. With this, a system of linear equations can be derived and subsequently solved.

For completeness we shortly described each of the methods, however, most grid-based astrophysical codes known to the author use FVM (e.g., FLASH, Fryxell et al., 2000; RAMSES, Teyssier, 2002; AREPO, Springel, 2010b; see a comprehensive list of astrophysical simulation codes in Klingenberg, 2017).

In a grid code, refined resolution criteria can be defined, tailored to the specific problem at hand. This results in a hierarchy of cell sizes, with smaller sizes, i.e., higher resolution, in regions of interest. The grid can also be refined on the fly during the simulation time adapting to the changing conditions. This is then called adaptive mesh refinement (AMR), and adopted in many grid-based codes (e.g., FLASH, RAMSES). However, it is known that Eulerian grid codes can lack Galilean invariance (e.g., Wadsley et al., 2008; Tasker et al., 2008).

Moving-mesh codes such as AREPO (Springel, 2010b) hold an in-between place between particle-based and grid-based methods. They use an unstructured grid to divide the simulation domain, but this grid is defined by mesh-generating points that move with the fluid flow. Therefore, the grid changes substantially from time step to time step. This results in a quasi-Lagrangian fluid description that generally achieves Galileian invariance. From SPH codes this method inherits the density-based adaptivity of resolution, but still gives the possibility for additional refinement criteria. We discuss AREPO in more detail in Section 2.1.

Discretization in time

These are the basics for solving the equations of hydrodynamics (or any other partial differential equation) in discretized space. But to follow a flow, also time has to be discretized, as the partial differential equations are solved at discrete time steps. In general, any time step suitable to the simulated problem can be chosen, i.e., a time step of the order of Megayears or even Gigayears for astrophysical simulations, or down to fractions of a second for fluid flows on small scales.

However, the time step has to be small enough. The logic in grid codes is such that, in order to properly follow a flow, the time step has to be smaller than the time a fluid parcel (or information on it) would need to move from one grid point to the next at the maximum velocity of matter or information propagation. This means, when the grid resolution increases, the time step needs to decrease. This condition was first formulated by Courant et al. (1928), and is therefore called Courant or Courant-Friedrichs-Lewy (CFL) condition. This can be formulated by (LeVeque, 2002)

$$\mathrm{CFL} = \left| \frac{v \Delta t}{\Delta x} \right| \leq 1, \tag{1.38}$$

where Δt is the time step, Δx is the distance between grid points and v is the maximum velocity of flow or information propagation between the grid cells.

This formulation is true for a global time step. However, if the used grid is not uniform, as in the case of AMR or a moving mesh, one can either compute the whole simulated space on the lowest time step to make sure the CFL-criterion is met everywhere (which is computationally inefficient), or use a hierarchy of time steps where grid cells of different sizes are computed on different time steps (this is done, e.g., in Arepo; Springel, 2010b).

For particle based methods, the calculation of a maximum time step is not as straight-forward as for a grid-based method and highly depends on the dynamics of the problem. For an example calculation see e.g., Neal (2011, pp. 23-24).

Solving for Gravity

To calculate the gravitational acceleration of a fluid element in a simulation, in principle one would have to calculate the force all other particles/cells exert on the element. Such a description would have a computational complexity of $\mathcal{O}(N^2)$, which is unfeasible for large astrophysical (or other) simulations. Therefore, other approaches are used.

Particle-based methods work well together with tree-methods (e.g., Barnes & Hut, 1986; Barnes, 1989) to calculate gravity. In its most general functionality, a hierarchical spatial tree is constructed, with each node of the tree representing a region of the simulation space. The particles within this region are treated as a single mass. If a node is too near to the particle for which the total gravitational acceleration shall be calculated, the node is 'opened', i.e., the contribution is treated in a more fine-grained manner, which results in a complexity of $\mathcal{O}(N \log N)$ (e.g., Barnes & Hut, 1986; Tokuue & Ishiyama, 2024).

For grid-based codes, Poissons' equation

$$\Delta\Phi = 4\pi G\rho \tag{1.39}$$

is solved on the grid. For a regular grid, the natural choice is to do this in Fourier space, where the calculation is easily done. This is then called a particle mesh (PM) algorithm. In particle-based codes, the particles can be scaled on a grid and the calculation of the gravitational potential then treated in the same manner.

For the calculation of gravity it is of utter importance that the considered masses have a finite radius > 0. Otherwise, gravitational forces diverge. As masses in simulations are often approximated as point-like, a technique called gravitational softening is applied, which, basically, assigns each particle an artificial radius. The exact design of this may differ between codes, giving the gravitational potential different forms at low distances.

Subgrid Models at the Example of Star Formation

Even the best code cannot reach infinite resolution, meaning that processes below a certain scale cannot be resolved. This raises the need for a subgrid description of those processes. This means, the processes are not longer treated by explicitly simulating them, but some simplified assumptions about their state is made and implemented in the code. It basically describes some predefined condition at which the hydrodynamical treatment is exchanged for some different treatment the simulator has to define.

A typical example in astrophysical codes is the process of star formation. If a collapsing gas cloud occurs, at some point the gas is too dense to still be simulated with a resolvable time step, and processes other than hydrodynamics occur. At this point, in large scale simulations (i.e., simulations where the pc to au scales of star formation are below the grid scale, e.g., simulations of significant parts of a galaxy or larger), the description of the star formation process is usually wrapped in a subgrid model of some form (see e.g., Springel & Hernquist, 2003; Dubois & Teyssier, 2008; Federrath et al., 2010). A very simple formulation of such a model would be, for example, that all gas that reaches a predefined density threshold gets converted into a particle decoupled from the gas flow (in that case, particles would also be added to grid-based codes, however, they are not used in the treatment of hydrodynamics except for gravity). However, the conditions in which gas gets converted into a particle can also be much more refined, taking into account the gas composition, internal energy, or any other property the simulator considers suitable and that is tracked by the simulation.

These particles inherit properties of the gas they formed from, like mass and velocity, and can get assigned additional characteristics to the choice of the simulator. This could be some feedback rate of ionizing radiation or supernovae. The parti-

cles are often implemented in a form called 'sink particles' (e.g., Bate et al., 1995), where they are accreting surrounding gas, thus mimicking ongoing star formation (see e.g., Federrath et al., 2010). Another form, called 'star particles' (Weinberger et al., 2020) does not interact with the surrounding gas except for gravitational interaction. However, this is just a very general description of one possible treatment of star formation in a simulation. Treatments can differ significantly from the one described here and vary substantially between simulations.

Here, we only briefly highlighted star formation as one form of a subgrid model, however, various processes can be formulated in such a way. Other typical examples are stellar feedback (e.g., Tress et al., 2020a), black holes and their effects (e.g., Weinberger et al., 2017) or turbulence (e.g., Schmidt & Federrath, 2011). We explain our treatment of subgrid models in the used simulations in Section 2.2.3 and 2.3.8.

1.4.2 Execution of Simulations at Different Scales

After introducing the basic principles of astrophysical simulations, we will now turn to considerations that need to be taken into account when simulating on different scales. We will do this with the example of cosmological simulations and simulations of isolated galaxies.

Cosmological simulations such as Illustris (Vogelsberger et al., 2014b,a; Genel et al., 2014; Sijacki et al., 2015), IllustrisTNG (Marinacci et al., 2018; Naiman et al., 2018; Pillepich et al., 2018b; Nelson et al., 2018; Springel et al., 2018; Pillepich et al., 2019; Nelson et al., 2019b), EAGLE (Schaye et al., 2015; Crain et al., 2015), or SIMBA (Davé et al., 2019), start from initial conditions constrained by observations of the CMB and develop self-consistently from there, making them one of the best tools to study galaxy formation and evolution, but also to test different cosmological models (Vogelsberger et al., 2020). Their backbone is DM, which provides the basic framework for further structure formation. Older simulations (and more recent very large scale ones), like the Millennium simulation (Springel et al., 2005), only simulate DM, as here the only active force is gravity. Simulations suitable to follow the formation and evolution of galaxies, however, also contain baryonic matter, which, because of its various interactions (radiation, electric & magnetic fields, heating & cooling processes, etc.) is a lot harder to simulate (Vogelsberger et al., 2020).

While the basic principles of hydrodynamics of course do not differ, the main

challenge in cosmological simulations lays in the enormous range in space and time they cover. Cosmological simulations can cover boxes of up to tenth of thousands of Mpc in side length (e.g., DEUS FUR, Alimi et al., 2012, Dark Sky Simulations, Skillman et al., 2014, PKDGRAV3, Potter et al., 2017) in pure DM and up to hundredth of Mpc in side length with baryonic matter (e.g., BlueTides, Feng et al., 2016, BAHAMAS, McCarthy et al., 2017) and often start at redshifts of $z > 100$ (e.g., IllustrisTNG). These huge covered ranges come at the cost of resolution. Most cosmological simulations including baryons have a spatial resolution between a few hundredths of pc and several kpc (see Vogelsberger et al., 2020), meaning that for a galaxy such as the Milky Way the scale height of the disk would be resolved by just one to a few resolution elements. This means that many processes have to be modeled in a subgrid manner. However, cosmological simulations hold the unique advantage of covering such large ranges in space and time, that the complete formation of galaxies, galaxy clusters and even the cosmic web can be traced from first principles. Also, because of the relative uniformity of the early universe, the selection of initial conditions is relatively simple and is usually achieved via displacement of simulation particles from a uniform grid or glass-like configuration of simulation particles accounting for the power spectrum at the chosen starting time (Vogelsberger et al., 2020).

Isolated galaxy simulations, on the other hand, cover the much smaller scale of just a single galaxy, and typically span a much shorter time than cosmological simulations of a few hundred Myr to a few Gyr (see e.g., Jeffreson et al., 2020; Konstantinou et al., 2024). They sample not multiple, but just a single galaxy, and the setting usually is an idealized one, in the sense that the galaxies evolve in isolation, without any form of interaction than those implemented in the simulation on purpose. However, this also is the undeniable strength of isolated galaxy simulations - they enable the study of effects of isolated processes on a system, which under normal conditions is governed by multiple processes interacting and overlapping each other. These simulations give full control for everything that happens to the galaxy like feedback schemes, magnetic fields or even the gravitational potential (see e.g., Jeffreson et al., 2020; Konstantinou et al., 2024). Systematic studies of the influence of inclination angle on the stripping of galaxies, for example, are only possible by being able to define the impact angle and velocity of wind interacting with a galaxy in a box (wind-tunnel simulations Marcolini et al., 2003; Roediger & Brüggen, 2006). Or examining

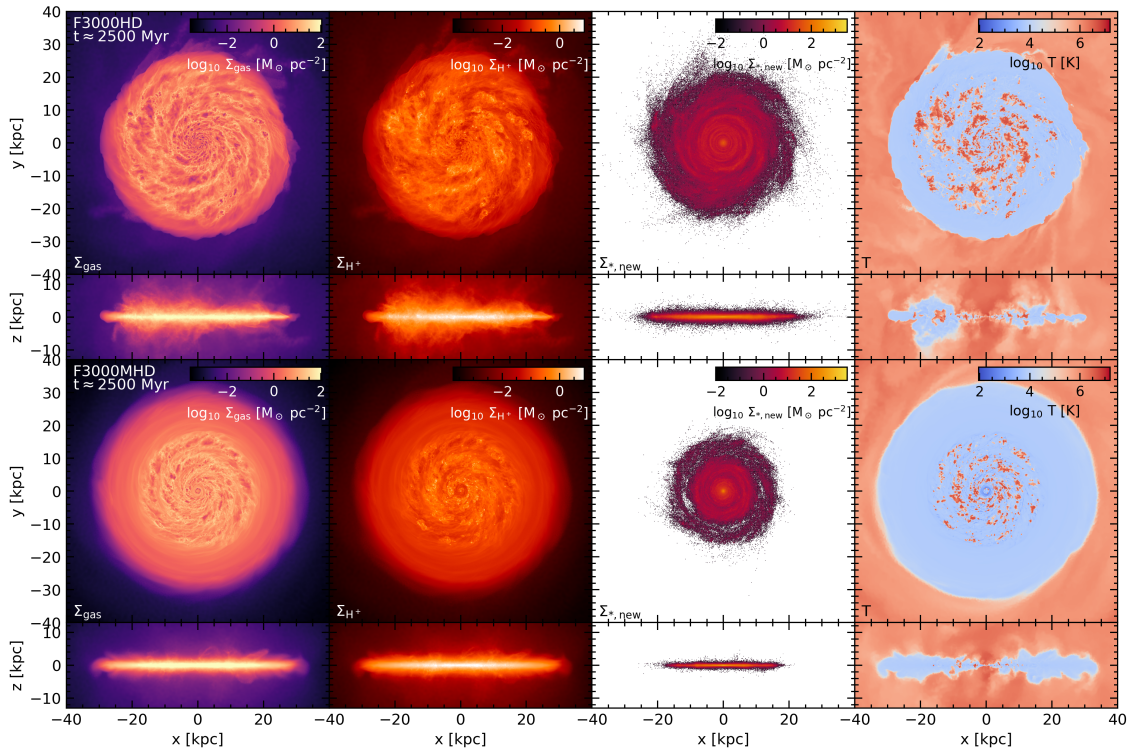

Figure 1.11: Two simulations from the Rhea simulation suite, where the sole difference is the introduction of a magnetic field. From left to right: Gas surface density, H^+ surface density, stellar surface density and a temperature slice in face-on and edge-on projection.

the possibility of different feedback processes to shape a galaxy can only be done with the same galaxy subsequently being put under the subject of those different feedbacks. Moreover, the limited simulated range allows for much higher resolution than in cosmological simulations, of a few to a few tenth of pc (e.g., Jeffreson et al., 2020; Konstantinou et al., 2024), and the lower computational costs often allow for multiple runs with slightly changed conditions, that enable an in-detail analysis of any examined process.

In short, isolated galaxy simulations provide a large freedom of choice, however, this also places large responsibility on the simulator. Initial conditions have to be chosen with great care, as any change there can (and in many cases will) have a great influence on the resulting simulated systems. In Fig. 1.11 we show two examples from the Rhea simulation suite developed by us, whose only difference is the introduction of a small magnetic field in the galaxy in the bottom row. This already changes the

behavior of the galaxy significantly. This is also true for cosmological simulations of course, but the cosmological initial conditions are very well defined (see Vogelsberger et al., 2020), which is not the case for individual galaxies as many of their formation processes and features are unexplained to this day. In *both* kinds of simulations, however, the conditions during the simulations, i.e., the exact physics treatment, influence the simulation outcome greatly and therefore have to be treated with uttermost care in isolated galaxy and cosmological simulations alike.

2 Used Code and Simulations

2.1 Arepo

All simulations discussed in this thesis were run with Arepo, which was initially introduced in Springel (2010b) and released to the public (with a reduced functionality) in 2019, accompanied by the public release paper Weinberger et al. (2020). This section is a very shortened and simplified overview of the most important features of Arepo necessary to understand numerical choices made in the simulations presented in the following sections. If not marked otherwise, all information in this section comes from Springel (2010b) and Weinberger et al. (2020). For a more complete and detailed explanation of all facets of Arepo, as well as performance and accuracy tests, we refer the reader to these publications.

Arepo has been used in a wide range of astrophysical problems: For cosmological simulations such as Illustris and IllustrisTNG, in zoom-in simulations such as Auriga (Grand et al., 2017), for simulations of isolated galaxies such as that of Jeffreson et al. (2020) or Tress et al. (2020a), or parts of galaxies like in Tress et al. (2020b) and Sormani et al. (2020a), in stratified (Simpson et al., 2016) and turbulent (Bauer & Springel, 2012; Mocz et al., 2017) box simulations and even down to the scales of individual stars (Goicovic et al., 2019) and protoplanetary accretion disks (Muñoz et al., 2014). Due to its wide range of possible applications it is a widely used tool with a large developer basis.

Construction and Treatment of Simulation Elements

The signature feature of Arepo is its quasi-Lagrangian treatment of hydrodynamics on a moving mesh. The simulation domain is tessellated by a Voronoi mesh, which is constructed on the basis of mesh-generating points that carry the volume-averaged primitive variables like density or internal energy of the fluid. A Voronoi cell is defined as the space closer to the mesh-generating point of this cell than to

any other mesh-generating point. The points move with the fluid's bulk velocity, therefore in each timestep the mesh has to be constructed anew. However, because of the movement of the mesh-generating points, the flux over the cell boundaries is minimized and solved in a finite volume fashion, utilizing an iterative Riemann solver or an approximate Harten-Lax-van Leer-Contact (HLLC) solver (HLLD for MHD). In the case of MHD, the Powell (Powell et al., 1999) divergence-cleaning method is adopted (Pakmor & Springel, 2013; Weinberger et al., 2020).

In this method it is not straight-forward to give a specific spatial resolution of the code, as each cell has a different size and also has a different size in each dimension. Arepo therefore uses mass resolution instead of spatial resolution, i.e., the desired resolution is given in terms of the mass each Voronoi cell should have. The spatial resolution then depends on the density of the examined simulation space. Cells can differ from the desired mass resolution by a set factor (often chosen to be 2, as in the simulations used in this thesis), which means cells more massive than twice the set mass resolution get split, i.e., a new mesh generating point is spawned, and cells less massive than half the mass resolution are removed, their mesh-generating point is deleted and neighbouring cells claim their volume. It is also possible to set maximum and minimum cell volumes, placing additional constraints on the size of Voronoi cell, overriding the mass criterion.

In addition to the Voronoi mesh, Arepo allows for collisionless particles of matter not interacting in a hydrodynamical way, such as DM, stars or black holes. These particles are unaffected by the grid property and just interact with it via gravity (or in other simple non-hydrodynamical ways, like sink particles, Greif et al., 2011).

Gravity Calculations

To calculate gravity acting on simulation elements (= particles or cells), in Arepo one can use an oct-tree, a PM algorithm or a combination of both. The oct-tree follows the architecture of Barnes & Hut (1986) and is implemented in a way close to what is described in Springel (2005), but is reconstructed at every local timestep, which avoids correlations between gravitational force and the timestep hierarchy. This algorithm is computationally costly and hard to scale on multiple computing tasks, but allows for a high spatial force resolution and can efficiently handle large variations in spatial scales.

In the PM algorithm, the simulated mass distribution is binned on a Cartesian grid in a cloud-in-cell method (CIC, explained, e.g., in Birdsall & Fuss, 1969) and Fourier transformed. The Fourier transformed Poisson equation (Equation 1.39) is solved for the gravitational potential, which is then inverse Fourier transformed, differentiated and interpolated to the simulation elements position to get the gravitational acceleration. For zoom-in simulations, a second grid can be placed in the high-resolution region. This method is fast and can be easily scaled on many computing tasks, but is bound to a Cartesian grid, which limits its dynamic range of scales. When both methods are combined, forces are split into short-range and long-range components, divided by a split scale that is chosen by the simulator. Masses contributing to the short-range forces are then treated with the tree algorithm, long-range forces are calculated by the PM algorithm.

For gravitational softening, Arepo uses a gravitational potential kernel of the form

$$\phi(r,h) = -\frac{1}{r}\begin{cases} \frac{r}{2h}\left[3-\left(\frac{r}{h}\right)^2\right] & r \leq h \\ 1 & r > h \end{cases}, \tag{2.1}$$

where r is the distance to the simulation element, and h is the gravitational softening parameter, that for Voronoi cells with a volume V is

$$h = f_h \left(\frac{3V}{4\pi}\right)^{\frac{1}{3}}, \tag{2.2}$$

where f_h is another input parameter chosen by the simulator (usually $f_h \sim 1.0 - 1.5$). For other particle types the gravitational softening parameter is chosen by the simulator.

Timestepping

For the calculation of gravitational forces and hydrodynamical motions, Arepo adopts explicit time integration. In principle, each simulation element has different timestep constraints for gravity, hydrodynamics and possible other simulated physical processes (such as heating or cooling), but the most restrictive constraint is used for all calculations on the simulation element. The most general constraint on

the used timestep is the CFL criterion analogous to Equation 1.38. This can result in a large range of possible timesteps in the simulation domain. In order to get a stable and accurate integration scheme, it is desirable to integrate each simulation element with a timestep as large as possible but as small as necessary. Additionally, it is of advantage to still have a global timestep, at which all simulation elements are synchronized. Arepo therefore adopts a power-of-two hierarchy of timesteps Δt, where the simulation element is set on the highest power of 2 subdivision of the simulation time ($\Delta t = (t_{\mathrm{end}} - t_{\mathrm{start}})/2^N$, where t_{start} is the start time of the simulation, t_{end} is the end time of the simulation and N is the level in the timestep hierarchy) that is smaller than its most restrictive timestep constraint. This results in a nested hierarchy of timesteps, where simulation elements can change between levels if their timestep constraints change. Changing to a shorter timestep is always possible, changing to a larger timestep just if the simulation is currently synchronized with this timestep. Faces between cells on different timesteps are evolved on the smaller adjacent timestep.

2.2 IllustrisTNG

We now discuss the used simulations, which are based on Arepo. The first of the two discussed sets is IllustrisTNG (Marinacci et al., 2018; Naiman et al., 2018; Pillepich et al., 2018b; Nelson et al., 2018; Springel et al., 2018; Pillepich et al., 2019; Nelson et al., 2019b), a successor of the Illustris simulations (Vogelsberger et al., 2014b,a; Genel et al., 2014; Sijacki et al., 2015). It is a cosmological, large-scale gravity and magnetohydrodynamical simulation (Pillepich et al., 2018a), and consists of three flagship runs, namely TNG300, TNG100 (Marinacci et al., 2018; Naiman et al., 2018; Pillepich et al., 2018b; Nelson et al., 2018; Springel et al., 2018) and TNG50 (Pillepich et al., 2019; Nelson et al., 2019b) with different simulation box sizes and resolutions. In the following we concentrate on TNG50, as this is the run used for the analysis presented in this thesis, however, the descriptions are mostly valid for all runs.

TNG50s simulation box has a volume of $(51.7\,\mathrm{Mpc})^3$ (see Table 2.1 for basic properties of TNG50) and encloses ~ 6500 galaxies with a stellar mass larger than 10^8 $\mathrm{M}_\odot$ and even ~ 700 galaxies with a stellar mass larger than 10^{10} $\mathrm{M}_\odot$ (Pillepich et al.,

Simulation properties	
Box size	$(51.7\,\mathrm{Mpc})^3$
Mass resolution (gas)	8.5×10^4 $\mathrm{M}_\odot$
spatial resolution	up to ~ 100 pc (maximum reached 6.5 pc)
Simulation time	form $z = 127$ to $z = 0$ (nearly 13.8 Gyr)
CPU hours	$\sim 130 \times 10^6$

Table 2.1: Properties of TNG50: Simulation box size, adopted mass resolution for gas, spatial resolution, time spanned by the simulation and used CPU hours. All values taken from Pillepich et al. (2019).

2019). Despite this enormous simulated range, the mass resolution is 8.5×10^4 $\mathrm{M}_\odot$ (for comparison: that of TNG100 is 1.4×10^6 $\mathrm{M}_\odot$, that of TNG300 1.1×10^7 $\mathrm{M}_\odot$), which translates to an average spatial resolution in dense star-forming regions of 100-140 comoving pc (Nelson et al., 2019b; Pillepich et al., 2019). The simulation starts at a redshift of $z = 127$ from initial conditions generated with the N-GENIC code (Pillepich et al., 2019) and evolves with cosmological parameters in accordance with Planck Collaboration et al. (2016). The initial conditions contain a primordial seed magnetic field of 10^{-14} comoving Gauss, that evolves self-consistently (Pillepich et al., 2019). The simulators ran 60 realizations of the initial density field and finally selected the simulation with the most average cumulative DM halo mass function (for halos $> 10^{10}$ $\mathrm{M}_\odot$, Pillepich et al., 2019). For calculation of gravity, TNG50 uses a tree-particle-mesh algorithm (Pillepich et al., 2019).

2.2.1 Subgrid Models

In addition to gas, that is represented by the Voronoi mesh of AREPO, IllustrisTNG follows DM, stars and supermassive black holes (SMBH), as well as artificial wind particles (Pillepich et al., 2018a).

DM is modeled via collisionless particles (2160^3 upon initialization) with a mass of 4.5×10^5 $\mathrm{M}_\odot$ (Pillepich et al., 2019).

Star formation is treated in accordance with Springel & Hernquist (2003). Gas more dense than $n_\mathrm{H} \simeq 0.1$ cm^{-3} transforms into stars stochastically on a cell-basis, following the Kennicutt-Schmidt relation (Equation 1.14, Pillepich et al., 2018a). If the gas cell is less massive than two times its target mass, the full cell gets converted

into a star, if it is more massive, a star particle with the mass equal to the target mass is spawned (Vogelsberger et al., 2013). The star particles represent single-age stellar populations, sampled from a Chabrier IMF (Equation 1.24, Pillepich et al., 2018a). For the evolution of those populations, three pathways are taken into account: AGB stars (for stars of $1-8$ $M_\odot$), SN Type II (for stars of $8-100$ $M_\odot$) and SN Type Ia (Pillepich et al., 2018a). Because of the uncertainties associated with SNIa progenitor systems and the long time delay between stellar birth and SNIa, these events are not explicitly tied to the stellar population of the star particle, but the rate of SNIa is parameterized by a delay-time distribution $g(t)$ of the form (Vogelsberger et al., 2013)

$$g(t) = \begin{cases} 0 & t < \tau_{8M_\odot} \\ 1.3 \times 10^{-3} \frac{\mathrm{SN}}{M_\odot} \left(\frac{t}{\tau_{8M_\odot}}\right)^{-1.12} \frac{0.12}{\tau_{8M_\odot}} & t \geq \tau_{8M_\odot} \end{cases}, \tag{2.3}$$

where $\tau_{8M_\odot}$ is an offset time between the star particle's birth and the first SNIa. The number of SNIa per time step and solar mass for $t > t_0$ is then given by (Vogelsberger et al., 2013)

$$N_{\mathrm{SNIa}}(t, \Delta t) = \int_t^{t+\Delta t} g(t' - t_0) dt'. \tag{2.4}$$

During the evolution, the gas surrounding the star particles gets enriched with mass and metals (the simulation follows H, He, C, N, O, Ne, Mg, Si and Fe, Pillepich et al., 2019), the returned masses and metal yields are pretabulated and defined in Pillepich et al. (2018a).

In IllustrisTNG, wind particles driven by SNII energy spawn from star-forming gas and are injected isotropically in the surrounding medium (Pillepich et al., 2018a). Whether a star-forming cell spawns a wind particle or a star particle is decided by drawing a random number x between 0 and 1, if $x < 1/(1+\eta_w)$ (η_w is the wind's mass loading), the gas cell forms stars, otherwise it spawns wind particles (Vogelsberger et al., 2013). The wind particles velocity in IllustrisTNG is (Pillepich et al., 2018a)

$$v_w = \max \left[\kappa_w \sigma_{\mathrm{DM}} \left(\frac{H_0}{H(z)}\right)^{\frac{1}{3}}, v_{w,\mathrm{min}} \right], \tag{2.5}$$

where $\sigma_{\rm DM}$ is the DM velocity dispersion, $\kappa_w = 7.4$ is a dimensionless multiplicative factor and $v_{w,\rm min} = 350$ km s^{-1} is a velocity floor, such that the wind speed cannot become arbitrarily low in halos of low mass. The wind particles mass loading factor is (Pillepich et al., 2018a)

$$\eta_w = \frac{\dot{M}_w}{\dot{M}_{\rm SFR}} = \frac{2}{v_w^2} e_w (1 - \tau_w), \tag{2.6}$$

where $\dot{M}_w$ is the rate of gas mass converted into wind particles, $\dot{M}_{\rm SFR}$ the local SFR, $\tau_w = 0.1$ the fraction of SNII energy that is thermal, and the available wind energy (Pillepich et al., 2018a)

$$e_w = \bar{e}_w \left[f_{w,\rm Z} + \frac{1 - f_{w,\rm Z}}{1 + (Z/Z_{w,\rm ref})^{\gamma_{w,\rm Z}}} \right] \times N_{\rm SNII} E_{\rm SNII,51} 10^{51} \, {\rm erg} \, {\rm M}_\odot^{-1}, \tag{2.7}$$

where $\bar{e}_w = 3.6$ is a dimensionless factor of the model, $f_{w,\rm Z} = 0.25$ is a factor that reduces the energy available to gas cells with a metallicity much larger than $Z_{w,\rm ref} = 0.002$, and $\gamma_{w,\rm Z} = 2$ defines the reduction power. $N_{\rm SNII}$ is the number of SNII per formed stellar mass, and $E_{\rm SNII,51}$ is the available energy per SNII in units of 10^{51} erg. After formation, the massive wind particle is decoupled from hydrodynamics and only interacts gravitationally. It travels through the medium until it either reaches a cell whose density is lower than 0.05× the star formation density threshold, or 0.025× the current Hubble time has elapsed (Pillepich et al., 2018a). The particle then re-couples to the cell where it is currently located and its mass is donated to that cell.

Black holes (BH) are implemented as sink particles that accrete gas from their surrounding and inject feedback energy (Pillepich et al., 2018a). They are placed whenever the FoF-algorithm (see Section 2.2.3 for description) detects a halo of a mass larger than $5 \times 10^{10} h^{-1}$ M$_\odot$[1], where no BH is already present (Vogelsberger et al., 2013; Weinberger et al., 2017). The cell of highest density of the group is then turned into a BH particle (Vogelsberger et al., 2013), with a seed mass of $8 \times 10^5 h^{-1}$ M$_\odot$ (Weinberger et al., 2017). The location of the BH is tied to the potential minimum of the halo (Weinberger et al., 2017), in order to prevent it from artificially leaving the center of the halo. BH sink particles accrete from their

[1] h is chosen as $h = 0.6774$ (Pillepich et al., 2019).

surrounding at a Bondi-Hoyle accretion rate (Hoyle & Lyttleton, 1939; Bondi & Hoyle, 1944, see also Weinberger et al., 2017, 2018)

$$\dot{M}_{\mathrm{Bondi}} = \frac{4\pi G^2 M_{\mathrm{BH}}^2 \rho}{c_s^3}, \tag{2.8}$$

where M_{BH} is the BH mass, ρ is the density of the surrounding medium and c_s is the sound speed in the surrounding medium. This accretion rate is limited by the Eddington accretion rate (Weinberger et al., 2017, 2018)

$$\dot{M}_{\mathrm{Edd}} = \frac{4\pi G M_{\mathrm{BH}} m_{\mathrm{p}}}{\epsilon_r \sigma_{\mathrm{T}}} c, \tag{2.9}$$

where $\epsilon_r = 0.2$ is the BH radiative efficiency, m_{p} is the proton mass and σ_{T} is the Thompson cross-section. The accretion rate therefore is $\dot{M} = \min\left(\dot{M}_{\mathrm{Bondi}}, \dot{M}_{\mathrm{Edd}}\right)$. BH particles inject feedback in either a 'thermal' or a 'kinetic' mode (Weinberger et al., 2017, 2018):

$$\text{thermal} : \frac{\dot{M}_{\mathrm{Bondi}}}{\dot{M}_{\mathrm{Edd}}} \geq \chi \tag{2.10}$$

$$\text{kinetic} : \frac{\dot{M}_{\mathrm{Bondi}}}{\dot{M}_{\mathrm{Edd}}} < \chi \tag{2.11}$$

$$\chi = \min\left[0.002 \left(\frac{M_{\mathrm{BH}}}{10^8\,\mathrm{M}_\odot}\right)^2, 0.1\right]. \tag{2.12}$$

In a thermal injection mode, feedback energy is injected as thermal energy in the surrounding cells, in the case of the kinetic mode, it is injected as kinetic energy. The injected energy rate is $\dot{E}_{\mathrm{inj}} = \epsilon_{\mathrm{in}} \dot{M} c^2$, where for thermal mode $\epsilon_{\mathrm{in}}^{\mathrm{therm}} = \epsilon_f \times \epsilon_r = 0.02$ and for kinetic mode $\epsilon_{\mathrm{in}}^{\mathrm{kin}} = \min\left(\frac{\rho}{0.05\rho_{\mathrm{SF,thresh}}}, 0.2\right)$, where $\rho_{\mathrm{SF,thresh}}$ is the threshold density for star formation (Weinberger et al., 2018; Vogelsberger et al., 2013). Feedback is injected isotropically. In addition to accretion, BH are also allowed to merge with other BH particles (Weinberger et al., 2018).

2.2.2 Thermodynamical Processes

For cooling of the gas in the simulation, IllustrisTNG takes into account the contribution from primordial hydrogen, helium and their ions Λ_p, metal cooling Λ_m and

Compton cooling of the CMB Λ_C, such that the total cooling rate is (Vogelsberger et al., 2013)

$$\Lambda(T, \rho, z, Z) = \Lambda_p(T, \rho, Z) + \frac{Z}{\mathrm{Z}_\odot}\Lambda_m(T, \rho, z, \mathrm{Z}_\odot) + \Lambda_C(T, \rho, z), \tag{2.13}$$

where T is gas temperature, ρ is gas density, z is the current redshift and Z is the gas metallicity, while $\mathrm{Z}_\odot$ denotes solar metallicity. Λ_p is calculated directly from ionization equations, Λ_m is taken from precalculated lookup-tables, generated with Cloudy (Ferland et al., 1998, 2013, 2017).

The simulation box is subject to a spatially uniform, time dependent UV background following the description by Faucher-Giguère et al. (2009) (Pillepich et al., 2018a; Vogelsberger et al., 2013), which is switched on at $z = 6$ (Pillepich et al., 2018a). The simulation accounts for self-shielding of the gas (see Vogelsberger et al., 2013). The UV background is superimposed with radiation from active galactic nuclei (AGN, Pillepich et al., 2018a; Vogelsberger et al., 2013), in the thermal and kinetic feedback modes (see above), an energy fraction of $(1 - \epsilon_{\mathrm{in}}^{\mathrm{therm}}/\epsilon_r)$ and $(1 - \epsilon_{\mathrm{in}}^{\mathrm{kin}}/\epsilon_r)$ is used respectively. The AGN spectral energy distribution (SED) of the frequency ν is parameterized by (Vogelsberger et al., 2013)

$$f^{\mathrm{AGN}}(\nu) = \nu^{\alpha_{\mathrm{UV}}} \exp\left(-\frac{h\nu}{k_B T_{\mathrm{BB}}}\right) \exp\left(-\frac{10^{-2}\,\mathrm{Ryd}}{h\nu}\right) + a\nu^{\alpha_{\mathrm{X}}} \tag{2.14}$$

with

$$\frac{f^{\mathrm{AGN}}(2\,\mathrm{keV})}{f^{\mathrm{AGN}}(2500\,\mathrm{\AA})} = \left(\frac{2\,\mathrm{keV}}{2500\,\mathrm{\AA}}\right)^{\alpha_{0\mathrm{X}}} = 403.3^{\alpha_{0\mathrm{X}}}, \tag{2.15}$$

which is set through a corresponding choice of a. The SED is assumed to be fixed with $T_{\mathrm{BB}} = 10^6$ K, $\alpha_{0\mathrm{X}} = -1.4$, $\alpha_{\mathrm{UV}} = -0.5$ and $\alpha_{\mathrm{X}} = -1$.

2.2.3 Structure Finder

IllustrisTNG runs several on-the-fly analysis routines with the simulation (Pillepich et al., 2018a), two of them are structure finders: a Friends-of-Friends (FoF) algorithm (e.g., Davis et al., 1985), and Subfind (Springel et al., 2001, 2005).

The FoF algorithm links particles according to a linking length b, which is often

defined in a dimensionless way as a fraction of the mean inter-particle distance $\bar{l} = \bar{n}^{-1/3}$. A simulation element is linked to all elements which are separated from it by less than the linking length, and indirectly linked to all particles which are linked to particles it itself is linked to. In TNG, a linking length of $b = 0.2$ is used (Pillepich et al., 2018b). Structures found by this algorithm are called 'halos' and need to contain at least 32 DM particles to be recognized as a structure (Vogelsberger et al., 2014b). In a first stage, this algorithm just takes DM particles into account, i.e., it finds DM halos, which non-DM simulation elements are linked to in a second stage via their nearest DM particle (Vogelsberger et al., 2014b). This algorithm is used to decide for the placement of BH particles (see above).

The SUBFIND algorithm operates on the found FOF halos and identifies overdense gravitationally bound structures within them (Springel et al., 2001). Such structures are referred to as 'subhalos' in the following. The algorithm identifies subhalo candidates by isodensity contours. If the enclosing isodensity contours traverse a saddle point, the enclosed overdensity is a candidate and density peaks and connection points between structures are identified (Springel et al., 2001). Subsequently, all elements with a positive total energy are removed from the structure, such that only bound elements remain (Springel et al., 2001, 2005). If the remaining bound structure has more than 20 elements, it is identified as a subhalo (Springel et al., 2005).

Subhalos can be seen as analogues to galaxies in the TNG simulations, as halos are analogues to galaxy groups or clusters. The most massive subhalo of a FOF halo is the analogue to the central galaxy of a galaxy cluster, with the other, less massive subhalos being analogues to satellites.

2.3 Rhea

The second simulation suit we use is the set of Rhea simulations, introduced in Göller et al. (2025). This is a set of isolated galaxy simulations of Milky-Way-like galaxies, named after the Greek goddess Rhea (Ρεα), mother of Zeus, whose milk according to Hyginus (nd) (probably between 0 and 200 AC, also mentioned in Bertola 2009) formed the Milky Way. It includes HD and MHD runs as well as runs with CRs. In this section we will introduce the basic set-up of the simulations. Some

Simulation properties	
Box size	$(150\,\mathrm{kpc})^3$
Mass resolution (gas)	3.0×10^3 $M_\odot$
spatial resolution	maximum limit 100 pc, minimal limit 1 pc in the disk
Simulation time	4.0 Gyr
CPU hours	$10^5 - 10^6$ per simulation

Table 2.2: Properties of the Rhea simulation suit: Simulation box size, adopted mass resolution for gas, spatial resolution, time spanned by the simulation and used CPU hours. Values taken from Göller et al. (2025).

characteristics mentioned here are also described in Göller et al. (2025), and therefore Chapter 4. However, here we will expand on the description of the simulations given in that work and aim to give a comprehensive overview over all used methods and everything Rhea can do.

The Rhea simulations aim for a coherent simulation of the evolution of a Milky-Way-like Galaxy under the influence of different physical processes. Like IllustrisTNG, they are based on Arepo, but cover a different scale. Only a single, Milky-Way-mass Galaxy is placed in the simulation box, no satellites or other interfering systems are considered. The isolated Galaxy is simulated in a box with a sidelength of 150 kpc (even though the Galactic disk just reaches up to 30 kpc in radius) to avoid boundary effects on the Galaxy. The simulation just includes gas and subsequently formed stars, no DM or BH are explicitly simulated (even though their gravitational potential is included in the imposed external potential, see Section 2.3.7). The mass resolution is set to 3.0×10^3 $M_\odot$, with additional volume limitations. In the whole box, cells are not allowed to exceed a volume of 2 kpc^3 or become smaller than 1 pc^3 (this lower volume limit was set to limit the timestepping of the code). Moreover, in the region of the Galactic disk ($R < 30$ kpc, $|z| < 1$ kpc from the center of the simulation box) cells are not allowed to exceed a volume of 10^6 pc^3. From initial conditions, the Galaxy is evolved for 4 Gyr in two phases (for details see Section 2.3.2), during which star formation, stellar feedback and chemical evolution is followed. The first set of Rhea simulations consists of 6 runs: a run in HD, MHD and MHD+CR in two different potentials, respectively. In this thesis we will focus on the two HD-runs (but present the setup of the MHD and MHD+CR runs nonetheless in this section), which prove the feasibility and usefulness of the

Rhea setup and are presented in Göller et al. (2025), whereas the MHD+CR runs are the focus of Kjellgren et al. (2025). The MHD runs are mainly used for comparison to the MHD+CR runs to be able to quantify the impact of CRs. The basic properties of the Rhea simulation can be found in Table 2.2.

2.3.1 Hydrodynamical Treatment with Arepo

In the HD runs, we solve the equations of magnetohydrodynamics (Equations 1.29 to 1.31) with the closure function 1.37 as described in Section 2.1, with B set to 0. The gravitational potential $\Phi = \Phi_{\text{ext}} + \Phi_{\text{gas}} + \Phi_{\text{stars}}$ is the sum of the external potential (see Section 2.3.7), the self-gravity of gas and the potential of star particles. For the closure function we use $\gamma = 5/3$ everywhere, even in molecular gas. We justify this choice by the fact that, although molecular gas exists in our simulation, the vast majority of this gas has a temperature below 200 K, which is too low for the internal degrees of freedom of H_2 to be excited.

2.3.2 Initial Conditions and Evolution Phases

The initial conditions are identical for all runs. The simulations are started with a smooth gaseous disk in the center of the simulation box, that has a density distribution of (Sormani et al., 2019)

$$\rho_{\text{gal}}\left(R_{\text{gal}}, z\right) = \frac{\Sigma_0}{4 z_{\text{d}}} \exp\left(-\frac{R_{\text{m}}}{R_{\text{gal}}} - \frac{R_{\text{gal}}}{R_{\text{d}}}\right) \operatorname{sech}^2\left(\frac{z}{2 z_{\text{d}}}\right), \tag{2.16}$$

with $z_{\text{d}} = 85\,\text{pc}$, $R_{\text{d}} = 7\,\text{kpc}$, $R_{\text{m}} = 1.5\,\text{kpc}$ and $\Sigma_0 = 50\,\text{M}_\odot\,\text{pc}^{-2}$. This distribution is truncated at 30 kpc radius, further out we set the gas to $\rho_{\text{min}} = 10^{-31}\,\text{g}\,\text{cm}^{-3}$. In z-direction we do not impose a cut, but set a minimum density of the same value, such that the density is $\rho = \max(\rho_{\text{gal}}, \rho_{\text{min}})$. This results in a total mass of the simulated gas disk of $\sim 10^{10}$ $\text{M}_\odot$. Initially we set the gas temperature to 1.3×10^4 K everywhere in the simulation box. The initial velocity of each gas cell is set according to the imposed external potential (see Section 2.3.7). For the MHD and MHD+CR runs, a toroidal magnetic field scaling as $B = B_0(\rho/\rho_0)^{1/3}$ (Kjellgren et al., 2025) with a strength of $B_0 = 3$ μG (Ferrière, 2001; Beck, 2015; Han, 2017) at $\rho_0 = 10^{-24}$ g cm^{-3} is imposed on the initial conditions (Girichidis et al., 2018;

Whitworth et al., 2024; Kjellgren et al., 2025).

We let the simulations evolve in two phases. During phase I, which lasts 2 Gyr, we let the system evolve with a reduced stellar lifetime to avoid features caused by the initial conditions. Therefore we start the simulation with a temperature floor of 100 K, preventing the simulated gas from cooling too much. Star formation is enabled, but the lifetime of stars is reduced by a factor of 10, resulting in quasi-instantaneous feedback, feeding the turbulence in the disk. In addition to momentum and energy injection by SN feedback (see Section 2.3.4), in this phase we make each SN return $M_{\rm starP}/N_{\rm SN,tot}$ of mass into the surrounding medium, where $M_{\rm starP}$ is the mass of the star particle that injects the feedback, and $N_{\rm SN,tot}$ is the total number of SN that will explode in this star particle, i.e., the number of stars with a mass > 8 M$_\odot$. This ensures that with the last exploding SN all mass of the star particle is returned to the simulated gas and the star particle ceases to exist. Therefore, during this phase no mass is locked up in star particles permanently. We do not mean to resemble mass return by SN with this, as for that a much lower mass fraction of the star particle has to be returned (in a Kroupa IMF, only 17 % of mass resides in stars of mass > 8 M$_\odot$, Kroupa, 2001, and how much mass a star actually ejects in a SN depends on its initial mass is a non-trivial correlation, Limongi & Chieffi, 2010a,b), but to simply ensure that we do not loose gas from our simulation during this stage. Over a time of $t_{\rm inc} = 1$ Gyr we increase the stellar lieftimes to their normal, tabulated lifetimes via a development of the shortening factor $f_{\rm short} = f_0/((t/t_{\rm inc})(f_0-1)+1)$, with $f_0 = 10$. After we reached the tabulated lifetime we run for another Gyr with mass return still enabled.

During phase II, which lasts another 2 Gyr, we disable the mass return from SN and run with normal stellar lifetimes and energy and momentum injection by SN. The temperature floor is decreased to 20 K in this phase. This is below the characteristic temperature in the highest density gas in our simulation and we therefore do not expect this floor to significantly affect our simulation.

2.3.3 Star Formation

We treat stars via star particles that form from Jeans-unstable gas. The star particles have a mass comparable to that of a gas cell, i.e., about 3000 M$_\odot$, and therefore represent not a single, but multiple stars. However, each star particle gets populated

explicitly with individual massive stars sampled from a Kroupa IMF (Kroupa, 2001, 2002), which are responsible for the timing and strength of stellar feedback injected from the star particle. Contrary to sink particles, who are often implemented to represent a mix of stars and gas, our star particles consist only of stars, i.e., no gas is hidden within them.

To decide when and where star formation takes place, we inspect all active gas cells for their Jeans mass, Equation 1.19. If the mass of a cell exceeds 1/8th of its calculated Jeans mass, it is flagged as possibly star-forming. We then calculate the cells free-fall time (Equation 1.12) and star formation rate (Equation 1.13), using a SFE of $\epsilon = 1$ %. The probability of a cell to form a star then is (as given in Springel & Hernquist, 2003)

$$p = \frac{M_{\mathrm{cell}}}{M_{\mathrm{starP}}} \left[1 - \exp\left(-\mathrm{SFR} \frac{\Delta \mathrm{t}}{\mathrm{M_{cell}}} \right) \right], \tag{2.17}$$

where M_{cell} is the mass of the gas cell and M_{starP} is the mass of the formed star particle (which we set equal to the mass of the gas cell, except for cases in which the gas cell exceeds the set gas resolution mass (see Table 2.2) by more than a factor of 2, in which case only half of the cell's mass is converted into a star particle). We prevent p from becoming > 1 by limiting the timestep Δt of star-forming cells to

$$\Delta t < 0.1 \frac{M_{\mathrm{cell}}}{\mathrm{SFR}}. \tag{2.18}$$

Afterwards we draw a random number x_{SF} between 0 and 1 and convert the cell into a star particle if $x_{\mathrm{SF}} < p$.

If the mass of a cell already exceeds its Jeans mass, we enforce the formation of a star particle without the probabilistic approach, to prevent a resolution that falls below the local Jeans mass. The used approach was first introduced by Smith et al. (2021). After a star particle is formed, its birth properties like coordinates at birth, birthtime, density of its parent gas cell and ID are stored in an external output file.

It is worth noting that other criterion for star formation are possible and frequently used, starting from a simple density threshold, like it is used by Renaud et al. (2013) or Jeffreson et al. (2020), and reaching up to elaborate multi-step checks of gas stability, inflow rates and gravitational potentials. Several star formation schemes are actually implemented in the star particle implementation that was developed for

Rhea. In a first iteration, a simple density threshold, and subsequently a density threshold plus the described probabilistic approach was used, but finally changed to the Jeans mass criterion described here. This criterion has the great advantage over the density threshold, that it is impartial to changes in resolution, while a density threshold has to be chosen anew if the resolution is changed. Moreover, a density threshold, even if chosen carefully, is an arbitrary measure, while the Jeans mass has a physical foundation. Finally, we decided against an even more elaborate star formation criterion (the implementation includes the possibility to check for velocity dispersion and the gravitational potential of the flagged cell), because those come with additional computational complexity, which we seek to avoid.

In order to make the future usage of the simulations and star particle implementation in zoom-in simulations more easy, the star particle implementation also includes an option to decouple the star particle mass from the gas cell mass and set it to a smaller value. This can be used to safely create initial conditions for simulations with higher resolution than the current one, and prevents overly massive and clustered star particles to distort the gravitational field and feedback processes. We do not use this option in the simulations presented here, but will use it for future zoom-ins.

2.3.4 Stellar Feedback

As mentioned, each formed star particle is populated by individual stars drawn from a Kroupa IMF, following an algorithm described in Sormani et al. (2017). The whole mass of the star particle is sampled in stars, i.e., no mass is left to account for hidden gas. Stars with a mass between 8 and 120 $M_\odot$, i.e., those which will explode as SN, are then assigned a stellar lifetime in accordance to Maeder (2008), Table 25.6, where we linearly interpolate between the mass bins.

If the liefetime of a star within a star particle passed, SN feedback is injected from the star particle. This is done as either energy or momentum injection, this combined SN injection scheme was presented in Tress et al. (2020a). Which injection scheme is used is decided by the radius of the SN remnant at the end of the Sedov-Taylor phase, which is given by (Blondin et al., 1998; Gatto et al., 2015; Tress et al.,

2020a)

$$R_{\mathrm{ST}} = 19.1 \left(\frac{\bar{n}}{1\,\mathrm{cm}^{-3}} \right)^{-7/17} \mathrm{pc}, \tag{2.19}$$

where $\bar{n}$ is the local mean number density. In cases where R_{ST} is larger than the injection radius of the cell $R_{\mathrm{inj}} = 100$ pc, i.e., in cases where the Sedov-Taylor phase is resolved, we inject a thermal energy of 10^{51} erg isotropically into the cells of within R_{inj} and set their gas to being fully ionized. The gas subsequently is allowed to evolve self-consistently. The heated gas will expand and increase pressure on the surrounding medium, resulting in an expanding SN bubble, as expected (Gatto et al., 2015).

In cases where the Sedov-Taylor phase is not resolved, i.e., R_{ST} is smaller than the injection radius in regions of high density, the cells within the injection radius are injected with a momentum of (Blondin et al., 1998; Gatto et al., 2015; Kim & Ostriker, 2015; Martizzi et al., 2015)

$$p_{\mathrm{fin}} = 2.6 \times 10^5 \left(\frac{\bar{n}}{1\,\mathrm{cm}^{-3}} \right)^{-2/17} \mathrm{M}_\odot\,\mathrm{km\,s}^{-1} \tag{2.20}$$

and leave the ionization state and temperature of the cells untouched. This is, because in those regions the injected energy would be distributed over too much mass, resulting in insufficient heating, with the injected energy being cooled away too fast for a sufficient SN remnant to form (this is known as the overcooling problem). We therefore omit the heating phase, but make sure the momentum feedback is accounted for (Gatto et al., 2015).

SNe exploding in low-density environment, however, pose the risk of unphysically high temperatures in the injection region. The injected energy is distributed over little mass, heating the gas there to temperatures $\gtrsim 10^8$ K. Because of the characteristics of the cooling curve, gas of such high temperatures cools inefficiently, staying at these temperatures for a long time. To prevent this, we check the current temperature

$$T_{\mathrm{cur}} = \frac{e_{\mathrm{th}}(\gamma - 1)\mu m_p}{k_B} \tag{2.21}$$

of the cells in the injection region. If T_{cur} is larger than $T_{\mathrm{cut}} = 10^7$ K, no energy is

	Reaction	Reference for rate coefficient
1.	$H + H + \text{grain} \rightarrow H_2 + \text{grain}$	Hollenbach & McKee (1979)
2.	$H_2 + H \rightarrow 3H$	Mac Low & Shull (1986); Lepp & Shull (1983)
3.	$H_2 + H_2 \rightarrow 2H + H_2$	Martin et al. (1998); Shapiro & Kang (1987)
4.	$H_2 + \gamma \rightarrow 2H$	see details in Glover & Mac Low (2007a)
5.	$H + CR \rightarrow H^+ + e^-$	see details in Glover & Mac Low (2007a)
6.	$H + e^- \rightarrow H^+ + 2e$	Abel et al. (1997)
7.	$H^+ + e^- \rightarrow H + \gamma$	Ferland et al. (1992)
8.	$H^+ + e^- + \text{grain} \rightarrow H + \text{grain}$	Weingartner & Draine (2001)

Table 2.3: Reactions of hydrogen followed in NL97, taken from Glover & Mac Low (2007a,b).

injected. If we estimate the temperature after injection

$$T_{\text{est}} = \frac{(e_{\text{th}} + e_{\text{inj}})(\gamma - 1)\,\mu m_p}{k_{\text{B}}} \tag{2.22}$$

to be larger than this threshold, we reduce the injected energy e_{inj} by a factor

$$f_l = \frac{(T_{\text{cut}} - T_{\text{est}})k_{\text{B}}}{(\gamma - 1)\,\mu m_p e_{\text{inj}}} + 1. \tag{2.23}$$

2.3.5 Chemical Network and Thermodynamics

To model the non-equilibrium chemical composition and to reliably track ionization states of gas we adopt a chemical network in Rhea. We use the NL97 network presented in Glover & Clark (2012), which combines the hydrogen chemistry of Glover & Mac Low (2007a,b) with simplified CO chemistry from Nelson & Langer (1997).

In this network we explicitly follow hydrogen via reactions given in Table 2.3, which enables us to calculate abundances of H, H_2 and H^+ for each cell and timestep. Additionally, we set the elemental abundances of carbon and oxygen in accordance with Sembach et al. (2000) to $x_{\text{C}} = 1.4 \times 10^{-4}$ and $x_{\text{O}} = 3.2 \times 10^{-4}$. We assume carbon to be singly ionized and the ionization state of oxygen to be tied to that of hydrogen via charge transfer $O + H^+ \rightleftharpoons H + O^+$ (Glover & Mac Low, 2007a) such that $n_{\text{O}^+}/n_{\text{O}} = n_{\text{H}^+}/n_{\text{H}}$.

We track the conversion of C^+ to CO and vice versa with the effective conversion

pathway proposed by Nelson & Langer (1997), that ignores any intermediate species and approximates a direct conversion. They assume

$$C^+ + H_2 \rightarrow CH_2^+ + \gamma \tag{2.24}$$

to be the initial step (Nelson & Langer, 1997), which is a slow radiative association (Glover & Clark, 2012) and is therefore also assumed to be the rate-limiting step. Hydrocarbon radicals can subsequently react with oxygen to form CO. Any neutral carbon produced by photodissociation of CO or CH_x we assume to be photoionized instantly (Glover & Clark, 2012). The rate equation for CO can then be written as (Glover & Clark, 2012)

$$\frac{dn_{CO}}{dt} = k_0 n_{C^+} n_{H_2} \beta - \Gamma_{CO} n_{CO}, \tag{2.25}$$

where n_x is the number density of the given species, $k_0 = 5 \times 10^{-16}$ cm^3 s^{-1} (Nelson & Langer, 1997) is the rate coefficient of reaction 2.24. Here, β is the fraction of CH_x that successfully forms CO (Glover & Clark, 2012) and is given by (Glover & Clark, 2012; Nelson & Langer, 1997)

$$\beta = \frac{k_1 x_O}{k_1 x_O + \frac{\Gamma_{CH_x}}{n}}, \tag{2.26}$$

where $k_1 = 5 \times 10^{-10}$ cm^3 s^{-1} (Nelson & Langer, 1997) is the rate coefficient for the formation of CO from O and CH_x and n is the number density of hydrogen nuclei. Γ_{CO} and Γ_{CH_x} are the photodissociation rates of CO and CH_x respectively and (Glover & Clark, 2012)

$$\Gamma_{CO} = 2 \times 10^{-10} G_0 \exp(-2.5 A_V) f_{sh} \text{ s}^{-1} \tag{2.27}$$

and $\Gamma_{CH_x} = 5\,\Gamma_{CO}$. A_V is the V-band extinction and f_{sh} is a shielding factor for CO self-shielding and H_2 shielding of CO. Here, G_0 denotes the strength of the interstellar UV field in units of the Habing (1968) field. Unless noted otherwise, here we adopt $G_0 = 1.7$ (Draine, 1978) (for optical and infrared we adopt values from Mathis et al., 1983). In addition to the UV, optical and infrared ISRF, we take into account cosmic ray ionization at a rate of $\zeta_H = 3 \times 10^{-17}$ s^{-1} (Göller et al.,

2025). This accounts for the effect of low-energy cosmic rays, which dominate cosmic ray heating and ionization rates. The cosmic ray model we describe in Section 2.3.6 models the effects of the cosmic rays dominating the energy budget.

To calculate shielding of the ISRF, we use the TreeCol algorithm proposed by Clark et al. (2012). This tree-based scheme constructs a HEALPix sphere (Górski et al., 2005) at the location of each cell of the simulation box (Clark et al., 2019), and subsequently walks the gravity tree, adding up the contributions of all tree nodes whose line of sight contribute to the considered pixel (Clark et al., 2012). With that, it constructs 4π maps of column densities of H_2, CO and dust, which we then use to calculate self-shielding and dust absorption (Clark et al., 2019). For that, we use the shielding functions of Draine & Bertoldi (1996) and Visser et al. (2009).

With this chemical information of the gas we are able to accurately track also chemical contributions to heating and cooling in the simulation. The basic framework of Springel (2010b) already includes treatment of adiabatic expansion and contraction of gas and viscous dissipation in shocks. With the chemical network, we are able to calculate changes in the internal energy density due to processes listed in Table 2.4. Details of the thermodynamics of gas are given in Glover et al. (2010) and Mackey et al. (2019).

Moreover, we solve for the dust temperature, which is important for the H_2 formation rate on dust grains. Since dust cooling is an efficient process, we assume dust to be thermal equilibrium with its surrounding (Clark et al., 2019; Glover & Clark, 2012), i.e., solve for

$$\mathcal{H}_{\text{ext}} - \Lambda_{\text{dust}} + \mathcal{H}_{\text{gd}} + \mathcal{H}_{\text{H}_2} = 0. \tag{2.28}$$

Here, $\mathcal{H}_{\text{ext}}$ is the dust heating rate per unit volume from the ISRF, Λ_{dust} is the dust cooling rate, $\mathcal{H}_{\text{gd}}$ is the energy transfer rate from gas to dust and $\mathcal{H}_{\text{H}_2}$ is the dust heating rate from H_2 formation on the surface of dust grains. For $\mathcal{H}_{\text{ext}}$ we use(Glover & Clark, 2012)

$$\mathcal{H}_{\text{ext}} = \chi \mathcal{H}_{\text{ext},0}, \tag{2.29}$$

where $\mathcal{H}_{\text{ext},0}$ is the unattenuated heating rate from the ISRF, and χ accounts for attenuation due to dust absorption, which we calculate via the aforementioned

Process	Reference
Heating:	
Photoelectric effect	Bakes & Tielens (1994); Wolfire et al. (2003)
H_2 photodissociation (Reac. 4)	Black & Dalgarno (1977)
UV pumping of H_2	Burton et al. (1990)
H_2 formation on grains (Reac. 1)	Hollenbach & McKee (1989)
CR ionization (Reac. 5)	Goldsmith & Langer (1978)
Cooling:	
C^+ fine structure lines	Atomic data: Silva & Viegas (2002)
	H_2 collision rates: Flower & Launay (1977)
	H collision rates ($T < 2000$ K): Hollenbach & McKee (1989)
	H collision rates ($T > 2000$ K): Keenan et al. (1986)
	e^- collision rates: Wilson & Bell (2002)
O finestructure lines	Atomic data: Silva & Viegas (2002)
	H collision rates: Abrahamsson et al. (2007)
	H_2 collision rates: Glover & Jappsen (2007)
	e^- collision rates: Bell et al. (1998)
	H^+ collision rates: Pequignot (1990, 1996)
H_2 rovibrational lines	Glover & Abel (2008)
CO rovibrational lines	Neufeld & Kaufman (1993); Neufeld et al. (1995)
Gas-dust energy transfer	Hollenbach & McKee (1989)
Compton cooling	Cen (1992)
Coll. ionization of H (Reac. 6)	Abel et al. (1997)
Coll. dissociation of H_2 (Reac. 2&3)	Lepp & Shull (1983); Mac Low & Shull (1986)
	Martin et al. (1996, 1998)
	Shapiro & Kang (1987); Palla et al. (1983)
Recombination of H^+ (Reac. 7&8)	Ferland et al. (1992); Wolfire et al. (2003)

Table 2.4: Heating and cooling processes accounted for in this simulation with references. If applicable, the corresponding reactions from Table 2.3 are given. Please see Mackey et al. (2019) and Glover et al. (2010) for further references and information.

TreeCol algorithm. For $\Lambda_{\rm dust}$ we use (Glover & Clark, 2012)

$$\Lambda_{\rm dust}\left(T_{\rm dust}\right) = 4\pi\mathcal{D}\rho\int_0^\infty B_\nu\left(T_{\rm dust}\right)\kappa_\nu {\rm d}\nu, \tag{2.30}$$

where $\mathcal{D}$ is the dust-to-gas ration, which we set to that of solar metallicity gas, ρ is the gas density, $B_\nu\left(T_{\rm dust}\right)$ is the Planck function for $T_{\rm dust}$, and κ_ν is the dust opacity. For the energy transfer from gas to dust we use (see Table 2.4, Hollenbach & McKee, 1989)

$$\mathcal{H}_{\rm gd} = 3.8\times10^{-33}T^{\frac{1}{2}}\alpha\left(T-T_{\rm dust}\right)n^2\,{\rm erg\,s^{-1}\,cm^{-3}}, \tag{2.31}$$

where T is the gas temperature, n is the number density of hydrogen nuclei and $\alpha = 1.0 - 0.8\exp(-75/T)$ (Glover & Clark, 2012). For $\mathcal{H}_{H_2}$ we use (see Table 2.3, Hollenbach & McKee, 1979)

$$\mathcal{H}_{H_2} = 7.2 \times 10^{-12} f_{\rm dust} R_{H_2} \,{\rm erg\,s^{-1}\,cm^{-3}}, \tag{2.32}$$

where R_{H_2} is the formation rate of H_2 per unit volume and $f_{\rm dust} = 0.4$ (Glover & Clark, 2012; Takahashi & Uehara, 2001) is the fraction of the binding energy absorbed by the grain.

2.3.6 Cosmic Rays

In the case of MHD+CR simulations (which we do *not* analyze in this thesis, but include here for completeness), the equation of energy conservation gathers additional terms accounting for pressure $P_{\rm CR}$ from CRs and becomes (Pfrommer et al., 2017; Kjellgren et al., 2025)

$$\begin{aligned} \frac{\partial e}{\partial t} + \nabla \cdot \left[(e+P)\boldsymbol{v} - \frac{\boldsymbol{B}(\boldsymbol{v}\cdot\boldsymbol{B})}{4\pi} \right] = \\ -\rho(\boldsymbol{v}\cdot\nabla\Phi) + P_{\rm cr}\nabla\cdot\boldsymbol{v} - \boldsymbol{v}_{\rm st}\cdot\nabla P_{\rm cr} + \mathcal{H} - \Lambda, \end{aligned} \tag{2.33}$$

and, additionally, the CR energy density $e_{\rm CR}$ has to be followed:

$$\begin{aligned} \frac{\partial e_{\rm cr}}{\partial t} + \nabla \cdot \left[e_{\rm cr}\boldsymbol{v} + (e_{\rm cr}+P_{\rm cr})\boldsymbol{v}_{\rm st} - \kappa \frac{\boldsymbol{B}}{|\boldsymbol{B}|} \left(\frac{\boldsymbol{B}}{|\boldsymbol{B}|} \cdot \nabla e_{\rm cr} \right) \right] = \\ -\rho(\boldsymbol{v}\cdot\nabla\Phi) - P_{\rm cr}\nabla\cdot\boldsymbol{v} + \boldsymbol{v}_{\rm st}\cdot\nabla P_{\rm cr} + \mathcal{H}_{\rm cr} - \Lambda_{\rm cr}, \end{aligned} \tag{2.34}$$

where $\kappa = 4 \times 10^{28}$ cm^2 s^{-1} is the CR diffusion coefficient. The streaming velocity $v_{\rm st}$ here is defined as

$$\boldsymbol{v}_{\rm st} = -\boldsymbol{v}_A \,{\rm sign}(\boldsymbol{B}\cdot\nabla P_{\rm cr}), \tag{2.35}$$

where v_A is the Alfvén velocity. The total pressure P then is

$$P = (\gamma_{\rm th} - 1)\, e_{\rm th} + \frac{\boldsymbol{B}^2}{8\pi} + (\gamma_{\rm CR} - 1)\, e_{\rm CR}, \tag{2.36}$$

with $\gamma_{\rm th} = 5/3$ like before, and $\gamma_{\rm CR} = 4/3$ for the relativistic CR component.

In the MHD+CR runs, we have to follow additional CR sources ($\mathcal{H}_{\rm CR}$) and sinks ($\Lambda_{\rm CR}$), given in Equation 2.34. CR are treated as a second fluid in addition to gas, which is a so-called 'gray' approach, as we do not model the CR spectrum but the integrated total CR energy density (Kjellgren et al., 2025).

As sources $\mathcal{H}_{\rm CR}$ of CRs we put SNe, which represent unresolved diffuse shock acceleration in the SN remnants. We therefore inject 10 % of the total SN energy, i.e., 10^{50} erg, of CR energy (Kjellgren et al., 2025) into the cells in which the SN injects (see Section 2.3.4 for details). Equation 2.34 accounts for advection and diffusion, with diffusion going parallel to the magnetic field. The chosen diffusion coefficient $\kappa = 4\times10^{28}$ cm^2 s^{-1} is consistent with observations, which finds $(3-5)\times10^{28}$ cm^2 s^{-1} for CR at ~ 1 GeV(Strong et al., 2007; Kjellgren et al., 2025).

As sinks for CR energy $\Lambda_{\rm CR}$ we account for hadronic losses $\Lambda_{\rm hadr}$ and Coulomb losses $\Lambda_{\rm Coul}$, such that $\Lambda_{\rm CR} = \Lambda_{\rm hadr} + \Lambda_{\rm Coul}$. Hadronic losses account for interaction between a CR proton and a thermal proton, which produces mainly pions, if the relative momentum exceeds a threshold of $p_{\rm thr} m_{\rm p} c = 0.78$ GeV c^{-1}, where $m_{\rm p}$ is the proton rest mass. These pions then decay via (Ruszkowski & Pfrommer, 2023)

$$\pi^{\pm} \rightarrow \mu^{\pm} + \nu_{\mu}/\bar{\nu}_{\mu} \rightarrow e^{\pm} + \nu_e/\bar{\nu}_e + \nu_{\mu} + \bar{\nu}_{\mu}, \tag{2.37}$$

$$\pi^0 \rightarrow 2\gamma. \tag{2.38}$$

We model losses from this reaction via (Pfrommer et al., 2017; Kjellgren et al., 2025)

$$\Lambda_{\rm hadr} = 7.44 \times 10^{-16} \left(\frac{n_e}{1\,{\rm cm}^{-3}} \frac{e_{\rm CR}}{1\,{\rm erg\,cm}^{-3}} \right) \ {\rm erg\,s}^{-1}\,{\rm cm}^{-3}, \tag{2.39}$$

where n_e is the number of free electrons. From reaction 2.37 and 2.38, most energy escapes as gamma rays and neutrinos, we therefore just put 1/6 of the energy from hadron losses into heating of gas.

The deflection of CR ions in the Coulomb field of an electron results in bremsstrahlung, which takes energy from the ion. We model this energy loss from Coulomb interaction via (Ruszkowski & Pfrommer, 2023; Pfrommer et al., 2017; Kjellgren

et al., 2025)

$$\Lambda_{\mathrm{Coul}} = 2.78 \times 10^{-16} \left(\frac{n_e}{1\,\mathrm{cm}^{-3}} \frac{e_{\mathrm{CR}}}{1\,\mathrm{erg\,cm}^{-3}} \right) \mathrm{erg\,s}^{-1}\,\mathrm{cm}^{-3}. \tag{2.40}$$

All of this energy goes into heating of gas.

Moreover, in Equation 2.34, we account for Alfvén cooling to emulate losses from streaming instabilities (Wiener et al., 2017; Kjellgren et al., 2025) that indirectly transfer energy from CRs to gas (see Ruszkowski & Pfrommer, 2023 for an extensive review of the underlying physics). We model this process with the term (Wiener et al., 2013; Kjellgren et al., 2025)

$$\Lambda_{\mathrm{A}} = \boldsymbol{v}_{\mathrm{st}} \cdot \nabla P_{\mathrm{CR}}. \tag{2.41}$$

2.3.7 External Potential

As mentioned before, Rhea does not include DM or BHs into the simulation. Instead, we use an effective external potential that includes these components in addition to the potential from a disk of old stars. We use two different potentials, one very simple logarithmic potential designed to just resemble a flat rotation curve, which we therefore call the 'flat' potential, and a second complex potential model refined to several observational features of the Milky Way, which we will call the 'Milky Way' potential. For a comparison of the dynamical effects of the used potentials, please see Section 4.3.1.

The Flat Potential

The flat potential is an analytic potential, which is designed to recreate a flat rotation curve up to large radii of the Galaxy. It is completely axisymmetric, no features like a galactic bar or spiral arms are included. We model this potential according to Binney & Tremaine (2008), Equation 2.71a:

$$\Phi_{\mathrm{F}}(R, z) = \frac{1}{2} v_0^2 \ln \left(R_c^2 + R^2 + \frac{z^2}{q_\Phi^2} \right) + \mathrm{Constant}, \tag{2.42}$$

where we set $R_c = 100$ pc and $v_0 = 220$ km s^{-1}, and the axis ratio of equipotential surfaces is set to $q_\Phi = 0.8$. The corresponding density distribution is then given by

(Binney & Tremaine, 2008, Equation 2.71c)

$$\rho_{\mathrm{F}}(R,z) = \frac{v_0^2}{4\pi G q_\Phi^2} \frac{(2q_\Phi^2+1)\,R_c^2 + R^2 + (2-q_\Phi^{-2})z^2}{\left(R_c^2 + R^2 + z^2 q_\Phi^{-2}\right)^2}. \tag{2.43}$$

This is a purely analytical description that does not allow for any distinction of which galactic component (DM, gas, stars) contributes how much to the potential. It enables us to model a galaxy with a Milky Way mass and sized disk with a constant rotation velocity in the equatorial plane of (Binney & Tremaine, 2008, Equation 2.71b)

$$v_{\mathrm{rot,F}}(R) = \frac{v_0 R}{\sqrt{R_c^2 + R^2}}. \tag{2.44}$$

The Milky Way Potential

The Milky Way potential (abbreviation: MW potential) is a multi-component potential designed to match central features of the Milky Way as closely as possible, and was first presented in Hunter et al. (2024). We refer the reader to this work for an in-detail discussion of the potential and comparison to observation. Here, we present the basic properties of the potential, taken from Hunter et al. (2024). To calculate the potential, we make use of the Agama library (Vasiliev, 2019), which allows to model complex time-dependent potentials. The potential consists of several different components: the central Galactic BH, the nuclear stellar cluster, the nuclear stellar disk, the Galactic bar, the axisymmetric Galactic disk, spiral arm potentials and the DM halo.

The **potential of Sgr A***, the supermassive BH in the center of our Galaxy, is modeled with a Plummer (1911) potential

$$\Phi_{\mathrm{SgrA}^*} = -\frac{G M_{\mathrm{SgrA}^*}}{\sqrt{r^2 + b^2}}, \tag{2.45}$$

where r is the *spherical* Galactic radius (compared to the cylindrical radius R in Equation 2.42), and $b = 0.1$ pc is a scale radius used to avoid a singularity. The mass of SgrA* we set in accordance with GRAVITY Collaboration et al. (2019) to $M_{\mathrm{SgrA}^*} = 4.154 \times 10^6$ M$_\odot$.

To model the **nuclear stellar cluster (NSC)**, we follow Chatzopoulos et al. (2015) and use the density distribution

$$\rho_{\mathrm{NSC}} = \frac{(3-\gamma)M_{\mathrm{NSC}}}{4\pi q}\frac{a_0}{a^{\gamma}(a+a_0)^{4-\gamma}}, \tag{2.46}$$

with $a_0 = 5.9$ pc and

$$a(R,z) = \sqrt{R^2 + z^2/q^2}, \tag{2.47}$$

$q = 0.73$, $\gamma = 0.71$ and $M_{\mathrm{NSC}} = 6.1 \times 10^7$ $\mathrm{M}_{\odot}$, taken from their best fitting model. The NSC and Sgr A* contribute little to the overall potential.

The modeling of the **nuclear stellar disk (NSD)** we base on model 3 of Sormani et al. (2020b) and the density distribution is given by

$$\rho_{\mathrm{NSD}} = \rho_1 \exp\left[-\left(\frac{a}{R_1}\right)^{n_1}\right] + \rho_2 \exp\left[-\left(\frac{a}{R_2}\right)^{n_2}\right], \tag{2.48}$$

where we define a as given in Equation 2.47, $q = 0.37$, $n_1 = 0.72$, $n_2 = 0.79$, $R_1 = 5.06$ pc, $R_2 = 24.6$ pc, $\rho_2 = 1.53 \times 10^{12}$ $\mathrm{M}_{\odot}$ kpc^{-3} and $\rho_1 = 1.311\rho_2$. This component dominates between ~ 20 pc and ~ 300 pc in galactocentric radius.

The **galactic bar** component is modeled in accordance to Sormani et al. (2022), with individual density distributions covering the Galactic bulge and long bar:

$$\rho_{\mathrm{bar}} = \rho_{\mathrm{bar},1} + \rho_{\mathrm{bar},2} + \rho_{\mathrm{bar},3}, \tag{2.49}$$

where $\rho_{\mathrm{bar},1}$ describes the boxy/peanut structure of the bulge, $\rho_{\mathrm{bar},2}$ the short ellipsoid of the bar and $\rho_{\mathrm{bar},3}$ the long ellipsoid of the bar. We give the density distribution $\rho_{\mathrm{bar},1}$ by (Coleman et al., 2020; Freudenreich, 1998)

$$\begin{aligned}\rho_{\mathrm{bar},1}(x,y,z) =& \rho_1 \,\mathrm{sech}\,(a^m) \times \\ & \left\{1 + \alpha\left[\exp\left(-a_+^n\right) + \exp\left(-a_-^n\right)\right]\right\} \exp\left[-\left(\frac{r}{\mathrm{r_{cut}}}\right)^2\right],\end{aligned} \tag{2.50}$$

with

$$a = \left\{ \left[\left(\frac{|x|}{x_1} \right)^{c_\perp} + \left(\frac{|y|}{y_1} \right)^{c_\perp} \right]^{\frac{c_\parallel}{c_\perp}} + \left(\frac{|z|}{z_1} \right)^{c_\parallel} \right\}^{\frac{1}{c_\parallel}}, \tag{2.51}$$

$$a_\pm = \left[\left(\frac{x \pm cz}{x_c} \right)^2 + \left(\frac{y}{y_c} \right)^2 \right]^{\frac{1}{2}}, \tag{2.52}$$

$$r = \left(x^2 + y^2 + z^2 \right)^{\frac{1}{2}}. \tag{2.53}$$

The parameters $\alpha = 0.626$ and $c = 1.342$ define the strength and slope of the X-shape, the scale lengths are $x_1 = 0.49$ kpc, $y_1 = 0.392$ kpc, $z_1 = 0.229$ kpc, $x_c = 0.751$ kpc and $y_c = 0.469$ kpc, the shaping parameters are $c_\perp = 2.232$ and $c_\parallel = 1.991$, the exponents are $m = 0.873$ and $n = 1.94$, the normalization factor is $\rho_1 = 3.16 \times 10^9$ $\mathrm{M}_\odot$ kpc^{-3} and the cutoff radius is $r_{\mathrm{cut}} = 4.37$ kpc. The other components are given by (Sormani et al., 2022; Wegg et al., 2015; Portail et al., 2017)

$$\begin{aligned} \rho_{\mathrm{bar,i}}(x,y,z) =& \rho_i \exp\left(-a_i^{n_i}\right) \operatorname{sech}^2\left(\frac{z}{z_i}\right) \\ & \times \exp\left[-\left(\frac{R}{R_{\mathrm{i,\,out}}} \right)^{n_{\mathrm{i,\,out}}} \right] \exp\left[-\left(\frac{R_{\mathrm{i,\,in}}}{R} \right)^{n_{\mathrm{i,\,in}}} \right], \end{aligned} \tag{2.54}$$

with $i = \{2, 3\}$ and

$$a_i = \left[\left(\frac{|x|}{x_i} \right)^{c_{\perp,i}} + \left(\frac{|y|}{y_i} \right)^{c_{\perp,i}} \right]^{\frac{1}{c_{\perp,i}}}, \tag{2.55}$$

$$R = \left(x^2 + y^2 \right)^{\frac{1}{2}}. \tag{2.56}$$

We list the values of the different parameters for $\rho_{\mathrm{bar},2/3}$ in Table 2.5. The pattern speed of the bar is set to $\Omega_{\mathrm{bar}} = -37.5$ km s^{-1} kpc^{-1}.

The **axisymmetric Galactic disk** we model following McMillan (2017) via

$$\begin{aligned} \rho_{\mathrm{disk}}(R,z) =& \frac{\Sigma_1}{2h_1} \exp\left(-\frac{R}{R_{\mathrm{d},1}} - \frac{R_{\mathrm{cut}}}{R} - \frac{|z|}{h_1} \right) + \\ & \frac{\Sigma_2}{2h_2} \exp\left(-\frac{R}{R_{\mathrm{d},2}} - \frac{R_{\mathrm{cut}}}{R} - \frac{|z|}{h_2} \right), \end{aligned} \tag{2.57}$$

Parameter	Value	
	Component 2	Component 3
ρ_i $\left[\mathrm{M}_\odot\ \mathrm{kpc}^{-3}\right]$	0.5×10^9	1.743×10^{13}
x_i [kpc]	5.364	0.478
y_i [kpc]	0.959	0.297
z_i [kpc]	0.611	0.252
$R_{i,\,\mathrm{in}}$ [kpc]	0.558	7.607
$R_{i,\,\mathrm{out}}$ [kpc]	3.19	2.204
$c_{\perp,i}$	0.97	1.879
$n_{i,\,\mathrm{in}}$	3.196	1.63
$n_{i,\,\mathrm{out}}$	16.731	-27.291

Table 2.5: Parameter values for $\rho_{\mathrm{bar},2/3}$, taken from Hunter et al. (2024).

with $\Sigma_1 = 1.3719 \times 10^3\ \mathrm{M}_\odot\ \mathrm{pc}^{-2}$, $R_{d,1} = 2$ kpc, $h_1 = 300$ pc, $\Sigma_2 = 9.2391 \times 10^2\ \mathrm{M}_\odot\ \mathrm{pc}^{-2}$, $R_{d,2} = 2.8$ kpc, $h_2 = 900$ pc and $R_{\mathrm{cut}} = 2.4$ kpc.

To imprint **spiral arms** into the galactic disk, we use

$$\rho_{\mathrm{spiral}}\left(R, z, \phi\right) = \rho_{\mathrm{disk}}\left(R, z\right) \cdot \alpha \frac{R^2}{R_0^2} S(R, \phi), \tag{2.58}$$

with a shaping function S following Junqueira et al. (2013)

$$S(R,\phi) = \sum_{k=1}^{2} \left\{ \exp\left(-\frac{R^2}{\sigma_{\mathrm{sp}}^2} \left[1 - f_{m_k,\gamma_k}(R,\phi) \right] \right) - \exp\left(-\frac{R^2}{\sigma_{\mathrm{sp}}^2} \right) I_0\left(-\frac{R^2}{\sigma_{\mathrm{sp}}^2} \right) \right\}, \tag{2.59}$$

where

$$f_{m,\gamma}(R,\phi) = \cos\left(m(\phi + \gamma) - \frac{m}{\tan(\varphi)} \ln\left(\frac{R}{R_a} \right) \right). \tag{2.60}$$

We set $\varphi = 12.5°$, $R_a = 9.64$ kpc, $m_1 = m_2 = 2$, $\gamma_1 = 139.5°$ and $\gamma_2 = 69.75°$. The width parameter $\sigma_{\mathrm{sp}} = 5$ kpc corresponds to a physical width of the spiral arms of 1.082 kpc. I_0 is the modified Bessel function of the first kind of zeroth order. This results in a pattern with four spiral arms, with a pattern speed of $\Omega_{\mathrm{sp}} = -22.5\ \mathrm{km\ s^{-1}\ kpc^{-1}}$.

The **DM halo** finally is modeled by an Einasto (1969) profile

$$\rho_{\mathrm{DM}} = \rho_0 \exp\left[-\left(\frac{r}{a}\right)^{\frac{1}{n}}\right], \tag{2.61}$$

which we scale such that the total mass of the halo

$$M_{\mathrm{Einasto}} = 4\pi\rho_0 a^3 n\Gamma(3n) \tag{2.62}$$

is 1.1×10^{12} $\mathrm{M}_\odot$. Here, $n = 4.5$ is the Einasto index, Γ is the Gamma function and $a = 0.88$ pc is the scale radius.

2.3.8 Statement of Contribution

With this, we described all crucial elements working together to form the Rhea simulation suit. Junia Göller, the author of this thesis, developed and set up this simulations, resolving any problems occurring from interferences between the mentioned components of the simulation with some help from Dr. Philipp Girichidis and Dr. Noé Brucy. She developed, implemented and tested the star particles described in Section 2.3.3 and did provide the lifetime modulation of stars for the SN implementation described in Section 2.3.4, as well as some additional work on the SN feedback to couple them properly to the star particles. Some work and testing on the SN injection region was also done by Dr. Noé Brucy, the basic implementation of SN, initially meant for sink particles, was provided by Dr. Robin Tress. The chemistry network described in Section 2.3.5 is developed and maintained by Prof. Simon Glover, together with several colleagues. Please refer to Glover & Mac Low (2007a,b); Glover et al. (2010); Glover & Clark (2012); Clark et al. (2012) and Clark et al. (2019) for additional details. The integration of CR (Section 2.3.6) was done by Prof. Christoph Pfrommer and Dr. Rüdiger Pakmor, Dr. Philipp Girichidis led the Rhea runs including CRs. The Milky Way potential (Section 2.3.7) and the Arepo-Agama-interface was developed by Dr. Glen Hunter, with some subsequent work by Dr. Noé Brucy. Junia Göller tested this potential in 3D (initial version was 2D) and additionally implemented the flat potential.

3 Star Formation in Jellyfish Galaxies

This chapter is based on the paper Göller et al. (2023), published in Volume 525, Issue 3 of the Monthly Notices of the Royal Astronomical Society (MNRAS) in November 2023. Junia Göller, the author of this thesis, is the first author of the paper, conducted all of the analysis presented in this chapter and made all figures, except for Fig. 3.2 and 3.3, which were provided by Dr. Annalisa Pillepich and Dr. Gandhali Joshi. Dr. Elad Zinger led the production of the jellyfish galaxy catalogs from TNG50, which were used in this paper (see Zinger et al., 2024). Dr. Eric Rohr provided catalogs of SFR of jellyfish galaxies over time, which were used in Section 3.3.5. Junia Göller wrote the text of the paper, with help from Dr. Annalisa Pillepich and Dr. Gandhali Joshi. The text of this chapter was written only by Junia Göller.

Abstract

We start our analysis of star formation in different simulated galactic environments with jellyfish galaxies from the cosmological gravity+magnetohydrodynamical simulation TNG50. In this simulation we quantify the star formation activity and rates of more than 700 jellyfish galaxies with stellar masses between $10^{8.3}$ and $10^{10.8}$ $M_\odot$, which reside in halos with masses between $10^{10.5}$ and $10^{14.3}$ $M_\odot$, covering a redshift range of $z = 0 - 1$. In this chapter, we study the global SFR, differentiate the SFR between the main stellar bodies and tails of the jellyfish, and follow the star formation of individual galaxies along their evolutionary tracks. For comparison, we define control samples of satellite and field galaxies with matched redshift, stellar mass, host halo mass and gas fraction. We find that star formation and ram-pressure stripping are not mutually exclusive, but frequently occur simultaneously in the simulated jellyfish galaxies. Star formation can even occur within the ram-pressure stripped tails, even though this is subdominant to star formation in the main stellar bodies of the galaxies. The simulation does not predict a population-wide enhancement of SFRs in jellyfish galaxies compared to analogue satellite galaxies with an

equivalent stellar mass and gas fraction, as sometimes suggested from observations. The jellyfish galaxies do, however, often undergo bursts of star formation during their history.

3.1 Introduction

During the last few decades, significant differences between the galactic population in galaxy clusters and in the field (i.e., environments of low galaxy density) were found, as described in Section 1.3.1. These include that galaxies in clusters have a redder color (Kennicutt, 1983), a lower SFR (Bower & Balogh, 2004), are more HI deficient (e.g., Giovanelli & Haynes, 1985) and more frequently show non-disky morphologies (Dressler, 1980) than galaxies of similar mass in the field.

To explain these observational findings, several mechanisms have been proposed (Boselli et al., 2022; Moore et al., 1996; Larson et al., 1980), which we explain in detail in Section 1.3.4. Ram-pressure stripping (RPS), introduced by Gunn & Gott (1972), has been shown to strip a galaxy not only of its loosely-bound CGM, but also its cold and dense ISM, and produce a tail of gas opposite to the galaxy's direction of motion.

During this process of stripping the galaxies show an extremely asymmetric gas distribution, with long (several tens of kpc) wakes of gas originating from their stellar bodies. Those galaxies have been dubbed *jellyfish galaxies* in the literature (e.g., Ebeling et al., 2014), and have been observed across a wide range in wavelength from X-ray (Sun et al., 2010) to radio (Roberts et al., 2021a). For an extensive list of recent observational efforts dedicated to jellyfish galaxies, please see Section 1.3.4.

These observations show that jellyfish galaxies are not quenched but star-forming, despite their reduced ISM from ongoing RPS. Star formation has been observed in the compressed gas in the galactic bodies (Vulcani et al., 2018; Roberts et al., 2022), as well as in the tails (Vulcani et al., 2018; Cramer et al., 2019; Jáchym et al., 2019). As these consist of diffuse gas at much lower densities than in the galactic bodies, it remains an open question how and why stars form in this environment. Magnetic fields may play a role in this context (Safarzadeh & Loeb, 2019; Müller et al., 2021), but it is difficult to draw causal connections as star formation is not a linear process and, in the case of jellyfish galaxies, complex internal dynamics have to be taken

into account (Roediger, 2009).

As mentioned in Section 1.3.4, some observations even suggest an enhanced SFR in jellyfish galaxies (Vulcani et al., 2018; Ramatsoku et al., 2020; Vulcani et al., 2020) compared to samples of field or satellite galaxies. Yet, other studies find no sign of such an enhancement or even suggest the SFR to be reduced (Mun et al., 2021; Yoon et al., 2017). Moreover, the presence of Hα, which is often used as a tracer for ongoing star formation, in the tails might not be as tightly linked to star formation as in galactic disks (Boselli et al., 2016). SFRs derived from Hα measurements in the tails could be overestimated (Cramer et al., 2019). Therefore, the question of whether jellyfish galaxies have enhanced SFRs compared to field or satellite galaxies is still unanswered.

These difficulties in the extraction of reliable SFRs from observations, as well as the limited number of observed jellyfish galaxies, have led to many efforts in simulating jellyfish galaxies (e.g., Kronberger et al., 2008; Kapferer et al., 2009; Tonnesen & Bryan, 2012; Roediger et al., 2014; Steinhauser et al., 2016; Troncoso Iribarren et al., 2016; Ramos-Martínez et al., 2018; Yun et al., 2019; Troncoso-Iribarren et al., 2020). As we described most of them already in Section 1.3.4, we refrain from a detailed description of all of them and refer the interested reader to Göller et al. (2023) for details of the code and physical treatment in these simulations. However, it has to be mentioned that, with the exception of Steinhauser et al. (2016), Troncoso Iribarren et al. (2016) and Troncoso-Iribarren et al. (2020), all mentioned studies rely on wind-tunnel setups. These setups of isolated galaxy simulations allow for a great control of the initial conditions and physical processes (galaxy type, angle of infall, and inclusion of gas cooling and magnetic fields, see Section 1.4.2), but cannot show the large-scale picture of galaxy-galaxy interactions and pre-processing. Moreover, they cannot reproduce the diversity and large number statistics characterizing galaxy populations in the Universe.

Full cosmological galaxy simulations like EAGLE (Crain et al., 2015; Schaye et al., 2015) and IllustrisTNG (Springel et al., 2018; Naiman et al., 2018; Marinacci et al., 2018; Pillepich et al., 2018b,a, 2019; Nelson et al., 2018, 2019b) can take into account hierarchical growth of structures and mutual interactions between galaxies, as well as galaxies with the larger-scale structure in a self-consistent way. Processes like cosmological gas accretion, galaxy-galaxy mergers and interactions, tidal stripping and RPS, as well as gravitational heating can emerge naturally in these simulations,

and do not have to be artificially introduced in the conditions controlling the simulated galaxy. In these simulations, jellyfish galaxies form when satellite galaxies orbit within galaxy clusters and interact with the ICM. Such galaxies have been studied in Yun et al. (2019), Troncoso Iribarren et al. (2016) and Troncoso-Iribarren et al. (2020).

Here, we analyze jellyfish galaxies emerging in the TNG50 simulation. For details of the simulation setup, we refer the reader to Section 2.2.3. This cosmological simulation provides a large sample of galaxies at various evolutionary stages, across diverse environments and with largely different properties. From these we extract about 700 jellyfish galaxies at $z = 0 - 1$, together with several control samples, described below. This allows for a statistically robust analysis of the star formation activity in these galaxies.

This chapter is based on Göller et al. (2023), which is a companion paper of Zinger et al. 2024 and Rohr et al. 2023. In the former, we describe the identification of jellyfish galaxies in the simulation via the "Cosmological Jellyfish" Zooniverse project. Jellyfish galaxies were visually identified by non-professional citizen scientists. We compare the outcome to that of professionals and provide a first analysis of the jellyfish galaxy demographics. In the latter, we analyze the evolutionary properties of the galaxies and study the loss of cold gas during their evolution.

This chapter is organized as follows: We describe the identification of jellyfish galaxies in Section 3.2.1, in Section 3.2.2, 3.2.3 and 3.2.4 we define galactic stellar mass, SFR and the different galaxy samples. In Section 3.2.5 we describe the tracking of galaxies throughout cosmic epochs. We then study the demographics of the galaxy samples (Section 3.3.1) and examine the galaxies' SFRs in detail (Section 3.3.2 and 3.3.3) and finally investigate how SFR evolves with time (Section 3.3.4 and 3.3.5). The results and simulation details are then discussed in Section 3.4 and summarized in Section 3.5.

3.2 Methods and Data

3.2.1 Visually-identified IllustrisTNG Jellyfish

As we have shown in Section 2.2.3, TNG50 contains thousands of resolved galaxies. The visual classification of such a large number of galaxies is a challenging task. We

therefore developed a citizen science project on the portal "Zooniverse"[1] to classify the vast number of galaxies with the help of laymen volunteers.

After a short training exercise on a dedicated website[2], we present them with images of the gas mass surface density and stellar mass density contours and ask them to decide whether the shown galaxy resembles a jellyfish galaxy or not. To exclude tails formed by tidal stripping, we instructed volunteers to classify galaxies close to another object as non-jellyfish, even when gaseous tails are present. With this, we aimed for a pure (and therefore not necessarily complete) sample of classified galaxies. More than 6,000 volunteers took part in this visual identification process, classifying a total of 80,704 galaxies between $z = 0$ and $z = 2$ in TNG50 and TNG100 in two phases. The image of a given galaxy was retired from classification after 20 volunteers inspected it. The output of each inspection is binary, i.e., each volunteer either classifies the depicted galaxy as a jellyfish or not. This results in a raw score between 0 (not classified as a jellyfish by any inspecting volunteer) and 20 (classified as a jellyfish by all inspecting volunteers). We subsequently weight the classifications by the experience of the inspecting volunteers and their agreement with expert inspectors, and normalize the score to a value between 0 and 1. The details of this process are described in Zinger et al. (2024).

3.2.2 Galaxy Stellar and Total Mass

In this chapter we define the stellar mass of a galaxy as the sum of the mass of all star particles that are gravitationally bound to it according to the SUBFIND algorithm and that are within $2 \times r_{1/2,*}$ from the center of the galaxy, where $r_{1/2,*}$ denotes the stellar half-mass radius of the galaxy. Unless stated otherwise, M_* refers to this definition.

For gas mass, we do not impose a radial restriction, but take the sum of all gas gravitationally bound to the galaxy. This is, because (especially in jellyfish galaxies) a noticeable fraction of the gas may reside beyond $2 \times r_{1/2,*}$.

This definition is well defined for central as well as satellite galaxies and is valid even in the case when galaxies undergo RPS. We note, however, that it is not directly comparable to observations (for a discussion, see e.g., Pillepich et al., 2018b). But

[1] https://www.zooniverse.org/
[2] https://www.zooniverse.org/projects/apillepich/cosmological-jellyfish

as long as galactic samples are compared with consistent definitions for the gas and stellar mass, the exact definition is not important for the purpose of this thesis.

When we characterize galaxies by their total (or dynamical) mass, we refer to the summed mass of all their gravitationally bound stars, gas, dark matter and supermassive black holes (SMBHs) within $2 \times r_{1/2,*}$. We denote this as $M_{\rm dyn}$.

When we omit a radial restriction and refer to the summed mass of all gravitationally bound stars or gas, we denote this by $M_{*/\rm gas}^{\rm allgrav}$.

3.2.3 Measurements of Star-Formation Activity

Since the aim of this chapter is to characterize the star formation activity of simulated (jellyfish) galaxies, we now describe our definition of global (i.e., galaxy wide) SFR, star formation in galactic bodies and tails, the SFMS and a quenched galaxy.

3.2.3.1 Global SFRs

The galaxy-wide 'instantaneous' SFR is directly available from the simulation catalogs of TNG50. It describes the sum of SFRs in all gas cells gravitationally bound to the galaxy. In the case of jellyfish galaxies, it therefore covers SFR in the galactic bodies as well as in the tails. We therefore choose this definition as our fiducial SFR measure.

This definition, again, is not directly comparable to observational measures, which inevitably measure the SFR within a certain past time. However, differences between the 'instantaneous' SFRs and those based on e.g., the average of SF over the last $10-1000$ Myr are negligible at redshifts studied in this chapter, as shown by Donnari et al. 2019, 2020. This is true in terms of the location of the SFMS, as well as for quenched fractions of galaxies.

Moreover, in Appendix A we show that the results remain unchanged if two alternative definitions of the global SFR of a galaxy are used:

i) Including only the contribution of gas cells within $< 2 \times r_{1/2,*}$.

ii) Including also gas cells that are not currently gravitationally bound to the galaxy, but were so at the time of the galaxies infall into its host halo (we explain the procedure in Section A.1.2).

Because of the finite mass resolution of the simulation, there is a minimum resolvable SFR for any galaxy in TNG50, which is about $\sim 10^{-5}\,\mathrm{M}_\odot\ \mathrm{yr}^{-1}$ at $z = 0$. To any galaxy (or portion of it) with SFR below this resolution limit (which would otherwise have SFR=0), we therefore assign a random SFR value in between 10^{-6} and $10^{-5}\,\mathrm{M}_\odot\ \mathrm{yr}^{-1}$.

3.2.3.2 Star-forming Main Sequence and Definition of Quenched

We construct the star-forming main sequence (SFMS) at a given time by measuring the mean SFRs of *star-forming* galaxies at that time in bins of galactic stellar mass. To distinguish star-forming from quenched galaxies or galaxies in the green valley we use the 'Star Formation Activity Flags' with definitions from Pillepich et al. (2019), who use a recursive method (on SFR within $< 2 \times r_{1/2,*}$) to identify the SFMS. Star-forming galaxies are defined by having a logarithmic distance to the SFMS of $\Delta\log(\mathrm{sSFR}) > -0.5$. All other galaxies are quenched or belong to the green valley.

As quenched galaxies we define all galaxies with $\mathrm{sSFR} \leq 10^{-11}\ \mathrm{yr}^{-1}$. This is equivalent to the typical definition in observations and suitable at low redshift, as discussed in Donnari et al. (2020).

3.2.3.3 SF in the Main Body vs. Tails

In this chapter, we aim to not only characterize SFRs globally in the galaxies, but are also interested in where star formation occurs, especially if it occurs in the stripped gaseous tails of jellyfish galaxies. We therefore divide jellyfish galaxies into a body and tail component, of which we measure the SFRs individually. To do so, we define a distance R_{dist} to divide the galaxy by. Cells closer to the galactic center than R_{dist} are counted towards the galaxy's body, every cell further away is counted for the tail.

The most straightforward choice for R_{dist} would be to use $2 \times r_{1/2,*}$. We found, however, that for a small number of galaxies this choice underestimates the extent of the body component, such that cells which from visual inspection should belong to the galaxy's body component are counted as being part of the tail. Therefore, we instead define $R_{\mathrm{dist}} = \max[2r_{1/2,*}, R_{\mathrm{body}}]$, where R_{body} is defined as follows.

First, we define the vector $\vec{x}_{\mathrm{long}}$ pointing from the galactic center to the (gravitationally bound) gas cell with the largest distance to the center. Then we construct

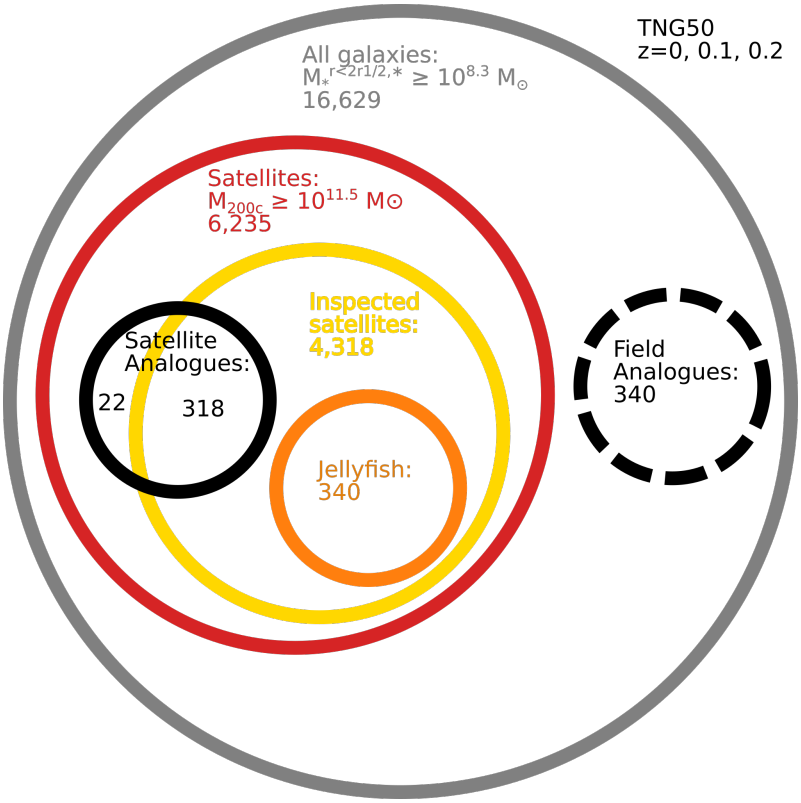

Figure 3.1: Overview of the chosen samples of simulated galaxies studied in this chapter, and their interconnection. The numbers of objects are for the combined redshifts of $z = 0$, 0.1 and 0.2. We focus on galaxies with stellar mass $\gtrsim 2 \times 10^8\,\mathrm{M}_\odot$ at $z < 1$.

a Cartesian coordinate system with its x-axis aligned with $\vec{x}_{\mathrm{long}}$ and its origin at the galactic center. We then measure the distance perpendicular to the x-axis for any gas cell with an x-coordinate $\pm \mathrm{r}_{1/2,*}$. The largest of such distances is set to be R_{body}.

3.2.4 Galaxy Selection, TNG50 Jellyfish, and Control Samples

In the study conducted in this chapter, we use galaxies from various cosmic epochs that satisfy certain criteria of stellar mass, gas fraction and satellite-vs-central fraction. Those are, in parts, dictated by the choices we adopted for the visual classification of the galaxies in the Cosmological Jellyfish Zooniverse project, which we describe below (also, see Section 3.2.1).

In this section we explain the criteria for the selection of galaxies from TNG50 and the division into subsamples we contrast against each other. An overview of the different samples is given in Fig. 3.1 for a selection of combined redshifts. In general, we use galaxies from snaphots of the simulation at $z = 0$, 0.1, 0.2, 0.3, 0.4, 0.5, 0.7 and 1.

All galaxies in this study: Here we only take into account galaxies with a stellar mass $M_* \geq 10^{8.3}\,\mathrm{M}_\odot$, to ensure that each galaxy consists of at least a few thousand star particles. We also ensure a cosmological origin of the galaxies by using the 'SubhaloFlags' (Nelson et al., 2019a). The sample of all galaxies in this study is the largest reference sample used in this chapter. We refer to it as 'All galaxies' throughout this chapter. It is represented in grey in Fig. 3.1.

Satellites: We refer to all galaxies which are not the central galaxy of their FoF halo (see Section 2.2.3 for an explanation of this concept), and whose host halo mass is larger than $M_{200\mathrm{c}} \geq 10^{11.5}\,\mathrm{M}_\odot$ as 'Satellites'. Here, $M_{200\mathrm{c}}$ is the total mass summed over all associated particles and cells of the halo enclosed in a sphere with an average density of 200 times the critical density of the universe at the considered time. These galaxies are a subset of 'All galaxies' and are depicted in red in Fig. 3.1.

Inspected satellites: We refer to all galaxies inspected in TNG50 in the Cosmological Jellyfish Zooniverse project (Section 3.2.1) at our considered redshifts as 'Inspected satellites'. The galaxies were selected for inspection by the fact that they are satellites and still contain gas at the time of the inspection. This is due to the fact that jellyfish galaxies are galaxies falling into a galaxy cluster, i.e., satellites in our definition, and to form a gaseous tail they still have to contain some gas. In particular, in accordance with Zinger et al. (2024), the galaxies in this sample fulfill the following criteria:

- they are satellites according to SUBFIND, i.e., are not the most massive galaxy of a FoF group;
- they have a stellar mass of $M_* > 10^{8.3}\,\mathrm{M}_\odot$;
- they have a gas fraction of $M_{\mathrm{gas}}^{\mathrm{allgrav}}/M_* > 0.01$.

This sample is a subset of 'Satellites' and is shown in yellow in Fig. 3.1.

Snapshot #	99	91	84	78	72	67	59	50
z	0.0	0.1	0.2	0.3	0.4	0.5	0.7	1.0
All galaxies	5635	5529	5465	5368	5274	5187	4971	4755
All satellites	2157	2064	2014	1952	1924	1849	1708	1472
Inspected satellites	1417	1434	1467	1488	1533	1501	1495	1423
Jellyfish	118	107	115	103	105	94	67	71

Table 3.1: Number of considered galaxies in each subsample described in Section 3.2.4 at each studied redshift.

Jellyfish: The sample of jellyfish galaxies consists of all galaxies in 'Inspected satellites' that got a weighted score of ≥ 0.8. This definition is identical to the one used in Zinger et al. (2024). We refer the reader to this paper for a detailed discussion of the different scoring and weighting schemes. Throughout this chapter we refer to galaxies in this sample as 'Jellyfish', they are depicted in orange in Fig. 3.1.

As the goal of this chapter is to find if jellyfish galaxies on average show an increased star formation activity compared to other galaxies, we construct two control samples of satellite and field analogues:

Satellite analogues: Galaxies in this sample are analogous to our found satellite galaxies in several different properties but are not classified as jellyfish themselves. They are satellites and the Euclidean nearest neighbours to a jellyfish galaxy in the phase space constructed by the total galactic stellar mass, gas-to-stellar mass fraction $M_{\rm gas}^{\rm allgrav}/M_{*}^{\rm allgrav}$ and host mass $M_{\rm 200c}$. We normalize all dimensions such that the values are between 0 and 1 to ensure an equal weighting between all dimensions. In this definition stellar and gas masses include all gravitationally bound star particles and gas cells. If galaxies from this sample are inspected in the Cosmological Jellyfish Zooniverse project, their weighted score is lower than 0.8. A galaxy is allowed to be part of this sample several times, i.e., a galaxy is allowed to be an analogue to more than one jellyfish, but ~ 79 % of the galaxies are unique. This 'Satellite analogues' sample contains the exact same number of objects as the jellyfish sample, at each redshift. As this sample has the same distribution of galactic stellar mass, gas fraction and host mass (which are known to affect the SFR of satellites, see e.g., Donnari et al., 2021 and Joshi et al., 2021 for galaxies in TNG), we can pinpoint any differences more easily to the jellyfish nature of galaxies by

comparing this sample to the jellyfish one. We show this sample in black in Fig. 3.1.

Field analogues: We also create an analogues sample from TNG50 field galaxies. These galaxies are the central galaxy of a FoF halo with $M_{200c} < 10^{11.5}\,M_{\odot}$. We select the nearest neighbours of jellyfish galaxies in a 2D phase space constructed by the total galactic stellar mass and gas fraction, normalized as above. We again allow for galaxies to be present multiple times in this sample and find 47 % of the galaxies to be unique. By definition, this 'Field analogues' sample is disjunct from the 'Satellites' sample, as one can see in the black-dashed representation in Fig. 3.1. We construct this sample to be able to compare jellyfish galaxies to field galaxies without the potential bias that different distributions of other galactic properties could introduce.

We present the number of galaxies in each subsample at each considered time in Table 3.1.

3.2.5 Tracking Unique Jellyfish across Cosmic Time

The majority of this chapter focuses on the analysis of galaxy populations at a fixed redshift, however, for Section 3.3.5 we also follow individual jellyfish galaxies throughout their evolution. Due to the selection criteria used for the Cosmological Jellyfish Zooniverse project (see Section 3.2.1), individual galaxies were frequently inspected multiple times at different times along their evolutionary track. To follow individual galaxies through cosmic time we use the methodology developed and described in Rohr et al. 2023 (Section 2.3). We connect galaxies inspected at multiple times using the SUBLINK_GAL merger trees (Rodriguez-Gomez et al., 2015). Of 53,610 satellites inspected at tens of snapshots in TNG50, there are 5,023 unique galaxies (or branches), forming evolutionary tracks, which we can follow through cosmic time.

3.3 Results with TNG50 Jellyfish

With the visual inspection procedure described above we extract a total of 4144 jellyfish galaxies at $z \leq 2$ across all the 37 output snapshots of TNG50. This sample size is larger than that of any other simulation-based study, and more than

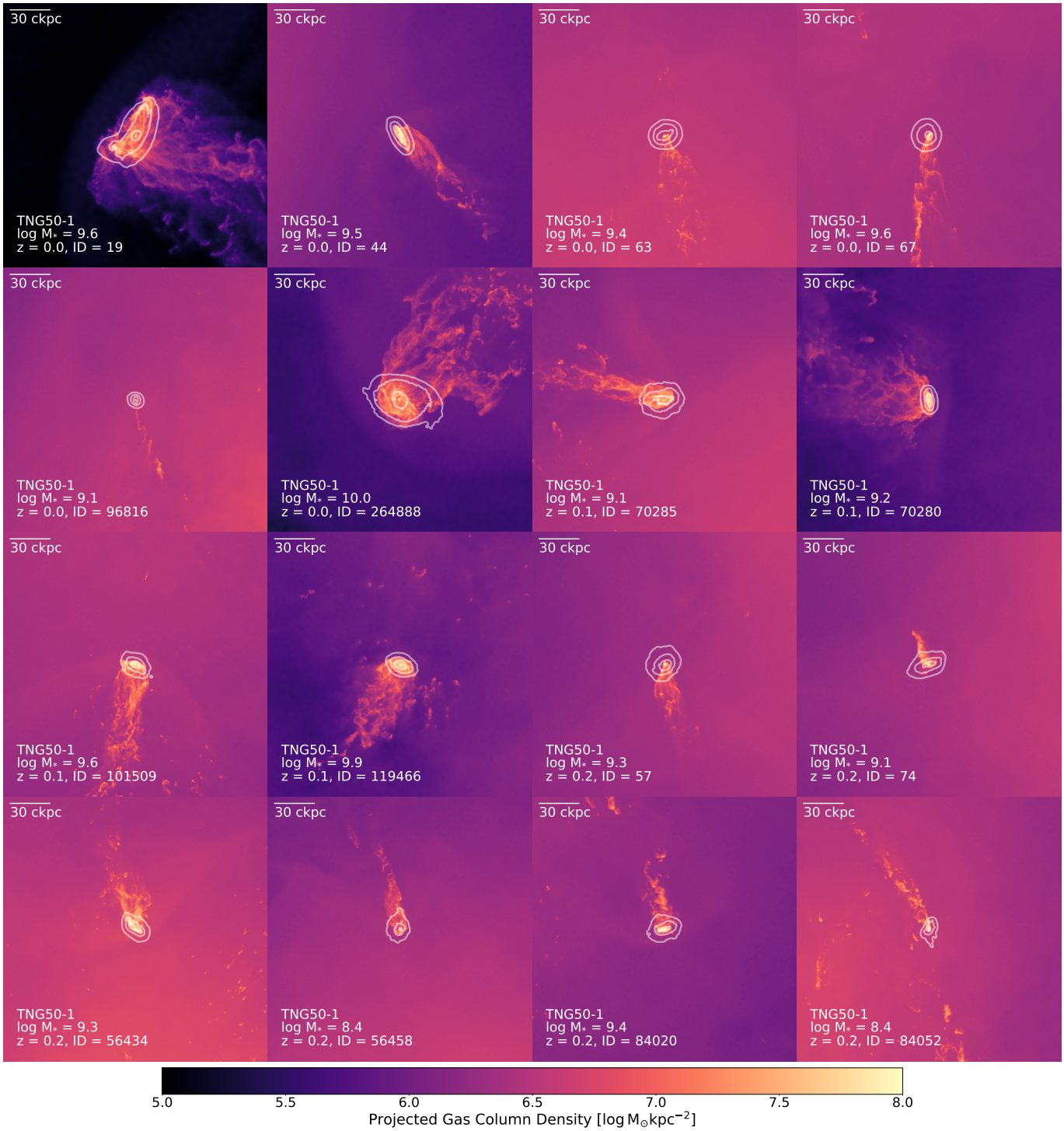

Figure 3.2: Projected gas column density of selected jellyfish galaxies with non-vanishing star formation in the RPS tails. Stellar mass surface density contour lines are overlaid in white, indicating 60, 70 and 80 % of peak stellar mass surface density. SFR in the gas of these galaxies is shown in Fig. 3.3.

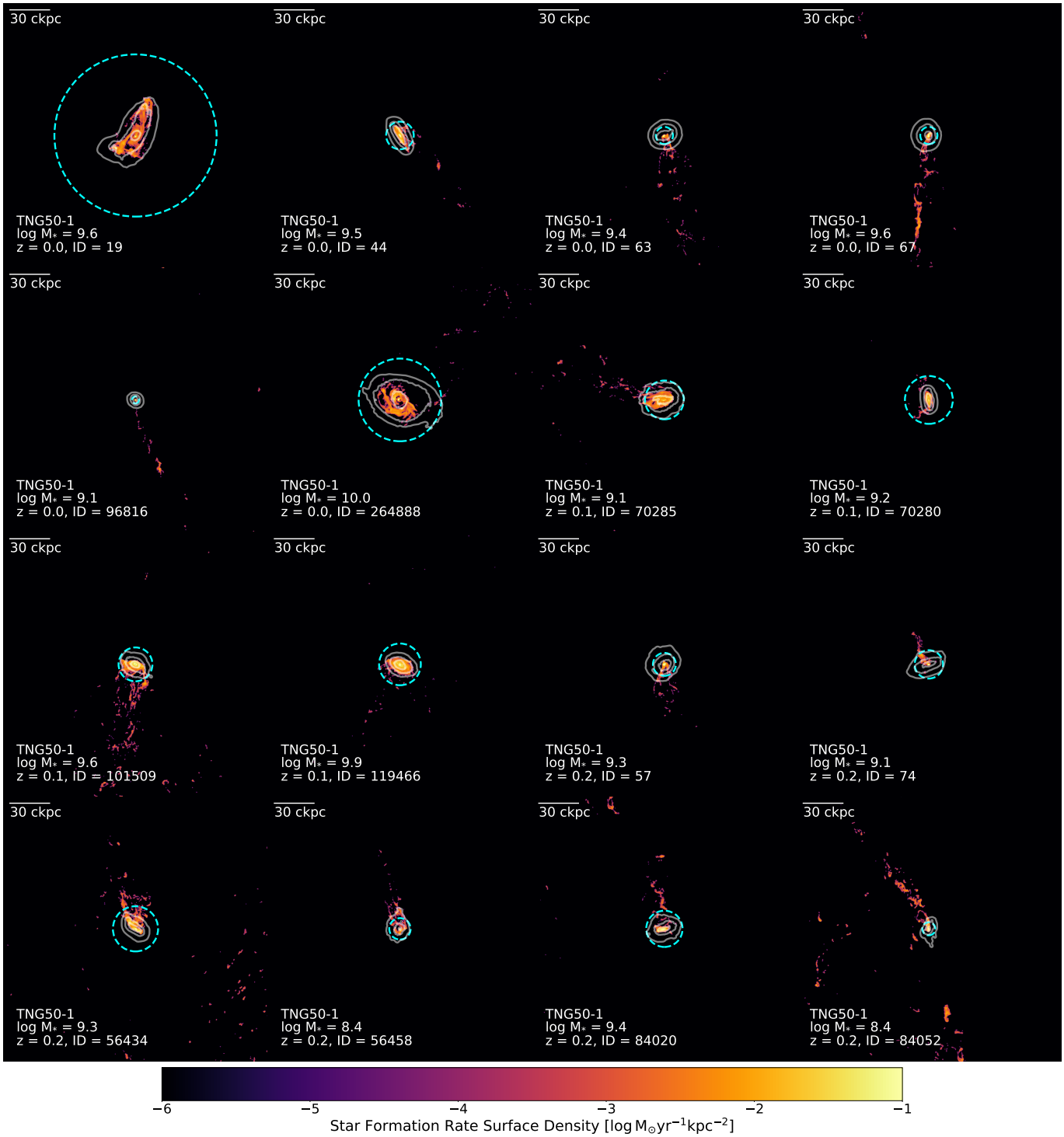

Figure 3.3: SFR surface density in all gas surrounding galaxies in the same selected galaxies as in Fig. 3.2. In turquoise we indicate the radius $R_{\rm dist}$ within which we count gas and corresponding star formation as being part of a galaxy's body (see Section 3.2.3.3). Gas and star formation outside of the turquoise circle is counted as being part of the galactic tail. In the TNG model, most gas in the tails is not star-forming. Tails should appear much less extended and massive in any proxy of SFR (like e.g., Hα).

an order of magnitude larger than any observational survey targeted at jellyfish galaxies we are aware of. Here, we focus on just 780 identified jellyfish in a smaller set of available snapshots at $z \lesssim 1$ (see Table 3.1).

We show a selection of these simulated jellyfish galaxies in Figs. 3.2 and 3.3. The former presents the projected gas mass column density of all gas associated with the galaxy, irrespective of its temperature or phase. The latter depicts the SFR surface density, again in all gas associated with the galaxy. Both figures also include stellar mass surface density contour lines, indicating 60, 70 and 80 % of the peak stellar mass surface density. From these figures, it is apparent that jellyfish galaxies can have a noticeable amount of gas left even in their main galactic body, despite undergoing RPS. Some of the depicted galaxies move through their ambient medium at supersonic velocities, producing bow shocks (see Fig. 3.2, ID 19, 44, 264888 and 101509 or Yun et al. 2019). It is also clear that, according to TNG50, most of the gas in both bodies and tails is not necessarily star-forming (see Fig. 3.3). For the jellyfish galaxies identified in this simulation, RPS acts directly on their cold gas, and the long-lived tails originate mostly from their cold ISM (Rohr et al., 2023).

3.3.1 Demographics and Properties of TNG50 Jellyfish Galaxies

To be able to set star formation activity in jellyfish galaxies into context, we first describe the demographics of such galaxies and the environment they live in.

In fact, in comparison to the inspected sample, jellyfish galaxies are more frequent at cluster-centric distances between 0.5 and $1\,\mathrm{R_{vir}}$, in more massive hosts and at smaller satellite masses, according to Yun et al. (2019) (TNG100) and Zinger et al. (2024) (TNG100 and TNG50). Typically they orbit at supersonic velocities.

It is well known that the stellar mass and host halo mass of a galaxy have an important role in determining environmental effects acting on the galaxy. To properly characterize our galaxy sample, we therefore examine the distributions of jellyfish and all galaxies in stellar mass (left panel), host halo mass (middle panel) and the ration of the *total* galaxy mass to host mass (right panel), i.e., the galaxy-to-host total mass ratio, for different redshifts in Fig. 3.4. The simulation returns galaxies in a wide range of galactic stellar masses, ranging from the set mass limit of a few $10^8\,\mathrm{M_\odot}$ up to massive galaxies of $\sim 10^{12}\,\mathrm{M_\odot}$ in stars (left panel, grey curves). We find no jellyfish galaxies with a stellar mass $M_* > 10^{11}\,\mathrm{M_\odot}$ (left panel, orange curves). This

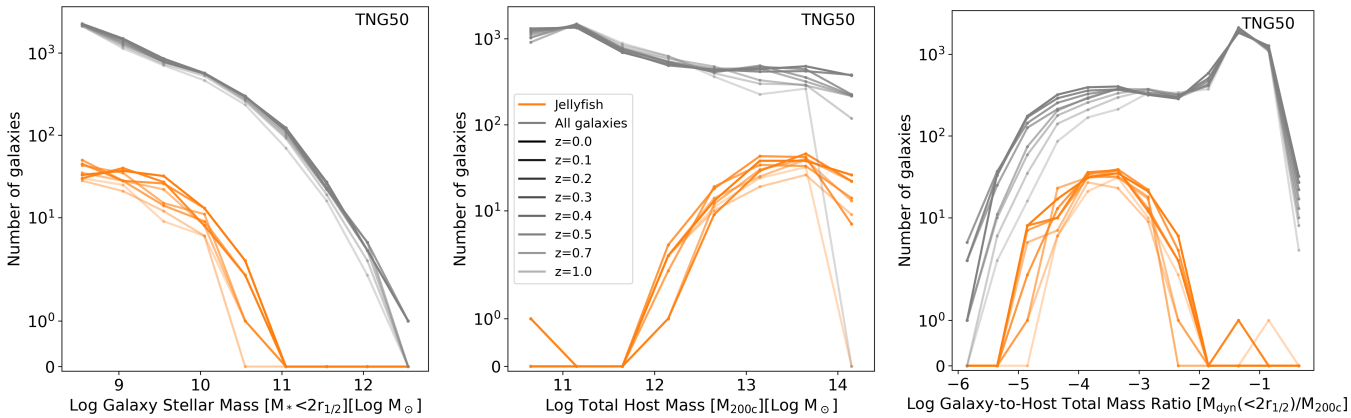

Figure 3.4: Number of jellyfish galaxies and all galaxies vs stellar mass, host halo mass and satellite-to-host mass ratio for different redshifts. Jellyfish galaxies get less frequent with increasing stellar mass, and more frequent at increasing host halo mass. Most jellyfish galaxies have a satellite-to-host mass ratio between 10^{-4} and 10^{-3}.

is because we require inspected galaxies to be satellites, which severely restricts the number of massive galaxies and consequently jellyfish galaxies. Moreover, Zinger et al. (2020) showed that at stellar masses $> 10^{10.5}\mathrm{M}_\odot$, feedback from supermassive black holes can remove large fractions of the gas of a galaxy, which lowers the possibility for it to be a jellyfish galaxy. A preliminary discussion of high-mass satellites being jellyfish galaxies is presented in Zinger et al. (2024).

It is also apparent that there is little evolution with redshift in the mass function of 'All galaxies', except for masses $M_* > 10^{11}\mathrm{M}_\odot$. There, with decreasing redshift a mild increase in galaxy numbers is present. This is expected as this region is dominated by central galaxies that grow in stellar mass over cosmic time. The shape of the mass function of jellyfish galaxies is similar to that of all galaxies, even though it is shifted to lower stellar masses. More jellyfish galaxies are found at lower redshifts, even though this trend is not clear for all masses.

Moreover, we clearly show that jellyfish galaxies are, in fact, not a frequent occurrence in galaxy populations of overall similar stellar mass, but represent less than a few percent (see also Yun et al., 2019, and Zinger et al. 2024). From Table 3.1 we note the fraction of jellyfish in the 'Inspected satellites' sample to increase from 5% at $z = 1.0$ to 8% at $z = 0$, implying that jellyfish represent an approximately constant (w.r.t. stellar mass, mildly increasing with redshift) fraction of all galaxies

(except for massive galaxies with $M_* \gtrsim 10^{10.3}\,\mathrm{M}_\odot$). This decreasing fraction at high galactic stellar masses is again mostly caused by the fact that jellyfish galaxies are satellites, and massive satellites ($M_* \gtrsim 10^{12}\,\mathrm{M}_\odot$) can only be hosted by very massive halos ($M_{200c} \sim 10^{15}\,\mathrm{M}_\odot$). Halos of such high masses are absent in the TNG50 volume. Gas in massive galaxies is moreover bound to its galaxy more strongly by the increased gravitational attraction, which therefore hinders RPS. Finally, at least in IllustrisTNG, supermassive black holes affect massive galaxies irrespective of their central or satellite nature (Donnari et al., 2021) by expelling large amounts of gas from their inner regions, again reducing the chances of the galaxy being a jellyfish (Terrazas et al., 2020; Zinger et al., 2020).

In the middle panel of Fig. 3.4, we show the distribution of the host halo masses M_{200c} for all galaxies (grey, including centrals and satellites) and jellyfish (orange). For the 'All galaxies' sample, halo masses span the full available halo mass range, with halos of 10^{11} to $10^{12}\,\mathrm{M}_\odot$ being slightly more frequent, as expected from the ΛCDM scenario. Jellyfish galaxies, on the other hand, are more frequent in halos of $M_{200c} = 10^{13-14}\,\mathrm{M}_\odot$. No sample shows a strong dependence on redshift, except for the highest host masses, likely caused by the low number of massive hosts at higher redshifts. Beyond the fact that jellyfish galaxies in this chapter are, by construction, satellites, this difference between the samples can be explained by two factors. Firstly, more massive hosts induce higher infall velocities, in turn inducing higher ram pressures acting on the galaxy. Secondly, more massive host halos show higher densities in their ICM (Domainko et al., 2006), which, again, increases the exerted ram-pressure. The decline in jellyfish number at very high host halo masses is again explained by the decreasing number of hosts at such high masses.

From these findings we can draw conclusions regarding the preferred properties for the occurrence of jellyfish galaxies, i.e., a low galactic mass and a high mass of the host halo. In fact, the resilience of a galaxy against stripping is controlled not only by the stellar mass, but by the total mass of the galaxy. In the right panel of Fig. 3.4 we therefore show the total mass ratios of the galaxies to their host halos. The 'All galaxies' sample shows a double-peaked distribution, with a narrow peak at high rations of $M_{dyn}/M_{200c} \sim 10^{-2} - 10^{-1}$, probably dominated by centrals in the sample, and a more broad peak at lower ratios of $M_{dyn}/M_{200c} \sim 10^{-5} - 10^{-3}$, most likely from satellites. A time-evolution is present in the low-ratio regime, where the least massive satellites and most massive halos can be found, representing the evolution

of numbers of galaxies found in massive hosts (as seen in the middle panel of Fig. 3.4). Jellyfish galaxies, on the other hand, show a single-peak distribution, with a typical mass ratio of $M_{\rm dyn}/M_{\rm 200c} \sim 10^{-5} - 10^{-2}$ and a peak at $M_{\rm dyn}/M_{\rm 200c} \sim 10^{-3.5}$. As jellyfish galaxies are exclusively satellites, a second peak from centrals is missing. The decreasing number of jellyfish towards low mass ratios, analogous to the decrease in the 'All satellites' sample is caused by the fact that combinations of very low mass satellite galaxies in very high mass host halos are rare. We find more jellyfish galaxies at later redshifts for all values of $M_{\rm dyn}/M_{\rm 200c}$. The results found here are qualitatively consistent with those of Yun et al. (2019) (even though this study only considers galaxies in massive hosts of $M_{\rm 200c} \geq 10^{13}{\rm M}_{\odot}$), and with the findings of Zinger et al. (2024) and Rohr et al. (2023).

3.3.2 Star Formation in TNG50 Jellyfish, even in the Tails

Having introduced the demographic properties of jellyfish galaxies, we now continue by concentrating on their star formation activity. In this section we show that jellyfish galaxies from TNG50 are not quenched, but star-forming and in some cases even show star formation in the RPS tails.

We quantify this in Fig. 3.5, where we show the SFRs of jellyfish galaxies (green stars and pink crosses) and all galaxies (grey dots) as a function of the galactic stellar mass for $z = 0, 0.1, 0.2$. We combine the populations at these redshifts to gain a larger sample size and examine higher redshifts in Section 3.3.4 and 3.3.5. In Fig. 3.5 we also show the SFRs of jellyfish bodies (green stars) and tails (pink crosses) separately, with the separation constructed as explained in Section 3.2.3.3. Galaxies, or parts of them, with SFRs below the SFR resolution limit of TNG50 get assigned a random SFR value between 10^{-5} and $10^{-6}\,{\rm M}_{\odot}\ {\rm yr}^{-1}$, as explained in Section 3.2.3.1). In the main panel, we also present the TNG50 SFMSs (blue, see Section 3.2.3.1 and 3.2.3.2) corresponding to the given redshifts. As the SFMSs do not evolve considerably between the selected redshifts, we therefore conclude the combination of the populations at different redshifts to be valid. In the right panel, we also show the projected distribution of SFRs for jellyfish bodies and tails.

It is apparent that jellyfish galaxies in TNG50 are star-forming in their bodies and, in several cases, also their stripped tails. They are therefore not quenched, even though they undergo extreme RPS, and can even have star-forming regions

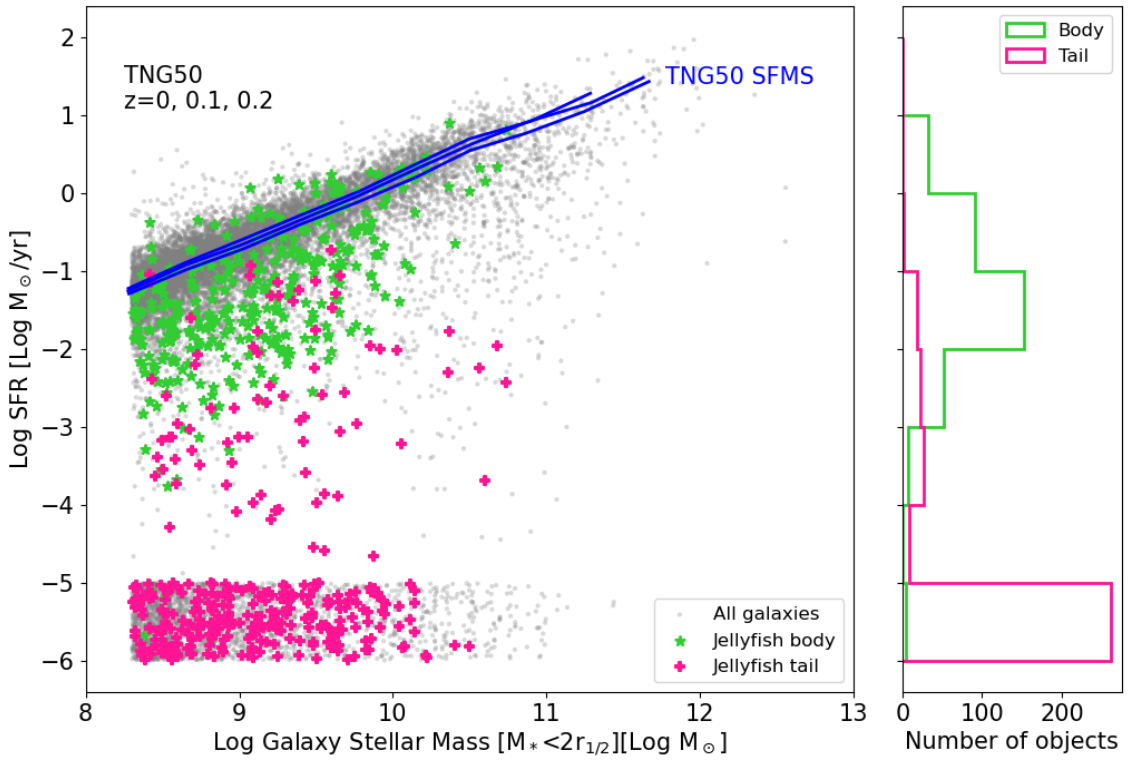

Figure 3.5: SFRs of the 'All galaxies' sample (grey) and jellyfish bodies (green) and tails (pink) as a function of galactic stellar mass for the redshifts $z = 0, 0.1, 0.2$. SFMSs for the considered redshifts are shown in blue (see Section 3.2.3.2 for details). Galaxies (or parts thereof) with SFRs below the resolution limit get assigned a random SFR between 10^{-5} and $10^{-6}\,\mathrm{M}_\odot\ \mathrm{yr}^{-1}$ (see Section 3.2.3.1). Jellyfish bodies on average have SFRs below the SFMS, but significantly larger than that of tails.

in their tails (which can be seen in Fig. 3.3). The median SFR in jellyfish bodies, however, is $3-4.8$ dex higher than in the tails. This difference is significantly larger than the one of Gullieuszik et al. (2020), who find the SFR in the tails compared to the bodies to be reduced by a factor of ~ 5. Our findings are more in line with that of Kronberger et al. (2008), where the SFR in the bodies is largely dominant over that in the tails. In our findings, the difference in SFR between jellyfish bodies and tails increases with increasing stellar mass of the galaxies. In our sample, more than three quarters of the jellyfish tails have SFRs below the resolution limit, while this is the case only for about 1 % of the jellyfish bodies.

Hence we can conclude that, according to TNG50, star formation can occur in the RP-stripped tails of jellyfish galaxies, even though at much lower levels than in the galactic bodies (see right panel of Fig. 3.5 and compare Fig. 3.2 and 3.3). From the maps in Fig. 3.2 and 3.3 it is also clear that the tails detected across gaseous phases are more broad, extended and pronounced than those detected in gas phases tracing star formation, if tails are present in these tracers at all. It therefore is interesting that a few systems at the presented low redshifts have star formation levels in the tails that are compatible with those of the SFMS. The exact levels of SFRs of course depend on the adopted method for separation between body and tail (see Section 3.2.3.3). We tried several approaches, but the overall picture remains qualitatively unchanged: Jellyfish galaxies in TNG50 show tails with ongoing star formation, however, this does not happen frequently and the star formation in the main galactic body clearly dominates that in the tail.

3.3.3 No Enhanced Population-Wide Star Formation in Jellyfish

With the result from the previous subsection, we can continue our analysis with a *global* SFR measure, knowing that for jellyfish galaxies it is dominated by star formation occurring in the galactic body rather than in the tail. In this section we compare the SFR and related properties to that of all other defined subsamples: all satellites, inspected satellites, satellite analogues, and field analogues, described in Section 3.2.4 and shown in Fig. 3.1. With this, we are able to distinguish differences due to selection effects (that also affect observational studies) and between satellite galaxies that do not undergo visually identifiable RPS and those which do, i.e., jellyfish galaxies. In this section we aim to find out if there is any population-wide enhancement (or suppression) of star formation in TNG50 jellyfish galaxies compared to other galaxy types.

To do so, we compare the median SFR of jellyfish galaxies as a function of galactic stellar mass to that of our defined comparison samples in the main panel of Fig. 3.6. These results we moreover interpret in the view of gas fraction (bottom left) and fraction of quenched galaxies (bottom middle) as a function of stellar mass, as well as the SFR as a function of gas fraction (bottom right). We include all TNG50 galaxies in the analysis, even those with non-resolved SFRs, which are placed at low but non-vanishing SFRs as described before and therefore still contribute to the

SFR medians.

3.3.3.1 SFRs in Jellyfish Galaxies and other Galaxy Types

The main panel of Fig. 3.6 shows the median SFRs of our selected galaxy samples in bins of galactic stellar mass, shaded areas indicate the 16th to 84th percentile for the jellyfish and 'All galaxies' sample. Here, we combine the samples of the redshifts $z = 0$, 0.1 and 0.2, bins are 0.37 dex wide and bins with less than 7 galaxies in them are discarded. In addition to median SFRs, we show the individual SFR values of galaxies from the jellyfish sample in orange dots.

The median SFR of the 'All galaxies' sample (depicted in grey), which includes star-forming, as well as green valley and quenched galaxies, is very similar to the SFMS (blue), except for the most massive galaxies. This is expected, as galaxies are more frequently centrals than satellites at all considered masses, and we know that centrals have higher SFRs than satellites at similar masses (see Section 1.2.2 and Section 1.3.4, as well as Section 3.1 of this chapter). The average SFR in high-mass galaxies is lowered by an increased fraction of quenched galaxies in this mass regime, irrespective of the satellite or central status of the considered galaxies (e.g., Donnari et al., 2019, 2021). At lower masses $M_* \lesssim 10^{10}\,\mathrm{M}_\odot$, galaxies (in TNG50 as well as observed) are typically star-forming, unless they are affected by environmental processes, i.e., satellites (e.g., Donnari et al., 2021; Joshi et al., 2021), which are not the dominant population in the grey curve.

Satellites (red) on the other hand are affected by environmental processes and therefore on average have lower SFRs than the general galaxy population. This is particularly true at stellar masses below $10^{10}\,\mathrm{M}_\odot$, where the median SFRs in satellites are $0.4 - 0.7$ dex below the SFMS. At stellar masses below $10^{9}\,\mathrm{M}_\odot$, the median SFRs of the 'satellites' sample even experiences a sharp drop-off due to a large number of galaxies with unresolved SFRs, that are placed at a random SFR between 10^{-6} and $10^{-5}\,\mathrm{M}_\odot\ \mathrm{yr}^{-1}$. We do not find such a drop-off in the 'Inspected satellites' sample (yellow), as for inspection we only consider galaxies with at least some gas, which are therefore more likely to have some ongoing star formation.

This selection effect is also the reason that the median SFRs of 'Inspected satellites' are close to that of the general galaxy population (compare grey and yellow curve), even though they are satellites. Jellyfish galaxies (orange), however, exhibit

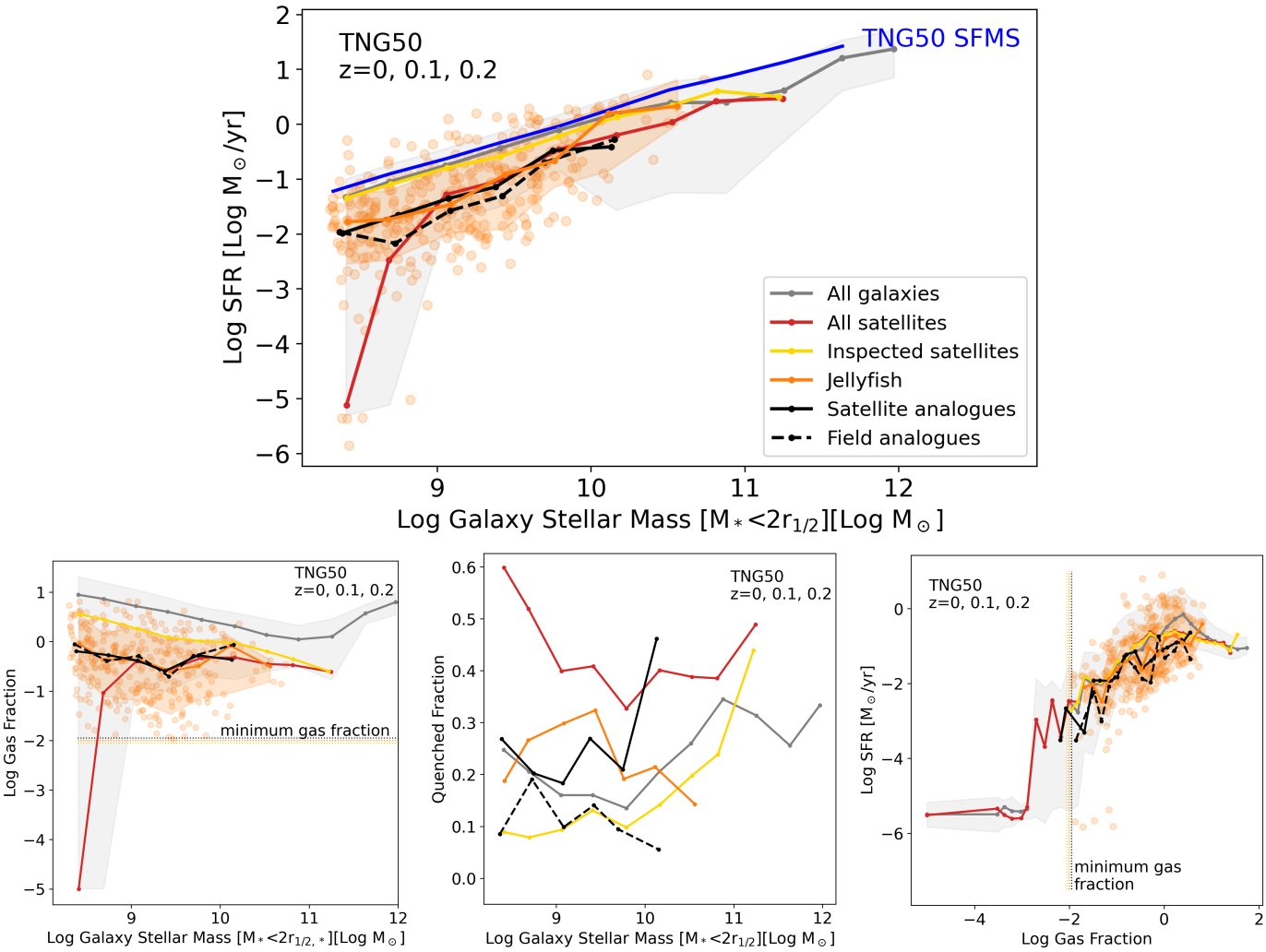

Figure 3.6: Overview over SFRs and related properties in all galaxies (grey), all satellites (red), inspected satellites (yellow), jellyfish galaxies (orange) and their satellite (black) and field (black dashed) analogues. We show the median SFR in bins of galactic stellar mass (top panel) and gas fraction (lower right), as well as the gas fraction (lower left) and fraction of quenched galaxies (lower middle) as a function of galactic stellar mass. Bins in stellar mass are 0.37 dex wide, bins in gas fraction are 0.17 dex wide. Each bin contains at least seven galaxies, otherwise they are discarded. Shaded areas represent the 16th to 84th percentile for jellyfish galaxies and all galaxies. SFRs in jellyfish galaxies are lower than that of both galaxies from the 'All galaxies' and the 'Inspected satellites' sample at similar galactic stellar masses. We therefore find no evidence for a population-wide enhanced SFR in jellyfish galaxies. The lowered SFRs correlate with lower overall gas fractions and a somewhat increased quenched fraction, but show a general agreement between samples at similar gas fractions.

median SFRs about $0.6 - 0.8$ dex lower than the SFMS at stellar masses below $10^{10}\,\mathrm{M}_\odot$ (compare orange and blue curve), and $0.3 - 0.7$ dex lower than that of satellite galaxies they were identified from (orange vs. yellow curve). That is, the median SFRs of jellyfish galaxies are up to 0.7 dex lower than that of the sample they were selected from.

This shows that jellyfish galaxies not only typically have lower SFRs than the general galaxy population, which is explained by the fact that the latter sample is dominated by centrals. Their star formation activity is also not enhanced population-wide compared to galaxies from the 'Satellites' sample, except for stellar masses $\lesssim 10^9\,\mathrm{M}_\odot$. We can, in fact, go one step further and compare the median SFRs of jellyfish galaxies to that of the selected control samples of analogous galaxies (see Section 3.2.4), to ensure that our result is not caused by differences in the distributions of stellar mass or gas fraction, or the host halo mass in the case of 'Satellite analogues'. We find the median SFRs of 'Satellite' (black) and 'Field analogues' (black dashed) to follow that of jellyfish galaxies closely. 'Satellite analogues' show deviations from jellyfish galaxies up to 0.6 dex, however, we think this is an effect of low number statistics. Hence the results confirm that SFRs of jellyfish galaxies in TNG50 do not differ significantly from that of satellite and field galaxies with similar masses and gas fractions.

Our findings are therefore more in line with observational results that find no population-wide enhanced SFRs in jellyfish galaxies (see Section 1.3.4 and Section 3.1 of this chapter). They appear at odds with the findings of Vulcani et al. (2018); Ramatsoku et al. (2020) and Vulcani et al. (2020) based on the GASP survey. However, comparisons of observations and simulations are not trivial and in this case require careful examination of the used methods and quantities, which we discuss in more detail in Section 3.4.1. On the other hand, it is apparent from Fig. 3.6 and also Fig. 3.5 that jellyfish galaxies with above-SFMS SFRs do, in fact, exist in the simulation, and are especially frequent in galaxies with stellar masses of $M_* \sim 10^{9-10}\,\mathrm{M}_\odot$. Jellyfish galaxies with high SFRs also have high gas fractions (see lower right panel of Fig. 3.6) and mostly have gas-to-stellar mass fractions > 0.1 (see next section).

3.3.3.2 Gas Fractions

We quantify the typical gas fractions of the studied galaxies of the selected samples as a function of galactic stellar mass in the lower left panel of Fig. 3.6. Here, gas fraction means the ratio of the mass of gravitationally bound gas and the stellar mass within twice the stellar half-mass radius, i.e., $M_{\rm gas}^{\rm allgrav}/M_*$. We assign a gas fraction of $10^{-5.0}$ (which is the lowest measured gas fraction in any of the studied galaxies) to galaxies without a resolvable gas mass. Shaded areas again indicate the 16th to 84th percentile for jellyfish galaxies and the 'All galaxies' sample. We study the gas fraction of galaxies in the selected samples to emphasize that not all galaxies can provide an equal amount of gas as fuel for star formation, and that this is caused often by explicit or implicit selection effects. Such selection effects are also unavoidable in observational studies.

The horizontal black, orange and yellow lines in this panel mark the minimum gas fraction imposed on galaxies of the 'Inspected satellites', 'Jellyfish' and their analogue control samples. While we impose this criterion a priori in our analysis, it is apparent that jellyfish galaxies detected in observational surveys also tend towards higher gas fractions compared to the typical satellite population, as the presence of a pronounced gaseous tail proves the existence of a non-ignorable amount of gas in these galaxies.

This is reflected also in the lower left panel of Fig. 3.6. A clear separation distinguishes the general galaxy population ('All galaxies', grey), which has a median gas fraction of unity or higher, from the 'Satellite' (red) and 'Jellyfish' (orange) galaxies and their analogues (black). The typical gas fractions of jellyfish and satellite galaxies are nearly identical (except for the lowest stellar masses), as well as for the two analogue samples (as expected from the design of these samples). The median gas fraction of the 'Inspected satellites' (yellow) on average falls in between these two regimes. This indicates that, even though jellyfish are identified from a certain subsample limited to a given gas fraction, the fact that they undergo RPS leads to a lowered overall gas fraction compared to their non-jellyfish counterparts. This also explains why jellyfish in TNG50 typically show lower SFRs than the 'Inspected satellites' sample (as we noted in the main panel of Fig. 3.6), as gas is the fuel for star formation in the galaxies.

3.3.3.3 Quenched Fractions

The quantifications of SFRs and gas fraction as a function of galactic stellar mass that we provided above hide an underlying complexity of such comparisons: Satellite galaxies often show very low levels of star formation, because they are affected by strong environmental effects. Their SFRs can be so low that they cannot be measured in observations or resolved in simulations. This results in a bimodal SFR-stellar mass distribution, which, in turn, makes averages and medians inconclusive. Therefore, environmental and secular quenching processes are typically measured by fractions of quenched galaxies in samples (see e.g., Kauffmann et al., 2003, and all subsequent studies). We provide this measure of the quenched fraction in the lower middle panel of Fig. 3.6.

There, we measure the fraction of quenched galaxies as a function of galactic stellar mass for the different selection samples. As quenched, we count galaxies with an sSFR below 10^{-11} yr^{-1}, as is common in literature.

We find the highest quenched fraction - between 0.33 and 0.60, over the whole mass range - in the 'Satellite' galaxies (red curve), as we would expect from the construction of this sample. More than half of all $10^{8-9}\,\mathrm{M}_\odot$ galaxies in this sample are quenched. As these galaxies orbit in environments of cosmological high-density in galaxy groups and clusters, and therefore undergo noticeable environmental effects (as mentioned in Section 3.1, see also Donnari et al., 2019, 2020, 2021; Joshi et al., 2021 for extensive characterizations of quenched fractions in the IllustrisTNG simulations across galaxy and host masses and cosmic epochs), this is an expected outcome.

Even though they undergo severe RPS, the quenched fractions of jellyfish galaxies are strictly lower than those of satellites as they are quenched in just $14 - 32$ % of the cases. Again, this is because of the exclusion of gas-depleted galaxies from this sample, which are included in the satellites. Jellyfish galaxies are, however, more frequently quenched than their 'Field analogues', and, for stellar masses $\lesssim 10^{10}\,\mathrm{M}_\odot$, than galaxies in the 'Inspected satellites' sample. Jellyfish galaxies are also more frequently quenched than their 'satellite analogues' at stellar masses between $10^{8.5}$ and $10^{9.5}\,\mathrm{M}_\odot$. It therefore seems that extreme RPS increases the likelihood of a galaxy to be quenched, compared to its non-stripped analogue, even though it has no noticeable effect on the median SFR and even though the gas fractions between

the samples are similar.

The quenched fraction in the general galaxy population ('All galaxies', grey) increases with galactic stellar mass $\gtrsim 10^{10}\,\mathrm{M}_{\odot}$. This is consistent with observations and also known to be caused by quenching effects of feedback from supermassive black holes in IllustrisTNG (see Donnari et al., 2019). The same effect is present in galaxies from the 'inspected satellites' sample (yellow).

3.3.3.4 SFR as a Function of Gas Fraction

We now close this analysis with the question: At a similar gas content, do we find any indication that the star formation activity is altered in jellyfish galaxies compared to non-jellyfish galaxies? This question is addressed in the lower right panel of Fig. 3.6, where we show the median SFR of the galaxy samples as a function of the gas fraction. Additionally, we show the SFRs and gas fractions of individual jellyfish galaxies as orange dots. The quantities and annotations are the same as in the previous sections.

The figure shows a general trend of increasing SFR with increasing gas fraction for all galaxies, regardless of the sample. This is expected, as higher gas fractions result in more fuel for star formation. The correlation is very similar for all selection samples, whether they are centrals, satellites, jellyfish or non-jellyfish. As long as some gas is present in the galaxy, i.e., the gas fraction is larger than 1 %, the samples behave similar to one another.

The results of the left and right bottom panel in Fig. 3.6 indicate that the reason for suppressed SFRs in jellyfish and satellite galaxies compared to the sample of inspected galaxies is a lower typical gas fraction in the first two samples. We discuss the implications of this finding in more detail in Section 3.4.

3.3.4 SFRs across Cosmic Epochs

So far we focused the analysis on galaxy populations at low redshifts $z = 0$, 0.1 and 0.2. Now we examine if the findings of Section 3.3.3 hold at higher redshifts as well, or if the evolution of median SFRs differs from that of the SFMS.

To do so, in Fig. 3.7 we present the median SFR of the galaxies with galactic stellar masses of $M_* = 10^{9-10}\mathrm{M}_{\odot}$ from the 'Jellyfish' (orange) and 'Satellite analogues' (black) sample as a function of redshift. Additionally, we show the SFR from the

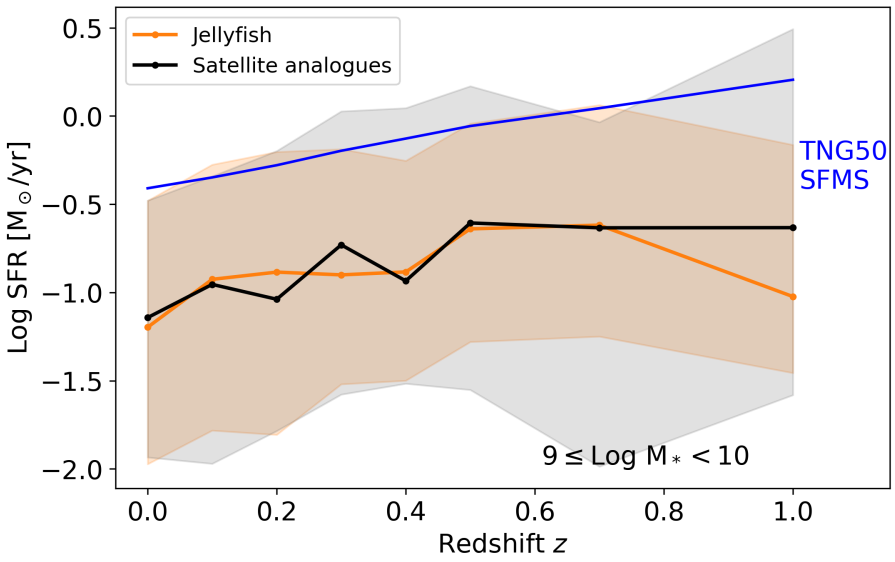

Figure 3.7: Evolution of meidan star formation rates of 'Jellyfish' (orange) and 'Satellite analogues' (black) for galaxies with a galactic stellar mass of $9 \leq \log(M_*/\mathrm{M}_\odot) < 10$ over cosmic time. The SFR predicted in this mass bin by the SFMS is depicted in blue. There are no significant differences in SFR between jellyfish and satellite analogues at any given redshift.

SFMS at the same mass bin at each presented redshift in blue.

We can draw two conclusions from this figure. First, we find that the median SFR (at a constant stellar mass) of jellyfish galaxies does not evolve significantly up to a redshift of $z \sim 0.4$, after which we find a mild increase at higher redshifts. We note that results at higher redshifts are more susceptible to low-number statistics, due to lower numbers of massive galaxies falling in the given mass bin at these epochs. The lack of evolution in the typical star formation activity of jellyfish galaxies at redshifts $\lesssim 0.4$ contrasts with the SFMS, which exhibits a mild but constant increase in SFR with increasing redshift.

Second, we find no significant differences between the SFR of jellyfish galaxies and that of (stellar mass-, host mass- and gas-fraction-matched) satellite analogues at any studied redshift. We therefore conclude that, in TNG50, we find no enhancement in SFR in jellyfish galaxies at the population level since a redshift of $z = 1$ (in our study). In fact, the overall suppression of star formation activity in jellyfish galaxies found in Section 3.3.3 is seen to be somewhat stronger at higher redshifts, at least

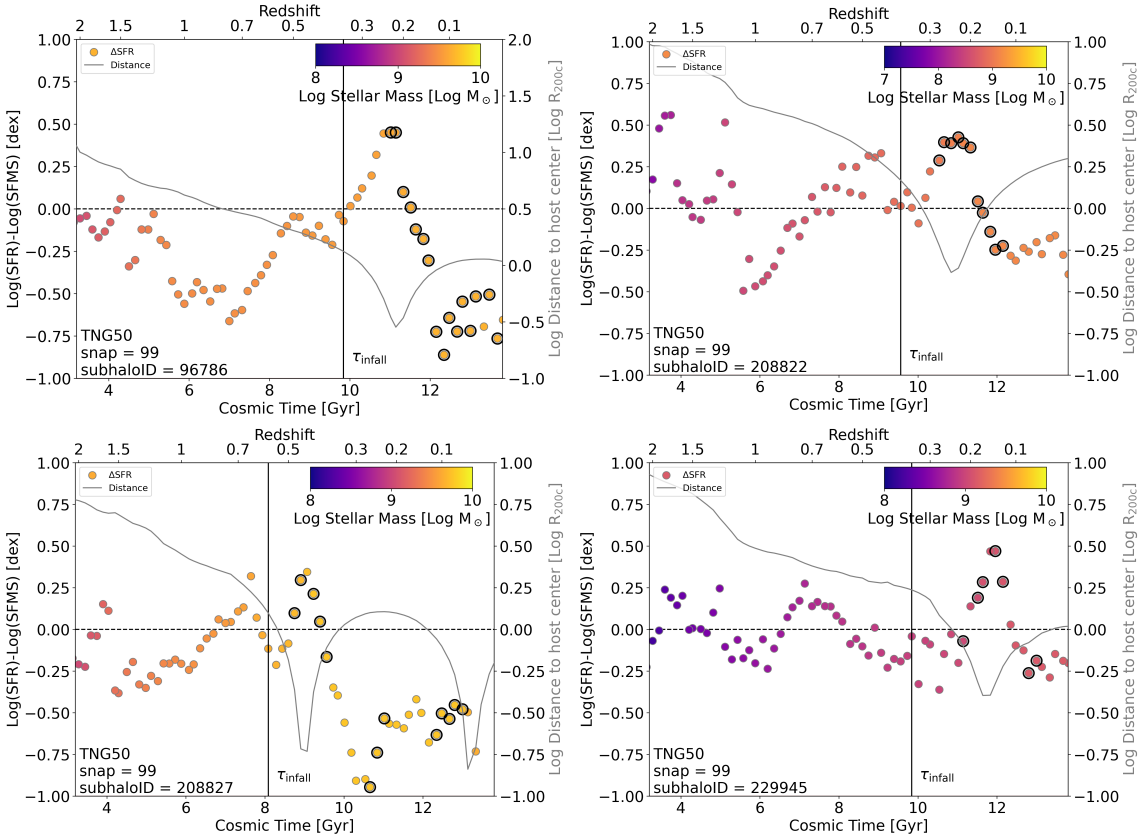

Figure 3.8: Star formation activity in relation to the SFMS of individual jellyfish galaxies across their evolutionary tracks. We present the offset of SFR in the galaxies from the SFMS (Δ SFR; color-coded dots), and the distance to the center of their host halo (grey curve) of selected jellyfish galaxies over time. The color of the colored dots indicates the stellar mass of the galaxy, black circles around the dots indicate snapshots at which the galaxy was visually identified as a jellyfish. The vertical line denotes the time of infall of the galaxy into its host halo. Many galaxies during their evolution show peaks in their SFR, at which their SFR exceeds that expected from the SFMS. Such peaks almost always coincide with the first pericenter passage of the galaxy within its host halo. This figure is continued in Fig. 3.9.

up to $z \sim 0.4$.

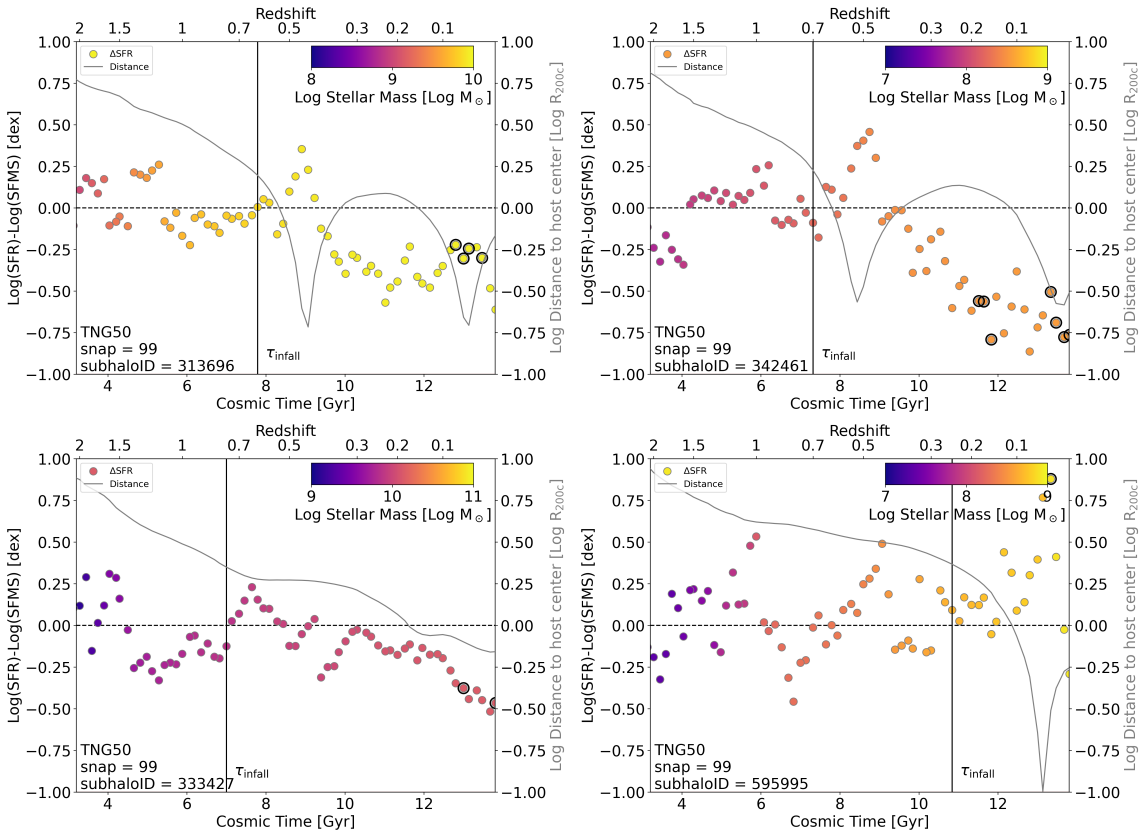

Figure 3.9: Continuation of Fig. 3.8.

3.3.5 Bursts of Star Formation in the Jellyfish' Past

So far, we did not find any evidence for a population-wide enhancement of SFR in jellyfish galaxies. We find, however, some jellyfish galaxies with levels of SFR that exceed those expected from the SFMS at their mass and cosmic epoch. Moreover, the previous results do not rule out the possibility for jellyfish galaxies to have temporarily enhanced SFRs during their evolution. To examine this, we turn from studying the galaxy samples on a population level towards assessing the development of individual jellyfish galaxies, i.e., we inspect the SFRs of individual galaxies along their evolutionary tracks (which we identified by the merger trees as explained in Section 3.2.5, further details are given in Rohr et al., 2023). We compare this evolution of SFRs to that of the SFMS in the respective mass bins. This comparison was done for the full sample of jellyfish galaxies, in Fig. 3.8 and 3.9 we present a few example tracks to demonstrate the variety of scenarios encountered.

Each panel shows the distance of the galaxy's SFR to that expected from the SFMS at the given redshift and the mass bin the galaxy falls in at this point in time (ΔSFR; colored points). We color code the dots according to the galactic stellar mass of the galaxy at the given time. Additional black circles surrounding the dot indicate snapshots at which the galaxy was identified as a jellyfish galaxy upon visual identification as described in Section 3.2.1. We also present the cluster-centric distance of the galaxy to its corresponding host halo, normalized by the virial radius of the host (grey circles). The time of infall of the galaxy into the host, i.e., the time at which it becomes a FoF member of the host halo, is indicated by a vertical line and $\tau_{\rm infall}$.

We indeed identify several galaxies in the simulation that are identified as jellyfish galaxies at some snapshot and that show a sharp increase and decrease, i.e., a peak or burst, of SFR with respect to the SFMS. During this period of enhanced star formation activity, the SFR of the galaxy can exceed that of a galaxy on the SFMS by up to an order of magnitude, even while it follows the SFMS quite closely during large parts of its evolution. Examples of this bursty behavior are shown in Fig. 3.8 and the first row of Fig. 3.9. We measure a maximum positive deviation of SFR from the SFMS in any analyzed jellyfish galaxy of 1.76 dex. We find short periods of super-SFMS star formation even in galaxies which, temporarily or overall, show SFRs much lower than the SFMS (see left panels of Fig. 3.8).

From the comparison of ΔSFR to the galaxies' distance to the center of their host halo (color-coded dots vs. grey curve) it is apparent that bursts in SFR almost always correlate with a pericenter passage of the given galaxy, i.e., fall in the time of the closest proximity of the galaxy to the center of their host halo. However, in most cases, only the first pericenter approach results in a burst in SFR, while subsequent ones do not lead to an equally high increase. Examples for this are shown in Fig. 3.8, panel 3, and Fig. 3.9, panel 1 and 2. We speculate that this burst in SFR is caused by compression of gas in the galaxy (Mistani et al., 2016; Roberts et al., 2022), and the resulting disruption of the pressure balance which stabilizes the gas against collapse. This compression will get increasingly stronger as the galaxy moves through regions of higher and higher ambient-gas densities while it approaches the central galaxy, and finally peaks at the pericentric passage. A second or third peak in SFR at subsequent pericentric passages is probably suppressed because the galactic gas by then is either already stripped from the galaxy or used up during the first

star formation burst.

Of the full sample of jellyfish galaxies, the majority experiences an epoch of increased star formation during their evolution. After the inspection of all evolutionary tracks of galaxies from TNG50 that have been flagged as jellyfish at some point during their lifetime we find 74 % to have a ΔSFR of ≥ 0.5 dex at some point during their lifetime and ~ 30 % experience such an increase at $z \leq 2$.

It is worth to notice that most jellyfish galaxies are identified as such in snapshots following peaks in ΔSFR during a pericentric passage, or at least at snapshots at its descending flank, i.e., in a phase of decreasing SFR compared to the SFMS. We show examples of such a behavior in the upper two panels Fig. 3.8. We find this typical for the general sample. Upon visual inspection, about 70 % of jellyfish galaxies that experience a ΔSFR increase of 0.5 dex or higher at $z \leq 2$ are, in fact, identified as jellyfish close to their time of a pericentric passage. The identifications then usually fall in the time of decreasing SFR in the galaxy. It has to be remembered, however, that even though many jellyfish galaxies show the aforementioned behavior, there are still numerous galaxies in this sample that experience a SFR history with low variability and without pronounced peaks. We show an example of this in the bottom left panel of Fig. 3.9.

We therefore conclude that, while we find no evidence (at late cosmic times) for an enhanced global SFR on a population level in jellyfish galaxies in TNG50, the majority of jellyfish galaxies do show short periods of SFRs above the SFMS, i.e., starbursts. This usually happens during pericentric passage. It also appears that, in most cases, the jellyfish galaxies are identified as such by the identifying volunteers during the time of decreasing SFR following such a burst, or soon after it. This implies that, within the TNG model, there are indeed some jellyfish galaxies that experience an enhancement in global SFR during their lifetime. We provide an in-depth analysis of the evolution of individual jellyfish galaxies in Rohr et al. (2023).

3.4 Discussion

3.4.1 Do jellyfish produce stars at higher rates than other satellites and field galaxies, according to TNG50?

The main goal of this chapter is to study if jellyfish galaxies in TNG50 experience enhanced SFRs compared to other field and satellite galaxies, as is seen in several observational studies (see Section 1.3.4 and 3.1). From the analysis of the global SFR of jellyfish galaxies and the comparison to different control samples in Section 3.3.3, we, in fact, find no increased population-wide SFR in jellyfish galaxies, as is found in observational studies such as Vulcani et al. (2018), Ramatsoku et al. (2020) and Vulcani et al. (2020). In TNG50, jellyfish galaxies instead typically show levels of SFR that are comparable to that of the constructed control samples, and lowered by $0.6 - 0.8$ dex at $M_* \lesssim 10^{10}\,\mathrm{M}_\odot$ compared to the general galaxy population. Compared to their governing sample of 'Inspected satellites', jellyfish galaxies show a SFR lowered by $0.3 - 0.7$ dex. This is true for all examined redshifts $z \lesssim 1$ (Section 3.3.4). This lowered SFR correlates with a lowered gas fraction in satellites, jellyfish galaxies and their analogue samples up to a galactic stellar mass of $\sim 10^{10}$ $\mathrm{M}_\odot$. At higher masses, jellyfish galaxies in TNG50 typically behave similarly to the general galaxy population in terms of SFR. These findings are more similar to those of Yoon et al. (2017) and Mun et al. (2021) as well as the outcomes from the study of Roberts et al. (2021b) in galaxy groups.

We believe this discrepancy between the findings in this chapter based on TNG50 and those from the GASP survey to be at least partially due to selection effects and the detailed method used for identification of jellyfish galaxies. Vulcani et al. (2020), for example, compare only resolved star-forming regions between jellyfish galaxies and control samples to find enhanced SFRs. Ramatsoku et al. (2020) find increased SFRs in jellyfish galaxies at fixed HI gas mass, whereas Moretti et al. (2020), on the other hand, find that jellyfish galaxies show SFRs comparable to other star-forming galaxies when the total gas mass is considered (as we find in Fig. 3.6). Galaxy clusters targeted in the GASP survey are moreover much more massive ($M_{200c} = 10^{13.6-15.2}\mathrm{M}_\odot$) than those studied in our samples, and the survey identifies galaxies that are gas-stripping based on B-band imaging as those that show indications of debris or morphological disturbances (Poggianti et al., 2017). Their

control sample consists of galaxies that have no such signs of stripping. They then collect complete IFU data of candidates with MUSE, where they include the tail regions of the galaxies, to allow for a study of the gaseous and stellar components of the galaxies. For this study, we instead include all galaxies that contain a minimum gas fraction in the sample of 'Inspected satellites', and subsequently identify jellyfish galaxies by their gas mass column density together with contours of their stellar density. The used maps include all the gas in the simulation in the vicinity of the galaxy, irrespective of its phase, surface density or brightness. We therefore find it possible that the GASP survey candidate selection might not be sensitive to jellyfish galaxies that have small gas tails and do not show obvious morphological disturbances in optical imaging. However, the extent in which this insensitivity affects the results is unknown, but it is possible that the used selection method biases the GASP jellyfish galaxies towards more extreme stripping conditions than typical for the survey presented in this chapter. The increase in SFR found in Vulcani et al. (2018) and Vulcani et al. (2020) are hypothesized to be caused by gas compression in the leading edge of the galaxy, but whether this process takes place preferentially under more extreme stripping conditions is yet to be seen. By comparing Fig. 3.2 and Fig. 3.3, we finally notice that according to TNG50 it is clearly easier to identify tails of jellyfish galaxies based on gas phases that are not tracers of star formation and very dense gas than e.g., Hα.

The findings of comparison studies like the one conducted in Section 3.3.3 are furthermore sensitive to the exact definition of the chosen control samples, as well as to any additional cuts that are applied to the data. Outcomes might be strongly altered by any changes in the selection criteria of jellyfish galaxies and their control sample. This complexity is shown by our comparison of galaxy samples with different cuts in gas fraction, which results in a different availability of fuel for star formation in these galaxies. Selection biases may therefore affect the gas fraction distribution in selected galaxy samples, and this may increase or decrease the star formation activity in samples such as the jellyfish galaxy sample, even if RPS and their resulting appearance as jellyfish galaxies may not be the cause of this changed star formation behavior per se.

On the other hand, at any time in our simulation we find a small number jellyfish galaxies that are located above the SFMS. About three quarters of jellyfish galaxies experience bursts of star formation during their lifetime (see Section 3.3.5).

Even though jellyfish galaxies in general are rare objects, we hypothesize that star bursting galaxies might be more prominent in observations, of course depending on the detection method. This may result in a selection bias similar to the one described above, where jellyfish galaxies in observations are found to have enhanced SFRs. Another implication for galaxies missing from observational searches for jellyfish galaxies is the higher relative number of jellyfish galaxies found in IllustrisTNG compared to those in observations. Among the inspected galaxies, we find a fraction of jellyfish galaxies of about 8 % in TNG50 (Zinger et al., 2024). Poggianti et al. (2016), on the other hand, in their observational sample of 76 galaxy clusters and 176 galaxy groups find a total of 2 % to be jellyfish candidates. This deviation could be explained by a preferential observation of star-bursting galaxies.

3.4.2 Possible Limitations of the Current Work and Looking Ahead

In this chapter we use a sample of TNG50 jellyfish galaxies unmatched in size by any other theoretical analysis or observational survey. This allows for a statistically robust study of the star formation activity in jellyfish and non-jellyfish galaxies. However, we have to point out to the reader that some of the presented results in this chapter might be driven by the particularities of the IllustrisTNG model and possible other limitations. Here, we discuss the study's limitations, even though most issues affect the SFRs in the tails of jellyfish galaxies, and less so the global SFR and comparisons based on this property. Moreover, the IllustrisTNG model has been shown to recreate galactic star formation activity and quenched fractions in satellites in the range of observations in the regimes examined in this chapter (see e.g., Donnari et al., 2019, 2021, 2020; Joshi et al., 2021). This lends credibility to the effective results of the model when evaluated across galaxy populations (for a comparison of environmental effects across different simulations, see also Kukstas et al., 2023).

3.4.2.1 Star Formation and ISM Model in IllustrisTNG

The IllustrisTNG model uses a simplistic non-multi-phase modeling of the ISM. Moreover, the nature of subgrid star formation is stochastic, i.e., if a gas cell ex-

ceeds a density threshold, a star particle is formed with a certain probability (see Springel & Hernquist, 2003; Pillepich et al., 2018a). This process is designed to follow the Kennicutt-Schmidt relation (Equation 1.14) with a Chabrier IMF (Equation 1.24, (Chabrier, 2003a; Chabrier, 2003b)). Other properties of the gas that might hinder or support star formation (such as temperature, pressure, magnetic field, gravitational potentials or the presence of flows, etc.) are not explicitly included. Ultimately the star formation process is approximately calibrated to follow certain observed galaxy scalings at $z = 0$. It therefore is best matched to star formation in the main body of isolated galaxies, and does not necessarily account for the conditions in the tails of jellyfish galaxies in an appropriate way. This, of course, might affect SFRs in the tails of jellyfish galaxies. However, we do not expect this to impact the outcome of our study of global SFRs in the galaxies, as those are dominated by the galaxy's main body.

3.4.2.2 Spatial Resolution Effects

As Arepo is a moving-mesh code, a defining feature of this framework is that the spatial resolution of the gas cells depend on the local density of the gas (Pillepich et al., 2019, 2021). This results in an increased resolution in the central regions of galaxies, where gas reaches high densities, but also means that regions of lower gas density, such as tails of jellyfish galaxies, are less resolved. Knots of dense gas that might be star-forming (i.e., regions similar to the Hα knots observed in jellyfish tails, Vulcani et al., 2018 and Poggianti et al., 2017) would therefore require a mesh adaption to increase the spatial resolution locally (as is the case for the cold small gas clouds in the circumgalactic medium of TNG50 galaxies Nelson et al., 2020; Ramesh et al., 2023), but ultimately the spatial resolution in TNG50 galaxies is limited and regions like that may therefore remain under resolved. This, in turn, might result in the SFRs in jellyfish tails being underestimated, but we expect the impact on global SFRs to be minimal.

3.4.2.3 Temporal Resolution Effects

We also inspected the evolutionary tracks of individual jellyfish galaxies and showed that the majority of them experience bursts of star formation during their evolution, which usually correlates with the first pericentric passage of the galaxy with their

host halo (see Section 3.3.5). This analysis conducted here is based on the instantaneous SFR of the galaxy at the given snapshot, and therefore depends on the time interval between consecutive snapshots, which is about 150 Myr in TNG50 (this is separate from the time resolution during the simulation run, which is considerably higher). These set time intervals in principle could prevent us from capturing star formation bursts that occur on shorter time scales and therefore take place between the given snapshots. However, from Fig. 3.8 and 3.9 it appears that peaks in star formation activity encompass multiple snapshots, i.e., have durations longer than the snapshot separation. Yet, we cannot rule out the possibility of star formation bursts on shorter timescales. This could only be assessed in simulations with a lower time interval in between snapshots, or by relying on the stored ages of star particles in TNG50. We postpone this analysis to future work.

3.4.2.4 Measurement of SFRs

Discrepancies between the results presented in this chapter and observations could also be caused by the measurement of SFR itself (see also Appendix A). Observations rely on tracers of star formation, such as Hα luminosity or IR emission, and a corresponding calibration to measure SFRs of galaxies, but those tracers are sensitive to different timescales. In simulations, however, we have direct access to the SFR as we can access the information of the whole star formation history of any given galaxy. As the observed SFRs depend on the precise calibration used for the measurement, these might not be appropriate for extreme environments such as jellyfish tails, even though they are usually robust for the overall SFR of galaxies. For example, Hα may not be as tightly connected to star formation activity in jellyfish tails as it is in the disks of galaxies (Boselli et al., 2016; Cramer et al., 2019, see also Section 3.1).

3.5 Summary and Conclusions

In this chapter we have quantified the star formation activity in jellyfish galaxies and carefully selected control samples in the cosmological+magnetohydrodynamical simulation TNG50 (Nelson et al., 2019b; Pillepich et al., 2019). For the analysis we used an unprecedented sample of 780 jellyfish in selected snapshots at $z \leq 1$, which were visually classified from more than 50000 satellites (Zinger et al.,

2024) at galactic stellar masses $> 10^{8.3}\,\mathrm{M}_\odot$, belonging to galaxy clusters of $M_{200c} = 10^{10.5-14.3}\,\mathrm{M}_\odot$ and having a gas fraction of > 1 %.

The SFRs of the identified jellyfish galaxies were contrasted to that of variously defined comparison samples, including the general galaxy population, its SFMS, satellite galaxies, all satellite galaxies inspected for jellyfish galaxies, and two control samples of non-jellyfish field and satellite galaxies, that closely resemble jellyfish galaxies in terms of galactic stellar mass, gas fraction and the mass of their host halo (see Section 3.2.4 and Fig. 3.1, as well as Table 3.1). We have examined the galaxy-wide SFRs of each galaxy, as well as, in the case of jellyfish, the star formation in the galactic body and the ram-pressure stripped tails separately (see Section 3.3.2). For our study, we compared the galaxies on a population level (Section 3.3.3 and 3.3.4), and followed the evolution of individual galaxies (Section 3.3.5).

We find our main results to be the following:

- Jellyfish galaxies are typically not quenched but star-forming, even though they are severely affected by RPS (Figs. 3.2, 3.3, 3.5 and 3.6). We find this even though our method of identification of jellyfish galaxies is completely agnostic to tracers of star formation.

- Star formation also occurs in the ram-pressure stripped tails of jellyfish galaxies, although at much subdominant rates compared to the galaxies' main bodies (Fig. 3.5).

- At any cosmic epoch, in TNG50 we find jellyfish galaxies with SFRs that exceed that expected from the SFMS (Figs. 3.5 and 3.6).

- However, we do not find a population-wide enhancement of SFR in jellyfish galaxies compared to satellite galaxies inspected for jellyfish galaxies, or comparable satellite or field galaxies. At a given stellar mass the median SFR of jellyfish galaxies lies below the SFMS and is comparable to that of control samples of galaxies with analoguous galactic properties (Fig. 3.6, top). These findings remain true up to $z \sim 1$ (Fig. 3.7).

- We find jellyfish galaxies to be quenched less often than the general population of satellite galaxies (Fig. 3.6, bottom center). As jellyfish galaxies are biased

towards higher gas fractions than the general satellite population (as they otherwise could not exhibit gaseous tails), this follows naturally, as gas is the fuel for ongoing star formation.

- Our study discloses that in TNG50 the majority of jellyfish galaxies experience phases of increased SFR during their evolution(Fig. 3.8). At some point during their lifetime, about 74 % of jellyfish galaxies experienced periods of super-SFMS SFRs. This usually occurs during pericentric passage. This, however, does not result in a population-wide enhancement of SFR at any studied cosmic epoch.

The findings of this chapter qualitatively contrast some (though not all) observational findings on star formation activity in jellyfish galaxies. The large sample size of jellyfish galaxies drawn from TNG50 allowed for a statistically robust study of star formation in jellyfish and non-jellyfish galaxies. We were thus able to emphasize the importance of awareness of implicit and explicit biases affecting jellyfish samples, whether simulated or observed. In future work, we aim to overcome the simplified numerical treatment of star formation and ISM, and thus aim to assess the impact of physical and numerical models on the prediction of star formation in jellyfish galaxies and especially their tails.

4 The Rhea Simulations - General Characterization and Star Formation

In Chapter 3 we studied the star formation activity of jellyfish galaxies, which are usually satellite galaxies of low mass. We now move on to a different galactic environment, the Milky Way, which is one of the two largest galaxies in its group of galaxies. In this chapter, we study star formation in a single galaxy modeled after the Milky Way. This galactic environment differs a lot from jellyfish galaxies, as the Milky Way is not in the process of RPS, i.e., is not actively losing gas. The process of star formation therefore is less disturbed on a galactic scale, no gaseous tail has to be taken into account. In this chapter, we therefore focus on the distribution of star formation within the galactic disk and its effects, while also introducing and characterizing the hydrodynamical Rhea simulations.

This chapter is based on Göller et al. (2025), submitted to Astronomy & Astrophysics. Junia Göller, the author of this thesis, is the first author of this paper and developed the simulations presented in this chapter. She is the main author of the text of the paper, with input from Dr. Philipp Girichidis, Dr. Noé Brucy and Prof. Simon Glover. The text of this chapter was written by Junia Göller only. All presented figures are from Junia Göller, except for Fig. 4.1 and 4.6 that were provided by Dr. Noé Brucy.

Abstract

In the complex ecosystem of the Milky Way, detailed observations can probe the physical mechanisms forming and affecting the interstellar medium. For a better understanding of the basis of observed features, galactic models customized to the Milky Way are needed. However, as details of the Galactic structure are not fully determined by observations, generalizations have to be made to allow for flexibility in the used models. In this chapter, we present the hydrodynamical Rhea simula-

tions, a set of simulations of a Milky Way-like galaxy, that contain detailed physics of the interstellar medium, star formation and stellar feedback. The presented simulations differ in terms of the adopted gravitational potential: One is fitted to several structural details seen in observations, the other just reproduces the most basic axisymmetric quantities of the Galaxy. Except for the bar region, we find few morphological differences between the evolved galaxies with different potentials. The radial distribution of star formation differs slightly, whereas the global star formation rate is unaffected by the chosen potential. When a non-axisymmetric bar potential is used, the constant gas funneling towards the Galactic inner region prevents quenching of the Galactic center. Such a potential also lowers the size and lifetime of actively star-forming regions in the Galactic center, whereas we find no influence of a spiral arm potential on those properties. We therefore conclude that the Galactic bar potential has a noticeable influence on the star formation and subsequent stellar feedback in the Galactic center, mainly within the innermost 3 kpc, but up to $5-6$ kpc. A spiral arm potential, on the other hand, does influence properties of star formation in the simulated Milky Way by producing spiral structures that are longer-lived than the transients spiral features produced when no such potential is used.

4.1 Introduction

While in the last chapter we studied star formation in a more cosmological context of multiple galaxies in galaxy clusters across different redshifts, we now move on to smaller scales within a single, relatively unperturbed galaxy. This allows us to study star formation on smaller scales within the galactic disk, and to examine the influence of the *intragalactic* environment on the star formation activity, contrary to the *extragalactic* environment, which we studied in the context of jellyfish galaxies. We choose the Milky Way as a laboratory example for this study, because it is a typical galaxy in our present-day universe, and because extensive observations of it allow for detailed modeling of this galactic system.

As introduced in Section 1.3.5, our home galaxy, the Milky Way, is not only an example of the type of spiral galaxies that dominate present-day star formation (Kennicutt & Evans, 2012; Bland-Hawthorn & Gerhard, 2016), but also provides

the unique opportunity for small-scale processes in the ISM, such as the formation of molecular clouds and stars as well as stellar feedback. No other galaxy allows for a study of these processes in such detail as in our own, even though the named processes are crucial for the evolution of any present-day galaxy.

But even in the Milky Way, the galactic context of star formation and the corresponding stellar feedback remains poorly understood. Especially the interplay between the large-scale galactic potential and induced galactic dynamics with the small-scale local star formation is still an open debate. This will be the focus of this chapter. From Section 1.2.3 we know that star formation is a relatively inefficient process (for a review, see e.g., Girichidis et al., 2020), but it is unknown to what extent the galactic potential and galactic dynamics play a role in the regulation of star formation, next to feedback, magnetic fields, turbulence and similar.

The galactic potential, for example, plays a role in the star formation within the CMZ. This compact region of about $3-7\times10^7$ $M_\odot$ (Molinari et al., 2011; Tokuyama et al., 2019) consists of cold, dense clouds, fueled by the dust lanes. The observed SFR is low, just $0.06-0.14$ $M_\odot$ yr^{-1} (Yusef-Zadeh et al., 2009; Immer et al., 2012; Longmore et al., 2013), which is more than a factor of 10 lower than what would be expected from its gas mass and density (Longmore et al., 2013; Kruijssen et al., 2014). This is probably because the SFR in this region is more closely related to the gas inflow rate than to the actual mass of the region, as simulations suggest (e.g., Seo & Kim, 2013; Seo et al., 2019; Sormani et al., 2020a; Moon et al., 2021). In this region, the Galactic potential therefore seems to be crucial for the regulation of star formation, because its bar component controls the gas inflow rate. Moreover, it has been shown that the presence of a bar itself can alter the SFR of a galaxy (e.g., Vera et al., 2016; Scaloni et al., 2024).

Another example of the influence of the Galactic potential are spiral arms, whose effect on star formation is still heavily debated (which we discuss in Section 1.2.2 and 1.3.5 with respect to the MW, especially). As mentioned before, it is unclear if they serve as triggers of star formation, in the sense that the SFE is increased in the spirals, or if they merely reorganize star-forming gas without any impact on the star formation process itself. For example, Seigar & James (2002) found the SFR significantly enhanced in the vicinity of spiral arms, pointing towards triggered star formation. Foyle et al. (2010) on the other hand found SFEs of the arm and interarm regions of NGC 5194 and NGC 628 to be very similar. Numerical simulations

tend to find no triggering of star formation in spiral arms, however, Dobbs et al. (2011b) found that a spiral potential can increase the SFR indirectly by enabling the formation for long-lived and strongly-bound clouds. Kim et al. (2020) found the global SFR only moderately enhanced by a spiral arm potential, but the SF reorganized such that the majority of SF happens in the spiral arms. The question of the influence of spiral arms on star formation is even harder to answer without the knowledge of whether they are long-lived (as suggested by the density wave theory, Lin & Shu, 1964; Shu, 2016, see Section 1.2.2) or transient features (as suggested by the self-propagating star formation model, Mueller & Arnett, 1976; Gerola & Seiden, 1978, see Setion 1.2.2).

Such reorganizations of SF throughout the galactic disk can have substantial consequences for the galaxy's appearance. Star formation itself shapes the surrounding gas, however, subsequent stellar feedback such as stellar winds and supernovae affect the galactic disk up to several hundreds of pc (see Section 1.3.3). Clustered SF, resulting in subsequent clustered winds and SN, can form superbubbles, tearing enormous holes in the gaseous structure of the galaxy (e.g., Ferrière, 2001). Strong star formation activity might even be the reason for the formation of the Fermi bubbles (Su et al., 2010; Dobler et al., 2010) in the galactic center (Crocker & Aharonian, 2011; Crocker, 2012). Local variations of the SFR are therefore of utter importance for the general appearance of a galaxy, and are a driver for the galactic evolution.

Even though the proximity of structures in the Milky Way allow for unrivaled detail in observations, our peculiar position within the Galactic disk makes it challenging to estimate the true Galactic potential and also star formation properties anywhere outside the greater solar neighborhood (see Section 1.3.5 for details on observational surveys on the Milky Way). The accuracy of knowledge about properties of important Galactic elements, such as the bar length and pattern speed or scale lengths of the thin and thick disk, therefore remains limited (see Section 1.3.5). For that reason one might wish for a more general description in terms of potential and structure when modeling a Milky Way like galaxy, in order to not introduce additional uncertainties needlessly. Part of the question therefore is: How detailed does one have to model the Milky Way potential? And how important are the different parts of the potential?

Isolated galaxy simulations such as the Rhea simulations are suited perfectly for

determining this. In this chapter, we present the hydrodynamical Rhea runs with the flat and Milky Way potential (Section 2.3.8, refer to Section 1.3.5 for a review of previous simulations of Milky Way-like galaxies), which include a detailed treatment of chemical processes in the ISM, star formation and stellar feedback. The elaborate external Milky Way potential (with non-axisymmetric features of a bar and spiral arms) allows for a close match to observations of dynamical properties, whereas the flat potential provides us with a galaxy simulation recreating just the most basic features of a Milky Way-like galaxy, excluding any time-dependent dynamics of the potential.

After introducing some analysis methods in Section 4.2 (in addition to simulation methods described in Section 2.3.8), in the first half of this chapter we present a general characterization of the simulations and study the influence of the galactic potential on the general morphology in Section 4.3. In the second half we focus on star formation in the simulated galaxies, how it is distributed throughout the disk and how the potential influences its clustering (Section 4.4). In Section 4.5 we then briefly discuss the caveats of our study and summarize our findings in Section 4.6.

4.2 Methods

4.2.1 Used Simulations

As we are using the hydrodynamical (HD) runs of the Rhea simulation suite, the simulation methods are identical to those described in Section 2.3.8. However, as we include a short comparison of runs with different resolutions in Appendix B, in addition to the fiducial simulation resolution of 3000 $M_\odot$, we also run both the flat (F) and Milky Way (MW) potential with a resolution of 1000 $M_\odot$ for some time. These higher resolution runs we only use in Appendix B, throughout this chapter only the resolution of 3000 $M_\odot$ is used. This results in a total of 4 different simulations, whose abbreviations and differences are given in Table 4.1. We choose the fiducial analysis time to be $t = 2500$ Myr, based on morphology and the global SFR of the simulated galaxies.

	mass resolution [$M_\odot$]	potential
F3000HD	3000	flat
MW3000HD	3000	MW
F1000HD	1000	flat
MW1000HD	1000	MW

Table 4.1: Specifications of the simulations presented in this chapter.

4.2.2 Clustering with Hdbscan

For the analysis of clustering of star formation and stellar feedback, we use the Python clustering library HDBSCAN (Campello et al., 2013). This library, together with other clustering algorithms, was tested on Gaia data to detect open clusters from coordinates, proper motion and parallax by Hunt & Reffert (2021). In this study, it had the highest sensitivity of all tested algorithms and in general was found to work best on Gaia data.

HDBSCAN is a hierarchical clustering algorithm and can detect clustering in regions of vastly different densities. It does this by using a minimum spanning tree weighted by nearest-neighbour distances. Via single-linkage, it then checks if the termination of a single connection would divide a cluster into two, where each still has a number of members greater than a predefined number (`min_cluster_size`), or if the point with the terminated link would merely fall out of the cluster. If the former is true, the two new clusters are kept as individual clusters, whereas in the latter case the cluster keeps its former structure. This results in a hierarchy of clusters. The flat clustering is derived from this hierarchy by checks for stability of the clusters in the hierarchy. This means that HDBSCAN, unlike other clustering algorithms, does not utilize some pre-defined density threshold, but instead can adapt to the local background and find overdensities in it. It therefore works in a wide range of background densities, as found in a (simulated) galaxy.

The parameter `min_cluster_size` mentioned before sets the lowest number of members a detected cluster can have. It is the single parameter of control for HDBSCAN. For this analysis we set it to 5, i.e., we do not take into account any associations with fewer than five star particles.

We search for groupings of newly formed stars in a four dimensional phase space

of birth coordinates and birth time, i.e., star particles identified to be in the same group by the algorithm have to be formed in close spatial vicinity and soon after each other (for a more quantitative description, see Fig. 4.11). For SNe, the phase space consists of the coordinates and time of explosion (see Fig. 4.12, correspondingly). As the median of the distribution of the number of group members is 10, i.e., well above the selected minimum number, and the distribution is very similar across simulations and galactic regions (ranging from the minimum number of 5 to several hundreds of members), we do not expect the selected minimum number to affect the properties of detected groups significantly.

In this chapter, we are simply interested in the properties of regions of ongoing star formation, i.e., where those regions are located, how large they are and for how long star formation goes on in them. We therefore do not label the detected structures as 'clusters', as 'cluster' is a widely used term in astronomical context. We use 'groups' instead, because the associations found with HDBSCAN are not meant to resemble stellar clusters, as each star particle itself already represents several (massive) stars.

4.3 Morphology

The Milky Way is a complex system, with many processes affecting its evolution and shape, and the gravitational potential is only one of them. In this section we examine the effect the gravitational potential has on the morphology of the gas and newly created stars in the simulated galaxies. We study the large scale structures of the bar and spiral arms, as well as the vertical structure of the disk.

4.3.1 Global Dynamic Effects of the Galactic Potential

In this section we aim to better understand the properties of the external potentials used for the simulations, to be able to quantify their effects on morphology and star formation later on. In our simulations, the full gravitational potential at work is the sum of an external potential and the (self-)gravity of the gaseous disk and newly formed stars. The external potential accounts for the gravity from DM and old stars and is defined as explained in Section 2.3.7. We remind the reader that the external potential does not evolve in a self-consistent way, as its individual gravity-generating components (i.e., stars and DM particles) are not simulated explicitly, but merely

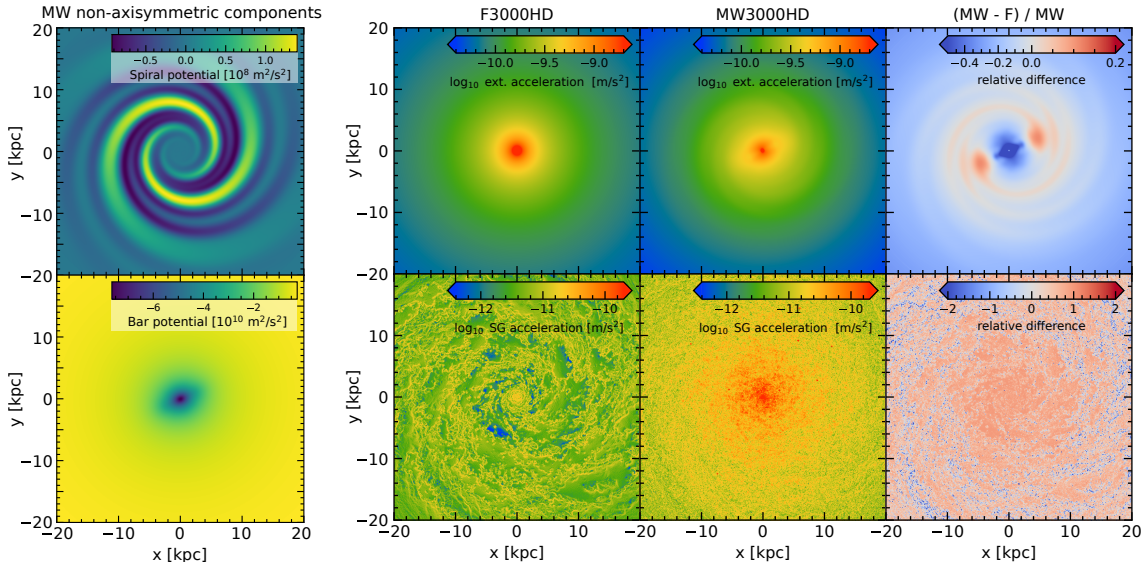

Figure 4.1: Gravitational potentials and accelerations. We show the non-axisymmetric components of the external potential of MW3000HD (left panel) and slices through the center of the galaxy of the acceleration parallel to the Galactic plane (right panel) in simulations F3000HD (left column) and MW3000HD (center column) at $t \approx 2500$ Myr, as well as the relative difference between the two (right column). The first row of the right panel shows the acceleration from the external potential, the second presents the contribution from self-gravity of the gas and newly created stars.

their dynamical effects.

In the left panel of Fig. 4.1, we show the non-axisymmetric components of the MW potential (again, see Section 2.3.7 or Hunter et al., 2024 for details), i.e., the potential used in MW3000HD, namely the bar and spiral arm potential. Because the bar potential is much stronger than the spiral arm potential, we show them separately in the top and bottom panel, respectively. The flat potential used in F3000HD does not include such non-axisymmetric components. In the top row of the right panel of Fig. 4.1 we then illustrate the accelerations parallel to the midplane corresponding to the flat (left) and MW (center) potential. Because of the reasons explained before, the contribution from the bar for the MW potential in the upper right is clearly visible, while the accelerations from spirals are about two orders of magnitude weaker and therefore only vaguely visible. However, their position is outlined by a slightly higher acceleration than the background. The acceleration

from the flat external potential on the other hand is fully axisymmetric and the induced accelerations are of similar absolute magnitude.

By subtracting the external potential accelerations from the total accelerations we obtain the accelerations induced by gravity from gas and stars that are simulated explicitly. We present those in the bottom row of the right panel of Fig. 4.1. It is apparent that the accelerations from self-gravity (SG) are severely subdominant compared to the accelerations from the external potential, but much more structured. While the flat potential lacks any spiral component, the SG acceleration map clearly shows a filamentary structure resembling tightly-wound spirals. In the case of the MW potential, the external potential has a clear effect on the SG accelerations as well, as those are more strongly centered in MW3000HD than in F3000HD. This is because of the constant channeling of gas (and therefore mass, see later sections) into the galactic center by the bar potential, that then induces gravitational accelerations itself.

In the right column of the right panel of Fig. 4.1 we moreover present the relative difference between the two potentials, i.e., the difference of the acceleration in MW3000HD and F3000HD, divided by that of MW3000HD. The accelerations from the external potential differ by up to 60% in the galactic center; where the spiral arm potential is located, the gravitational acceleration from the external potential is about 10% larger in MW3000HD than in F3000HD. Differences are particularly large in the inner 10 kpc of the galaxy. Especially at the tips of the galactic bar the accelerations differ strongly between the potentials, with a higher acceleration in MW than in F. From the right column it is also apparent that the flat potential is more centralized than the MW potential. From the bottom right column it is evident that acceleration from self-gravity is much more important in MW3000HD than in F3000HD, up to 100%, i.e., the gas has more freedom to reorganize independently from the external potential. Because of these strong local differences between the gravitational potential, as well as the larger importance of self-gravity in the MW potential compared to the flat potential, one expects noticeable differences in the gas dynamics and organization and therefore in the star formation behavior in the simulations, at least locally. In the following we will quantify these differences induced by the gravitational potentials.

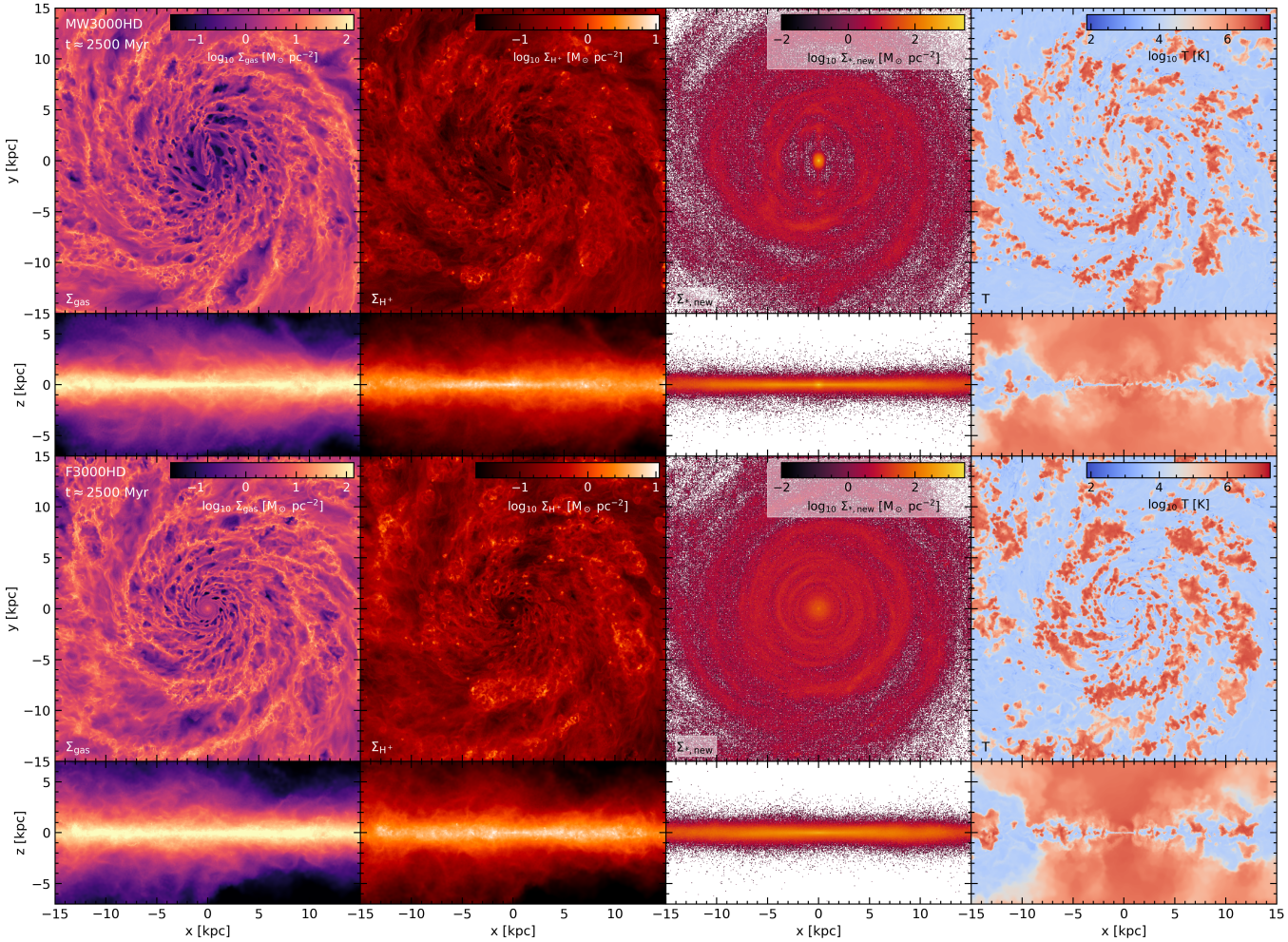

Figure 4.2: Surface density of total gas (first column), ionized hydrogen (second column), stars (third column) and the temperature in a slice through the midplane (fourth column) for simulations MW3000HD (first row) and F3000HD (second row) for the inner 15 kpc of the simulation.

4.3.2 Overall Morphology

We now qualitatively examine the effect of the aforementioned different acceleration profiles on the galaxies. The overall appearance of our simulated galaxies change substantially with the used gravitational potential, as expected. Differences in the general morphology appear early in the simulation evolution, which is apparent from gas column densities at the end of phase I, which we show in Fig. B.1. In Fig. 4.2 (a depiction of the whole galactic disk can be found in Fig. B.5) we present the

evolved galaxies at our fiducial analysis time of $t = 2500\,\mathrm{Myr}$, MW3000HD at the top, F3000HD at the bottom (see Table 4.1). From left to right we show the total gas surface density Σ_{gas}, the surface density of H^+ Σ_{H^+}, the stellar surface density Σ_* and the gas temperature T in a slice through the disk midplane, in both a face-on and edge-on projection. The influence of the bar potential in MW3000HD can be seen in both gas and stars, when comparing to F3000HD. The constant funneling of gas to the galactic center leads to high levels of star formation compared to F3000HD (compare also Section 4.4), resulting in a stellar bulge-like structure, also visible in the edge-on projection. The region of influence of the bar reaches up to a galactocentric distance of about 5 kpc, further out the morphology of the disk is only marginally affected. The region of low gas-surface density surrounding the galactic center in MW3000HD is a 'depleted' region due to the bar, where it channeled all gas to the galactic center. In our interpretation, it is part of the gap that forms around the Lindblad resonance (Sormani et al., 2024, see also Querejeta et al., 2021).

In both potentials we see the emergence of spiral arms in stars as well as gas. Visually, they appear very similar, even though they emerge for different reasons: The potential of MW3000HD includes a spiral arm potential explicitly, resulting in long-lived (see also Section 4.4.3) spirals within the potential wells of this potential (this resembles what would be expected from the density-wave theory, see Section 1.2.2). The spirals in F3000HD evolve spontaneously from instabilities in the gas and are not driven by an explicit spiral component in the potential. From inspection for different simulation times, we find them to be short-lived features, continuously reforming and disintegrating (as expected from the self-propagating star formation model, again see Section 1.2.2)

The spiral pattern is also traced by hot regions produced by recent SN activity, which can be seen in the temperature slice. As expected from SN remnants, those hot regions also have equivalents in the surface density of ionized hydrogen. In MW3000HD, such SN remnants are also present in the center of the disk ($R_{\mathrm{gal}} \leq 2.5$ kpc), whereas this region is more quiescent for F3000HD. For both simulations we find hot outflows from the galactic center, which are visible in the edge-on temperature slice.

We therefore conclude that especially the inclusion of a non-axisymmetric bar potential changes the morphology of the central disk dramatically, with an increase in star formation and supernova feedback. Spiral structures on the other hand form

via self-gravity even if they are not imposed by a gravitational potential.

4.3.3 Thermodynamic Properties

We have now seen that the introduction of a barred external potential not only changes the structure of gas and stars in the galactic center but also the amount of star formation and SN explosions there. In this section we follow up on this and examine how this affects the temperature and density of the simulated ISM, i.e., the ISM phases (see Section 1.3.2 for theory on the ISM phases).

To do so, in Fig. 4.3 we present the temperature-density distribution of MW3000HD (left column) and F3000HD (right column) for the whole simulation box (top row), the Galactic disk ($|z| < 1$ kpc and $R_{\rm gal} < 25$ kpc, middle row) and the Galactic center ($|z| < 1$ kpc and $R_{\rm gal} < 2.5$ kpc, bottom row). The color-coding shows the mass fraction of the respective part of the simulation.

For the full simulation box (top row), the phase plots of the two simulations show remarkably similar features: Most gas resides in the warm neutral and warm ionized medium at temperatures around T $\sim 10^4$ K. At densities $> 10^{-24}$ g cm^{-3} this warm medium extends into the cold neutral medium. At densities below $\sim 10^{-28}$ g cm^{-3} gas is found only at high temperatures at about $10^{5.5} - 10^7$ K, and therefore forms the hot phase of the ISM. In addition some hot gas is also present at densities of $10^{-28} - 10^{-23}$ g cm^{-3}. This gas is heated by SN feedback, but did not yet expand.

Also when zooming into the galactic disk (middle row), the two simulations barely differ. As most of the hot gas is in the circum-galactic medium, this phase is mostly absent in this region, and therefore only very low fractions of gas are at densities below $\sim 10^{-28}$ g cm^{-3}. In the disk, most gas is instead located in the warm and cold phases of the ISM.

Only when zooming further into the galactic center (bottom row) one can see clear differences induced by the galactic potential. Here, again, most gas is found in the warm phases, however, for F3000HD a higher fraction of gas is in the cold phase than in MW3000HD. There, some gas at hot temperatures ($\sim 10^6$ K) and low densities ($\lesssim 10^{-28}$ g cm^{-3}) is present instead. This is the result of the higher star formation rate and corresponding SN feedback, which we already saw in Section 4.3.2, and will analyze further in the Sections 4.4.2, 4.4.4 and 4.4.5.

Thus we can conclude that the gravitational potential leaves the overall temperature-

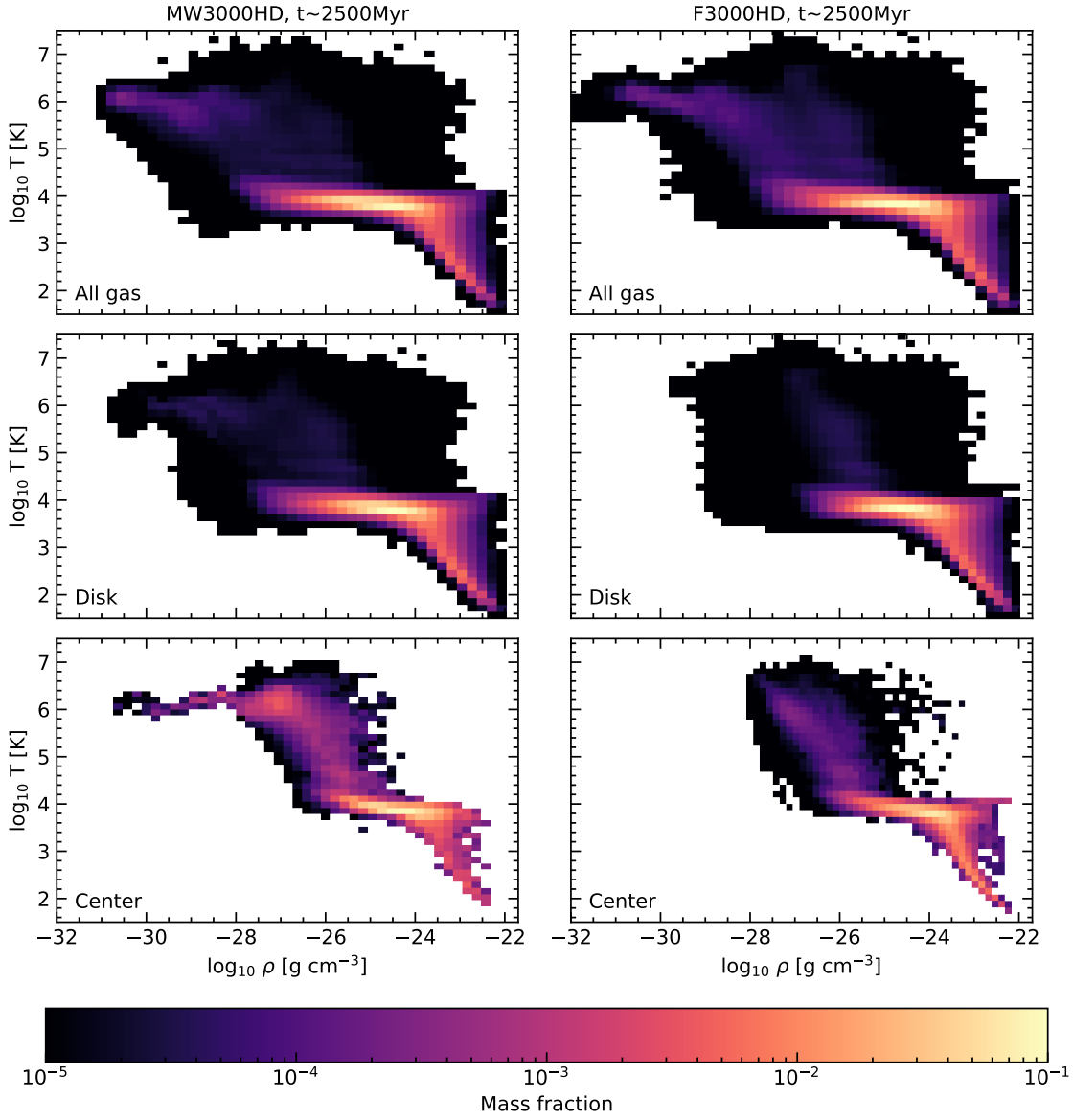

Figure 4.3: Temperature-density plot for MW3000HD (left) and F3000HD (right) at the fiducial time of 2500 Myr. Color coded is the relative mass fraction of gas in the different phases. All plots show a three-phase structure of the gas, with a phase of hot, low-density gas and a colder phase extending to higher densities, as well as a cold phase at densities $\rho > 10^{-24}$ g cm^{-3}.

density distribution of the ISM unchanged, and affects it indirectly only in the galactic center.

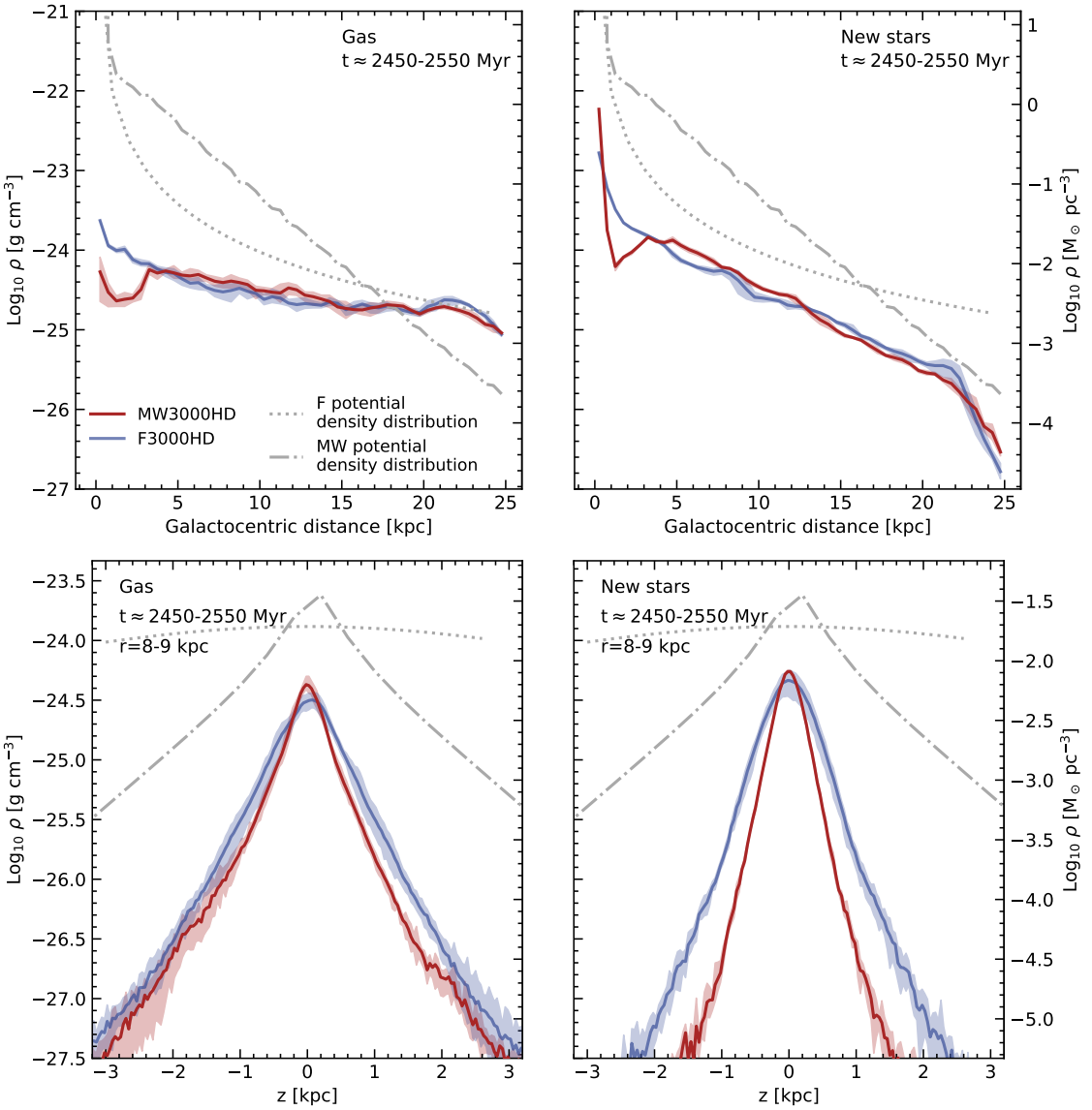

Figure 4.4: Volume-weighted radial (top) and vertical (bottom) density distribution of gas (left) and stars (right) for F3000HD (blue) and MW3000HD (red) averaged from 2450 to 2550 Myr. Shaded regions indicate 16th to 84th percentile. The density distributions generating our adopted external potentials are indicated in grey, dotted for the flat potential and dash-dotted for the Milky Way model. For the radial distribution, we take into account mass up to $z = \pm 50$ pc.

4.3.4 Radial Structure

Given the observed changes in the overall morphology of the simulated galaxies (see Fig. 4.2), we now investigate the impact of the gravitational potential on the radial distribution of gas and stars. In the top row of Fig. 4.4, we present the volume-weighted radial distribution of gas (left) and star particles (right), averaged from 2450 to 2550 Myr. We point out that the density distributions only change minimally during phase II. We find the radial distribution to be very similar between the simulations, in both, gas and stars. For gas, we find a relatively flat radial distribution, decreasing from $\sim 10^{-24}$ g cm^{-3} close to the center to $\sim 10^{-25}$ g cm^{-3} at the edge of the disk. From the previous section we know that gas in this density regime is predominately warm ($T \sim 10^4$ K; see Figure 4.3), again illustrating that the volume of the disk is primarily filled by ISM in the warm neutral and warm ionized phase. For star particles, the radial distribution is significantly steeper but again independent from the choice of the potential. We see a steady decline of stellar mass density from the galactic center towards the edge of the galaxy, with a knee in the distribution short of 25 kpc (see also Chapter 5 for a more in-depth analysis of this effect). A noticeable difference between F3000HD and MW3000HD is present at a galactocentric distance of $1 - 3$ kpc, in the gas density as well in the star particles. This is the effect of the stronger star formation in the center of MW3000HD compared to F3000HD, manifesting in a central peak (at < 1 kpc) in the distribution of stars, and a dip in gas and star particle density at ~ 2 kpc, because the galactic center depletes star-forming material from that zone.

Note, however, that the depicted curves do not represent the full stellar population in the simulation boxes, but only those formed during the simulation time. Additional stellar mass is 'hidden' in the external potentials, which consists of the gravity mainly from old stars and DM (which are not simulated explicitly as individual particles). We indicated those with grey curves in Fig 4.4. For MW3000HD (grey dash-dotted curve), the DM component is excluded from the shown potential density distribution, as it would otherwise dominate the density from old stars. As the used potential in F3000HD (grey dotted curve) is a purely analytic potential that does not distinguish between contributions from stars and DM, this is not possible there, and the presented distribution therefore accounts for the full mass density from this potential. The depicted curve therefore follows Equation 2.43 for

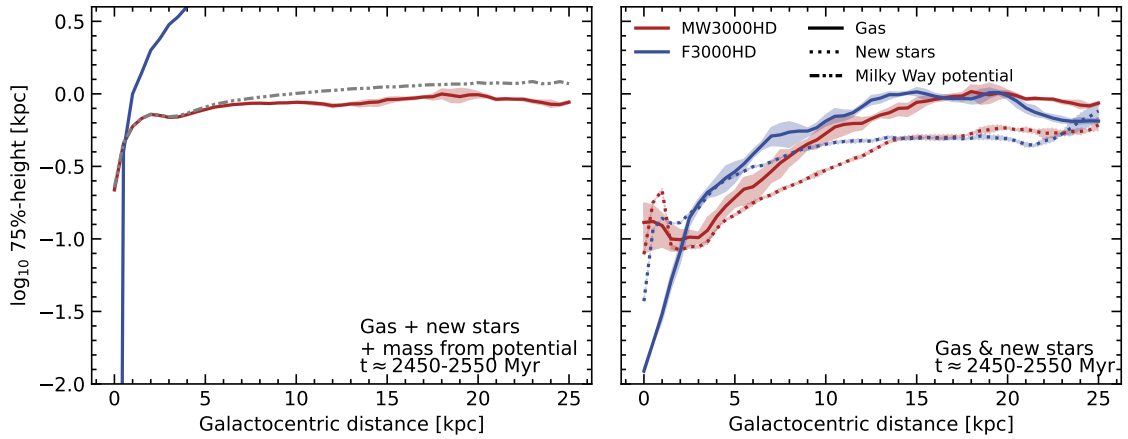

Figure 4.5: Height above and below the galactic midplane containing 75% of the mass at a given radius, for all simulated mass (left), simulated gas and newly formed stars (right) in MW3000HD (red) and F3000HD (blue). In grey we present height for stars in the MW potential, i.e., the underlying, not explicitly simulated mass distribution. Shaded regions indicate 16th to 84th percentile. In both simulations, stars are more concentrated to the disk plane than gas.

$z = 0$ kpc.

From this we conclude that in the Rhea simulation the used galactic gravitational potential has very little influence on the radial distribution of mass, except for the central bar region.

4.3.5 Vertical Structure

In Fig. 4.4, we also present the vertical distribution of gas and star particles (bottom row) at the solar radius, as the external potential is expected to change the vertical equilibrium through the disk, because of the different scale heights of the adopted potentials. However, as for the radial distribution we find little difference in the vertical distribution of gas between the two simulations, even though the potential's contribution differs significantly. This is probably due to the identical set-up of the gaseous disk, which results in identical pressure gradients. As star particles are not sensitive to such pressure gradients, we indeed see a different vertical distribution of star particles between MW3000HD and F3000HD. For MW3000HD, the distribution is narrower, i.e., the star particles are more concentrated towards the galactic plane

than in F3000HD, as one would expect from the form of the used potentials (compare the grey curves, F3000HD again follows Equation 2.43 for $R_{\rm gal} = 8.5$ kpc).

We complete this analysis of mass distribution within the simulated galaxies by an examination of the radial evolution of the vertical distribution. We do so by defining a '75 %-height', which is the height above and below the disk containing 75 % of the disk mass at a given radius. Again, we average from 2450 to 2550 Myr and present the outcome in Fig. 4.5. There we present the 75 %-height for all mass in the simulation, i.e., gas, newly-formed stars and mass in the external potential, in the left panel and indicate the 75 %-height for the MW potential (with DM excluded) in grey. In the right panel we show the 75 %-height for simulated gas and star particles separately.

It is apparent that the mass distribution of the external potential dominates the 75 %-height for F3000HD completely (see left panel). There, we do not show the underlying mass distribution of the external potential explicitly, as it is identical with the general distribution of F3000HD, i.e., the blue curve. This is because, as in Fig. 4.4, in this potential it is not possible to distinguish between DM and old stars, i.e., the shown distribution also contains DM, which is the dominant component here. As DM is fuzzy in nature, it drives the 75 %-height to higher values. For the MW potential we removed the DM component, therefore it shows much lower 75 %-heights. The 75 %-height of MW3000HD is dominated by its potential as well (compare grey dash-dot-dotted curve vs solid red curve) up to about 5 kpc. But at higher galactocentric distances, the simulated mass components decrease the 75 %-height, i.e., they are more closely concentrated towards the galactic plane than the mass which fuels the potential.

In both, star particles and gas (right panel) we see an increase in 75 %-height with galactocentric distance $R_{\rm gal}$ up to 10-15 kpc, with a saturation at higher distances. This saturation 75 %-height for gas is about 1 kpc; for star particles it is at about 0.5 kpc. This is true for both potentials. At $R_{\rm gal} \gtrsim 5$ kpc star particles have generally a lower 75 %-height than gas, i.e., they are confined closer to the galactic midplane than gas, as we already saw in Fig. 4.4. Within about 2 kpc, the 75 %-height of star particles shows an increased bump, which is most probably caused by local turbulence from close interactions of star particles in this region. This bump is less pronounced in F3000HD than in MW3000HD, where it reaches about ~ 0.5 dex in height. This difference is very likely caused by a combination of several

reasons: increased turbulence caused by the rotating bar, higher frequency of star-particle interaction because of more star particles in this region and a lower potential strength there compared to F3000HD.

From Equation 2.16 it is easy to show that the 75 %-height $x_{75\%}$ is about twice the scale height z_d by $\int_{-x_{75\%}}^{x_{75\%}} \rho(\Sigma, z)dz = 0.75 \int_{-\infty}^{\infty} \rho(\Sigma, z)dz$ which results in $x_{75\%} \approx 1.94 z_d$. Therefore, in MW3000HD in gas we find a scale height at the solar radius of ~ 200 pc, and in stars of ~ 120 pc. Observed scale heights of the thin and thick stellar disk of the Milky Way are about 140 pc and 400 pc, respectively (see Bland-Hawthorn & Gerhard, 2016; Vieira et al., 2023, after transfer into our measure of z_d). The scale height of the stellar disk in our simulation falls close to that of the thin stellar disk, as expected as it consists solely of stars formed during the simulation time. It is even slightly lower, however, our simulated galaxy is dynamically young and lacks interaction with satellite galaxies; the stellar disk would probably increase in scale height if run for a longer time. Ferrière (2001) quotes (exponential) scale heights up to 1000 pc (WIM) for Galactic gas (which corresponds to about 900 pc in sech^2). Our found scale height falls well within this limit for both the solar circle as well as at saturation further out in the galaxy.

From this, we conclude the influence of the gravitational potential on the vertical density distribution to be little in gas, but stronger in stars, with the star particles being more centered towards the galactic midplane in MW3000HD than in F3000HD, especially up to about 15 kpc.

4.3.6 Azimuthal Structure

The external potential used in MW3000HD contains two non-axisymmetric components, the bar and the spiral arms. In this section we examine the influence of these components in detail. To do so we inspect the redistribution of gas and star particles in the azimuthal direction at different galactocentric distances.

In Fig. 4.6 we present the azimuthal profile of the gas (top) and stellar (middle) surface density at $3-4$ kpc, $6-7$ kpc and $9-10$ kpc for both conducted simulations. We also show the contribution of the dominant non-axisymmetric external component from the MW potential (bar for $3-4$ kpc, bar and spirals for $6-7$ kpc and spirals for $9-10$ kpc). Since we focus on the changes of surface density of the examined galaxy component (X), rather then its absolute value, we normalize each

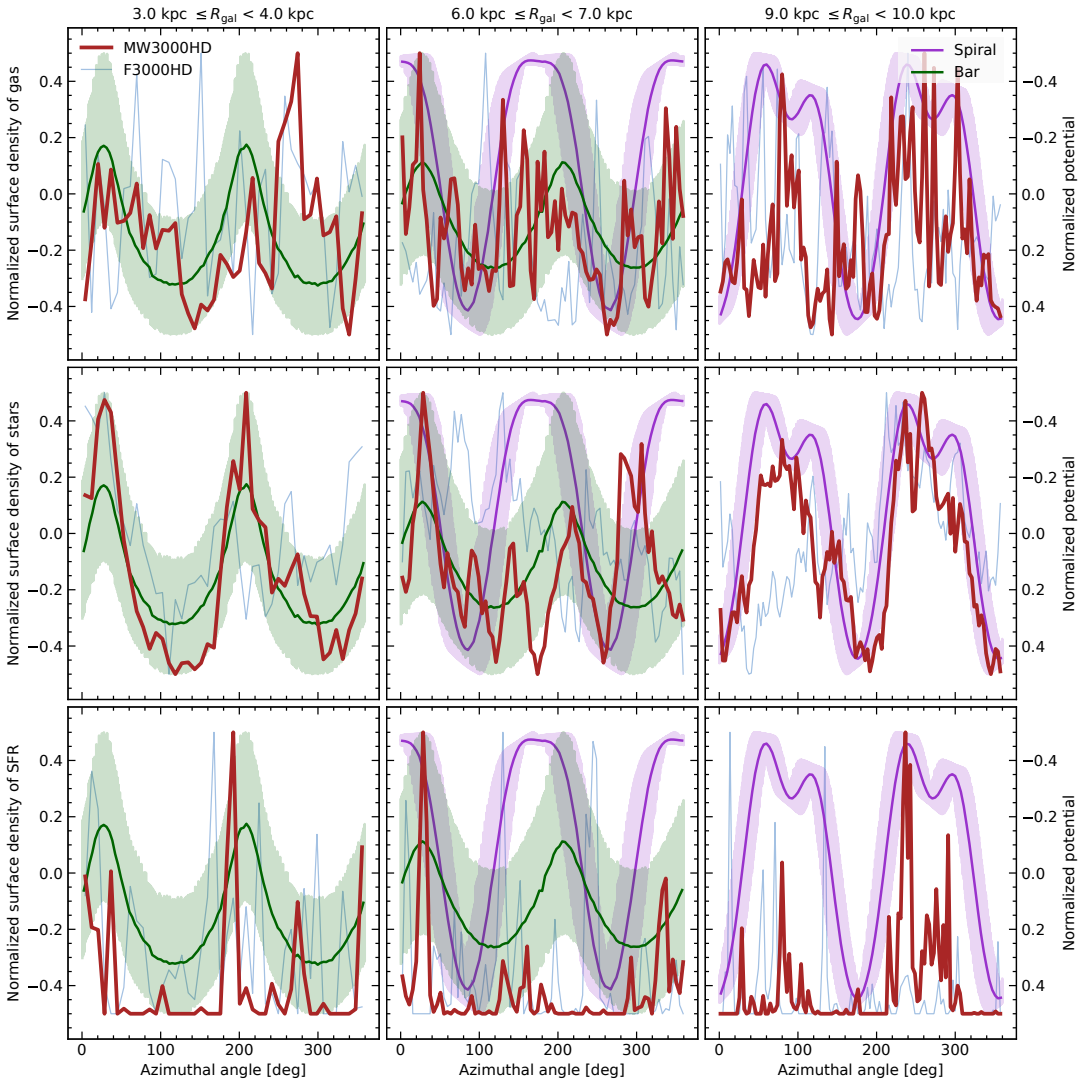

Figure 4.6: Azimuthal profile of the normalized surface density fluctuations of the gas (top), stars (middle) and SFR (bottom) surface densities within $z = \pm 100$ pc at $t \approx 2500$ Myr. We compare with the normalized fluctuations of the contributions of the external non-axisymmetric components of the potential, with the bar (green) and the spirals (pink), associated to the right vertical axis of each panel (in arbitrary units), reversed so that lower values are on top. The values are averaged over a 1 kpc and the shaded area represent the radial variations.

value with

$$\Sigma_{\mathrm{X,norm}} = \frac{\Sigma_{\mathrm{X}} - (\Sigma_{\mathrm{X,max}} + \Sigma_{\mathrm{X,min}})/2}{\Sigma_{\mathrm{X,max}} - \Sigma_{\mathrm{X,min}}}. \tag{4.1}$$

This results in a dimensionless quantity varying between -0.5 and 0.5 that can be easily plotted and compared.

In F3000HD, we find no clear azimuthal structure at any of the examined radii. Instead, the surface densities of gas and stars show arbitrary variations in the azimuthal direction. For the inner region, this is expected, as no clear structure is found there, however, also the self-emerging spiral patterns (which can be clearly seen in Fig. 4.2) do not show up clearly in the surface density variation. Only for the stellar surface density from $9 - 10$ kpc (middle right panel), one might see an azimuthal trend of two distinct overdensities. MW3000HD, on the other hand, at the lowest and highest examined radii shows clear, structured variation in the azimuthal surface density of both gas and star particles, that is well correlated with the potential wells of the dominating non-axisymmetric potential component. The best correlation is found for the star particles, which clearly follow the potential minima of the bar (middle left panel) and the spiral arms (middle right panel). At intermediate galactocentric distances (middle center panel), the contributions of the bar and spiral arms overlap to a large degree, such that none of the components clearly dominated the other. The behavior of the azimuthal surface density profile there is therefore more chaotic, without the clear azimuthal structure present at the other radii.

In general, we find that an elaborate description of the galactic gravitational potential explicitly including non-axisymmetric features changes very little in the radial and vertical density distribution of gas and stars, except for the inner, bar-dominated region. However, in the azimuthal direction the inclusion of the non-axisymmetric potential features cause a reorganization of the galactic components along this direction, in both the inner and outer galactic disk. In the inner disk, this reorganization is driven by the galactic bar and can be clearly seen also in the other analyses performed so far. In the outer disk we find the spiral arm potential to force the redistribution of gas and stars into long-lived spiral features, which are not seen in the purely radial and vertical examination.

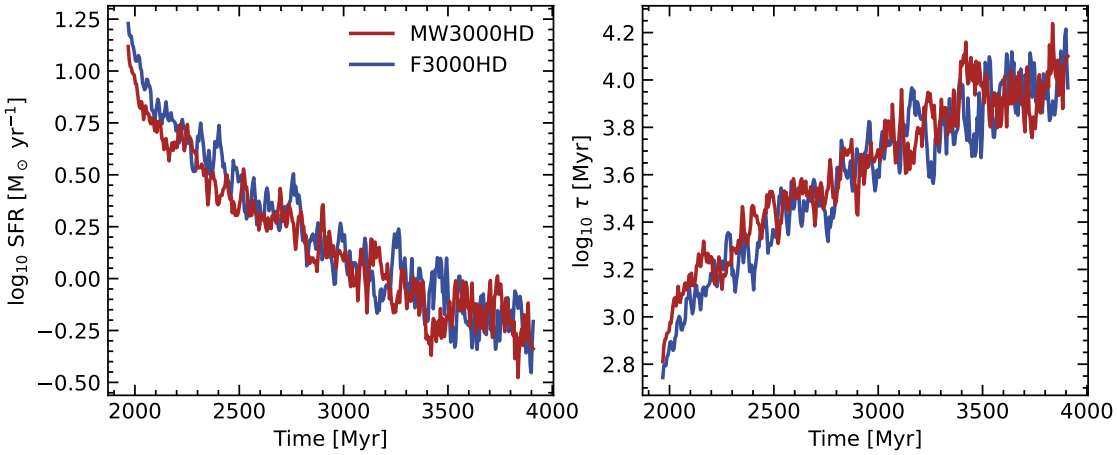

Figure 4.7: SFR (left) and depletion time τ (right) as a function of simulation time for F3000HD (blue) and MW3000HD (red). We limit the measurement to ± 1 kpc around the Galactic plane. A change of the used external gravitational potential does not result in a change of the overall SFR.

4.4 Star Formation and Stellar Feedback

In the previous section we focused on the structure of the gas and stars of the simulated galaxies, analyzing their morphology and distribution and how the galactic gravitational potential affects them. We find small but significant changes, which we expect to be reflected in the location of star formation in the galactic disk, as well as the properties of such star-forming regions. This is the focus of this section. We examine the star formation activity of the simulated galaxies, beginning at a global point of view and subsequently refining in the radial and azimuthal direction. Finally, we study the properties of star-forming regions, e.g., their mass, for how long they exist and what fraction of the total stellar mass is formed in them. We also do the same for the corresponding stellar feedback.

4.4.1 Global SFR is agnostic of Potential

We start this analysis with the global SFR of our simulation, i.e., all stellar mass formed in the galactic disk, as a function of time. Here, we define SFR as

$$\mathrm{SFR}_n = \frac{M_*(t_{n+1}) - M_*(t_n)}{t_{n+1} - t_n}, \tag{4.2}$$

where t_n and t_{n+1} are the times of two consecutive snapshots, and $t_{n+1} - t_n \approx 5\,\mathrm{Myr}$ in our case. We present the SFR alongside the gas depletion time, which we consequently define as

$$\tau = \frac{\overline{M}_{\mathrm{gas}}}{\mathrm{SFR}}, \tag{4.3}$$

where $\overline{M}_{\mathrm{gas}}$ is the arithmetic mean of the gas mass of two consecutive snapshots.

We present the results in Fig. 4.7, with the SFR history in the left panel and the gas depletion time as a function of time in the right panel. The two simulations show very similar global SFRs. We see an initial peak in both simulations, which results from an initial collapse of the disk when mass return from SN is turned off at the end of phase I, and the corresponding additional pressure is eliminated. After that, the SFRs decline constantly with time, which is consistent with the increasing depletion of the simulated gaseous disk by star formation. As we do not simulate any processes replenishing the gaseous disk, this is an expected effect. At our fiducial analysis time of 2500 Myr, we find global SFRs of 2.9 $\mathrm{M}_\odot\,\mathrm{yr}^{-1}$ and 2.6 $\mathrm{M}_\odot\,\mathrm{yr}^{-1}$ for F3000HD and MW3000HD, respectively. Observations mostly suggest a global SFR for the MW of about $1 - 3$ $\mathrm{M}_\odot\,\mathrm{yr}^{-1}$ (see e.g., Chomiuk & Povich, 2011; Licquia & Newman, 2015; Bland-Hawthorn & Gerhard, 2016; Elia et al., 2022, and references therein), which our values fall well within. The global SFR decreases to about 1.5 $\mathrm{M}_\odot\,\mathrm{yr}^{-1}$ (F3000HD), 1.3 $\mathrm{M}_\odot\,\mathrm{yr}^{-1}$ (MW3000HD) at a simulation time of 3000 Myr, after about 3500 Myr the global SFR falls below 1 $\mathrm{M}_\odot\,\mathrm{yr}^{-1}$ for both simulations, and is therefore too low for a Milky Way analog.

Corresponding to the decreasing SFR, the gas depletion time τ increases during the simulation from less than 10^3 to more than 10^4 Myr, again for both simulations. Observationally, the molecular gas depletion time of low redshift main sequence galaxies is found to be between 900 and 2000 Myr (Wang et al., 2022). Our simulations exceed this range after about 2500 Myr, however, since observational depletion times rely only on molecular gas, which we cannot reliably resolve at the resolution run in these simulations (hence we take the full gas mass $\overline{M}_{\mathrm{gas}}$ for the calculation of τ), our *molecular gas* depletion time is lower. Moreover, as stated in the previous paragraph, our decreasing SFR is partially caused by the lack of replenishment of the gaseous disk, again driving the depletion time to higher values.

As a conclusion we find no influence of the used gravitational potential on the

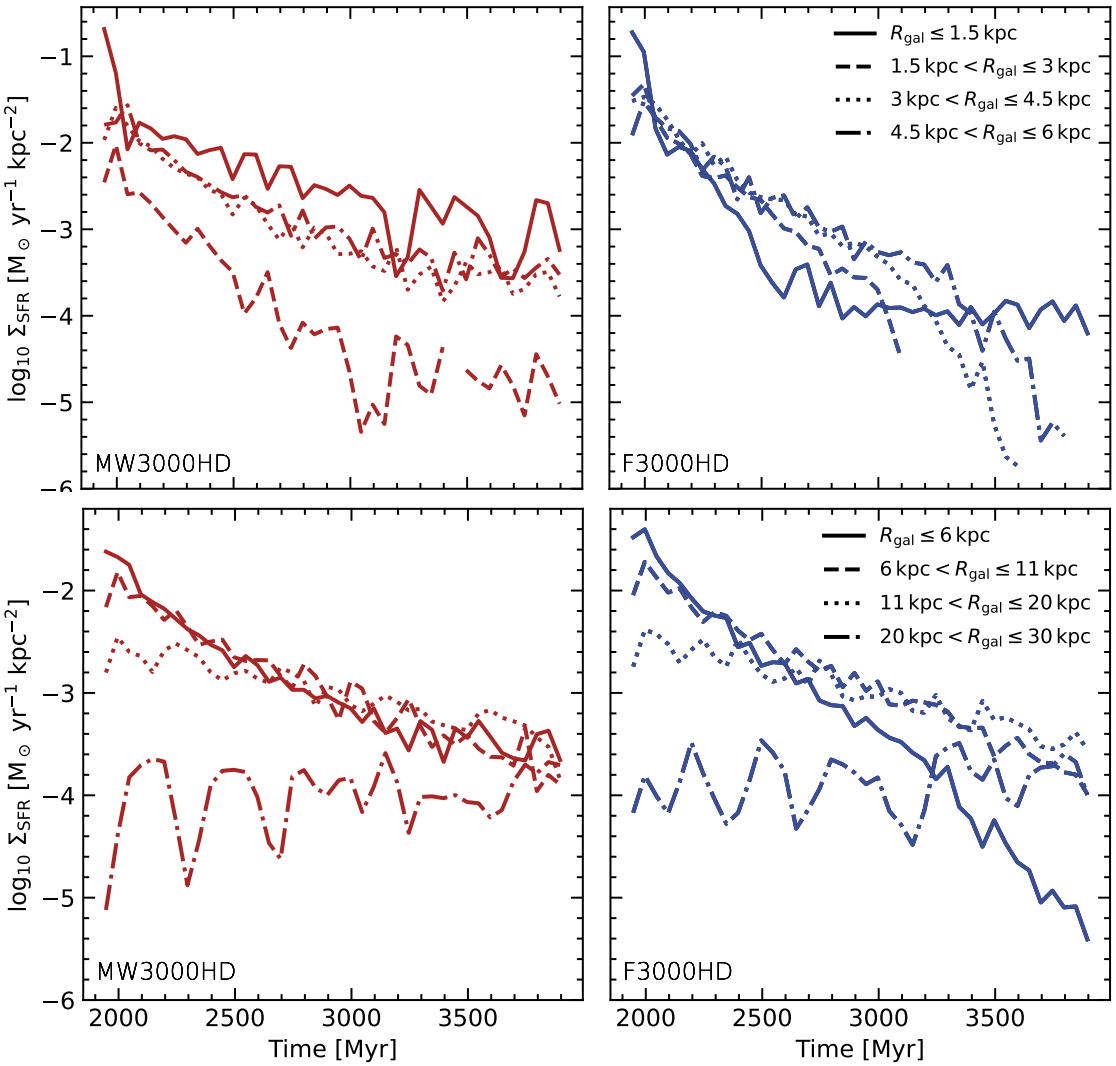

Figure 4.8: SFR surface density in MW3000HD and F3000HD in radial bins for the central ($R_{gal} \leq 6$ kpc) region (top row) and whole disk (bottom row). The introduction of a bar potential prevents quenching in the central galaxy.

global SFR or gas depletion time.

4.4.2 Radial Distribution of Star Formation

Since the global SFR is nearly identical for both potentials, in Fig. 4.8 we show the star formation rate surface density Σ_{SFR} in radial bins for the galactic center (top

row) and the whole disk (bottom row). For all galactocentric distance bins we see a decline in $\Sigma_{\rm SFR}$ over time, except for the outermost 20-30 kpc, which remain at a constant but low $\Sigma_{\rm SFR}$. Comparing between the two simulations (i.e., between left and right columns), $\Sigma_{\rm SFR}$ in different radial bins largely agrees in both the absolute values and their evolution over time. The only exception is the innermost 6 kpc. For F3000HD, $\Sigma_{\rm SFR}$ in this region declines steeply with time and falls below the average values of the rest of the galactic disk after about half the time of phase II. In MW3000HD, the $\Sigma_{\rm SFR}$ in the innermost 6 kpc does not decline to such low levels, but becomes about equal to $\Sigma_{\rm SFR}$ in bins further out in the galactic disk shortly after the beginning of phase II. This, again, is caused by the constant channeling of gas towards the galactic center by the bar potential. This gas is then used for star formation and prevents quenching. For MW3000HD, and also for F3000HD outside of the innermost 6 kpc, that at a given time $\Sigma_{\rm SFR}$ is largely constant throughout the disk, i.e., the curves corresponding to the different radial bins overlap to a large degree (except for the outermost $20-30$ kpc).

Again, we find more differences between the simulations when zooming into the galactic center (top row). For F3000HD, we find the star formation to be mostly evenly distributed throughout the innermost 6 kpc, i.e., the curves of different radial bins overlap to a large degree, and is lowest in the innermost 1.5 kpc (after an initial peak and before the quenching of the distance bins further out). We find a severe drop-off and even complete stop of star formation after about 3000 Myr in the center of this simulation. For MW3000HD, we see a radial change instead: $\Sigma_{\rm SFR}$ is highest in the innermost 1.5 kpc, roughly equal between 3 and 6 kpc, but about ~ 0.5 dex below the innermost bin, and lowest for 1.5 to 3 kpc. The $\Sigma_{\rm SFR}$ in this region between 1.5 and 3 kpc is comparable or even lower than that at $R > 20$ kpc, i.e., this zone is quenched. At $R_{\rm gal} \leq 1.5$ kpc, on the other hand, star formation is not quenched throughout the simulation time, because of the aforementioned channeling of gas mass towards the inner galaxy by the galactic bar potential in MW3000HD.

We therefore conclude that gas streaming due to bar dynamics has a large influence on star formation in the center of the galaxy. To quantify this more, in Fig. 4.9 we present the total mass enclosed (normalized to the initial mass at the beginning of phase II) in a radius of 1.5 kpc, 3 kpc, 4.5 kpc and 6 kpc, i.e., the outer edges of the radial bins used in Fig. 4.8. This shows the strong redistribution of mass in the bar potential. Whereas the different radial bins in F3000HD change their mass by less

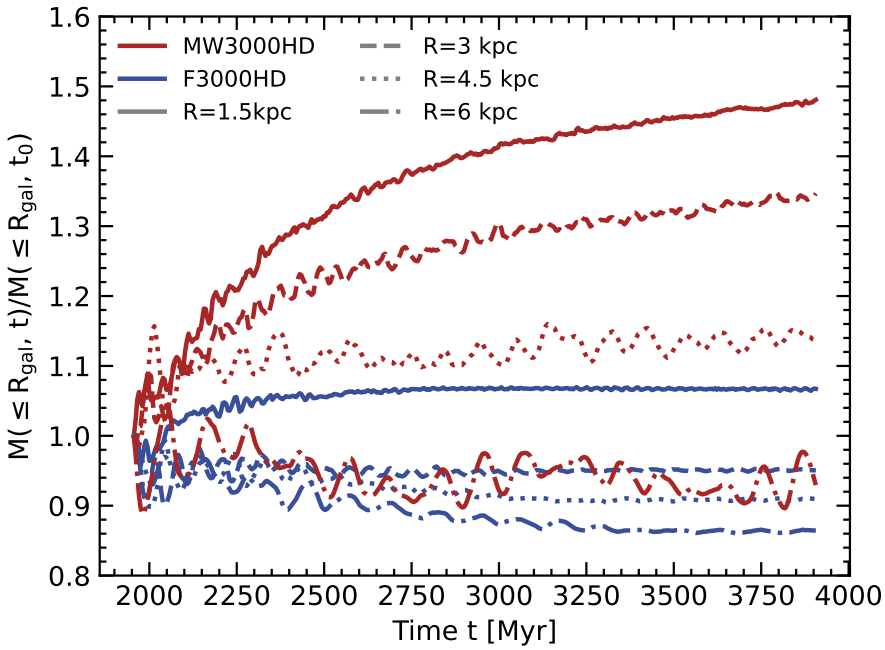

Figure 4.9: Total mass enclosed in 1.5 kpc, 3 kpc, 4.5 kpc and 6 kpc, normalized by the initial mass within this radius at the beginning of phase II at time t_0 for F3000HD (blue) and MW3000HD (red). For MW3000HD we find a strong increase in enclosed mass in the innermost 1.5 kpc.

than 20 % compared to the beginning of phase II, in MW3000HD the mass within the innermost 1.5 kpc increases by nearly 50 %. As the mass within 6 kpc stays roughly constant, this is a redistribution of mass within the galactic center itself (compare the gas depleted region around the bar seen in Fig. 4.2).

As a summary, we can say that we find the introduction of a bar potential to prevent the galactic center from quenching, as it constantly channels gas into the center. In the rest of the disk, outside of the bar-dominated region, we find few changes in the radial distribution of star formation when the gravitational potential is changed.

4.4.3 Azimuthal Distribution of Star Formation

Even though we find few differences in the radial star formation rate profile between different used potentials, we have seen in Section 4.3.6 that the MW potential in MW3000HD has a strong influence on the azimuthal distribution of gas and stars in

the galactic disk. Therefore we conclude this analysis by looking at the azimuthal distribution of the normalized $\Sigma_{\rm SFR}$ fluctuations, which we do in the bottom row of Fig. 4.6. The procedure is the same as explained in Section 4.3.6.

As expected from the previous findings, F3000HD shows no distinct periodicity of $\Sigma_{\rm SFR}$ in azimuthal direction in any of the studied radial bins. In MW3000HD, on the other hand, $\Sigma_{\rm SFR}$ correlates well with the gravitational wells of the dominating non-axisymmetric potential, especially in the spiral-arm-dominated region (see right panel). In these potential minima, SFR is increased. In the region of overlap of non-axisymmetric gravitational patterns (center panel), $\Sigma_{\rm SFR}$ shows no clear correlation with one or the other potential. This is in line with the behavior of gas in this region (top center panel of Fig. 4.6), as star formation is tied to gas being available to it.

To see if this analysis is robust at different times, in Fig. 4.10 we present rotation corrected R-Φ-projection showing the total stellar mass formed in different regions of the galaxy during the simulation time. This figure spans the whole simulation time of phase II, and for MW3000HD (top row) is corrected for the pattern speed of the galactic bar potential (top left) and the spiral arm potential (top center). In the bar region we do not find a clear pattern in where stars form at $R_{\rm gal} \gtrsim 4.5$ kpc, as bar and spiral arm potential begin to overlap in this region. On the other hand, between 1 kpc and 3 kpc star formation happens only in the streams of gas connecting the galactic center with the tips of the bar (they can be seen in Fig. 4.2). At their tips we find zones of high star formation (see contour lines), but most star formation happens in a circular region at Rgal $\lesssim$ 1 kpc. In the disk region of MW3000HD (top center panel) we cross out the interarm regions, to indicate the location of spiral arms. To do so, we define spiral arms as regions where the non-axisymmetric spiral arm potential is lower than 0 m^2 s^{-2}. Again, we find star formation to preferentially occur within the spiral arms (as seen in Fig. 4.6). At galactocentric distances $>$ 14 kpc we find star-forming regions to get out of sync with the spiral arm potential, as the rotation speed of the gas at this distances falls below the pattern speed of the spiral arms (compare Fig. 5.8 in next chapter). It is also apparent that this spiral arm potential enforces long-lived spiral patterns, as otherwise no clear spiral structure would emerge when plotting all formed stellar mass over the whole simulation time in such a projection. We quantify this finding by showing the mass fraction of star particles formed within spiral arms (with the aforementioned definition) as a function of galactocentric distance (top right). For

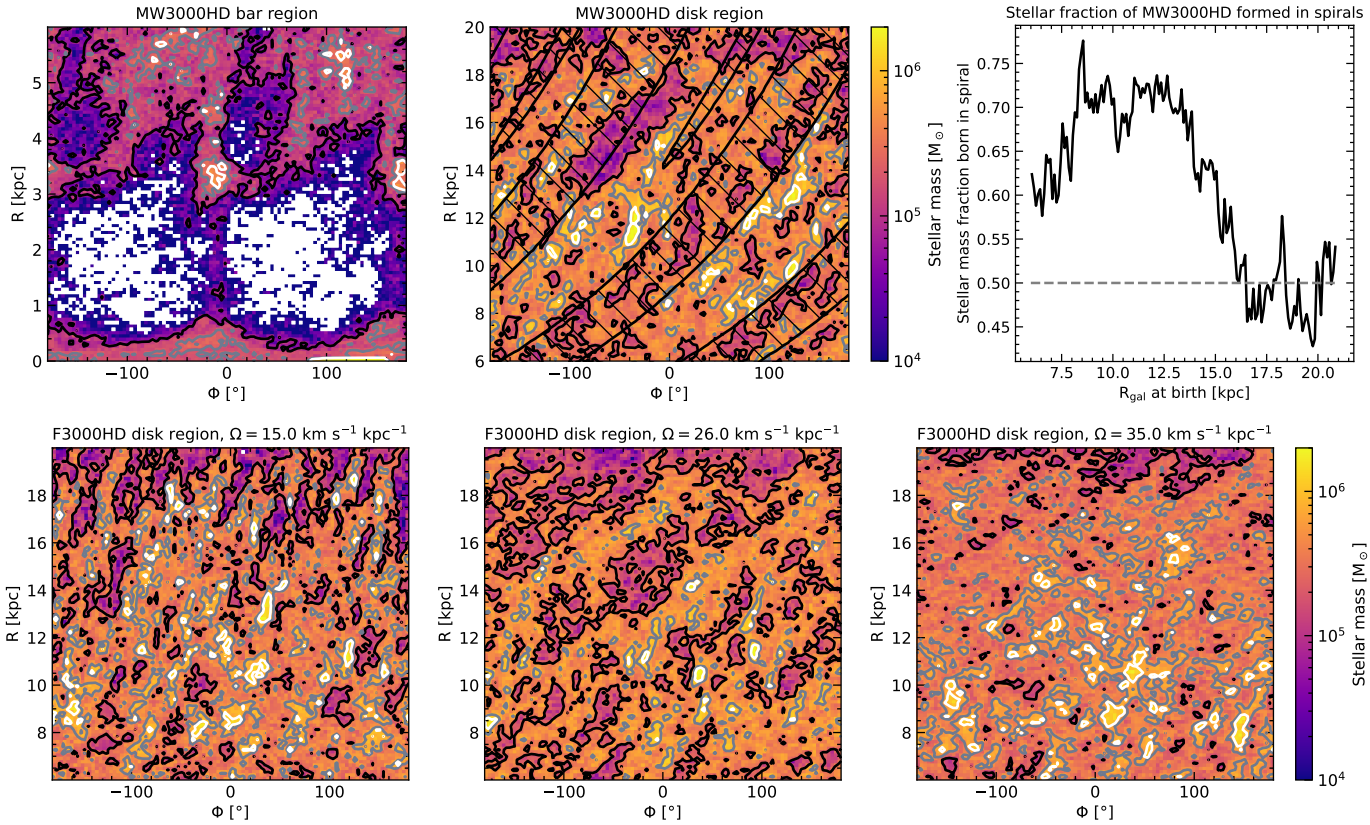

Figure 4.10: Stellar mass formed in a R_{gal}-Φ-projection for MW3000HD in the bar region ($R_{\mathrm{gal}} < 6$ kpc, top-left panel) and the disk region ($6\,\mathrm{kpc} \leq R_{\mathrm{gal}} < 20$ kpc, top-middle panel, interarm regions are shaded out), corrected for the corresponding pattern rotation of bar and spirals, as well as the stellar mass fraction formed in spirals (top-right panel). We also show the stellar mass formed in the disk region of F3000HD in a R_{gal}-Φ-projection, corrected for different pattern speeds, $\Omega = 15.0$, 26.0 and 35.0 km s^{-1} kpc^{-1} (bottom row, from left to right). Contour lines in projection plots indicate 10 %, 30 % and 50 % of maximum stellar mass formed (excluding the region of extremely high formed stellar mass at < 0.1 kpc for MW3000HD bar region, upper left).

galactocentric distances $6\,\mathrm{kpc} \leq R_{\mathrm{gal}} \leq 16$ kpc, more than 50 % of all formed stellar mass is born in spiral arms, with a peak of 70-75 % between 9 and 14 kpc. At distances larger than 14 kpc, the mass fraction formed in spiral arms shows a steep decrease and reaches an equal distribution between spirals and interarm region at about 16 kpc. This reinforces our interpretation of the projection in the top center panel. Of all stars formed beyond 6 kpc in MW3000HD, a total of about 62 % are

formed in spiral arms.

For the disk of F3000HD (lower row of Fig. 4.10) we cannot find similar long-lived spiral features. We do see the emergence of spiral structures in this simulation as well (see Fig. 4.2), but they are more short-lived. To show this, we present a series of R-Φ-projections like for MW3000HD, corrected for different pattern speeds from 15 to 35.0 km s^{-1} kpc^{-1} in steps of 0.5 km s^{-1} kpc^{-1}, and show three examples($\Omega =$ 15, 26 and 35 km s^{-1} kpc^{-1}). We do not find a coherent spiral pattern for any of the tested pattern speeds. The R-Φ-projections of recently-formed stellar mass that best resembles that of the spirals in MW3000HD is found for a correction of 26.0 km s^{-1} kpc^{-1}, but even there we do not find regions as pronounced and contiguous as for MW3000HD. For any other pattern speed we do not see any structure emerging at all (see the R-Φ-projections of $\Omega = 15$ and 35 km s^{-1} kpc^{-1}).

In Section 3.3.3 we found the global SFR of the simulated galaxies to be unaffected by the used gravitational potential, but found in Section 4.4.2 and 4.4.3 the potential to influence *where* stars from, i.e., the potential influences the local SFR, but not the SFE. This is in line with former work on both, simulational and observational basis. Kim et al. (2020) found star formation to preferentially occur in their simulated spirals, as the gas is denser in this regions, but the SFE was not enhanced. Observational comparisons of the SFE in spiral arms and interarm regions of the Milky Way (Ragan et al., 2018) and other nearby galaxies (Sun et al., 2023; Querejeta et al., 2024) find little or no systematic effects as well.

4.4.4 Clustering of Star Formation

We now end this analysis by studying the clustering behavior of newly formed stars in the different potentials, i.e., if the used potential influences the local star-forming regions, by clustering star particles according to their birth position and birth time using HDBSCAN (see Section 4.2.2 for details of the method). We present our findings in Fig. 4.11. From left to right we select different radial ranges: $R_{\rm gal} \leq 2.5\,$kpc (left), $R_{\rm gal} \leq 5\,$kpc (middle), $R_{\rm gal} > 5\,$kpc (right). Again, we show our outcomes for both simulations, MW3000HD (red) and F3000HD (blue).

As mentioned in Section 4.2.2, the distribution of numbers of group members is very similar between the two simulations, which is directly reflected in the distribution of the group mass (top row), as the star particles of our simulations have

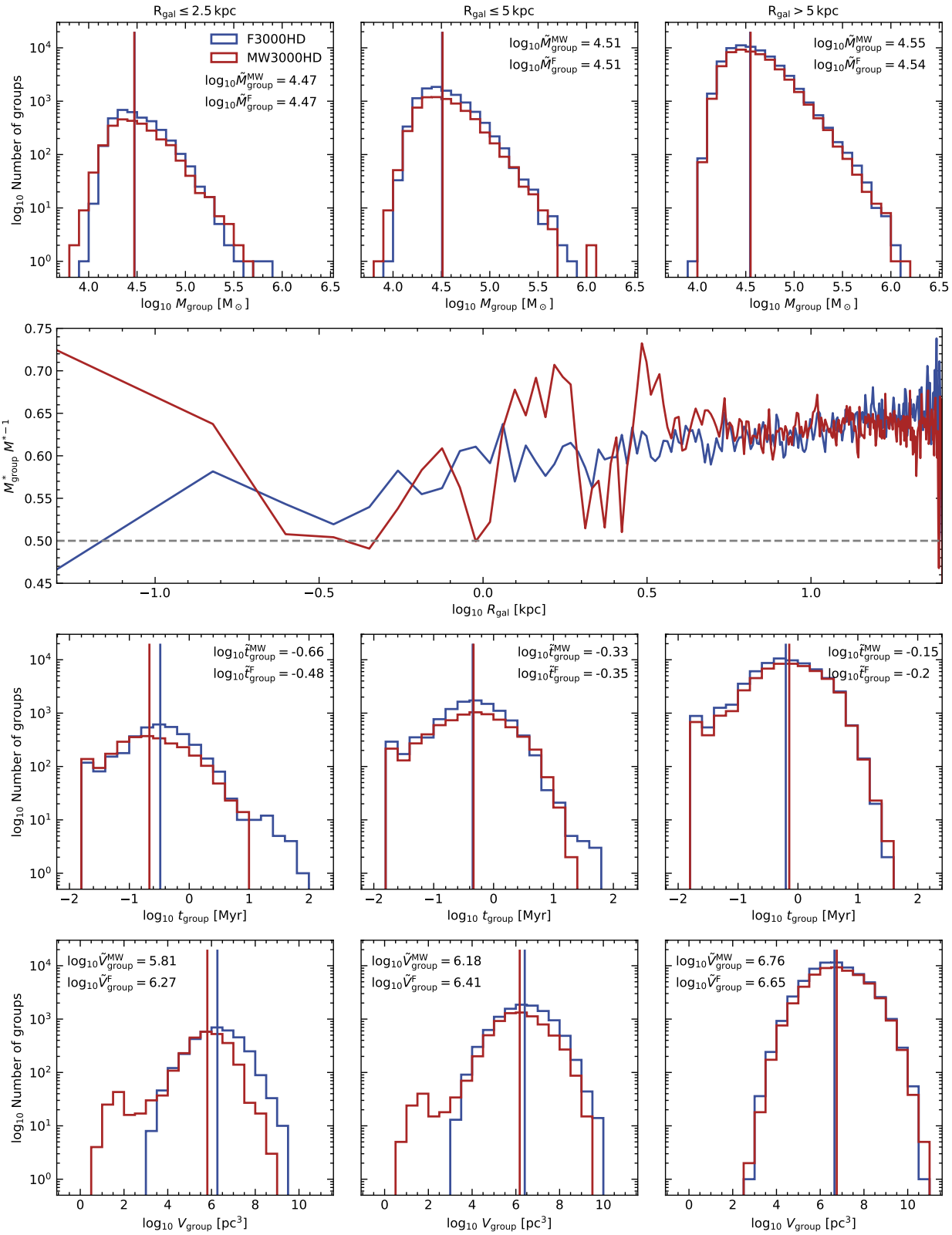

Figure 4.11: Grouped star formation: Mass of group (first row), mass fraction of stars born in groups (second row), activity time (third row) and extend of groups (fourth row) for F3000HD (blue) and MW3000HD (red) in Galactic center ($\leq$ 2.5 kpc, left column), inner region ($\leq$ 5 kpc, middle column) and disk ($>$ 5 kpc, right column). Vertical lines indicate median values, which are written out at the upper left or right.

little spread in mass. The distributions of group mass are therefore very similar between the simulations, ranging from about 10^4 to 10^6 $M_\odot$, with a median at about $10^{4.5}$ Msun and a tail towards higher masses in both simulations.

We also show the fraction of formed stellar mass born in identified groups $M^*_{\rm group}/M^*$ as a function of galactocentric distance (second row). For the galactic disk region at $R_{\rm gal} > 5$ kpc ($\approx 10^{0.7}$ kpc) this fraction is about the same for both simulations, ranging around 65 % without noticeable trends in galactocentric distance. In this region, MW3000HD does not show enhanced grouping, as one might expect from the concentration of star formation in the spiral arms. At $R_{\rm gal} < 5$ kpc, on the other hand, for F3000HD we find the fraction of stellar mass formed in groups increasing with galactocentric distance, from about 50 % in the very center to the aforementioned 65 %. For MW3000HD, no such trend is present, instead we find large fluctuations between ∼50 % to ∼70 % of star particles being formed in groups. This is probably because of stirring from the galactic bar potential.

In the third row of Fig. 4.11 we present the distribution of activity time $t_{\rm group}$ of the groups, i.e., the difference between the birth time of the first and last star particle of the group. This value represents the time over which a star-forming region is actively producing star particles. We group star-forming regions with activity times lower than the global timestep together in the lowest bin. In the galactic center ($R_{\rm gal} \leq 2.5$ kpc), the used gravitational potential changes the activity time. There, the median activity time of star-forming regions is about 0.2 dex lower than in F3000HD, whose distribution has a tail towards longer activity times. This, again, is caused by the bar potential which stirs the gas in this region, making it harder to form long-living conglomerates of overdense gas cells forming stars. The median activity time also increases with galactocentric distance in both simulations, i.e., star-forming regions persist for longer in the galactic disk than in the center, again supporting our point.

Another effect of the bar potential is the prevalence of smaller groups in the center of MW3000HD compared to F3000HD. We show this in the bottom row of Fig. 4.11. By 'smaller', we here mean a lower occupied volume $V_{\rm group} = (\max(x) - \min(x))\,(\max(y) - \min(y))(\max(z) - \min(z))$ (compared to a dynamical range of 10 orders of magnitude, the actual measure of the occupied volume, be it cuboid, spherical or a convex hull, is negligible). We find the median extent of star-forming regions in the galactic center ($R_{\rm gal} \leq 2.5$ kpc) to be about

0.5 dex lower than in F3000HD, with a tail to lower volumes. Such a difference is not present in the galactic disk ($R_{\rm gal} > 5$ kpc), again pointing towards the bar potential as the cause. This rotating potential stirs the gas, breaking up larger contiguous star-forming regions into smaller ones. In the disk, median extents of star-forming regions are up to 1 dex larger than in the center, showing that this process only takes place in the bar region. In the less turbulent environment of the galactic disk, star-forming regions can grow to larger sizes.

We therefore, again, find the difference between the used gravitational potentials to affect the star formation most in the bar-dominated region, especially in the very center. There, groups of stars are more compact (but not less massive) and form faster in MW3000HD than in F3000HD. Outside of this region, star-forming regions show remarkably similar statistical properties, i.e., are nearly unaffected by the used gravitational potential.

4.4.5 Clustering of Supernova Feedback

When star particles from from gas, they decouple from the hydrodynamic flow and just follow gravitational forces. Therefore the impact of the gravitational potential on their dynamics increases compared to the gas. Stellar feedback, as it is just tied to the dynamics of star particles, is thus an interesting probe of the effect of the galactic potential. Moreover, clustered explosions of SNe have a substantial impact on their environment, as described in Section 1.3.3 and 4.1.

We therefore perform the clustering analysis on SN explosions as well. Since the number of exploding SN is much higher than that of star particles (as each star particles can hold several massive stars that explode during its lifetime), we can perform this analysis for SN only for a limited time, and not for the whole simulation time as we did in Section 4.4.4 for star particles. As analysis time we choose our fiducial time of 2450-2550 Myr and present our findings in Fig. 4.12.

We find the number distribution of SN group members (top row) being very similar to that of star particles, with a median of 10 SN per SN group. However, some groups contain hundreds or even thousands of SN. We cannot find a clear difference in number distribution between the used gravitational potentials, in both simulations the found SN groups have about the same number of members.

However, while for star particles we find more than 50 % of the stellar mass to

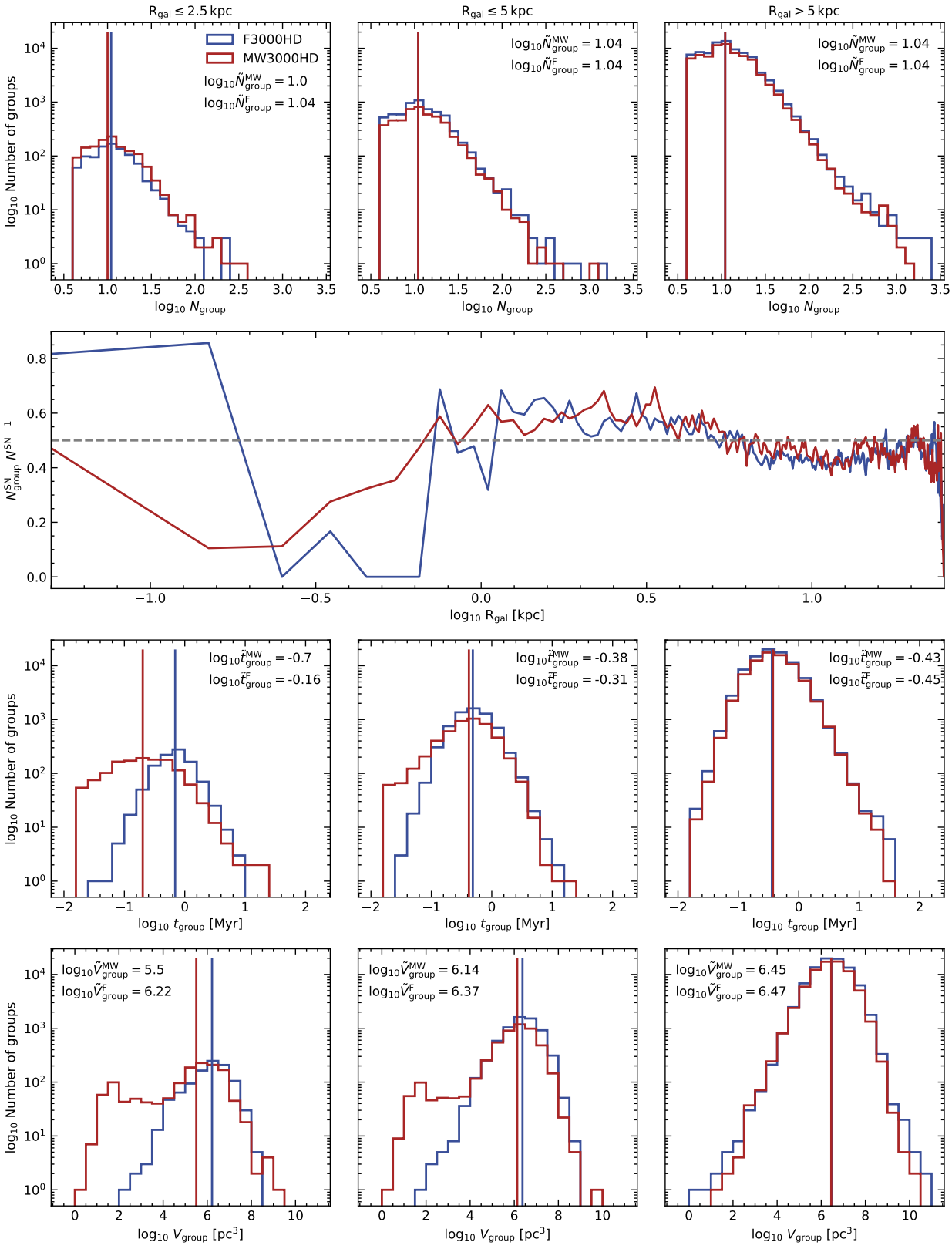

Figure 4.12: Number of SN group members (top row), number fraction of SN in groups (second row), activity time (third row) and extend of groups (last row) for F3000HD and MW3000HD for t=2450-2550 Myr. Vertical lines indicate median values.

be formed in groups of newly formed stars throughout the whole disk and center, this is not the case for SN. The number fraction of SN exploding in groups of SN explosions (second row) is very volatile and ranges from 0 % to about 60 %. In the innermost 1 kpc, the number fraction of SNe in groups is lower in MW3000HD than in F3000HD (for this small radius we were able to check grouping for a longer timespan than 100 Myr, giving a clearer result, but we show data for the selected timespan here for consistency). Between 1 kpc and about 5 kpc ($\approx 10^{0.7}$ kpc), on the other hand, it is steadily at about 60 %, interestingly again for both simulations, i.e., we do not see a clear impact of the bar potential. Further out ($R_{\rm gal} > 5$ kpc), the number fraction falls below 50 % (where it is about 65 % for stars formed). This suggests that groups of stars are broken up in between the formation of its stars and the explosion times of SN.

Consistent with our findings for star particles, the activity time of SN groups (i.e., the time difference between the first and last explosion of a SNe in this group with treatment analog to that of star particle clustering, third row) in the galactic center is ~ 0.54 dex shorter than in MW3000HD, but does not differ between simulations at radii > 5 kpc. In the disk region, we find the median activity time of SN groups to be $0.2 - 0.3$ dex lower that of star-forming regions (see Fig. 4.11). This, again, indicates a break up of groups of young stars formed together in between their time of birth and the time of their SN explosion.

We also find SN groups in the galactic center to have a ~ 0.7 dex lower median extent in MW3000HD than in F3000HD. The size distribution of SN groups in MW3000HD shows a similar and even stronger bimodal pattern than in the star particles, i.e., many groups of SN in the galactic center ($R_{\rm gal} < 2.5$ kpc) of MW3000HD are more compact than those found in F3000HD, but host the same number of SN explosions (compare first row). We do not find such differences at $R_{\rm gal} > 5$ kpc. In general, the sizes of SN groups are slightly lower than that of star particle formation groups (compare Fig. 4.11).

With this, we find the largest differences in the grouping of SNe induced by the gravitational potential again induced by the non-axisymmetric bar component. The bar makes SN groups more compact and less long-lived, i.e., the time difference between the first and last SN in the group is shorter in a galactic center dominated by a bar potential than without one.

4.5 Caveats

As simulations always include simplifications of processes too complex to be treated in detail, outcomes have to be interpreted carefully. The Rhea simulations are no exception of this rule.

When we show the global SFRs of our simulated galaxies, they decline over time. We do not account for gas accretion from the CGM onto the disk, in order to study the prevailing physical processes in our simulations in detail. Therefore, the only gas accretion on the galactic disk is gas previously ejected from it. As no fresh supply of gas is present, the gas in the simulation is continuously depleted by conversion into star particles. This, in parts, is a desired result, but also results in a limited time during which the simulated galaxies can be directly compared to the Milky Way before the lack of gas leads to a SFR below the Milky Way limit of 1 $M_\odot$ yr^{-1}.

The approach to simulate our galaxies as isolated galaxies also includes a lack of satellites. As mentioned in Section 1.3.5, the Milky way is accompanied by multiple smaller satellite galaxies, with the Large and Small Magellanic Cloud being the largest ones. However, these satellites influence the dynamics (see e.g., Correa Magnus & Vasiliev, 2022) and evolutionary history (e.g., Sotillo-Ramos et al., 2022; Malhan et al., 2022) of the Galaxy. Past mergers are still present in today's Galaxy as stellar streams or globular clusters. We do not take into account this additional detail of the Milky Ways dynamics.

Moreover, we ignore pre-supernova feedback such as photoionization and stellar winds from our simulated stars. The addition of these processes will alter the ISM structure, by increasing the amount of ionized gas, and the effectiveness of SN. We therefore plan to include them in future iterations of the Rhea simulations.

By focusing on the hydrodynamic runs in this chapter, we also omit the influence of magnetic fields on the galaxy structure. These have significant impact on the galaxy morphology (see Fig. 1.11), however, we exclude them from this work for conciseness. Work accompanying this one (Kjellgren et al., 2025, Girichidis et al., in prep.) study the Rhea simulations including magnetic field and also cosmic rays, which carry a significant amount of energy in the energy budget of the Galaxy as well (see Section 1.3.2).

4.6 Conclusion

In this chapter we introduced the hydrodynamical runs of the Rhea simulation suite, a set of Milky Way simulations with a varying external potential. We study the influence of the details of this external potential on the morphology, star formation and corresponding stellar feedback. We do so by comparing a detailed potential tuned to recreate several observational features of the Milky Way with a potenital resulting in a flat rotation curve.

We find that the introduction of a non-axisymmetric bar potential has the greatest influence on both galactic morphology and the location of star formation, as it ensures continuous fueling of the center of the galaxy. This prevents the center from quenching, the bar potential moreover makes star-forming regions more compact and short-lived. When an explicit spiral arm potential is used, star formation is favored in the gravitational wells of this potential, as it collects gas and stars. Otherwise this addition to the potential has little impact.

Our detailed findings are:

- Both conducted simulations show spiral arms and a feedback-driven bubble structure, i.e., the chosen potential influences the overall morphology very little besides the central bar structure, which only emerges when a barred potential is imposed. Since the bar potential channels gas into the center, star formation is higher there compared to a non-barred potential, which is reflected in the presence of SN bubbles also in the galactic center.

- A varying potential changes the radial distribution of stars and gas only marginally. In the bar region, the vertical spread is higher than in a non-barred potential in stars and gas.

- The global SFR is unaffected by the chosen potential, however, star formation is redistributed within the disk. With a barred potential, the SFR is highest in the innermost 1.5 kpc. In the disk region, when an explicit spiral arm potential is adopted, stars preferentially form in the potential wells of this potential, as gas density is higher there. Approximately 60 % of stars outside the bar region form within the potential of the spiral arms. With a completely axisymmetric potential, no such pattern is found and no long-lived star-forming spirals form.

- In both simulations, star particles preferentially form in groups with other star particles. A bar potential makes these groups of newly formed stars more compact and lowers the timespan between the first and last star of the group being formed. This can most likely be attributed to the fact that the rotating bar potential stirs the gas in the center, breaking up contiguous star-forming regions.

- In the galactic disk, most SN explode in isolation. In the innermost 5 kpc more SN explode in identified groups then alone, and the inclusion of a bar potential lowers the size and activity time of such groups compared to a non-barred potential.

We therefore find the largest differences between the simulations with different potentials to be induced by the non-axisymmetric bar potential. We find the bar potential to be substantial for the proper simulation of the galactic center within 5-6 kpc, in order to reach a Milky Way like morphology and an accurate distribution of star formation and stellar feedback. The inclusion of a spiral arm potential only has an impact on the organization of stars, gas and the corresponding star formation into long-lived spirals. Spiral arms, however, also form self-consistently from gas instabilities without such a potential. In that case, they are less long-lived than when enforced by a potential. We therefore conclude that if one just wishes to reproduce the overall star formation properties of a Milky Way like galaxy, and is more focused on the general disk region than the galactic center, the use of a simplified purely axisymmetric potential is sufficient. To simulate a proper galactic center, the inclusion of a barred potential is essential. An explicit spiral arm potential is just needed if long-lived spiral structures are desired.

5 Stellar Orbits and their Influence on the Galactic Rotation Curve in Rhea

In the last chapter we characterized the hydrodynamical runs of the Rhea simulation and had a look into how the galactic potential influences the star formation in the simulated galaxies. We now want to further study the effects the star formation and potential has on the stellar orbits and how those affect observables like the rotation curve of the galaxy.

Abstract

Stars move around the Galactic center on orbits tracing the gravitational potential. The resulting circular velocity can be measured in rotation curves and used to estimate the mass of the Galactic system. In this chapter, however, we will show that the distribution of ellipticities in stellar orbits influence the measured stellar rotation curve and can result in a decline in the outskirts of the Galactic stellar disk. We closely analyze how the properties of the star-forming disk influence the stellar orbits in the disk, and how these orbits in turn change the resulting rotation curve and derived Galactic mass. We find that from the outer star-forming disk, star particles on elliptical orbits regularly migrate outwards, making the stellar disk extend beyond the edges of the star-forming disk and forming a region dominated by migrating star particles. This leads to a stellar disk with a broken exponential density distribution, that cannot be modeled by a single exponential. If this is not accounted for, this can result in a kink in the rotation curve that can be misinterpreted as a cut-off in the Galactic mass distribution and a resulting Keplerian decline, which was recently found in stellar rotation curves of the Milky Way.

5.1 Introduction

As one of the few local galaxies where individual stars can be resolved, the MW poses the unique chance for direct observations of physical processes shaping spiral galaxies in the Universe. In the era of Gaia (Gaia Collaboration et al., 2023), we now know about positions and dynamics of stars of our Galaxy with unprecedented accuracy. This allows for detailed analysis of stellar dynamical processes resulting in observed properties of the Galaxy, such as the age-metallicity distribution (see e.g., Feuillet et al., 2019) or the Galactic rotation curve.

The circular velocity curve of a galaxy

$$V_{\mathrm{circ}}^2(R_{\mathrm{gal}}) = R_{\mathrm{gal}} \frac{\partial \Phi}{\partial R_{\mathrm{gal}}}\bigg|_{z\approx 0} \tag{5.1}$$

represents the velocity V_{circ} that an object on a circular orbit around the galactic center would have at a given galactocentric distance R_{gal}. This depends only on the potential Φ of a galaxy and is therefore an important measure for the enclosed galaxy mass and a primary indication for the existence and distribution of DM (Rubin et al., 1980; Persic et al., 1996). The MW's rotation curve, therefore was measured with various different methods and tracers. In gas, HI and CO lines can be used (Gunn et al., 1979; Fich et al., 1989; Levine et al., 2008; Sofue et al., 2009). Stellar tracers like Cepheids (Pont et al., 1997; Mróz et al., 2019), red giant branch and red clump stars (Bovy et al., 2012; Huang et al., 2016; Eilers et al., 2019; Zhou et al., 2023), RR Lyrae stars (Ablimit & Zhao, 2017; Wegg et al., 2019) and blue horizontal branch stars (Xue et al., 2009; Kafle et al., 2012) were used recently to constrain the rotation curve outside of the solar radius. Many rotation curves measured for the MW agree with the Galactic virial mass derived from other observables, such as globular clusters and satellite galaxies (Callingham et al., 2019; Eadie & Jurić, 2019; Posti & Helmi, 2019; Watkins et al., 2019), to be of the order of 10^{12} $\mathrm{M}_\odot$.

Lately, works constructing the Galactic rotation curve from Gaia data beyond 20 kpc (Eilers et al., 2019; Wang et al., 2023; Ou et al., 2024; Jiao et al., 2023) result in virial masses up to an order of magnitudes lower than this. The found rotation curves are gently declining outside of the bar dominated region (which was also found by Mróz et al., 2019), which is rarely seen in rotation curves of other

disk galaxies (compare e.g., Noordermeer et al., 2007; Dicaire et al., 2008; Zobnina & Zasov, 2020), which tend to have flat (e.g., Sofue et al., 2009) or even increasing (e.g., Rubin et al., 1980) rotation curves. However, the rotation curves of external galaxies are constructed from gaseous and dust components, which behave differently from stellar tracers, as we will show in this chapter. Moreover, the rotation curves by Eilers et al. (2019), Wang et al. (2023) and Ou et al. (2024) show a stronger decline at $R_{\rm gal} > 19$ kpc (> 20 kpc for Ou et al., 2024), which Jiao et al. (2023) identifies as a Keplerian decline indicating a cut-off in the Galactic mass distribution.

Galactic orbits of stars, however, are not necessarily purely circular, but can follow complex, non-closed orbits, as is seen in simulations (e.g., Röttgers et al., 2014). The effect of this on observational derivations of rotation curves is accounted for by asymmetric drift corrections (Binney & Tremaine, 2008), which include assumptions about the density distribution of the used tracers. This is usually assumed to follow a single exponential profile (e.g., Eilers et al., 2019; Wang et al., 2023; Zhou et al., 2023; Jiao et al., 2023; Ou et al., 2024).

On Galactic scales, stars can also radially migrate significantly (Sellwood & Binney, 2002; Roškar et al., 2008). Depending on whether this migration results in a change of the stars guiding radius or if the galactocentric distance is simply oscillating around the guiding radius, this is called churning or blurring, respectively (Sellwood & Binney, 2002; Daniel et al., 2019). Unambiguous observational evidence for this process is limited because the associated timescales are of the order of the Galactic rotational period. However, it is argued that the radial mixing of stars formed at different galactocentric distance will imprint on the age-metallicity distribution of stellar populations at a single present-day radius (Grand et al., 2015; Lian et al., 2022). Because of this migration, regions of a galaxy where no stars are born can be populated by those migrators, resulting in areas only populated by stars not native to them. Models of this migration in the Milky Way suggest that the outer stellar disk (beyond 15 kpc) might be populated solely by stars that migrated to this region (Lian et al., 2022).

In the Rhea hydrodynamical Milky-Way simulations (Göller et al., 2025), we can directly observe this effect, which in the simulation results in a broken exponential density distribution of the simulated stellar disk. This, in turn, severely affects the galactic rotation curve retrieved from the simulation, if not accounted for in the asymmetric drift corrections. We hypothesize that this effect could explain the found

decline in the stellar rotation curve found in observations of the extreme outskirts of the Milky Way.

This chapter is structured as follows: We first present the simulation framework and adopted definitions (Section 5.2). We then compare the star formation rate (SFR) surface density and stellar surface density in our simulations to that of observations (Section 5.3.1) and show how migrating stars influence the orbital properties in the outer disk (Section 5.3.2 and 5.3.3). Finally, we derive the azimuthal velocity and rotation curves from the stellar disk, and show how they are influenced by the changing stellar population in the galactic outskirts (Section 5.3.4). We discuss our findings with respect to observations in Section 5.4 and summarize it in Section 5.5.

5.2 Methods

5.2.1 The Simulations

In this chapter we use the same hydrodynamical simulations as in Chapter 4, namely F3000HD and MW3000HD, initialized as described in Section 2.3.8. However, we note that the initial density distribution (Equation 2.16) differs from observation in the Galactic outskirts, where the decline in density is steeper than modeled in our initial conditions. We therefore include an additional simulation, MW3000HD-moddens, with a modified initial density distribution of

$$\rho_{\rm gal}\left(R_{\rm gal}, z\right) = \frac{\Sigma_0}{4z_{\rm d}} \frac{\exp\left(-\frac{R_{\rm m}}{R_{\rm gal}} - \frac{R_{\rm gal}}{R_{\rm d}}\right)}{\exp\left(\frac{R_{\rm gal}-R_{\rm break}}{R_0}\right)+1} \mathrm{sech}^2\left(\frac{z}{2z_{\rm d}}\right) \ , \tag{5.2}$$

where we set $z_{\rm d} = 85\,{\rm pc}$, $R_{\rm d} = 9\,{\rm kpc}$, $R_{\rm m} = 1.5\,{\rm kpc}$, $\Sigma_0 = 50\,{\rm M_\odot\,pc^{-2}}$, $R_{\rm break} = 15\,{\rm kpc}$ and $R_0 = 5.5\,{\rm kpc}$. This introduces a decline in gas density (and subsequently in star formation) for $R_{\rm gal} \gtrsim 15$ kpc, compared to the fiducial case, and provides a better fit to the observed densities reported by Kalberla & Kerp (2009). We summarize the used simulations in Table 5.1.

5.2.2 Migrating Star Particles

Throughout this chapter we divide the stellar population of our simulations into migrating and non migrating star particles. We define migrating star particles (called

	Potential	Density distribution
F3000HD	flat	Eq. 2.16
MW3000HD	MW	Eq. 2.16
MW3000HD-moddens	MW	Eq. 5.2

Table 5.1: List of used simulations with the corresponding potentials and density distributions used.

'migrators' in the following) as star particles, whose galactocentric distance differs from the galactocentric distance they are formed at by more than 5 kpc at *some* point during their lifetime (i.e., a star particle is labeled as a migrator for its complete lifetime, even though $\Delta R = |R_{\rm gal} - R_{\rm gal}^{\rm birth}|$ might not be > 5 kpc during its entire lifetime). The chosen threshold of 5 kpc is rather generous in a sense that it allows for star particles to still occupy galactocentric distances that differ from their galactocentric distance of birth quite substantially without being labeled as a migrator. However, we find that the exact value of the threshold has little influence on the migrator population in the outer galaxy beyond 20 kpc (which is the focus of this paper). We show outcomes for different thresholds in Section C.1.

5.2.3 Eccentricity of Star Particle Orbits

The Rhea simulations allow us to follow individual star particles throughout the simulation time, enabling us to study their orbital properties, such as orbital eccentricity around the galactic center, ε. We calculate the eccentricity from the minimum and maximum galactocentric distance of a star particle during the ith orbit $R_{\rm gal}^{{\rm orbit}\,i}$ via

$$\varepsilon_i = \frac{c_i}{a_i} = \frac{\max\left(R_{\rm gal}^{{\rm orbit}\,i}\right) - \min\left(R_{\rm gal}^{{\rm orbit}\,i}\right)}{\max\left(R_{\rm gal}^{{\rm orbit}\,i}\right) + \min\left(R_{\rm gal}^{{\rm orbit}\,i}\right)}, \tag{5.3}$$

where c is the linear eccentricity, i.e., the distance between the center of the ellipse and its focus point, and a is the semimajor axis.

5.2.4 The Galactic Rotation Curve

In Section 5.3.5 we construct the stellar galactic rotation curve from the velocity parameters (in cylindrical coordinates) v_r, v_φ and v_z of the stellar population in the simulation. In observational studies (see e.g., Eilers et al., 2019; Zhou et al., 2023; Jiao et al., 2023), this is often done using the basic correlation of the Jeans equation in an axisymmetric system (see Binney & Tremaine, 2008, Equation 4.222a), which correlates the moments of the velocity distribution with the density field of the velocity tracers and the gravitational potential:

$$\frac{\partial\left(\nu\overline{v_r^2}\right)}{\partial R_{\mathrm{gal}}}+\frac{\partial\left(\nu\overline{v_r v_z}\right)}{\partial z}+\nu\left(\frac{\overline{v_r^2}-\overline{v_\varphi^2}}{R_{\mathrm{gal}}}+\frac{\partial\Phi}{\partial R_{\mathrm{gal}}}\right)=0, \tag{5.4}$$

where ν is the density distribution of the velocity tracer population and a bar denotes mean values. With this and the known correlation

$$V_{\mathrm{circ}}^2(R_{\mathrm{gal}})=R_{\mathrm{gal}}\frac{\partial\Phi}{\partial R_{\mathrm{gal}}}\bigg|_{z\approx 0} \tag{5.1}$$

one can derive an equation to find the circular velocity as a function of moments of the velocity distribution and the density field of the tracers (see e.g., Eilers et al., 2019; Jiao et al., 2023):

$$V_{\mathrm{circ}}^2=\overline{v_\varphi^2}+\frac{R_{\mathrm{gal}}-R_{\mathrm{sc}}}{R_{\mathrm{sc}}}\overline{v_r^2}-R_{\mathrm{gal}}\frac{\partial\overline{v_r^2}}{\partial R_{\mathrm{gal}}}, \tag{5.5}$$

where we assumed an exponential density profile of the tracer population $\nu \propto \exp\left(-R_{\mathrm{gal}}/R_{\mathrm{sc}}\right)$. We note that for deriving Equation 5.5 we ignored the second term of Equation 5.4, as is customary (see e.g., Eilers et al., 2019; Zhou et al., 2023), because it is considered subdominant compared to the other terms. We adopt this definition whenever we analyze the rotation curve $V_{\mathrm{circ}}\left(R_{\mathrm{gal}}\right)$.

The difference between V_{circ} and $\overline{v_\varphi}$ is called asymmetric drift and needs to be corrected for with the additional terms of Equation 5.5.

We note that in literature the terms ‘rotation curve’ and ‘circular velocity curve’ are often used synonymously. In the sense of the strict definition, this is not correct. The circular velocity curve as defined in Equation 5.1 depends only on the gravitational potential and is not a directly measurable quantity. It can only be

constrained by observables. The rotation curve, on the other hand, is derived from measurements as given in Equation 5.5, and therefore depends on the used tracers. It is an approximation of the circular velocity curve. The rotation curve again is not equivalent to the azimuthal velocity curve $\overline{v_\varphi}$ (even though the terms are again often used interchangeably), as is apparent in Equation 5.5. Only when the asymmetric drift is negligible, like it is often the case with gaseous velocity tracers, such an equalization is permissible. We take great care to distinguish between the two terms in this chapter.

5.3 Results

5.3.1 The Star-Forming and Stellar Disk

In Chapter 4, Fig. 4.10 we already found that the rate of star formation differs throughout the disk and also changes with time. We quantify this in Fig. 5.1 by showing the SFR surface density Σ_{SFR} of our simulations for three different times, and compare them to observational values from Elia et al. (2022); Zari et al. (2023); Guesten & Mezger (1982); Kennicutt & Evans (2012) and Lee et al. (2016) (also Soler et al., 2023). We show the simulation runs already used in Chapter 4, namely F3000HD and MW3000HD as well as the new simulation MW3000HD-moddens.

We find that values of Σ_{SFR} are very similar between all simulations, but differ substantially in slope and absolute values over time. Over the course of 1 Gyr, Σ_{SFR} differs by more than two orders of magnitude in the innermost 5 kpc, and about one order of magnitude between 5 and 10 kpc. Even though MW3000HD-moddens has a steeper decline of gas density in the galactic outskirts than MW3000HD and F3000HD, the radius of its star-forming disk is only marginally smaller. In general, the SFRs in our simulations are relatively stable throughout the disk up to a galactocentric radius of about 20 kpc, and then drop steeply between 20 kpc and 25 kpc. With time, SFR in the inner galaxy (up to about 10 kpc) declines, and is more stable over time further out, which is in line with Fig. 4.10.

For all times we find the star-forming disk in our simulations to be larger than what is inferred from observations. This is true even when the modified initial density distribution is used. We therefore find substantial star formation beyond the solar radius, where we would expect a declining SFR from observations. This,

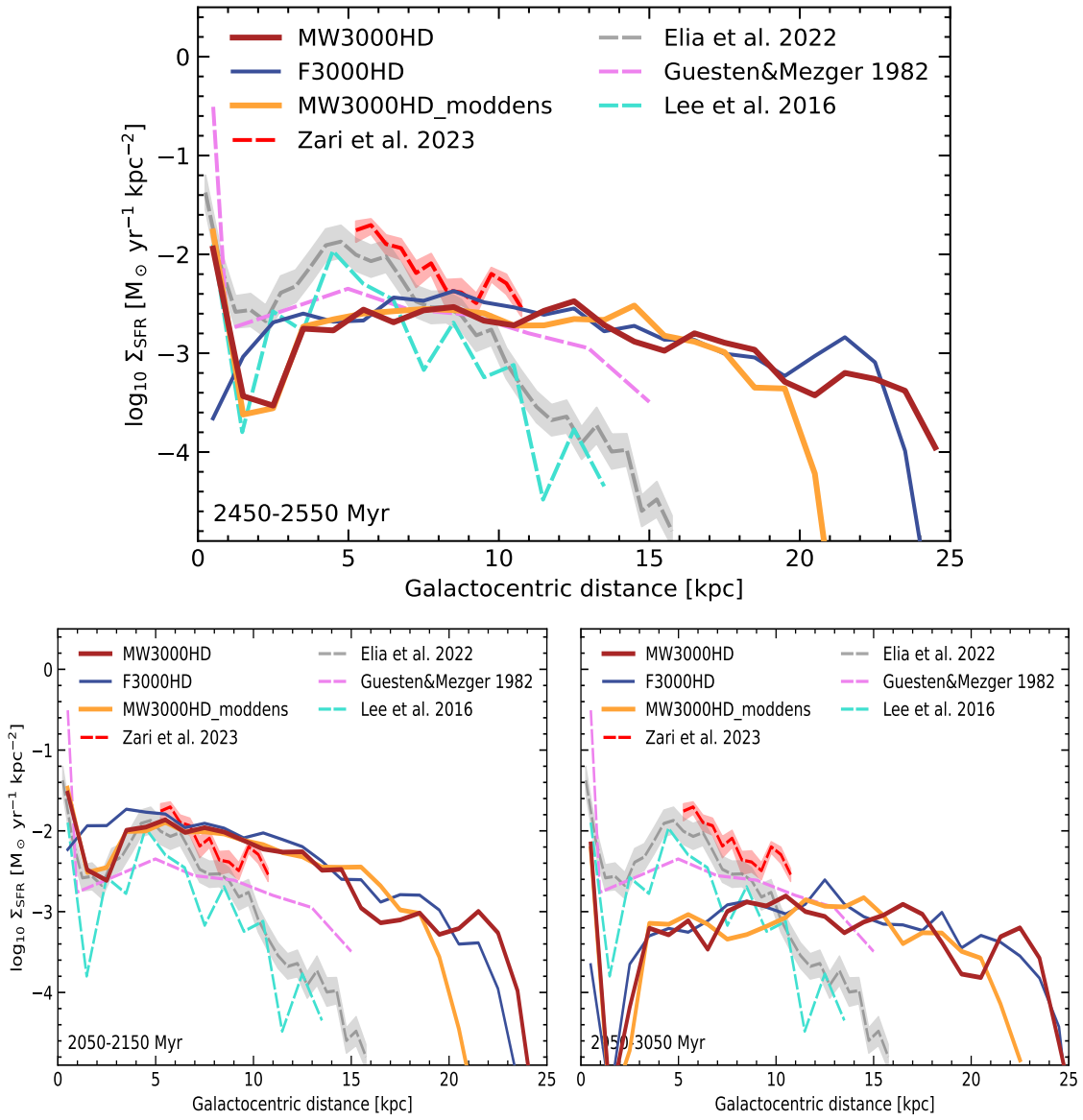

Figure 5.1: SFR profile of the simulations, averaged from 2450 to 2550 Myr (top, solid curves), from 2050 to 2150 Myr (bottom left, solid curves) and from 2950 to 3050 Myr (bottom right, solid curves), compared to observational data (dashed curves). At the fiducial analysis time (top), the SFR profiles of all simulations up to $R_{\rm gal} \approx 9$ kpc agree with observations from the MW to a reasonable degree. As expected, only the MW potential reproduces the dip in SFR at $R_{\rm gal} \approx 2$ kpc. At $R_{\rm gal} > 9$ kpc all simulations show a higher $\Sigma_{\rm SFR}$ than expected from observations. The shape of the SFR profile depends highly on the time used to produce this plot. Adapted from Elia et al. (2022); Zari et al. (2023); Guesten & Mezger (1982); Kennicutt & Evans (2012) and Lee et al. (2016) (also in Soler et al., 2023).

in parts, can be explained by a lack of magnetic stabilization of low-density gas in the galactic outskirts in these purely HD simulations. In the Rhea simulations including MHD treatment we find the star-forming disk to be mostly cut at 17 to 20 kpc, which is still slightly higher than observational values (see Kjellgren et al., 2025). For the inner galaxy, the simulations using the MW potential reproduce the observed dip in $\Sigma_{\rm SFR}$ at about 2 kpc very well, especially at early times. The flat potential lacks this dip, but otherwise follows the SFR profile of the MW simulations closely, indicating that the galactic potential has no strong effect on SFR outside of the innermost galaxy, as found in Chapter 4.

Even though the star-forming disk is truncated at a galactocentric radius between 20 and 25 kpc, the stellar disk is not. We present this difference in Fig. 5.2, where we show the (upscaled by 10^8) SFR surface density distributions ($\Sigma_{\rm SFR}$, dashed curves) together with the stellar surface density (Σ_*, solid curves) for all three simulation runs averaged between 2450 and 2550 Myr. In addition, with dotted curves corresponding to the right-hand ordinate, we indicate the mass fraction of migrating star particles in the total star particle population at different galactocentric radii (for definition of migrators, see Section 5.2.2, for a study of different thresholds see Appendix C.1). It is apparent that migrators start to dominate the stellar population from the edge of the star-forming disk outwards. This results in a peculiar shape of Σ_*, following a broken exponential, i.e., when modeling Σ_* as $\propto \exp\left(-R_{\rm gal}/R_{\rm sc}\right)$, where $R_{\rm sc}$ is the scale length of the distribution, it is not possible to model Σ_* with just a single scale length. In Table 5.2 we give the inner and outer scale lengths from fits to the average stellar surface density distribution presented in Fig. 5.2, as well as the approximate location of the kink in the distribution, $R_{\rm kink}$. We define $R_{\rm kink}$ as the galactocentric distance at which the migrator fraction is > 0.5 for the first time. It is apparent that in the migrator dominated regime, where no active star formation takes place, the scale length drops significantly. This is expected, as this region of the stellar disk is solely fueled by stars migrating outwards from the inner disk, and no active star formation is going on there itself. We are aware, that the quoted scale lengths of the order of 7 kpc and ~ 1.5 kpc are not in the regime of typical scale lengths quoted for the Milky Way. We remind the reader, however, that the depicted stars merely represent the newly formed stars in our simulation, and that more stellar mass is 'hidden' in the gravitational potential superimposed on our simulated disks. The quoted scale lengths therefore just represent the mea-

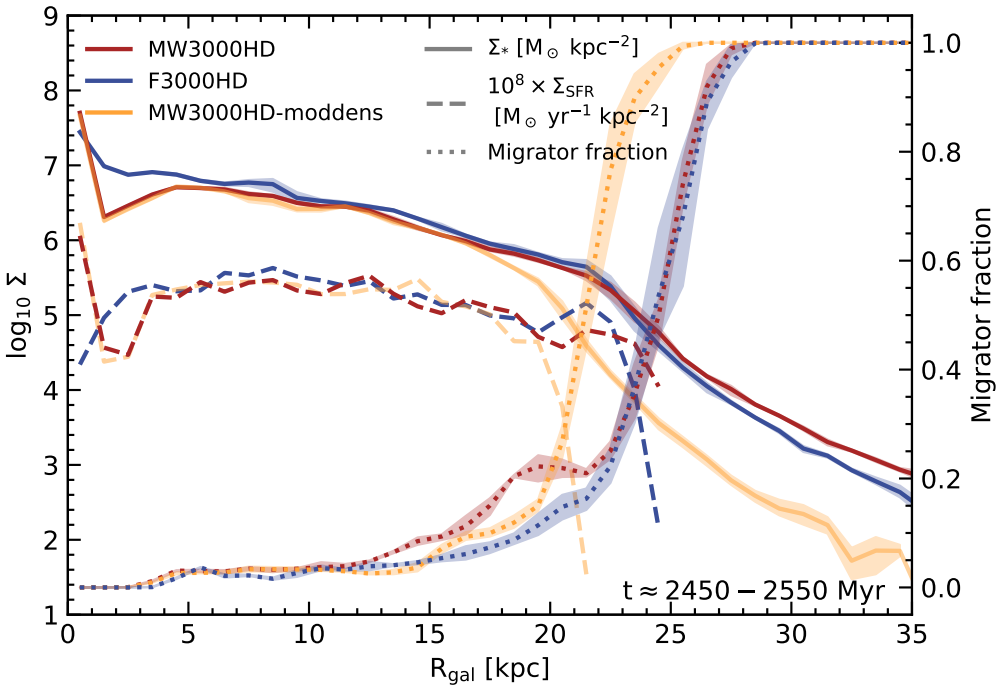

Figure 5.2: Stellar surface density Σ_* (solid curves, left vertical axis) and SFR surface density Σ_{SFR} scaled up by 10^8 (dashed curves, left vertical axis), together with the mass fraction of migrator star particles in the star particle population (dotted curve, right vertical axis). All values are averaged between 2450 and 2550 Myr, shaded regions give the 16th to 84th percentile. The stellar disk extends to larger galactocentric radii than the star-forming disk. The population of star particles beyond the star-forming disk is heavily dominated by migrators.

surable stellar population, as stellar mass represented in the external potential is not simulated on an individual particle basis, and therefore cannot be used for further measurement. We moreover note that the scale lengths derived from fits to the stellar surface density can differ substantially depending on the radial restrictions applied.

Again, the chosen potential does not have a systematic influence on this correlation between Σ_*, Σ_{SFR} and the migrator fraction, as the corresponding curves of F3000HD and MW3000HD lay very close together. The introduction of the modified initial density distribution moves the edge of the star-forming disk, and therefore the kink in Σ_* inwards by about 3 kpc, but the general picture remains the same: where the star-forming disk ends, the stellar disk gets quickly dominated by migrating star

Simulation	$R_{\rm kink}$ [kpc]	$R_{\rm sc}\,(5\,{\rm kpc} < R_{\rm gal} < R_{\rm kink})$ [kpc]	$R_{\rm sc}\,(R_{\rm gal} \geq R_{\rm kink})$ [kpc]
F3000HD	24.5	6.9 ± 0.5	1.65 ± 0.05
MW3000HD	24.5	7.1 ± 0.4	1.56 ± 0.09
MW3000HD-moddens	21.5	6.9 ± 0.5	1.20 ± 0.02

Table 5.2: Approximate location $R_{\rm kink}$, as well as the corresponding scale lengths $R_{\rm sc}$ of $\Sigma_* \propto \exp\left(-R_{\rm gal}/R_{\rm sc}\right)$ at galactocentric distances smaller and larger than $R_{\rm kink}$. For the fitting of $R_{\rm sc}$, we exclude the innermost 5 kpc.

particles. Here, we just show the correlation at the fiducial analysis time, however, the trend qualitatively remains the same for other simulation times. Because of the overall similarity of all shown simulation runs, we will concentrate on the two fiducial simulations F3000HD and MW3000HD in the following. MW3000HD-moddens behaves like MW3000HD, but with the transition to the migrator-dominated region moved slightly inwards.

5.3.2 Stellar Migration to the Outer Galaxy

Figure 5.2 already showed the necessity of outward migration of star particles to form the outer stellar disk, as no star particles form in-situ there. To quantify this, in Fig. 5.3 we present the correlation between the galactocentric distance of star particles at birth, $R_{\rm gal}^{\rm birth}$, and their mean galactocentric distance averaged over their lifetime $\overline{R}_{\rm gal}$. We find that non-migrators stay close to a one-to-one correlation, i.e., the galactocentric distances resulting from their orbits stay close to the galactocentric distances they are born at. Migrators, on the other hand, are predominantly below the one-to-one correlation. Their mean galactocentric distances are larger than the distance they are born at. This is true for both simulations.

Moreover, from Fig. 5.3 we can see that star particles with $\overline{R}_{\rm gal} > 25$ kpc predominately have a birth radius between 20 and 25 kpc. This means that the star particles forming the extended stellar disk are already formed at the outskirts of the star-forming disk. Star particles formed closer to the galactic center migrate within the extent of the star-forming disk, but rarely leave it.

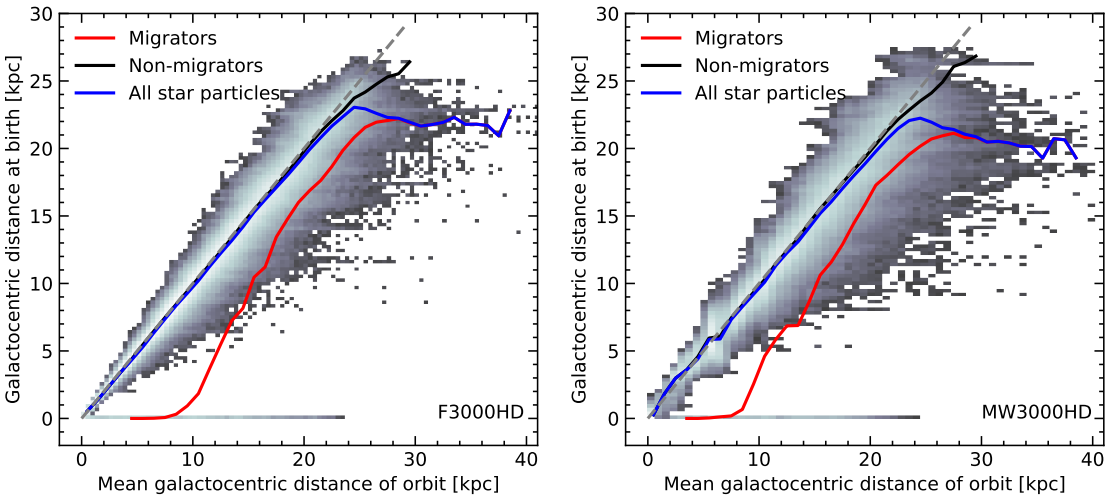

Figure 5.3: Galactocentric distance of star particles at birth as a function of their mean galactocentric distance averaged over their lifetime for F3000HD (left) and MW3000HD (right). In grey we plot the one-to-one correlation. We show the mass-weighted average of the full stellar population (blue), and distribute it into migrators (red) and non-migrators (black). Color coded in the background is the distribution of all star particles. Star particles predominately migrate outwards.

5.3.3 Orbital Properties of Star Particles

We now look at the properties of the orbits of those migrating stars, and the nature of their migration. Is their migration due to ellipticity in their orbits, or do they actually change their guiding radius? To answer this, in Fig. 5.4 we depict the distribution of eccentricity ε of the stellar orbits around the galactic center.

From Fig. 5.4 it is apparent that the average eccentricity of migrators (red) is larger than for non-migrators (black). For F3000HD, migrators have a mean eccentricity of about 0.16 and non-migrators 0.08, in MW3000HD mean eccentricity in migrators is 0.19 (for $R_{\rm gal}^{\rm birth} > 5$ kpc), that of non-migrators is 0.09 (for $R_{\rm gal}^{\rm birth} > 5$ kpc). Eccentricity in migrators therefore is about twice as high as in non-migrators. Moreover, this deviation is present right from the beginning of a star particles lifetime. We show the eccentricity PDF for the first orbit (solid) and after three orbits (dashed), as well as the average over all completed orbits (dotted). For migrators, those three PDFs do not show any significant differences (the means of the distributions, in fact, differ by less than 0.021 for both simulations), indicat-

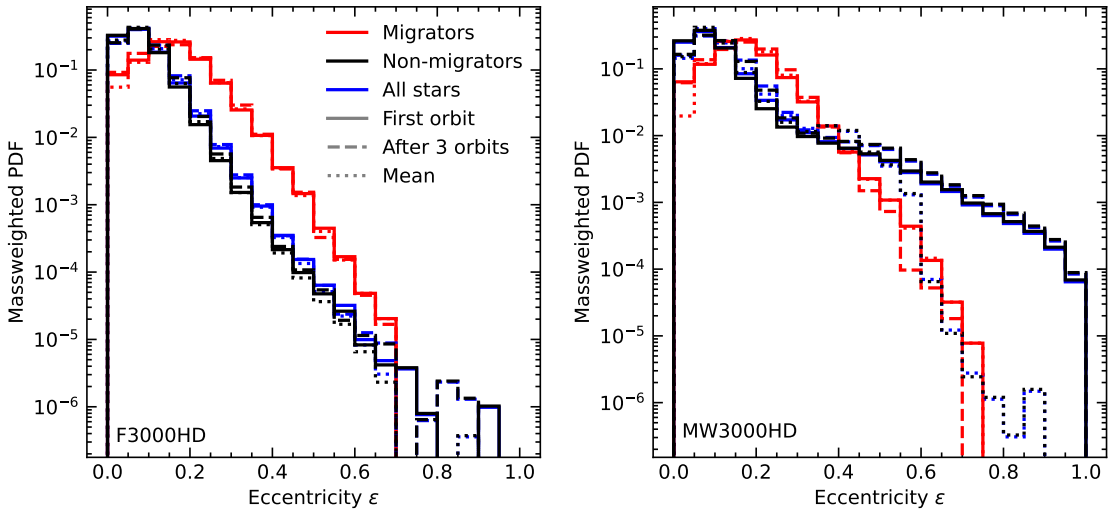

Figure 5.4: Mass-weighted probability density function (PDF) of orbital eccentricity for migrators (red), non-migrators (black) and all star particles (blue). Depicted are the distributions of eccentricities upon the first stellar orbit (solid lines), after 3 orbits (dashed lines) and the mean eccentricity averaged over all orbits (dotted lines). Orbital eccentricities do not change significantly over several orbits. Migrators on average have a larger orbital eccentricity than non-migrators.

ing that the orbital eccentricity does not change substantially over a star particles lifetime. Star particles, which have a mean galactocentric distance much larger than their galactocentric distance at birth do so, because they are on very elliptical orbits, and their orbits have this high eccentricity from birth.

The only exception of this are non-migrators in MW3000HD (and consequently the PDF of all star particles (blue), as they are dominated by non-migrators). For those star particles, the eccentricities in the first orbit and after three orbits are in good agreement and can reach very high ε-values, but the averaged eccentricity deviates from this. This behavior is solely caused by particles born in the innermost 5 kpc of the galaxy, as can be seen in Fig. 5.5, where we show the same PDF for MW3000HD as in Fig. 5.4, but only for star particles born at $R_{\mathrm{gal}}^{\mathrm{birth}} > 5$ kpc. This PDF closely resembles that of F3000HD in Fig. 5.4, with the eccentricity distributions from different orbits staying very similar to each other.

The reason for this can quickly be found in the dynamics of the bar region in MW3000HD. Contrary to the flat potential, in the bar region of MW3000HD the

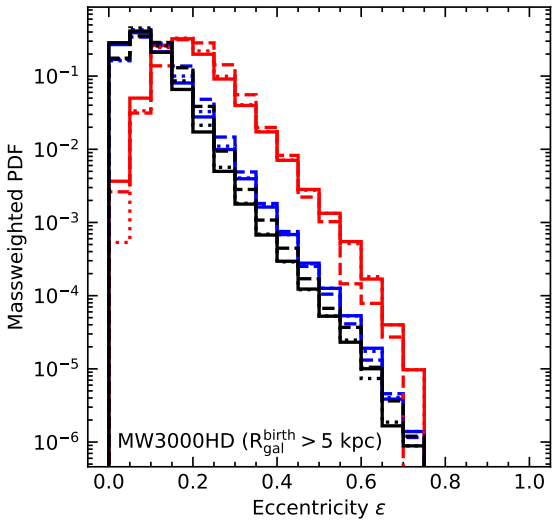

Figure 5.5: Same as Fig. 5.4, but only for star particles born at a galactocentric distance > 5 kpc for MW3000HD.

stellar orbits are highly unordered, as one can see in Fig. 5.6. There, we show the correlation between the mean difference in azimuthal velocity at the pericenter and apocenter of the stellar orbits $\Delta v_\varphi = v_\varphi^{\text{pericenter}} - v_\varphi^{\text{apocenter}}$ as a function of mean orbital eccentricity. For all regions except the innermost 5 kpc of MW3000HD we find the expected linear correlation: The larger the eccentricity of a stellar orbit is, the larger is the difference between its velocity at their pericenter and apocenter. This correlation, however, is broken in the gravitational potential of a galactic bar, simply because orbits in this potential partially loose their elliptical nature (see Chapter 1.2.2). Orbits of the x1 and x2 family can lead to retrograde orbits (see the large negative Δv_φ in Fig. 5.6). Moreover, the high stellar density in the galactic center (see the increase in Σ_* in the innermost 2 kpc in Fig. 5.2) leads to frequent and close gravitational interactions between star particles that disturb their orbit. This effect can also be seen in the center of F3000HD, where a small fraction of star particles is also scattered to retrograde orbits, but because of the overall ordered and non-time dependent potential to a much smaller extent than in the center of MW3000HD. Also, star particles close to the galactic center have short orbital periods, i.e., they complete many orbits during their lifetime. Therefore it is not surprising for their mean eccentricity over all orbits to deviate from that of their first and fourth orbit, showing a transition to lower eccentricities (the comparison of the first and fourth

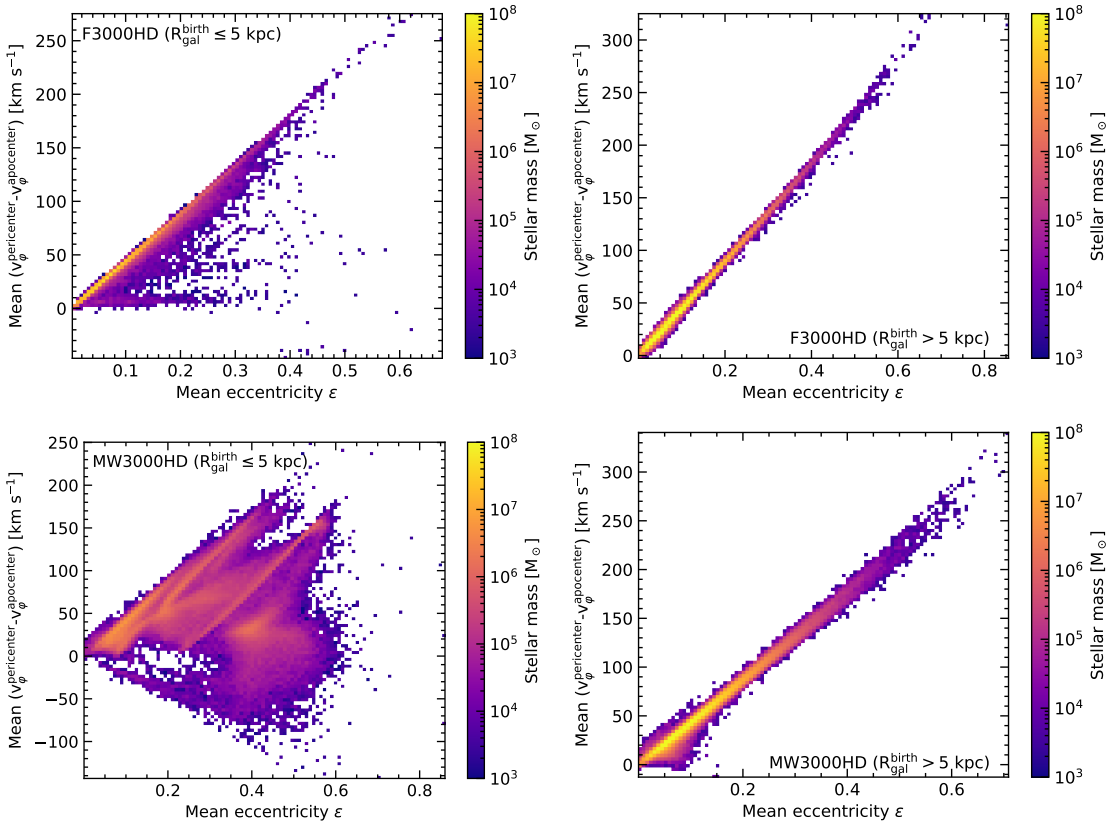

Figure 5.6: Differences in velocity at the pericenter and apocenter of stellar orbits as a function of eccentricity for star particles born in the galactic center with $R_{\mathrm{gal}}^{\mathrm{birth}} \leq 5$ kpc (left) and further out (right) for F3000HD (top) and MW3000HD (bottom). The expected linear correlation is present in all regions apart from the center of MW3000HD, where orbits tend to be highly unordered.

orbit was chosen to ensure that a substantial number of star particles also further out in the galaxy even reach that number of orbits, which is not the case for larger orbit numbers).

The combination of migrator-domination in the outer stellar disk and the higher orbital eccentricity of migrators compared to non-migrators leads to an increase of the average orbital eccentricity of star particles beyond $\sim 20 - 25$ kpc, as we show in Fig. 5.7. Since higher eccentricities lead to higher Δv_φ, and since star particles spend more time close to their apocenter than to their pericenter because of Kepler's second law, it is straight forward to expect an influence from this effect on the measured azimuthal velocities of a galaxy, that has to be corrected for.

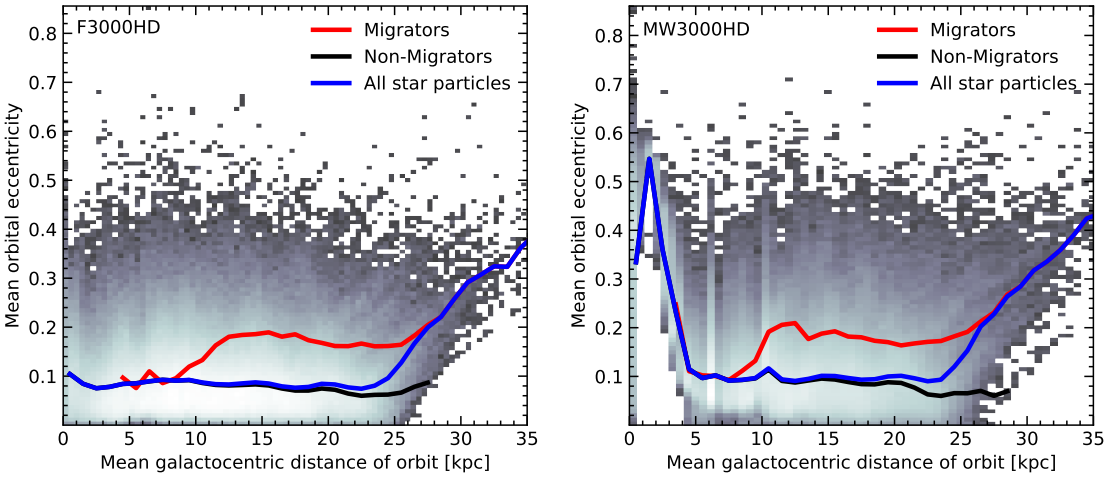

Figure 5.7: The mean orbital eccentricity of star particles as a function of the mean galactocentric distance averaged in radial bins in a mass-weighted average for migrators (red), non-migrators (black) and all star particles (blue) in F3000HD (left) and MW3000HD (right). Color-coded background gives the distribution of all star particles.

5.3.4 The Azimuthal Velocity Curve

To quantify this influence, we first retrieve the azimuthal velocities of F3000HD and MW3000HD for star particles with $|z| < 0.5$ kpc (no qualitative differences are seen for different $|z|$), together with the individual contribution of migrators and non-migrators in Fig. 5.8. We show this together with the rotation curve extracted in Jiao et al. (2023) from Gaia-DR3 data. By design, F3000HD has a flat azimuthal velocity distribution over large parts of its disk, up to about 25 kpc, when it starts to decline as migrators dominate the stellar population, as we expected from our previous analysis. If one takes into account only non-migrating star particles, the rotation curve also declines, but to a much lower degree. This is probably due to star particles that do not reach $\Delta R > 5$ kpc during their lifetime, but nevertheless are on eccentric orbits. We show how the azimuthal velocity distribution is affected by the eccentricity of orbits in Appendix C.2. The azimuthal velocities of MW3000HD, on the other hand, are steadily declining, but, as well, show a kink towards lower velocities at about 25 kpc (which is less noticeable due to the overall decline). The azimuthal velocities of non-migrators do not show such a kink. All this is expected behavior when taking into account the previous analysis. To derive a valid rotation

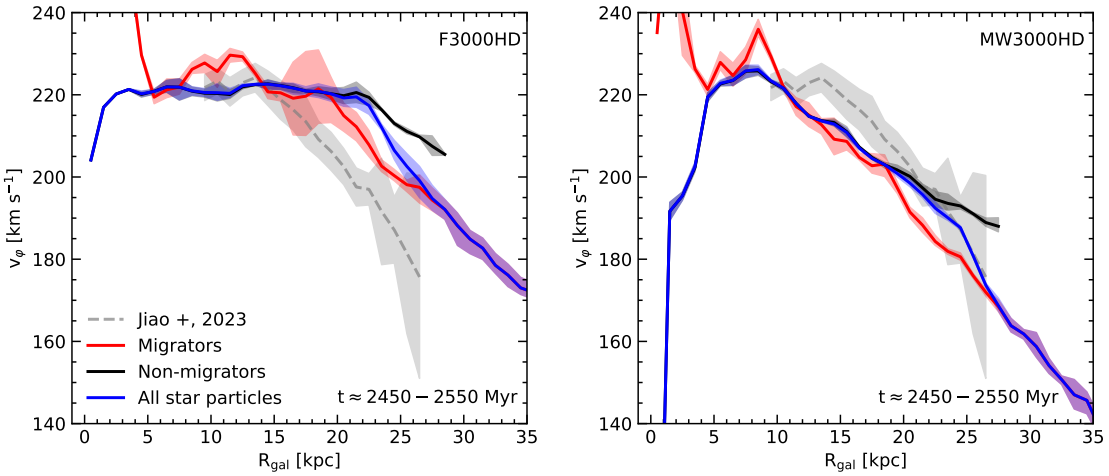

Figure 5.8: Azimuthal velocity distribution for F3000HD (left, blue) and MW3000HD (right, blue) with $|z| < 0.5$ kpc, averaged from 2450 to 2550 Myr. Contributions from migrators (red) and non-migrators (black) are depicted, shaded regions show the 16th to 84th percentile. Observational data from Jiao et al. (2023) is given in the grey dashed curve, the shaded region denotes $\pm 1\sigma$.

curve, it nevertheless has to be corrected for, as we do in Section 5.3.5.

To show the peculiarity of this migrator behavior in stars, in Fig. 5.9 we show the azimuthal velocity of all star particles together with that derived from the gaseous component and the theoretical rotation curve from the mass in our simulations. With this, we can show that the declining stellar azimuthal velocity is not caused by the applied potential in any of the simulations. It is apparent that the stellar azimuthal velocity in the migrator dominated region does not follow the rotation curve derived from the actual applied gravitational potential, but deviates from it towards lower velocities. The azimuthal velocity derived from gas in the simulation does not show this deviation, but follows the rotation curve defined by the potential closely up to the edge of the gaseous disk at 30 kpc. We therefore can only conclude that the decline in the stellar azimuthal velocity is caused by the outward migration of star particles, whose highly elliptical orbits cause the projected circular velocity to be lowered.

We also fit a power law of the form $v_\varphi = CR_{\rm gal}^{-n}$ to the migrator dominated region at $R_{\rm gal} > 25$ kpc of the stellar azimuthal velocity curve. For F3000HD, the azimuthal velocity in this region nearly perfectly resembles a Keplerian one with

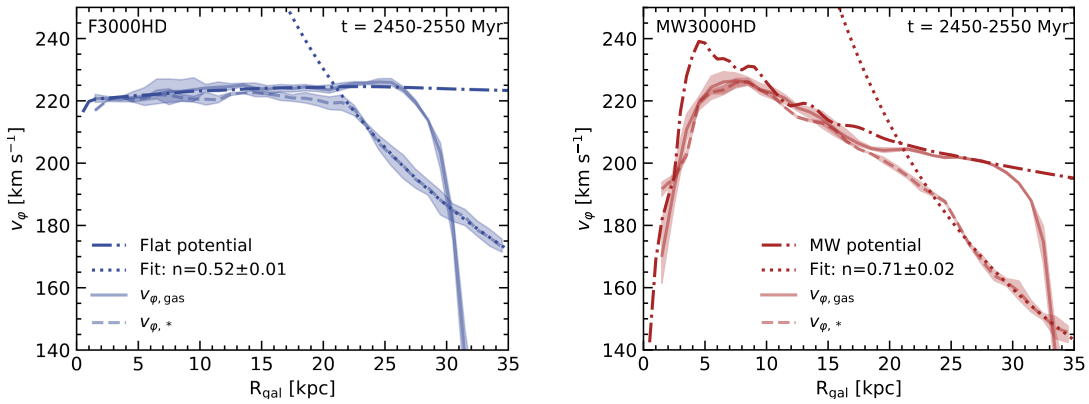

Figure 5.9: Azimuthal velocities derived from gas (solid), stars (dashed) and the underlying potential (dash-dotted) for F3000HD (left) and MW3000HD (right). The azimuthal velocity of gas follows the underlying gravitational potential closely, whereas that of stars deviates from it towards lower velocities in both potentials. A function of the form $v_\varphi = CR_{\rm gal}^{-n}$ is fitted to the stellar rotation curve beyond 25 kpc. Where the fit for F3000HD shows a nearly perfectly Keplerian decline, the decline for MW3000HD is steeper than Keplerian.

$n = 0.52 \pm 0.01$. MW3000HD's azimuthal velocity in this region, however, declines faster than Keplerian, with $n = 0.71 \pm 0.02$. Jiao et al. (2023) for their declining region find $n = 0.47 \pm 0.15$, which is close to a Keplerian decline. However, the decline found for MW3000HD is still in the 3σ interval of this value.

5.3.5 The Resulting Rotation Curve and Dynamical Mass

Finally, we calculate the rotation curves of the stellar component of our simulations. As shown in Section 5.3.1, the density distribution of our stellar component is not described by a single exponential and scale length, but at least two different scale lengths have to be adopted. We show the effect of just one adopted scale length as well as the correct rotation curve for F3000HD and MW3000HD in Fig. 5.10. Here, the left and center column show the rotation curves of the simulated star particles calculated with just a single scale length from Table 5.2, either the inner or outer $R_{\rm sc}$, respectively. If only the outer, lower scale length is used, the circular velocities are overestimated over large parts of the disk, up to $R_{\rm kink}$ as expected from Equation 5.5. This effect is especially strong for migrators, as these star particles on average

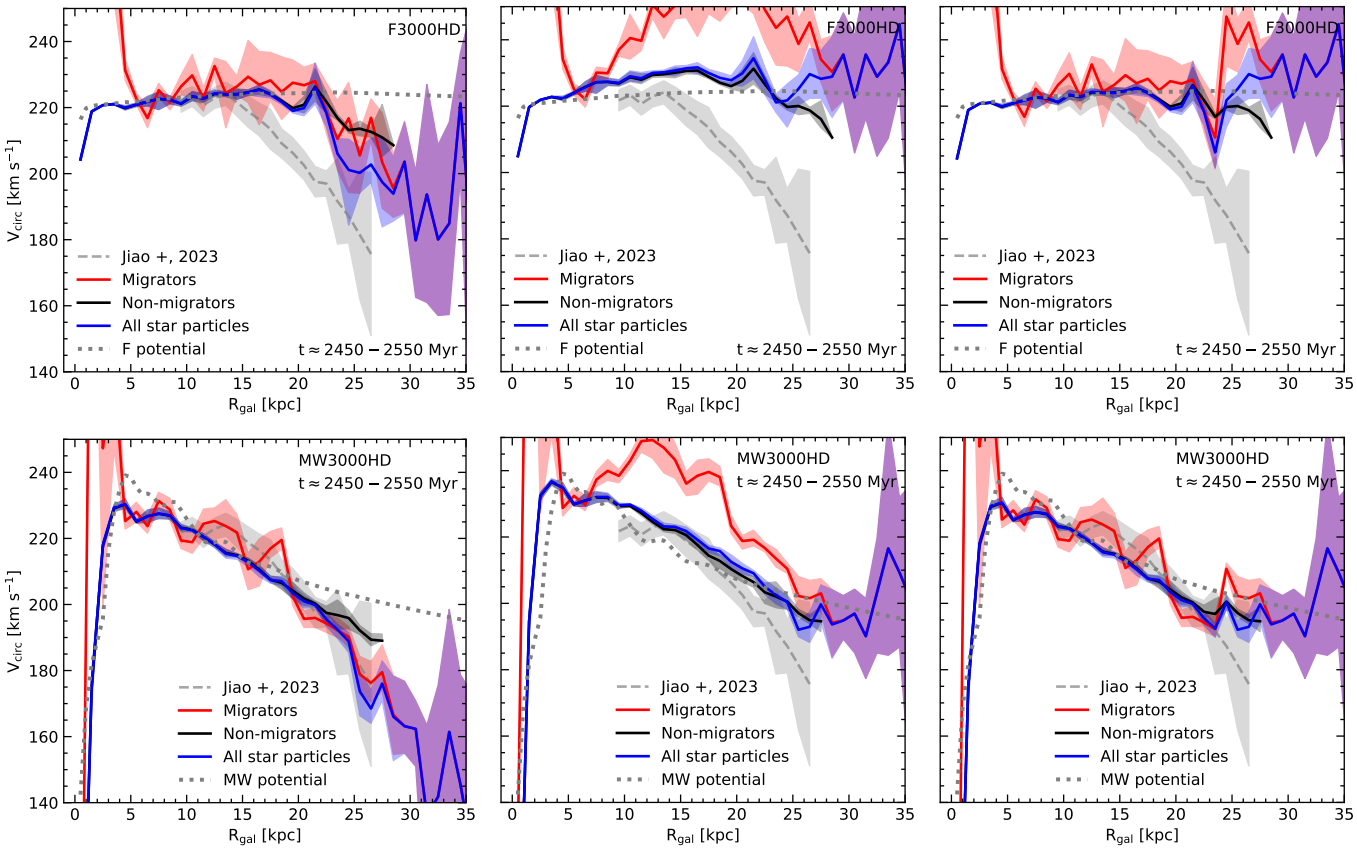

Figure 5.10: Rotation curve of F3000HD with R_{sc} = 6.9 kpc (top left), 1.64 kpc (top center) and 6.9 kpc up to a galactocentric distance of 24.5 kpc, and 1.64 kpc beyond (top right) and MW3000HD with R_{sc} = 7.1 kpc (bottom left), 1.56 kpc (bottom center) and 7.1 kpc up to 24.5 kpc, and 1.56 kpc further out. We show migrators (red), non-migrators (black) and all star particles (blue). Shaded regions indicate the 16th to 84th percentile. Grey dotted curve gives the rotation curve as expected from the corresponding gravitational potential. Rotation curve of Jiao et al. (2023) is given in grey dashed, shaded region denotes 1σ. Only the correction with two different scale lengths (right) gives a proper stellar rotation curve that follows the behavior of the underlying potential and does not overestimate V_{circ} at $R_{gal} < R_{kink}$. When only the scale length of the inner disk up to R_{kink} is used, the kink in azimuthal velocity curve remains clearly visible in the rotation curve of the galaxy.

show much larger v_r than non-migrators (see Fig. C.3). However, in the case of the lower R_{sc}, no kink is seen in the rotation curve.

If instead only the inner, higher R_{sc} from Table 5.2 is used, the rotation curve is

well behaved up to the galactocentric distance where migrator domination sets in. In that region, however, the rotation curve is still clearly tilted towards lower velocities, i.e., the kink seen in the azimuthal velocity curve (Fig. 5.8) is still present in the rotation curve, when it should have been corrected for. We will see in Fig. 5.11 that this directly translates into an stagnation or even decrease in the estimated enclosed mass of the galaxy. In the case of MW3000HD, the derived velocity curve matches the observational values of Jiao et al. (2023) well, especially at $R_{\mathrm{gal}} \gtrsim 20$ kpc.

If one finally uses two different scale lengths in different regimes of the galactic disk (right column of Fig. 5.10), the rotation curves match those expected from the galactic potential (compare Fig. 5.9) very well. No kink from the azimuthal velocity distribution can be seen, and the rotational velocities of star particles up to R_{kink} are not overestimated. We find this curve in the case of MW3000HD (our Milky Way analog) to match the observational values reasonably well up to R_{kink}. Further out in the disk, the rotation curve derived from our simulation, however, deviates from observational values towards higher rotational velocities, which matches the underlying potential.

From the rotation curve we can now calculate the enclosed dynamical mass (sum of DM and baryonic mass) that we would infer if the rotational velocity of the star particles would trace the gravitational potential via

$$M_{\mathrm{dyn},\,j} = \frac{V^2_{\mathrm{circ},\,j} R_{\mathrm{gal},\,j}}{G}. \tag{5.6}$$

We present this in Fig. 5.11, again for the same scale lengths used in Equation 5.5 as in Fig. 5.10. We moreover indicate the true mass distribution in our simulation (grey dotted), as well as the observed values from Jiao et al. (2023) (grey dashed).

It is apparent that with a correction including only the lower, outer scale lengths from Table 5.2 (center column), masses in the simulation are overestimated by the rotation curve. Dynamical masses calculated from the rotation curve up to galactocentric distances $R_{\mathrm{gal}} = R_{\mathrm{kink}}$ lay continuously above the true enclosed mass taken directly from the simulation. The effect is small, but noticeable nonetheless. However, from these rotation curves we find no indication for a cut-off in the mass distribution, as it is found in Jiao et al. (2023). The enclosed mass derived from the rotation curve keeps rising up to the edge of the disk.

When only taking the inner, lower scale length into account when calculating V_{circ},

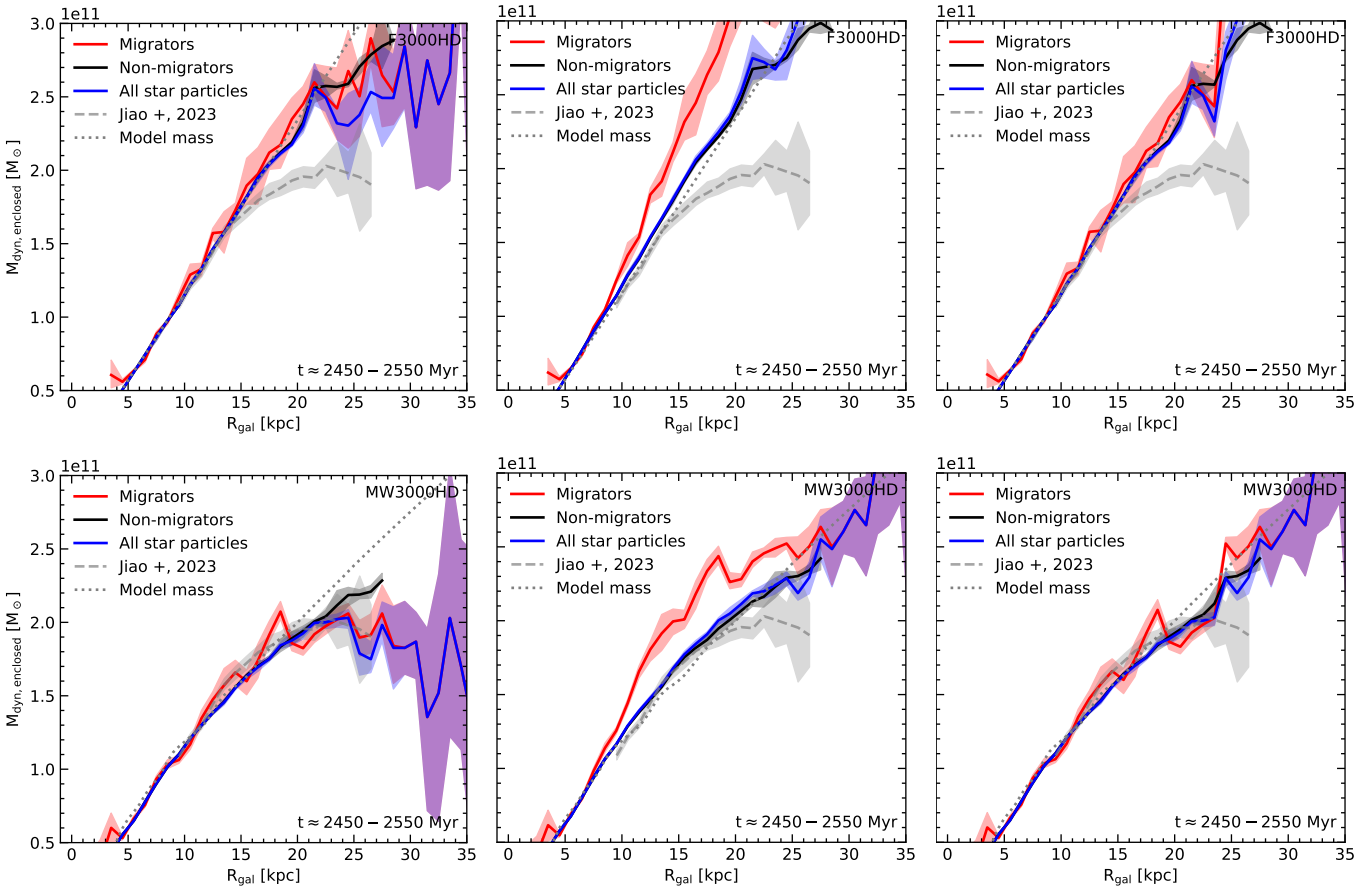

Figure 5.11: Dynamical enclosed mass derived from the rotation curves in Fig. 5.10 via Equation 5.6 for F3000HD with $R_{\rm sc} = 6.9$ kpc (top left), 1.64 kpc (top center) and 6.9 kpc up to a galactocentric distance of 24.5 kpc, and 1.64 kpc beyond (top right) and MW3000HD with $R_{\rm sc} = 7.1$ kpc (bottom left), 1.56 kpc (bottom center) and 7.1 kpc up to 24.5 kpc, and 1.56 kpc further out. Again, we distinguish between migrators (red), non-migrators (black) and all star particles (blue). We average from 2450 Myr to 2550 Myr, shaded areas indicate 16th to 84th percentile. True mass distributions taken from the simulations are given in grey dotted lines, observational values from Jiao et al. (2023) are indicated in grey dashed with an 1σ interval. If only a single, high scale length is used for the asymmetric drift correction (left), the mass distribution derived from the rotation curves shows an artificial mass cut-off.

the picture is different. In the left column, where the scale length of the star particle

distribution up to $R_{\rm kink}$ is used for the whole disk, one can clearly see a cut-off in the mass distribution derived from the rotation curve, both in F3000HD and MW3000HD. For both simulations, the estimated enclosed mass becomes constant beyond the point of domination by migrator star particles. However, if one takes into account only non-migrator stars, the estimated mass keeps rising, as it should since the mass distribution of our simulations extend beyond this point. This means that the rotation curve influenced by migrators mimics a cut-off in the mass distribution that is not really there, if the curve is not corrected according to its true scale lengths. The shape of our derived mass profiles for MW3000HD resembles that of Jiao et al. (2023) closely, who from their rotation curve derive a mass between 1.9 and 2.0×10^{11} $M_\odot$. For MW3000HD, our enclosed mass profile reaches a maximum of about 2.0×10^{11} $M_\odot$, and then starts to decline again. However, the mass of the DM halo in MW3000HD is set to 1.1×10^{12} $M_\odot$ (Hunter et al., 2024), therefore a saturation of the enclosed mass at these values cannot be true, as we see from the true mass distribution indicated in the figure. Jiao et al. (2023) even remark that their enclosed dynamical mass declines at $R_{\rm gal} > 23$ kpc, just like ours, but because the amplitude of the decay is smaller than the error bars, they discard this as simply unphysical noise (Jiao et al., 2023).

The only way to receive a dynamical enclosed mass from the rotation curve that follows the true mass distribution truthfully, at least in our simulations, is to use two different scale lengths for the asymmetric drift corrections. This we show in the right column of Fig. 5.11. There, we find no mass cut-off in any of the two simulations. Instead, the derived enclosed masses follow the true masses in the simulations closely and deviate from the observational values of Jiao et al. (2023) in the outer galactic disk.

5.4 Discussion

We showed that in the Rhea simulations, the density distribution of the stellar disk is best modeled by a broken exponential with two different scale lengths. The location of the change in scale length is determined by the edge of the star-forming disk, which divides the stellar disk in an inner region dominated by in-situ formed star particles, and an outer region dominated by star particles that migrated outwards.

The orbits of those migrating star particles in general have higher eccentricities than those of non-migrators. This, in turn, results in a general increase of the average orbital eccentricity of star particles in the outskirts of the stellar disk. The increased eccentricity leads to a lowered azimuthal velocity compared to star particles with more circular orbits. This effect has to be corrected for when deriving the galactic rotation curve, i.e. the impact of the broken exponential density distribution has to be taken into account. If that is not done and the outer stellar disk is modeled with the same scale length as in the in-situ dominated disk, the resulting rotation curve shows a decrease in the migrator dominated region, which can mimic a cut-off in the galactic mass distribution. This can result in an underestimation of the galactic mass.

The star-forming disk in our simulations extends up to a radius of 25 kpc, which is larger than expected from observations. This is probably due to a lack of physical (feedback) processes, like a galactic magnetic field and pre-supernova feedback that can dilute star-forming regions. This, however, even stresses our point. We find the transition to the migrator-dominated disk region, with all named consequences, at the edge of the star-forming disk. Jiao et al. (2023) reports a Keplerian decline at $R_{\mathrm{gal}} > 19$ kpc, in our simulations the kink in the rotation curve is located at about 25 kpc. With a smaller star-forming disk, however, it likely would be shifted towards lower galactocentric distances, in agreement with the observational results. Outside of the star-forming disk, our simulations predict a clear increase of the average orbital eccentricities of stars.

We have to note, however, that the derivation used for the rotation curve in this study (Equation 5.4 and 5.5), as well as in many observational studies, assume an axisymmetric system. The Milky Way is no such system, as it contains a bar and spiral arms, which are both non-axisymmetric features. However, the influence of those features vanishes in the outer galactic disk (> 20 kpc, see Göller et al., 2025). We therefore do not expect them to affect the outcome of this study significantly.

We also showed that migrators influence the azimuthal velocity curve in different galactic potentials, however, the used potential influences the strength of this effect. While for the flat potential we find a decline in the stellar azimuthal velocity resembling a Keplerian decline, in the MW potential the stellar azimuthal velocity declines with $\propto R_{\mathrm{gal}}^{-0.71}$, i.e., steeper than it Keplerian. This is probably caused by the fact, that the rotation curve of the MW potential is declining in an exponential

fashion itself, namely with $n \approx 0.12$. If one takes into account the stellar azimuthal velocity distribution in the non-migrator dominated region, the decline even scales as $n \approx 0.17 - 0.18$. If a process leading to an additional decline in the azimuthal velocity with $n \approx 0.5$ comes on top of this, the resulting exponent is close to the one found in our simulation.

From this, we can draw two conclusions: First, if the stellar disk is larger than the star-forming disk of a galaxy (and it was like this already for some time), then the stellar population of the disk most probably cannot be modeled by a single exponential profile. If such a profile is used nonetheless, with a scale length estimated at the solar circle, this will then lead to an underestimation of the rotation curve in the galactic outskirts. This can even mimic a cut-off in the mass distribution of the galaxy, which is not truly there. We note that the scale lengths from our simulation in Table 5.2 and used for the asymmetric drift correction do not resemble those obtained from observations of the Galaxy. We remind the reader, however, that the quoted scale lengths are *not the scale lengths of our full stellar population*, but just for the star particles newly formed during the simulation time. The majority of stars in our simulations are 'hidden' in the external potential applied to the galactic disk, i.e., not simulated explicitly. In MW3000HD (where we model the thin and thick disk explicitly), the the scale length for the thin stellar disk adopted in the potential is 2 kpc (see Hunter et al., 2024, or Section 2.3.7). However, as the stars forming the gravitational potential are not modeled explicitly, we cannot use them as tracers for the rotation curve, but can only use the star particles formed during the simulation, as they are modeled explicitly. Those star particles, due to the initialization of the gaseous disk in our simulation, show scale lengths close to 7 kpc in the non-migrator dominated disk region (see Equation 2.16). As the derivation of the rotation curve (Equation 5.5) asks for the density distribution of the *tracer particles* of the rotation curve, the scale lengths quoted in Table 5.2 are the one to be used. Observationally, scale lengths of the thin Galactic disk have been derived in numerous studies and span a wide range, from about 2.0 kpc (Siegel et al., 2002; Yaz Gökçe et al., 2015) to 3.9 kpc (Benjamin et al., 2005), with most of them seeming to fall in between 2.0 kpc and 2.5 kpc (e.g., Siegel et al., 2002; Jurić et al., 2008; Polido et al., 2013; Chen et al., 2017). The adopted values in the cited works on stellar rotation curves vary between 2.13 kpc (Zhou et al., 2023) and 3.0 kpc (Eilers et al., 2019; Ou et al., 2024), Jiao et al. (2023) (and Wang et al., 2023) use a scale length of 2.5 kpc (taken from

Jurić et al., 2008, according to the sources). By design, scale lengths derived from observational star counts focus on Galactic regions close to the sun. The highly cited scale length of 2.6 kpc from Jurić et al. (2008) for example is derived for the solar neighborhood with $D < 2$ kpc. It is therefore questionable if they are valid out to high galactocentric distances as far as 30 kpc (Wang et al., 2023). Moreover, broken exponential profiles are common in the outer disks of external galaxies (Pohlen & Trujillo, 2006). We therefore argue that the declining rotation curve in the outer stellar disk found in several observational studies (Eilers et al., 2019; Wang et al., 2023; Jiao et al., 2023; Ou et al., 2024) could be caused by the changing density distribution of the tracer stars in the outer Galactic disk.

Second, the reverse is also true, i.e., if a kink is detected in the stellar rotation curve of a galaxy modeled with a single exponential, this can indicate that the stellar population of the galaxy actually consists of two regimes, one migrator-dominated and one dominated by in-situ stars. The slope of the rotation curve beyond the disk contains information about the density distribution of stellar tracers in this migrator-dominated region, and the location of the kink most probably marks the edge of the star-forming disk, giving an idea on how extended star formation is in the galactic disk. If the observation allows for a differentiation between v_φ, v_r and v_z well enough to derive a distribution of the mean v_φ distribution, the slope of $\overline{v_\varphi}$ grants additional information on the slope further in, even when it is not observed directly, and therefore holds information on the galactic potential. This means that a relatively small fraction of the full velocity distribution, namely the part around the kink, holds information about several properties of the galaxy. Moreover, there is no special reason for this to only hold true for the Milky Way. In principle, this information can be taken from any stellar galactic rotation curve that holds an additional decline in the galactic outskirts. We note, however, that observations of declining rotation curves are rare (e.g., NGC 7793 has a declining rotation curve, even though not with a Keplerian decline, Dicaire et al. 2008). Noordermeer et al. (2007), for example, presents a study of rotation curves of 19 spiral galaxies and does not find a declining rotation curve for any of them. This probably is because the rotation curves in this work are taken from HI, i.e., gas, which we showed to actually trace the gravitational potential without any effects of ellipticity. The lack of Keplerian declines in the study of Zobnina & Zasov (2020) most probably is caused by the same reason.

Moreover, the MW has an especially quiet merger history (see e.g., Hammer et al., 2007; Bland-Hawthorn & Gerhard, 2016, and references therein), which sets it apart from other late-type galaxies. With more violent past mergers, especially in the more recent past of a galaxy, the effect reported here is probably hidden and washed out by stellar orbit changes induced by the merger, as well as chaotic stellar orbits from merger stars. This means that the appearance of a kink in the stellar rotation curve modeled with a single exponential additionally points to a quiet merger history. However, further examination fo this process has to be done, but is beyond the scope of this thesis.

5.5 Summary

We present an analysis of the orbit properties of the stellar population in the hydrodynamical Rhea runs and draw a connection on how these influence the observed stellar rotation curve of the Galaxy and the derived Galactic mass.

- The extent of the galactic star-forming disk is smaller than the stellar disk. The outer stellar disk is therefore dominated by star particles that migrated outwards from their birth position.
- The density distribution of the stellar population can therefore not be modeled by a single exponential, but is followed by a broken exponential with different scale lengths.
- Those migrating star particles have orbits with an eccentricity higher than the mean orbital eccentricity of star particles that stay close to their birth position. Our simulations therefore predict a sharp increase of average stellar orbital eccentricities outside of the star-forming disk.
- The eccentricity of their orbits leads to a low measured azimuthal velocity at their apocenter in the outer galactic disk, which, in turn, results in a decline of the rotation curve if not properly corrected for. Rotation curves derived from gas reliably trace the galactic potential out to the edge of the gaseous disk.
- For an otherwise flat azimuthal velocity distribution, this decline resembles a Keplerian decline. If the galactic potential itself results in a declining az-

imuthal velocity distribution, the decline of azimuthal velocity in the migrator dominated region is steeper.

- This decline is also seen in the rotation curve, if not properly corrected for. The rotation curve therefore has to be modeled with different scale lengths in the different regions of the stellar disc. If only the scale length derived at the solar circle is used, the resulting rotation curve mimics a cut-off in the galactic mass distribution that is not based in the true mass distribution.

We therefore propose that the observation of a kink in a galactic rotation curve modeled with just a single scale length holds additional information about the galactic stellar disk, namely the extent of the star-forming disk as the decline of the inner stellar rotation curve. It moreover indicates a quiet merger history.

6 Conclusion

6.1 Summary and Conclusion

We have investigated the influence of the extra- and intragalactic environment on star formation in galaxies for the examples of simulated jellyfish galaxies and Milky Way analogs. More explicitly, we studied properties of star formation, i.e., location within the galaxy, development over time and translation into observational properties of the galaxies, in two contrasting galactic environments: Predominantly low-mass galaxies in dense cluster environments, undergoing active ram-pressure stripping of their ISM, and a relatively massive (compared to most jellyfish galaxies) isolated galaxy predominantly formed by internal processes.

To do so, we used two different simulations both based on moving-mesh code Arepo: TNG50 (Pillepich et al., 2019; Nelson et al., 2019b) from the IllustrisTNG simulation suite (Marinacci et al., 2018; Naiman et al., 2018; Pillepich et al., 2018b; Nelson et al., 2018; Springel et al., 2018), and the hydrodynamic runs of the Rhea simulation suite (Göller et al., 2025).

TNG50 is a cosmological simulation encompassing a simulation box with a side-length of 51.7 comoving Mpc, including DM, a magnetohydrodynamical treatment of gas, stochastic star formation controlled by a density threshold, SN feedback and feedback from black holes. In this simulation we identify 780 jellyfish galaxies at different redshifts with the help of volunteers via visual classification. These jellyfish galaxies in TNG50 develop self-consistently from satellite galaxies falling into galaxy clusters and getting stripped of their gas. The long covered timespan in TNG50 allows us to follow the galaxies through different evolutionary stages and their corresponding star formation.

With this, in Chapter 3 we investigate the effect of ram-pressure stripping (a process controlled by the extragalactic environment of a galaxy cluster) on the star formation within the stripped galaxy. In particular, we address the question of

whether jellyfish galaxies show enhanced star formation rates compared to other, non-stripped star-forming galaxies, as suggested by some observations. For the general jellyfish population, we find no such effect.

However, even though they undergo extreme ram-pressure stripping, i.e., lose a lot of their gas, we find jellyfish galaxies to be typically not quenched, but still star-forming. We find star formation in the region of the main stellar bodies of the galaxies, but, more interestingly, also in the stripped gaseous tails, even though the SFR in the tails is much subdominant to the main body. The global SFR of the jellyfish galaxies, despite the stripping, is comparable to that of non-jellyfish counterparts with comparable galactic properties. In general, the SFR is well below that of the SFMS, even though at each redshift we also find jellyfish galaxies with SFRs exceeding the SFMS. This is explained by the fact that, when we follow the individual evolutionary paths of jellyfish galaxies, for the vast majority of them we find periods of star-bursts, during which their SFR exceeds that of the SFMS. However, we do not find a general, population-wide enhancement of SFR in jellyfish galaxies.

The discrepancies between the findings of our study of simulated jellyfish galaxies, which do not show a general SFR enhancement, and the observational studies finding such an increased SFR in jellyfish galaxies, therefore could be explained by a natural observational bias towards star-bursting galaxies. Since, from our study, most jellyfish galaxies undergo such a star-burst phase, observations might be more prone to find jellyfish galaxies during this phase, as they are brighter and therefore easier to observe.

Rhea, the second used simulation, is an isolated galaxy simulation of a Milky Way analog, tailored to resemble the Galaxy in terms of mass and dynamical features. It does not cover the full emergence of the Galaxy, but rather its evolution over a timespan of about 4 Gyr. The studied simulations include a hydrodynamical treatment of gas, stochastic star formation controlled by the local Jeans mass, SN feedback and a chemical network accounting for hydrogen and CO chemistry. The adoption of two different external gravitational potentials allows for a detailed examination of the influence of different (non-axisymmetric) potential components.

In Chapter 4 we move our focus to processes internal to a galaxy that might influence their star formation behavior. We particularly investigate the influence of the galaxy's gravitational potential on the star formation. Since a cosmological

simulation like TNG50 does not allow for a detailed control of the gravitational potential, we choose to conduct simulations of an isolated Milky Way analog with a modifiable external potential, the Rhea simulations. We find that the details of the potential influence *where* stars form within the galaxy. On the other hand, global SFR properties are only mildly affected.

We compare a completely axisymmetric potential, analytically targeted to reproduce a flat velocity curve, with a potential fitted to several dynamical features observed in the Milky Way, containing a non-axisymmetric bar and spiral arm potential. The bar potential has greater influence on the galaxy morphology than the spiral arm component. Spiral arms emerge in the axisymmetric potential from gas instabilities and, on a single snapshot basis, resemble that formed by the adopted spiral arm potential rather well. However, we find them to be more short-lived, whereas the explicit spiral arm potential serves as an efficient snow-plow, collecting gas and stars and thereby increasing the SFR within its potential wells. The bar potential channels a steady inflow of gas towards the galactic center, which fuels star formation there. Therefore, the galactic center in a barred potential does not quench and shows higher SFRs than in the axisymmetric potential. This also results in increased stellar feedback in the galactic center. A barred potential moreover changes the properties of star-forming regions and the corresponding clustering of SN in the galactic center. It makes star-forming regions more compact and lowers the time between the first and last formed star. Groups of SN are more compact and have a shorter activity time than in a non-barred potential as well.

From this we deduce the non-axisymmetric bar potential to have the strongest influence on star formation in a Milky Way-like spiral galaxy. Other parts of the potential, such as a spiral arm potential, alter the star formation only little. In general, the change of gravitational potential only redistributes star formation within the galaxy, but leaves the global SFR mostly unaltered, i.e., the global SFR is mostly controlled by the gas available to star formation, which is identical in both conducted simulations. This result might seem trivial, however, it is conceivable that the gravitational potential might alter the SFE, as it is hypothesized for spiral arms (see Section 1.2.2), thus altering also the global SFR of a galaxy. In our simulations, we see no such effect; changes in SFR can always be traced back to more available gas.

At this point we also want to make the reader aware that a change of the local

SFR of a galaxy can have dramatic effects on its appearance. We find this to be the case in the Rhea simulations as well, as we find the emergence of eRosita bubble-like structures (Predehl et al., 2020) in our Rhea simulations using the MW potential, but not in those using the flat potential. The eRosita bubbles observed in the Milky Way are X-ray analogs to the famous Fermi bubbles (Dobler et al., 2010; Su et al., 2010). We are able to trace back these structures to the increased SN rate and more compact clustering of SN in the galactic center using the MW potential compared to the flat potential. We currently prepare our findings regarding these structures in Girichidis et al., in prep.

In Chapter 5 we finally investigate how the star formation behavior might influence observational properties that we use to derive general properties of the observed galactic system. We do so by connecting the rotation curve, which we derive from our simulations, to the SFR-profile of the simulated galaxies.

We find an – in principle – very intuitive connection: The region of star formation in our galactic disks is smaller than the stellar disk we find, i.e., the outer stellar disk in our simulation is populated purely by star particles that migrated to this position. The radial profile of the stellar surface density therefore has the form of a broken exponential with one scale length in the region where stars are actively formed, and a different, steeper one in the region populated by migrating star particles. To derive the galactic rotation curve from the measured azimuthal velocities, assumptions (if not known) about the density distribution in the galaxy have to be made. If the density distribution is modeled with just a single exponential, instead of the (in our case) true broken exponential distribution, the resulting rotation curve shows an increased decline in the migrator-dominated region of the stellar disk. This results from the lowered azimuthal velocities of the migrators in this region, which have highly eccentric orbits. When the rotation curve is translated into an enclosed mass of the galaxy, as is often done, this decline can mimic a cut-off in the galactic mass distribution that is not based on reality. If the broken exponential profile is adopted, this effect is properly compensated and the decline in the rotation curve, and the corresponding mass cut-off, vanishes.

We propose this as an alternative explanation for the reports of a Keplerian decline in the outer stellar rotation curve of the Milky Way reported in recent studies (e.g., Jiao et al., 2023).

6.2 Open Questions and Uncertainties

We just discussed the strengths and results of the analyses presented in this thesis. However, simulations always use model systems which simplify the true conditions of a real galaxy. These simplifications have to be handled with care regarding the interpretation of results. In our simulations, possible shortcomings mainly fall into one of the three categories: Lack of resolution, abstraction in subgrid models and the complete absence of physical processes.

Both simulation setups, Rhea and TNG50, have aspects in which their limited resolution in time and space can reduce the informative value of the results of our studies. The nature of Arepo, the underlying framework of both setups, is that of a moving mesh. Spatial resolution therefore adapts to the local density, however, in low-density regions like the tails of jellyfish galaxies, this can lead to problems. Knots of dense gas in these regions in TNG50 might be under-resolved, which, in turn, can result in an underestimation of SFR in the tails of jellyfish galaxies. However, since we find star formation in jellyfish galaxies to be severely dominated by the galactic main stellar body, we expect this to affect the global SFR of the studied galaxies very little. In Rhea, we reach higher spatial resolution than in TNG50, but it is nevertheless limited by our lower bound of 1 pc. Gas cells are not allowed to get smaller than this, which hinders the formation of any structure on scales smaller than this. This means that, while we can resolve GMCs, clumps and cores are not properly resolved, the same is true for details of the galactic center. This limited resolution is also reflected in star particles, as they inherit the mass of their parent gas cell, i.e., less massive gas cells result in less massive (and more) star particles.

The simulations are not only limited in spatial, but also in time resolution. Especially the cadence of simulation outputs has to be taken into account. For TNG50, this cadence is about 150 Myr, i.e., processes acting on shorter timescales cannot be captured from the simulation outputs alone. As in Chapter 3 we examine the star formation rate history of individual galaxies, we have to take into account that star bursts with a duration lower than the output cadence can be lost from our study. However, we find star bursts to typically cover several snapshots and therefore assume this to be a minor problem. In Rhea, the same is true, even though the output cadence is about a factor of 30 higher. For the time-dependent studies we conduct in this thesis, we expect any influence to be minor, as any time developments we

see are quite steady in nature. However, for future analyses of more short-term processes, such as the development of SN-driven bubbles, this has to be accounted for.

The main subgrid models of interest in our simulations are the formation of star particles and also the SN feedback. For the formation of star particles, in TNG50 the main point of concern is the fact that it is controlled by a simple density threshold (even though the subsequent process is stochastic) and is therefore agnostic to any additional gas properties, such as temperature, magnetic fields or flows, which might support or hinder the star formation. Moreover, the star formation process is calibrated to observed galaxy scalings in the present day Universe, and therefore matches best the star formation in the main body of isolated galaxies. This means that in regions where the conditions differ significantly from that (like in tails of ram-pressure stripped galaxies) the star formation might not be modeled appropriately. Again, as the total star formation in jellyfish galaxies is dominated by the galactic body, we do not expect significant influence on the main outcome of the study. For Rhea, the problem is a bit less severe, as the beginning of the star formation process is controlled by the Jeans mass, i.e., takes the internal energy of the gas into account. However, it still excludes aspects such as the convergence or divergence of flows or the presence of gravitational potentials.

At this point, we also want to point towards the peculiarities of the star particle treatment in Rhea. As explained in Section 1.4.1 and 2.3.3, star particles form from gas fulfilling the formation requirements and are subsequently decoupled from it. Contrary to the often used sink particles, they do not accrete gas from their surrounding, and all stars within the star particle are formed at the same time, the formation time of the star particle. This, of course, is a highly unnatural treatment of star formation, especially for star particles as massive as the ones used in our analysis. The stellar population within a star particle is treated as a highly dense, mono-age population without any chance of divergence. Stars born together in a star particle stay so for the rest of the simulation lifetime. This treatment therefore will, to some degree, lack dynamics and spread in stellar ages. On small scales, this might for example lead to a degree of clustering in stellar feedback too high for a proper comparison to the real Universe. On large scales, however, we do not expect the effects to be severe. As we form a multitude of star particles in the simulations, the general spread in age of the stars is sufficient, and stars within observed star

clusters (which are the objects star particles are best comparable to) also show very similar ages. Moreover, this treatment of star formation makes star particles much more efficient than accreting sink particles. The decoupling of star particles from the gas means that no communication overhead from searching for neighboring gas cells occurs, which is constantly the case for sink particles. Only in the case of a SN explosion a star particle needs to search for its nearest gas cells. Moreover, sink particles are often treated such that they suppress the formation of more sink particles in their close environment (such as the sink particles used in Tress et al., 2020a,b; Sormani et al., 2020a). This also suppresses close gravitational interactions between them, which are especially interesting for the migration of stars within the galactic disk, as they might scatter stars to orbits different from their birth orbit. This is not the case for star particles, making them better suited for studies of stellar orbits over time, as we conduct them in Chapter 5.

Our treatment of SN feedback consists of the injection of thermal energy or momentum (controlled by the radius of the Sedov-Taylor phase) within a fixed radius around the star particle. This ignores any mass return from the exploding star, thus accelerating the gas depletion of the galaxy. However, the mass return from a single SN is a non-trivial question (Limongi & Chieffi, 2010a,b) and depends on several stellar properties, some of which we do not even simulate.

With this, we already reach the additional physical processes which are not (yet) included in the simulations. Such a limited model has some benefits, as it makes the study of the influences of individual processes more easy. On the other hand it, of course, limits the comparability to real astronomical systems and have to be kept in mind when comparing to observations.

Both, Rhea and TNG50, do not include pre-supernova feedback such as photoionization (TNG50 includes winds from AGB stars, though, Rhea does not include any winds) in their treatment of the ISM. This means that the regions in which SN explode are unprocessed and more dense than when such feedback is included. In Rhea, as multiple SN explode per star particle, we expect this to mainly affect the first of such SNe, lowering its efficiency as it might explode in a too dense environment. Since SNe are the energetically dominant feedback sources, we do not expect large changes for subsequent SN apart from extreme case of very massive clouds. On the cosmological scales of TNG50, the effects are most probably minor.

In the hydrodynamical runs of Rhea, we also ignore the galactic magnetic field,

which is known to have severe effects on the ISM structure of the Milky Way. However, this is just the case for the hydrodynamical runs analyzed in this thesis. The accompanying MHD and MHD+CR runs of Rhea include an magnetic field and also cosmic rays. Their effects are analyzed in companion works (e.g., Kjellgren et al., 2025).

As we model our Milky Way analog in Rhea as an isolated galaxy, we do not take into account any satellite galaxies, i.e., do not model any mergers or their influence on the galactic dynamics. In addition, our simulated galaxies do not have any noteworthy CGM, limiting their star formation as no replenishing of the gaseous disk from CGM takes place.

6.3 Future Plans for Rhea

In this thesis we presented the first 'proof-of-concept' runs from the Rhea simulation suite, characterizing the general model. Ultimately, the aim is a simulated reproduction of the observed Milky Way, as faithful to its known appearance as possible.

Subsequent runs will therefore increase the resolution significantly, reaching sub-pc scales in the galaxies densest regions. This will allow for the use of data from these simulations as initial conditions for simulations on even smaller scales, studying the formation of individual stars. In a second branch, we (already currently) conduct zoom-in simulations from the fiducial runs, targeted on regions of interest such as analogs of the Local Bubble (see the upcoming work of Shuyu Tan for this). Moreover, resimulations at higher time and spatial resolution of the eRosita bubble like structures are under conduction.

For these higher resolution simulations we will couple the star particles to pre-existing sink particles, allowing to switch between the two within one simulation. This will have the immediate advantage that the computationally efficient and fast star particles can be used in regions of low resolution, and then be switched to sink particles which are more suited to model star formation on small scales in a more realistic fashion. This will enable us to keep the full galactic context even when simulating just a small region at high resolution and to follow gas accretion in such regions.

We will also employ photoionization (via SWEEP, Peter et al., 2023) in the next simulation runs. This will result in more realistic stellar feedback, allowing for a better modeling of environments such as the Local Bubble and also outflows and bubble-like structures in the galactic center. Feedback from stellar winds is not yet implemented, but actively worked on and will probably be adopted in a future generation of Rhea.

In the current simulations including CRs, we use the so called 'grey' approach, i.e., do not model the full spectrum of CRs but instead give them an effective energy. A selection of future runs will move one step further, adopting a full spectral treatment of CRs. As CRs are an important component in the Galaxies energy budget, this will enable use to model CR related processes such as galactic outflows more realistically and to follow them in more detail.

With the first iteration of Rhea simulations, we lay a solid foundation for future works. They will and do serve as a basis for development of even more elaborate simulations, which will enable qualitative and quantitative comparisons of a simulated Milky Way to observations. The controlled experiments in the computer made possible by these will lead to further insight into the interplay between physical processes shaping the Galaxy.

7 Acknowledgments

An ancient academic proverb says “It takes a village to earn a PhD”, and throughout the years of learning, working, studying, teaching, getting frustrated and being delighted by the endless obstacles and joys of PhD life, I found this to be true again and again. There are so many people to thank for this incredible experience, and I surely cannot express my gratitude enough, but I will try my best.

Of all the people, I first want to thank Prof. Ralf Klessen for the chance to conduct the research presented here in his group, but also for his immeasurable support and advice I received during my time at ITA. I am truly grateful to work with and learn from a person like you.

My gratitude also belongs to Prof. Jim Hinton for agreeing to be the second corrector of this thesis, and to Prof. Henrik Beuther and Prof. Jörg Jäckel for serving as examiners at my PhD examination. Your work is greatly appreciated.

I thank Dr. Annalisa Pillepich for being a real role model in my life, for supporting and challenging me throughout my masters and also my PhD. Your guidance and support have been invaluable in shaping me into the scientist I am today.

A big “Thank you!” also belongs to Prof. Simon Glover, for being on my thesis committee, but more so for the countless talks and mails explaining the chemistry network of Arepo to me. And, of course, also for taking the time to proofread, comment and improve this thesis.

To Dr. Philipp Girichidis I literally owe my sanity (and perhaps some cheese). Without you, I would not have made it this far (no, really!) and would probably have choked on a sarcastic comment at some point. Oh yeah, and thanks for correcting my thesis! So, yes, cheese it is for you.

It was a pleasure to work with Dr. Noé Brucy, who has one of the greatest minds and the most unjustifiably poor opinion on German food. Thanks for your tips, your dedication, and your patience, but really, it’s not that bad.

There are countless more awesome people at ITA that I had and have the chance

to work with: Karin Kjellgren (Tack så mycket), Dr. Robin Tress (Danke/Grazie), Jia Wei Teh (感謝您所做的一切，祝您擁有世界上最好的鋼琴, and also thanks a lot for the proofreading), Dr. Glen Hunter (Thank you, my dear), Loke Ohlin (Tack så mycket), Dr. Joe Lewis (Merci), Paul Meehan (Danke für den Kaffee), Dr. Lise Ramambason (Merci pour tout, especially for the proofreading), Andrea Romanelli (Grazie, e per favore prendetevi cura del drago), Nika Lipatova (Дякую), Carolin Kimmig (Danke dir), Andrej Herrmann (Dankeschön), Dr. David Whitworth (Thanks a lot), Dr. Viktor Ksoll (Danke), Dr. Stefan Reißl (Danke), Prof. Mattia Sormani (Grazie), Shuyu Tan (謝謝), Aaron Kordt (Danke), Katrin Lehle (Danke dir).

Of course, there are awe-inspiring people outside of ITA as well. The people of the ECOGAL consortium were a wonderful group to work with. Especially Dr. Juan Soler I have to thank for the invaluable insight into an observers mind I got through him, and for sharing his observational data.

Moreover, I want to thank Dr. Davide Elia and Prof. Przemysław Mróz for generously sharing their data and Prof. Hans-Walter Rix for the interesting and helpful discussion.

Dr. Rüdiger Pakmor was the greatest help whenever Arepo was not working as intended. Thanks a lot!

And again Dr. David Whitworth, Dr. Noe Brucy, Dr. Robin Tress - because Manchester. Without you, this conference could not have happened. It was a wonderful (exhausting, though) experience.

Even though one might not expect it, there are great people even outside of astronomy! Dr. Carina Mathy-Peckmann, my oldest, dearest friend. Thank you for being by my side, honoring me with your friendship. After all this time, this is done.

Maurice Morgenthaler, having you as a friend is like a warm hug all day long. Thank you for being there, even when I was not. And a big “Thanks!” to Penelope Hoffmann for the proofreading.

Niklas Conen, look at us, nearly 10 years later. I made it, you will make it (I believe in you). Now you can mock me all you want. Oh, and thanks for the help with numerical theory.

My infamous “das Lerngruppe”, you are the reason I did not quit years ago. For that alone, you guys deserve all the praise. Thanks for being the most epic group of friends one could ever imagine.

And my family, of course, old and new. Mom, dad, Naëmi, thanks for your everlasting trust in my abilities, and your unwavering support through the ups and downs of this journey. I can feel your love every second. Rita, Harry, thank you for taking me into your family and treating me as one of your own. I am more grateful for that than you could ever imagine. Thank you!

And, most important of all, Felix, my favorite human. You are the steady rock in my life that I stand upon to reach for the stars. Thank you for being all I ever asked for, and more. I cannot wait for the rest of our life together.

List of Publications

Parts of this thesis have been published or prepared in the following articles

- J. Göller, G. D. Joshi, E. Rohr, E. Zinger, A. Pillepich. *Jellyfish galaxies with the IllustrisTNG simulations - No enhanced population-wide star formation according to TNG50.* MNRAS, 525(3):3551-3570, Nov. 2023. DOI: 10.1093/mnras/stad2551

- J. Göller, P. Girichidis, N. Brucy, G. Hunter, K. Kjellgren, R. Tress, R. S. Klessen, S. C. O. Glover, P. Hennebelle, S. Molinari, R. Smith, J. D. Soler, M. C. Sormani, L. Testi. *Introducing the Rhea simulations of Milky-Way-like galaxies I - Effect of gravitational potential on morphology and star formation.* Subm. to A&A, DOI: 10.48550/arXiv.2502.02646

Additional publications with co-authorship relevant to this thesis:

- G. H. Hunter, M. C. Sormani, J. P. Beckmann, E. Vasiliev, S. C. O. Glover, R. S. Klessen, J. D. Soler, N. Brucy, P. Girichidis, J. Göller, L. Ohlin, R. Tress, S. Molinari, O. Gerhard, R. Smith, P. Hennebelle, L. Testi. *Testing kinematic distances under a realistic Galactic potential: Investigating systematic errors in the kinematic distance method arising from a non-axisymmetric potential.* A&A, 692, id.A216, Dec. 2024. DOI:10.1051/0004-6361/202450000

- K. Kjellgren, P. Girichidis, J. Göller, N. Brucy, R. S. Klessen, R. Tress, J. D. Soler, C. Pfrommer, M. Werhahn, S. C. O. Glover, R. Smith, L. Testi, S. Molinari. *The dynamical impact of cosmic rays in the Rhea magnetohydrodynamics simulations.* Subm. to A&A, DOI: 10.48550/arXiv.2502.02635

Bibliography

Aartsen M. G., et al., 2013, Phys. Rev. D, 88, 042004

Abadi M. G., Moore B., Bower R. G., 1999, MNRAS, 308, 947

Abadi M. G., Navarro J. F., Steinmetz M., Eke V. R., 2003, ApJ, 597, 21

Abadi M. G., Navarro J. F., Steinmetz M., 2006, MNRAS, 365, 747

Abbott D. C., 1982, ApJ, 263, 723

Abel T., Anninos P., Zhang Y., Norman M. L., 1997, New Astron., 2, 181

Ablimit I., Zhao G., 2017, ApJ, 846, 10

Abrahamsson E., Krems R. V., Dalgarno A., 2007, ApJ, 654, 1171

Agertz O., et al., 2021, MNRAS, 503, 5826

Aguerri J. A. L., Méndez-Abreu J., Corsini E. M., 2009, A&A, 495, 491

Alimi J.-M., et al., 2012, arXiv e-prints, p. arXiv:1206.2838

Alinder S., McMillan P. J., Bensby T., 2024, A&A, 690, A15

Allende Prieto C., 2010, in Cunha K., Spite M., Barbuy B., eds, IAU Symposium Vol. 265, Chemical Abundances in the Universe: Connecting First Stars to Planets. pp 304–312 (arXiv:0911.3598), doi:10.1017/S1743921310000785

Attwood R. E., Goodwin S. P., Stamatellos D., Whitworth A. P., 2009, A&A, 495, 201

Bakes E. L. O., Tielens A. G. G. M., 1994, ApJ, 427, 822

Ballesteros-Paredes J., Klessen R. S., Mac Low M. M., Vazquez-Semadeni E., 2007, in Reipurth B., Jewitt D., Keil K., eds, Protostars and Planets V. p. 63 (arXiv:astro-ph/0603357), doi:10.48550/arXiv.astro-ph/0603357

Barnes J. E., 1989, Nature, 338, 123

Barnes J., Hut P., 1986, Nature, 324, 446

Bate M. R., Bonnell I. A., Price N. M., 1995, MNRAS, 277, 362

Bauer A., Springel V., 2012, MNRAS, 423, 2558

Beck R., 2015, A&AR, 24, 4

Beck R., Wielebinski R., 2013, in Oswalt T. D., Gilmore G., eds, , Vol. 5, Planets, Stars and Stellar Systems. Volume 5: Galactic Structure and Stellar Populations. p. 641, doi:10.1007/978-94-007-5612-0_13

Bell K. L., Berrington K. A., Thomas M. R. J., 1998, MNRAS, 293, L83

Bell E. F., et al., 2004, ApJ, 608, 752

Belokurov V., 2013, New Astron. Rev., 57, 100

Benedettini M., et al., 2020, A&A, 633, A147

Benincasa S. M., Wadsley J., Couchman H. M. P., Keller B. W., 2016, MNRAS, 462, 3053

Benjamin R. A., 2009, in Andersen J., Nordströara m B., Bland-Hawthorn J., eds, IAU Symposium Vol. 254, The Galaxy Disk in Cosmological Context. pp 319–322, doi:10.1017/S1743921308027750

Benjamin R. A., et al., 2005, ApJ Letters, 630, L149

Bergin E. A., Tafalla M., 2007, Annu. Rev. Astron. Astrophys., 45, 339

Berkhuijsen E. M., 1999, in Plasma Turbulence and Energetic Particles in Astrophysics. pp 61–65

Bertola F., 2009, in Rubiño-Martín J., Belmonte J., Prada F., Alberdi A., eds, Astronomical Society of the Pacific Conference Series Vol. 409, Cosmology Across Cultures. p. 237

Bertram E., Federrath C., Banerjee R., Klessen R. S., 2012, MNRAS, 420, 3163

Besla G., Kallivayalil N., Hernquist L., Robertson B., Cox T. J., van der Marel R. P., Alcock C., 2007, ApJ, 668, 949

Beuther H., et al., 2016, A&A, 595, A32

Bigiel F., Leroy A., Walter F., Brinks E., de Blok W. J. G., Madore B., Thornley M. D., 2008, AJ, 136, 2846

Binney J., Tremaine S., 2008, Galactic Dynamics: Second Edition

Birdsall C. K., Fuss D., 1969, Journal of Computational Physics, 3, 494

Black J. H., Dalgarno A., 1977, ApJSuppl., 34, 405

Bland-Hawthorn J., Gerhard O., 2016, ARA&A, 54, 529

Blitz L., 1993, in Protostars and Planets III. pp 125–161

Blondin J. M., Wright E. B., Borkowski K. J., Reynolds S. P., 1998, ApJ, 500, 342

Bodenheimer P. H., 2011, Principles of Star Formation, doi:10.1007/978-3-642-15063-0.

Bonamente M., Joy M. K., LaRoque S. J., Carlstrom J. E., Reese E. D., Dawson K. S., 2006, ApJ, 647, 25

Bondi H., Hoyle F., 1944, MNRAS, 104, 273

Boselli A., Gavazzi G., 2006, PASP, 118, 517

Boselli A., et al., 2016, A&A, 587, A68

Boselli A., Fossati M., Sun M., 2022, The Astronomy and Astrophysics Review 2022, 30, 1

Boulares A., Cox D. P., 1990, ApJ, 365, 544

Bourke T. L., Myers P. C., Robinson G., Hyland A. R., 2001, ApJ, 554, 916

Bournaud F., Combes F., 2002, A&A, 392, 83

Bournaud F., Combes F., Semelin B., 2005, MNRAS, 364, L18

Bournaud F., Elmegreen B. G., Elmegreen D. M., 2007, ApJ, 670, 237

Bovy J., et al., 2012, ApJ, 759, 131

Bower R. G., Balogh M. L., 2004, in Mulchaey J. S., Dressler A., Oemler A., eds, Clusters of Galaxies: Probes of Cosmological Structure and Galaxy Evolution. p. 325 (arXiv:astro-ph/0306342), doi:10.48550/arXiv.astro-ph/0306342

Bromm V., Yoshida N., Hernquist L., McKee C. F., 2009, Nature, 459, 49

Brook C. B., Gibson B. K., Martel H., Kawata D., 2005, ApJ, 630, 298

Brunthaler A., et al., 2021, A&A, 651, A85

Buck T., Obreja A., Macciò A. V., Minchev I., Dutton A. A., Ostriker J. P., 2020, MNRAS, 491, 3461

Burkert A., 2006, Comptes Rendus Physique, 7, 433

Burton M. G., Hollenbach D. J., Tielens A. G. G. M., 1990, ApJ, 365, 620

Butcher H., Oemler Jr. A., 1984, ApJ, 285, 426

Callingham T. M., et al., 2019, MNRAS, 484, 5453

Campello R. J. G. B., Moulavi D., Sander J., 2013, in Pei J., Tseng V. S., Cao L., Motoda H., Xu G., eds, Advances in Knowledge Discovery and Data Mining. Springer Berlin Heidelberg, Berlin, Heidelberg, pp 160–172

Carey S. J., et al., 2009, PASP, 121, 76

Carney B. W., Seitzer P., 1993, AJ, 105, 2127

Carniani S., et al., 2024, Nature, 633, 318

Carroll B. W., Ostlie D. A., 2017, An introduction to modern astrophysics, Second Edition

Caselli P., Benson P. J., Myers P. C., Tafalla M., 2002, The Astrophysical Journal, 572, 238

Castor J. I., Abbott D. C., Klein R. I., 1975, ApJ, 195, 157

Cen R., 1992, ApJSuppl., 78, 341

Chabrier G., 2003a, PASP, 115, 763

Chabrier G., 2003b, ApJL, 586, L133

Chandrasekhar S., Fermi E., 1953, ApJ, 118, 113

Chatzopoulos S., Fritz T. K., Gerhard O., Gillessen S., Wegg C., Genzel R., Pfuhl O., 2015, MNRAS, 447, 948

Chen B. Q., et al., 2017, MNRAS, 464, 2545

Chevance M., et al., 2020, MNRAS, 493, 2872

Chevance M., et al., 2022, MNRAS, 509, 272

Chomiuk L., Povich M. S., 2011, AJ, 142, 197

Chua K. T. E., Pillepich A., Rodriguez-Gomez V., Vogelsberger M., Bird S., Hernquist L., 2017, MNRAS, 472, 4343

Clark P. C., Glover S. C. O., Klessen R. S., 2012, MNRAS, 420, 745

Clark P. C., Glover S. C. O., Ragan S. E., Duarte-Cabral A., 2019, MNRAS, 486, 4622

Coleman B., Paterson D., Gordon C., Macias O., Ploeg H., 2020, MNRAS, 495, 3350

Cooper A. P., Parry O. H., Lowing B., Cole S., Frenk C., 2015, MNRAS, 454, 3185

Corbelli E., et al., 2017, A&A, 601, A146

Correa Magnus L., Vasiliev E., 2022, MNRAS, 511, 2610

Courant R., Friedrichs K., Lewy H., 1928, Mathematische Annalen, 100, 32

Crain R. A., et al., 2015, MNRAS, 450, 1937

Cramer W. J., Kenney J. D. P., Sun M., Crowl H., Yagi M., Jáchym P., Roediger

E., Waldron W., 2019, ApJ, 870, 63

Crocker R. M., 2012, MNRAS, 423, 3512

Crocker R. M., Aharonian F., 2011, Phys.Rev.Lett., 106, 101102

Crutcher R. M., 1999, ApJ, 520, 706

Crutcher R. M., Wandelt B., Heiles C., Falgarone E., Troland T. H., 2010, ApJ, 725, 466

Daniel K. J., Schaffner D. A., McCluskey F., Fiedler Kawaguchi C., Loebman S., 2019, ApJ, 882, 111

Davé R., Anglés-Alcázar D., Narayanan D., Li Q., Rafieferantsoa M. H., Appleby S., 2019, MNRAS, 486, 2827

Davis M., Efstathiou G., Frenk C. S., White S. D. M., 1985, ApJ, 292, 371

Dedner A., Kemm F., Kröner D., Munz C.-D., Schnitzer T., Wesenberg M., 2002, Journal of Computational Physics, 175, 645

Demachi F., et al., 2024, Publications of the Astronomical Society of Japan, 76, 1059–1083

Dicaire I., Carignan C., Amram P., Marcelin M., Hlavacek-Larrondo J., de Denus-Baillargeon M. M., Daigle O., Hernandez O., 2008, AJ, 135, 2038

Dobbs C. L., Theis C., Pringle J. E., Bate M. R., 2010, MNRAS, 403, 625

Dobbs C. L., Burkert A., Pringle J. E., 2011a, MNRAS, 413, 2935

Dobbs C. L., Burkert A., Pringle J. E., 2011b, MNRAS, 417, 1318

Dobler G., Finkbeiner D. P., Cholis I., Slatyer T., Weiner N., 2010, ApJ, 717, 825

Domainko W., et al., 2006, A&A, 452, 795

Donnari M., et al., 2019, MNRAS, 485, 4817

Donnari M., et al., 2020, MNRAS, 500, 4004

Donnari M., Pillepich A., Nelson D., Marinacci F., Vogelsberger M., Hernquist L., 2021, MNRAS, 506, 4760

Douvion T., Lagage P. O., Cesarsky C. J., Dwek E., 2001, A&A, 373, 281

Draine B. T., 1978, ApJSuppl., 36, 595

Draine B. T., 2011, Physics of the Interstellar and Intergalactic Medium

Draine B. T., Bertoldi F., 1996, The Astrophysical Journal, 468, 269

Draine B. T., Lee H. M., 1984, ApJ, 285, 89

Dressler A., 1980, ApJ, 236, 351

Drimmel R., 2000, A&A, 358, L13

Drlica-Wagner A., et al., 2020, ApJ, 893, 47

Dubois Y., Teyssier R., 2008, A&A, 477, 79

Duley W. W., Williams D. A., 1981, MNRAS, 196, 269

Dunne L., Eales S., Ivison R., Morgan H., Edmunds M., 2003, Nature, 424, 285

Eadie G., Jurić M., 2019, ApJ, 875, 159

Ebeling H., Stephenson L. N., Edge A. C., 2014, ApJ Letters, 781, L40

Eilers A.-C., Hogg D. W., Rix H.-W., Ness M. K., 2019, ApJ, 871, 120

Einasto J., 1969, Astronomische Nachrichten, 291, 97

Einasto M., et al., 2007, A&A, 476, 697

Eisenhauer F., Schödel R., Genzel R., Ott T., Tecza M., Abuter R., Eckart A., Alexander T., 2003, ApJ Letters, 597, L121

Elia D., et al., 2022, ApJ, 941, 162

Elias L. M., Sales L. V., Creasey P., Cooper M. C., Bullock J. S., Rich R. M., Hernquist L., 2018, MNRAS, 479, 4004

Elmegreen B. G., Elmegreen D. M., Chromey F. R., Hasselbacher D. A., Bissell B. A., 1996, AJ, 111, 2233

Endres C. P., Schlemmer S., Schilke P., Stutzki J., Müller H. S. P., 2016, Journal of Molecular Spectroscopy, 327, 95

Eskridge P. B., Frogel J. A., 1999, Astrophys. Space Sci., 269-270, 427

Evans II N. J., et al., 2009, ApJSuppl., 181, 321

Fattahi A., et al., 2016, MNRAS, 457, 844

Faucher-Giguère C.-A., Lidz A., Zaldarriaga M., Hernquist L., 2009, ApJ, 703, 1416

Federrath C., Banerjee R., Clark P. C., Klessen R. S., 2010, ApJ, 713, 269

Feng Y., Di-Matteo T., Croft R. A., Bird S., Battaglia N., Wilkins S., 2016, MNRAS, 455, 2778

Ferland G. J., Peterson B. M., Horne K., Welsh W. F., Nahar S. N., 1992, ApJ, 387, 95

Ferland G. J., Korista K. T., Verner D. A., Ferguson J. W., Kingdon J. B., Verner E. M., 1998, PASP, 110, 761

Ferland G. J., et al., 2013, RMxAA, 49, 137

Ferland G. J., et al., 2017, RMxAA, 53, 385

Ferriere K. M., 1995, ApJ, 441, 281

Ferrière K. M., 2001, Reviews of Modern Physics, 73, 1031–1066

Ferziger J. H., Perić M., Street R. L., 2020, Numerische Strömungsmechanik. Springer Vieweg

Feuillet D. K., Frankel N., Lind K., Frinchaboy P. M., García-Hernández D. A., Lane R. R., Nitschelm C., Roman-Lopes A., 2019, MNRAS, 489, 1742

Fich M., Blitz L., Stark A. A., 1989, ApJ, 342, 272

Fichtner Y. A., Mackey J., Grassitelli L., Romano-Díaz E., Porciani C., 2024, A&A, 690, A72

Field G. B., Saslaw W. C., 1965, ApJ, 142, 568

Field G. B., Goldsmith D. W., Habing H. J., 1969, ApJ, 155, L149

Flower D. R., Launay J. M., 1977, Journal of Physics B Atomic Molecular Physics, 10, 3673

Font A. S., McCarthy I. G., Crain R. A., Theuns T., Schaye J., Wiersma R. P. C., Dalla Vecchia C., 2011, MNRAS, 416, 2802

Fossati M., Fumagalli M., Boselli A., Gavazzi G., Sun M., Wilman D. J., 2016, MNRAS, 455, 2028

Foyle K., Rix H. W., Walter F., Leroy A. K., 2010, ApJ, 725, 534

Freedman W. L., Madore B. F., Scowcroft V., Burns C., Monson A., Persson S. E., Seibert M., Rigby J., 2012, ApJ, 758, 24

Freudenreich H. T., 1998, ApJ, 492, 495

Fryxell B., et al., 2000, ApJSuppl., 131, 273

Furlong M., et al., 2015, MNRAS, 450, 4486

GRAVITY Collaboration et al., 2019, A&A, 625, L10

Gaia Collaboration et al., 2023, A&A, 674, A1

Gatto A., et al., 2015, MNRAS, 449, 1057

Genel S., et al., 2014, MNRAS, 445, 175

Gensior J., Feldmann R., Mayer L., Wetzel A., Hopkins P. F., Faucher-Giguère C.-A., 2023, MNRAS, 518, L63

Gerola H., Seiden P. E., 1978, ApJ, 223, 129

Gingold R. A., Monaghan J. J., 1977, MNRAS, 181, 375

Giovanelli R., Haynes M. P., 1985, ApJ, 292, 404

Girichidis P., Seifried D., Naab T., Peters T., Walch S., Wünsch R., Glover S. C. O., Klessen R. S., 2018, MNRAS, 480, 3511

Girichidis P., et al., 2020, Space Science Reviews, 216, 1

Glover S. C. O., Abel T., 2008, MNRAS, 388, 1627

Glover S. C. O., Clark P. C., 2012, MNRAS, 421, 116

Glover S. C. O., Jappsen A. K., 2007, ApJ, 666, 1

Glover S. C. O., Mac Low M.-M., 2007a, ApJSuppl., 169, 239

Glover S. C. O., Mac Low M.-M., 2007b, ApJ, 659, 1317

Glover S. C. O., Federrath C., Mac Low M. M., Klessen R. S., 2010, MNRAS, 404, 2

Goicovic F. G., Springel V., Ohlmann S. T., Pakmor R., 2019, MNRAS, 487, 981

Goldbaum N. J., Krumholz M. R., Matzner C. D., McKee C. F., 2011, ApJ, 738, 101

Goldreich P., Lynden-Bell D., 1965, MNRAS, 130, 125

Goldsmith P. F., Langer W. D., 1978, ApJ, 222, 881

Göller J., Joshi G. D., Rohr E., Zinger E., Pillepich A., 2023, MNRAS, 525, 3551

Göller J., et al., 2025, arXiv e-prints, p. arXiv:2502.02646

Górski K. M., Hivon E., Banday A. J., Wandelt B. D., Hansen F. K., Reinecke M., Bartelmann M., 2005, ApJ, 622, 759

Gould R. J., Salpeter E. E., 1963, Astrophysical Journal, vol. 138, p. 393, 138, 393

Grand R. J. J., Kawata D., Cropper M., 2015, MNRAS, 447, 4018

Grand R. J. J., et al., 2017, MNRAS, 467, 179

Gravity Collaboration et al., 2023, A&A, 677, L10

Greif T. H., Springel V., White S. D. M., Glover S. C. O., Clark P. C., Smith R. J., Klessen R. S., Bromm V., 2011, ApJ, 737, 75

Groves B. A., Cho J., Dopita M., Lazarian A., 2003, PASA, 20, 252

Grudić M. Y., Guszejnov D., Hopkins P. F., Offner S. S. R., Faucher-Giguère C.-A., 2021, MNRAS, 506, 2199

Guesten R., Mezger P. G., 1982, Vistas in Astronomy, 26, 159

Gullieuszik M., et al., 2020, ApJ, 899, 13

Gunn J. E., Gott III J. R., 1972, ApJ, 176, 1

Gunn J. E., Knapp G. R., Tremaine S. D., 1979, AJ, 84, 1181

Habing H., 1968, Bulletin of the Astronomical Institutes of the Netherlands, Vol. 19, p. 421, 19, 421

Haffner L. M., Reynolds R. J., Tufte S. L., Madsen G. J., Jaehnig K. P., Percival J. W., 2003, ApJSuppl., 149, 405

Hammer F., Puech M., Chemin L., Flores H., Lehnert M. D., 2007, ApJ, 662, 322

Han J. L., 2017, ARA&A, 55, 111

Hani M. H., Gosain H., Ellison S. L., Patton D. R., Torrey P., 2020, MNRAS, 493, 3716

Hayato A., et al., 2010, ApJ, 725, 894

Heesen V., et al., 2023, A&A, 669, A8

Helmi A., 2008, A&AR, 15, 145

Helmi A., White S. D. M., de Zeeuw P. T., Zhao H., 1999, Nature, 402, 53

Hocuk S., Szűcs L., Caselli P., Cazaux S., Spaans M., Esplugues G. B., 2017, A&A, 604, A58

Hodge P. W., 1983, PASP, 95, 721

Höfner S., Gautschy-Loidl R., Aringer B., Jørgensen U. G., 2003, A&A, 399, 589

Hollenbach D., McKee C. F., 1979, ApJSuppl., 41, 555

Hollenbach D., McKee C. F., 1989, ApJ, 342, 306

Hollenbach D., Salpeter E. E., 1971, ApJ, 163, 155

Hou L. G., Han J. L., 2014, A&A, 569, A125

Hoyle F., Lyttleton R. A., 1939, Proceedings of the Cambridge Philosophical Society, 35, 405

Huang Y., et al., 2016, MNRAS, 463, 2623

Hunt E. L., Reffert S., 2021, A&A, 646, A104

Hunter G. H., Clark P. C., Glover S. C. O., Klessen R. S., 2023, MNRAS, 519, 4152

Hunter G. H., et al., 2024, A&A, 692, A216

Hwang H. S., Shin J., Song H., 2019, MNRAS, 489, 339

Hyginus n.d., De astronomia

Ibata R. A., Wyse R. F. G., Gilmore G., Irwin M. J., Suntzeff N. B., 1997, AJ, 113, 634

Immer K., Schuller F., Omont A., Menten K. M., 2012, A&A, 537, A121

Jáchym P., et al., 2019, ApJ, 883, 145

Jeffreson S. M. R., Kruijssen J. M. D., 2018, MNRAS, 476, 3688

Jeffreson S. M. R., Kruijssen J. M. D., Keller B. W., Chevance M., Glover S. C. O., 2020, MNRAS, 498, 385

Jeffreson S. M. R., Ostriker E. C., Kim C.-G., Gensior J., Bryan G. L., Davis T. A., Hernquist L., Hassan S., 2024, ApJ, 975, 113

Jiao Y., Hammer F., Wang H., Wang J., Amram P., Chemin L., Yang Y., 2023, A&A, 678, A208

Jijina J., Myers P., Adams F. C., 1999, The Astrophysical Journal Supplement Series, 125, 161

Joshi G. D., Pillepich A., Nelson D., Zinger E., Marinacci F., Springel V., Vogelsberger M., Hernquist L., 2021, MNRAS, 508, 1652

Junqueira T. C., Lépine J. R. D., Braga C. A. S., Barros D. A., 2013, A&A, 550, A91

Jurić M., et al., 2008, ApJ, 673, 864

Kafle P. R., Sharma S., Lewis G. F., Bland-Hawthorn J., 2012, ApJ, 761, 98

Kalberla P. M. W., Dedes L., 2008, A&A, 487, 951

Kalberla P. M. W., Kerp J., 2009, ARA&A, 47, 27

Kalberla P. M. W., Dedes L., Kerp J., Haud U., 2007, A&A, 469, 511

Kapferer W., Sluka C., Schindler S., Ferrari C., Ziegler B., 2009, A&A, 499, 87

Kauffmann G., et al., 2003, MNRAS, 341, 33

Kawamura A., et al., 2009, ApJSuppl., 184, 1

Kazantzidis S., Bullock J. S., Zentner A. R., Kravtsov A. V., Moustakas L. A., 2008, ApJ, 688, 254

Keenan F. P., Lennon D. J., Johnson C. T., Kingston A. E., 1986, MNRAS, 220, 571

Kennicutt R. C. J., 1983, AJ, 88, 483

Kennicutt Jr. R. C., 1998, ApJ, 498, 541

Kennicutt R. C., Evans N. J., 2012, ARA&A, 50, 531

Kim C.-G., Ostriker E. C., 2015, ApJ, 802, 99

Kim J., Balsara D., Mac Low M.-M., 2001, Journal of Korean Astronomical Society, 34, 333

Kim W.-T., Kim C.-G., Ostriker E. C., 2020, ApJ, 898, 35

Kjellgren K., et al., 2025, arXiv e-prints, p. arXiv:2502.02635

Klessen R. S., Hennebelle P., 2010, A&A, 520, A17

Klingenberg C., 2017, in Abgrall R., Shu C.-W., eds, Handbook of Numerical Analysis, Vol. 18, Handbook of Numerical Methods for Hyperbolic Problems. Elsevier, pp 465–477, doi:https://doi.org/10.1016/bs.hna.2016.11.001, `https://www.sciencedirect.com/science/article/pii/S1570865916300412`

Knabner P., Angermann L., 2000, Numerik partieller Differentialgleichungen. Springer

Knacke R. F., Thomson R. K., 1973, PASP, 85, 341

Komatsu E., et al., 2009, ApJSuppl., 180, 330

Konstantinou A., Ntormousi E., Tassis K., Pallottini A., 2024, A&A, 686, A8

Kordopatis G., et al., 2011, A&A, 535, A107

Kramer C., Stutzki J., Rohrig R., Corneliussen U., 1998, Astronomy and Astrophysics, 329, 249

Kronberger T., Kapferer W., Ferrari C., Unterguggenberger S., Schindler S., 2008, A&A, 481, 337

Kroupa P., 2001, MNRAS, 322, 231

Kroupa P., 2002, Science, 295, 82

Kruijssen J. M. D., Longmore S. N., Elmegreen B. G., Murray N., Bally J., Testi L., Kennicutt R. C., 2014, MNRAS, 440, 3370

Krumholz M. R., Tan J. C., 2007, ApJ, 654, 304

Kukstas E., et al., 2023, MNRAS, 518, 4782

La Marca A., et al., 2024, A&A, 690, A326

Lada C. J., Forbrich J., Petitpas G., Viaene S., 2024, ApJ, 966, 193

Larson R. B., Tinsley B. M., Caldwell C. N., 1980, ApJ, 237, 692

Latter W. B., Black J. H., 1991, Astrophysical Journal, Part 1 (ISSN 0004-637X), vol. 372, May 1, 1991, p. 161-166. NSERC-supported research., 372, 161

Launhardt R., Zylka R., Mezger P. G., 2002, A&A, 384, 112

Lazarian A., 2007, JQSRT, 106, 225

LeVeque R. J., 2002, Numerik partieller Differentialgleichungen. Cambridge University Press

Lee E. J., Miville-Deschênes M.-A., Murray N. W., 2016, ApJ, 833, 229

Lee J. H., Lee M. G., Mun J. Y., Cho B. S., Kang J., 2022, ApJ Letters, 931, L22

Leger A., Puget J. L., 1984, A&A, 137, L5

Lepp S., Shull J. M., 1983, ApJ, 270, 578

Leroy A. K., et al., 2017, ApJ, 846, 71

Levine E. S., Heiles C., Blitz L., 2008, ApJ, 679, 1288

Li Q., Narayanan D., Torrey P., Davé R., Vogelsberger M., 2021, MNRAS, 507, 548

Lian J., et al., 2022, MNRAS, 511, 5639

Licquia T. C., Newman J. A., 2015, ApJ, 806, 96

Limongi M., Chieffi A., 2010a, in Journal of Physics Conference Series. IOP, p. 012002, doi:10.1088/1742-6596/202/1/012002

Limongi M., Chieffi A., 2010b, in Tanihara I., Ong H. J., Tamii A., Kishimoto T., Kajino T., Kubono S., Shima T., eds, American Institute of Physics Conference Series Vol. 1269, 10th International Symposium on Origin of Matter and Evolution of Galaxies: OMEG - 2010. AIP, pp 110–119, doi:10.1063/1.3485121

Lin C. C., Shu F. H., 1964, ApJ, 140, 646

Łokas E. L., 2019, A&A, 629, A52

Longmore S. N., et al., 2013, MNRAS, 429, 987

Loren R. B., 1989, Astrophysical Journal, 338, 925

Lucy L. B., 1977, AJ, 82, 1013

Lynden-Bell D., 1979, MNRAS, 187, 101

Lynden-Bell D., Lynden-Bell R. M., 1995, MNRAS, 275, 429

Mac Low M.-M., Klessen R. S., 2004, Reviews of Modern Physics, 76, 125

Mac Low M. M., Shull J. M., 1986, ApJ, 302, 585

Mackey J., Walch S., Seifried D., Glover S. C. O., Wünsch R., Aharonian F., 2019,

MNRAS, 486, 1094

Madau P., Dickinson M., 2014, ARA&A, 52, 415

Maeder A., 2008, Physics, formation and evolution of rotating stars. Springer Science & Business Media

Majewski S. R., Skrutskie M. F., Weinberg M. D., Ostheimer J. C., 2003, ApJ, 599, 1082

Malhan K., et al., 2022, ApJ, 926, 107

Manna S., Roy S., 2023, ApJ, 944, 86

Marcolini A., Brighenti F., D'Ercole A., 2003, MNRAS, 345, 1329

Marinacci F., et al., 2018, MNRAS, 480, 5113

Martin P. G., Schwarz D. H., Mandy M. E., 1996, ApJ, 461, 265

Martin P. G., Keogh W. J., Mandy M. E., 1998, ApJ, 499, 793

Martizzi D., Faucher-Giguère C.-A., Quataert E., 2015, MNRAS, 450, 504

Mathis J. S., Rumpl W., Nordsieck K. H., 1977, ApJ, 217, 425

Mathis J. S., Mezger P. G., Panagia N., 1983, A&A, 128, 212

May J., Bronfman L., Alvarez H., Murphy D. C., Thaddeus P., 1993, A&AS, 99, 105

McCarthy I. G., Font A. S., Crain R. A., Deason A. J., Schaye J., Theuns T., 2012, MNRAS, 420, 2245

McCarthy I. G., Schaye J., Bird S., Le Brun A. M. C., 2017, MNRAS, 465, 2936

McKee C. F., Ostriker J. P., 1977, ApJ, 218, 148

McMillan P. J., 2017, MNRAS, 465, 76

Meidt S. E., et al., 2015, ApJ, 806, 72

Minter A. H., Spangler S. R., 1997, ApJ, 485, 182

Mistani P. A., et al., 2016, MNRAS, 455, 2323

Mocz P., Burkhart B., Hernquist L., McKee C. F., Springel V., 2017, ApJ, 838, 40

Molinari S., et al., 2010, A&A, 518, L100

Molinari S., et al., 2011, ApJ Letters, 735, L33

Monaghan J. J., 1992, ARA&A, 30, 543

Moon S., Kim W.-T., Kim C.-G., Ostriker E. C., 2021, ApJ, 914, 9

Moore B., Katz N., Lake G., Dressler A., Oemler A., 1996, Nature, 379, 613

Moretti A., et al., 2020, ApJ Letters, 897, L30

Motte F., André P., Neri R., 1998, Astronomy and Astrophysics, v. 336, p. 150-172 (1998), 336, 150

Motwani B., et al., 2022, ApJ, 926, 139

Mróz P., et al., 2019, ApJ Letters, 870, L10

Muñoz D. J., Kratter K., Springel V., Hernquist L., 2014, MNRAS, 445, 3475

Mueller M. W., Arnett W. D., 1976, ApJ, 210, 670

Müller A., et al., 2021, Nature Astronomy, 5, 159

Mun J. Y., Hwang H. S., Lee M. G., Chung A., Yoon H., Lee J. C., 2021, Journal of Korean Astronomical Society, 54, 17

Murray N., Rahman M., 2010, ApJ, 709, 424

Naiman J. P., et al., 2018, MNRAS, 477, 1206

Neal R., 2011, in , Handbook of Markov Chain Monte Carlo. pp 113–162, doi:10.1201/b10905

Nelson R. P., Langer W. D., 1997, ApJ, 482, 796

Nelson D., et al., 2018, MNRAS, 475, 624

Nelson D., et al., 2019a, Computational Astrophysics and Cosmology 2019, 6, 1

Nelson D., et al., 2019b, MNRAS, 490, 3234

Nelson D., et al., 2020, MNRAS, 498, 2391

Neufeld D. A., Kaufman M. J., 1993, ApJ, 418, 263

Neufeld D. A., Lepp S., Melnick G. J., 1995, ApJSuppl., 100, 132

Newberg H. J., et al., 2002, ApJ, 569, 245

Niklas S., Beck R., 1997, A&A, 320, 54

Noordermeer E., van der Hulst J. M., Sancisi R., Swaters R. S., van Albada T. S., 2007, MNRAS, 376, 1513

O'Neill T. J., Zucker C., Goodman A. A., Edenhofer G., 2024, ApJ, 973, 136

Oka T., Hasegawa T., Sato F., Tsuboi M., Miyazaki A., Sugimoto M., 2001, The Astrophysical Journal, 562, 348

Oort J. H., 1954, Bull Astron Inst Neth, 12, 177

Ortega-Martinez S., Obreja A., Dominguez-Tenreiro R., Pedrosa S. E., Rosas-Guevara Y., Tissera P. B., 2022, MNRAS, 516, 197

Ortolani S., Renzini A., Gilmozzi R., Marconi G., Barbuy B., Bica E., Rich R. M., 1995, Nature, 377, 701

Ou X., Eilers A.-C., Necib L., Frebel A., 2024, MNRAS, 528, 693

Pakmor R., Springel V., 2013, MNRAS, 432, 176

Palla F., Salpeter E. E., Stahler S. W., 1983, ApJ, 271, 632

Parker E. N., 1966, ApJ, 145, 811

Peñarrubia J., Ma Y.-Z., Walker M. G., McConnachie A., 2014, MNRAS, 443, 2204

Pequignot D., 1990, A&A, 231, 499

Pequignot D., 1996, (Erratum) Populations of the O I metastable levels., Astronomy and Astrophysics, v.313, p.1026-1026

Persic M., Salucci P., Stel F., 1996, MNRAS, 281, 27

Peter T., Klessen R. S., Kanschat G., Glover S. C. O., Bastian P., 2023, MNRAS, 519, 4263

Peterson J. R., Fabian A. C., 2006, Phys. Rep., 427, 1

Pettitt A. R., Dobbs C. L., Acreman D. M., Price D. J., 2014, MNRAS, 444, 919

Pfrommer C., Pakmor R., Schaal K., Simpson C. M., Springel V., 2017, MNRAS, 465, 4500

Pillepich A., Madau P., Mayer L., 2015, ApJ, 799, 184

Pillepich A., et al., 2018a, MNRAS, 473, 4077

Pillepich A., et al., 2018b, MNRAS, 475, 648

Pillepich A., et al., 2019, MNRAS, 490, 3196

Pillepich A., Nelson D., Truong N., Weinberger R., Martin-Navarro I., Springel V., Faber S. M., Hernquist L., 2021, MNRAS, 508, 4667

Planck Collaboration et al., 2016, A&A, 594, A13

Planck Collaboration et al., 2020, A&A, 641, A6

Plummer H. C., 1911, MNRAS, 71, 460

Poggianti B. M., et al., 2016, The Astronomical Journal, 151, 78

Poggianti B. M., et al., 2017, ApJ, 844, 48

Pohlen M., Trujillo I., 2006, A&A, 454, 759

Polido P., Jablonski F., Lépine J. R. D., 2013, ApJ, 778, 32

Pont F., Queloz D., Bratschi P., Mayor M., 1997, A&A, 318, 416

Portail M., Gerhard O., Wegg C., Ness M., 2017, MNRAS, 465, 1621

Posti L., Helmi A., 2019, A&A, 621, A56

Potter D., Stadel J., Teyssier R., 2017, Computational Astrophysics and Cosmology, 4, 2

Powell K. G., Roe P. L., Linde T. J., Gombosi T. I., De Zeeuw D. L., 1999, Journal of Computational Physics, 154, 284

Predehl P., et al., 2020, Nature, 588, 227

Predehl P., et al., 2021, A&A, 647, A1

Pringle J., Allen R. J., Lubow S., 2001, MNRAS, 327, 663

Querejeta M., et al., 2021, A&A, 656, A133

Querejeta M., et al., 2024, arXiv e-prints, p. arXiv:2405.05364

Quinn P. J., Hernquist L., Fullagar D. P., 1993, ApJ, 403, 74

Ragan S. E., Moore T. J. T., Eden D. J., Hoare M. G., Urquhart J. S., Elia D., Molinari S., 2018, MNRAS, 479, 2361

Ramatsoku M., et al., 2020, A&A, 640, A22

Ramesh R., Nelson D., Pillepich A., 2023, MNRAS,

Ramos-Martínez M., Gómez G. C., Pérez-Villegas Á., 2018, MNRAS, 476, 3781

Rees M. J., Ostriker J. P., 1977, MNRAS, 179, 541

Reid M. J., Menten K. M., Zheng X. W., Brunthaler A., Xu Y., 2009, ApJ, 705, 1548

Renaud F., et al., 2013, MNRAS, 436, 1836

Reynolds S. P., 2008, ARA&A, 46, 89

Rhee J., et al., 2024, ApJ, 971, 111

Riess A. G., et al., 2009, ApJ, 699, 539

Riess A. G., et al., 2022, ApJ Letters, 934, L7

Rigby A. J., et al., 2016, MNRAS, 456, 2885

Roberts I. D., et al., 2021a, A&A, 650, A111

Roberts I. D., van Weeren R. J., McGee S. L., Botteon A., Ignesti A., Rottgering H. J. A., 2021b, A&A, 652, A153

Roberts I. D., et al., 2022, ApJ, 941, 77

Rodriguez-Gomez V., et al., 2015, MNRAS, 449, 49

Roediger E., 2009, Astronomische Nachrichten, 330, 888

Roediger E., Brüggen M., 2006, MNRAS, 369, 567

Roediger E., Bruggen M., Owers M. S., Ebeling H., Sun M., 2014, MNRAS, 443, L114

Rohr E., Pillepich A., Nelson D., Zinger E., Joshi G. D., Ayromlou M., 2023, MNRAS, 524, 3502

Roman-Duval J., Jackson J. M., Heyer M., Rathborne J., Simon R., 2010, ApJ, 723, 492

Röttgers B., Naab T., Oser L., 2014, MNRAS, 445, 1065

Roškar R., Debattista V. P., Quinn T. R., Stinson G. S., Wadsley J., 2008, ApJ Letters, 684, L79

Rubin V. C., Ford Jr. W. K., Thonnard N., 1980, ApJ, 238, 471

Ruszkowski M., Pfrommer C., 2023, A&AR, 31, 4

Safarzadeh M., Loeb A., 2019, MNRAS: Letters, 486, L26

Salpeter E. E., 1955, ApJ, 121, 161

Sandin C., Höfner S., 2004, A&A, 413, 789

Scaloni L., et al., 2024, A&A, 687, A255

Schaye J., et al., 2015, MNRAS, 446, 521

Schmidt M., 1959, ApJ, 129, 243

Schmidt W., Federrath C., 2011, A&A, 528, A106

Schneider P., 2015, Extragalactic Astronomy and Cosmology: An Introduction, doi:10.1007/978-3-642-54083-7.

Schönrich R., Aumer M., Sale S. E., 2015, ApJ Letters, 812, L21

Schuller F., et al., 2009, Astronomy & Astrophysics, 504, 415

Schuller F., et al., 2017, A&A, 601, A124

Schulz N. S., 2012, The Formation and early evolution of stars: from dust to stars and planets. Springer Science & Business Media

Searle L., Zinn R., 1978, ApJ, 225, 357

Sedov L. I., 1959, Similarity and Dimensional Methods in Mechanics

Seigar M. S., James P. A., 2002, MNRAS, 337, 1113

Sellwood J. A., Binney J. J., 2002, MNRAS, 336, 785

Sellwood J. A., Carlberg R. G., 1984, ApJ, 282, 61

Sembach K. R., Howk J. C., Ryans R. S. I., Keenan F. P., 2000, ApJ, 528, 310

Seo W.-Y., Kim W.-T., 2013, ApJ, 769, 100

Seo W.-Y., Kim W.-T., Kwak S., Hsieh P.-Y., Han C., Hopkins P. F., 2019, ApJ, 872, 5

Shapiro P. R., Kang H., 1987, ApJ, 318, 32

Sheen Y.-K., et al., 2017, ApJ Letters, 840, L7

Shen J., Zheng X.-W., 2020, Research in Astronomy and Astrophysics, 20, 159

Shu F. H., 1992, The physics of astrophysics. Volume II: Gas dynamics.

Shu F. H., 2016, ARA&A, 54, 667

Siegel M. H., Majewski S. R., Reid I. N., Thompson I. B., 2002, ApJ, 578, 151

Sijacki D., Vogelsberger M., Genel S., Springel V., Torrey P., Snyder G. F., Nelson D., Hernquist L., 2015, MNRAS, 452, 575

Silva A. I., Viegas S. M., 2002, MNRAS, 329, 135

Simpson C. M., Pakmor R., Marinacci F., Pfrommer C., Springel V., Glover S. C. O., Clark P. C., Smith R. J., 2016, ApJ Letters, 827, L29

Skillman S. W., Warren M. S., Turk M. J., Wechsler R. H., Holz D. E., Sutter P. M., 2014, arXiv e-prints, p. arXiv:1407.2600

Smith M. C., 2018, PhD thesis, University of Cambridge, UK

Smith R. J., et al., 2020, MNRAS, 492, 1594

Smith M. C., Bryan G. L., Somerville R. S., Hu C.-Y., Teyssier R., Burkhart B., Hernquist L., 2021, MNRAS, 506, 3882

Sofue Y., Honma M., Omodaka T., 2009, PASJ, 61, 227

Soler J. D., et al., 2023, A&A, 678, A95

Sormani M. C., Treß R. G., Klessen R. S., Glover S. C. O., 2017, MNRAS, 466, 407

Sormani M. C., et al., 2019, MNRAS, 488, 4663

Sormani M. C., Tress R. G., Glover S. C. O., Klessen R. S., Battersby C. D., Clark P. C., Hatchfield H. P., Smith R. J., 2020a, MNRAS, 497, 5024

Sormani M. C., Magorrian J., Nogueras-Lara F., Neumayer N., Schönrich R., Klessen R. S., Mastrobuono-Battisti A., 2020b, MNRAS, 499, 7

Sormani M. C., Gerhard O., Portail M., Vasiliev E., Clarke J., 2022, MNRAS, 514,

L1

Sormani M. C., Sobacchi E., Sanders J. L., 2024, MNRAS, 528, 5742

Sotillo-Ramos D., et al., 2022, MNRAS, 516, 5404

Speagle J. S., Steinhardt C. L., Capak P. L., Silverman J. D., 2014, ApJSuppl., 214, 15

Spitzer L., 1968, Diffuse matter in space

Springel V., 2005, MNRAS, 364, 1105

Springel V., 2010a, ARA&A, 48, 391

Springel V., 2010b, MNRAS, 401, 791

Springel V., Hernquist L., 2003, MNRAS, 339, 289

Springel V., White S. D. M., Tormen G., Kauffmann G., 2001, MNRAS, 328, 726

Springel V., et al., 2005, Nature, 435, 629

Springel V., Frenk C. S., White S. D. M., 2006, Nature, 440, 1137

Springel V., et al., 2018, MNRAS, 475, 676

Stecher T. P., Williams D., 1967, Astrophysical Journal,(Ltrs), 149, p. L29, 1967., 149, L29

Steinhauser D., Schindler S., Springel V., 2016, A&A, 591, A51

Steinmetz M., 2012, Astronomische Nachrichten, 333, 523

Stewart K. R., Bullock J. S., Wechsler R. H., Maller A. H., Zentner A. R., 2008, ApJ, 683, 597

Stil J. M., et al., 2006, AJ, 132, 1158

Strömgren B., 1939, ApJ, 89, 526

Strong A. W., Moskalenko I. V., Ptuskin V. S., 2007, Annual Review of Nuclear and Particle Science, 57, 285

Stuber S. K., et al., 2023, A&A, 680, L20

Su M., Slatyer T. R., Finkbeiner D. P., 2010, ApJ, 724, 1044

Sun M., Donahue M., Roediger E., Nulsen P. E. J., Voit G. M., Sarazin C., Forman W., Jones C., 2010, ApJ, 708, 946

Sun J., et al., 2023, ApJ Letters, 945, L19

Suyu S. H., Marshall P. J., Auger M. W., Hilbert S., Blandford R. D., Koopmans L. V. E., Fassnacht C. D., Treu T., 2010, ApJ, 711, 201

Takahashi J., Uehara H., 2001, ApJ, 561, 843

Tasker E. J., Brunino R., Mitchell N. L., Michielsen D., Hopton S., Pearce F. R., Bryan G. L., Theuns T., 2008, MNRAS, 390, 1267

Tasker E. J., Wadsley J., Pudritz R., 2015, ApJ, 801, 33

Taylor G., 1950, Proceedings of the Royal Society of London Series A, 201, 159

Tecce T. E., Cora S. A., Tissera P. B., 2011, MNRAS, 416, 3170

Terrazas B. A., et al., 2020, MNRAS, 493, 1888

Teyssier R., 2002, A&A, 385, 337

Tissera P. B., Scannapieco C., Beers T. C., Carollo D., 2013, MNRAS, 432, 3391

Tokuue T., Ishiyama T., 2024, MNRAS, 528, 821

Tokuyama S., Oka T., Takekawa S., Iwata Y., Tsujimoto S., Yamada M., Furusawa M., Nomura M., 2019, PASJ, 71, S19

Tonnesen S., Bryan G. L., 2012, MNRAS, 422, 1609

Toomre A., 1964, ApJ, 139, 1217

Toomre A., 1977, in Tinsley B. M., Larson D. Campbell R. B. G., eds, Evolution of Galaxies and Stellar Populations. p. 401

Trenti M., et al., 2012, ApJ, 746, 55

Tress R. G., 2021, PhD thesis, Heidelberg University, Germany, doi:10.11588/heidok.00031003

Tress R. G., Smith R. J., Sormani M. C., Glover S. C. O., Klessen R. S., Mac Low M.-M., Clark P. C., 2020a, MNRAS, 492, 2973

Tress R. G., Sormani M. C., Glover S. C. O., Klessen R. S., Battersby C. D., Clark P. C., Hatchfield H. P., Smith R. J., 2020b, MNRAS, 499, 4455

Troncoso Iribarren P., Padilla N., Contreras S., Rodriguez S., García-Lambas D., Lagos C. d. P., 2016, Galaxies, 4, 77

Troncoso-Iribarren P., Padilla N., Santander C., Lagos C. D. P., García-Lambas D., Rodríguez S., Contreras S., 2020, MNRAS, 497, 4145

Vasiliev E., 2019, MNRAS, 482, 1525

Vega-Martínez C. A., Gómez F. A., Cora S. A., Hough T., 2022, MNRAS, 509, 701

Vera M., Alonso S., Coldwell G., 2016, A&A, 595, A63

Vieira K., Korchagin V., Carraro G., Lutsenko A., 2023, Galaxies, 11, 77

Villalobos Á., Helmi A., 2008, MNRAS, 391, 1806

Visser R., van Dishoeck E. F., Black J. H., 2009, A&A, 503, 323

Vogelsberger M., Genel S., Sijacki D., Torrey P., Springel V., Hernquist L., 2013, MNRAS, 436, 3031

Vogelsberger M., et al., 2014a, MNRAS, 444, 1518

Vogelsberger M., et al., 2014b, Nature, 509, 177

Vogelsberger M., Marinacci F., Torrey P., Puchwein E., 2020, Nature Reviews Physics, 2, 42

Voges W., et al., 1999, A&A, 349, 389

Vulcani B., et al., 2018, ApJ Letters, 866, L25

Vulcani B., et al., 2020, ApJ, 899, 98

Wadsley J. W., Stadel J., Quinn T., 2004, New Astron., 9, 137

Wadsley J. W., Veeravalli G., Couchman H. M. P., 2008, MNRAS, 387, 427

Wang T.-M., et al., 2022, A&A, 660, A142

Wang H.-F., Chrobáková Ž., López-Corredoira M., Sylos Labini F., 2023, ApJ, 942, 12

Waters L. B. F. M., 2004, in Witt A. N., Clayton G. C., Draine B. T., eds, Astronomical Society of the Pacific Conference Series Vol. 309, Astrophysics of Dust. p. 229

Watkins L. L., van der Marel R. P., Sohn S. T., Evans N. W., 2019, ApJ, 873, 118

Wegg C., Gerhard O., Portail M., 2015, MNRAS, 450, 4050

Wegg C., Gerhard O., Bieth M., 2019, MNRAS, 485, 3296

Weinberger R., et al., 2017, MNRAS, 465, 3291

Weinberger R., et al., 2018, MNRAS, 479, 4056

Weinberger R., Springel V., Pakmor R., 2020, ApJSuppl., 248, 32

Weingartner J. C., Draine B. T., 2001, ApJ, 563, 842

Wetzel A. R., Hopkins P. F., Kim J.-h., Faucher-Giguère C.-A., Kereš D., Quataert E., 2016, ApJ Letters, 827, L23

Whitworth D. J., et al., 2024, arXiv e-prints, p. arXiv:2407.18293

Wibking B. D., Krumholz M. R., 2023, MNRAS, 521, 5972

Wiener J., Zweibel E. G., Oh S. P., 2013, ApJ, 767, 87

Wiener J., Pfrommer C., Oh S. P., 2017, MNRAS, 467, 906

Williams J. P., De Geus E. J., Blitz L., 1994, The Astrophysical Journal, 428, 693

Wilson N. J., Bell K. L., 2002, MNRAS, 337, 1027

Wolfire M. G., McKee C. F., Hollenbach D., Tielens A. G. G. M., 2003, ApJ, 587, 278

Xu Y., Hao C. J., Liu D. J., Lin Z. H., Bian S. B., Hou L. G., Li J. J., Li Y. J., 2023, ApJ, 947, 54

Xue X.-X., Rix H.-W., Zhao G., 2009, Research in Astronomy and Astrophysics, 9, 1230

Yaz Gökçe E., et al., 2015, PASA, 32, e012

Yoon H., Chung A., Smith R., Jaffé Y. L., 2017, ApJ, 838, 81

Yoshida M., et al., 2008, ApJ, 688, 918

Yun K., et al., 2019, MNRAS, 483, 1042

Yusef-Zadeh F., et al., 2009, ApJ, 702, 178

Zari E., Frankel N., Rix H.-W., 2023, A&A, 669, A10

Zhou Y., Li X., Huang Y., Zhang H., 2023, ApJ, 946, 73

Zinger E., et al., 2020, MNRAS, 499, 768

Zinger E., Joshi G. D., Pillepich A., Rohr E., Nelson D., 2024, MNRAS, 527, 8257

Zobnina D. I., Zasov A. V., 2020, Astronomy Reports, 64, 295

Zucker C., et al., 2022, Nature, 601, 334

Zuckerman B., Palmer P., 1974, ARA&A, 12, 279

van der Marel R. P., Fardal M., Besla G., Beaton R. L., Sohn S. T., Anderson J., Brown T., Guhathakurta P., 2012, ApJ, 753, 8

Part I

Appendix

A Appendix to Chapter 3

This chapter is based on the appendix of Göller et al. (2023), published in Volume 525, Issue 3 of the Monthly Notices of the Royal Astronomical Society (MNRAS) in November 2023. Junia Göller, the author of this thesis, is the first author of the paper, conducted all analysis presented in this chapter, wrote the text and made all figures. Dr. Annalisa Pillepich and Dr. Gandhali Joshi contributed by working on the text.

A.1 Different measures for SFR

In this appendix, we use different methods to measure a galaxy's SFR, aiming for a study of robustness of results from Chapter 3.

A.1.1 Influence of Accounted Galaxy Volume

As mentioned in Section 3.2.3.1, output of TNG50 already provides several measurements of galactic SFR. In Chapter 3, we present results drawn from SFR within all gravitationally bound gas cells. A second measurement we use in this appendix is all star formation within $2 \times r_{1/2,*}$, which approximately covers the region where the stellar body of the galaxy is observable. By design, this value is lower than the one used in Chapter 3. We nevertheless include it to show that, in fact, a change to this SFR measure does not affect the outcome of our study in any significant way.

In the case of jellyfish galaxies, one has to keep in mind that, by taking into account only gas *currently* gravitationally bound to the galaxy one might miss gas from the extended gaseous tails, which is considered detached from the galaxy by SUBFIND. We therefore construct a third measure of SFR, which includes all gas that was bound to the galaxy at the time of its infall into its host halo. Some of this gas, by the time of measurement of the SFR, might not be bound to the galaxy any more, but form an extended tail in the wake of the jellyfish galaxy. We describe the

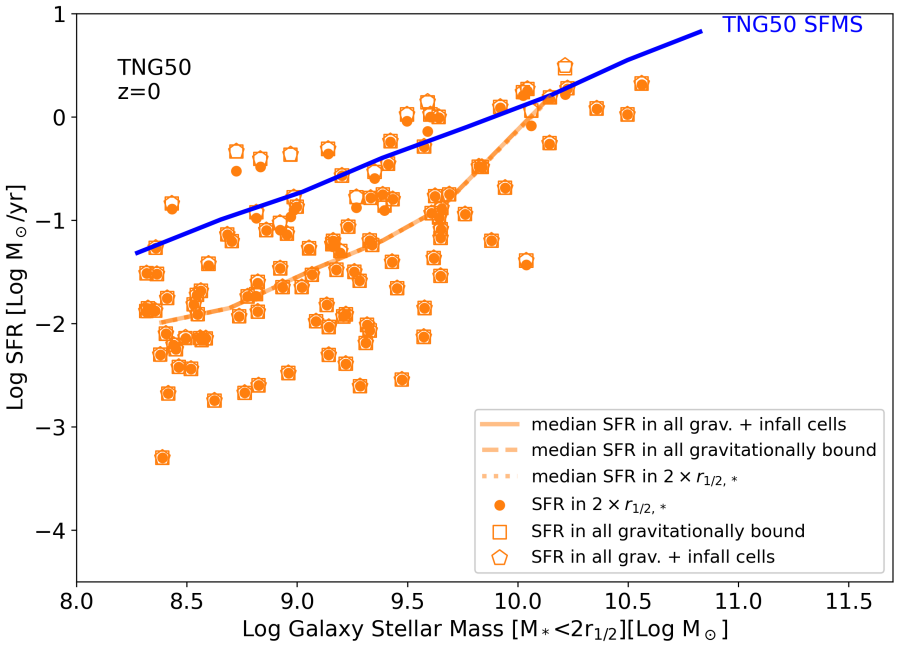

Figure A.1: Global SFR as a function of galactic stellar mass for jellyfish galaxies showing SFR within $2\times R^*_{1/2}$ (dot, dotted curve), all gravitationally bound gas (square, dashed curve) and with additional gas cells from galaxy infall (pentagon, solid curve). Any changes in SFR by changes in the accounted galactic volume is barely noticeable. Addition of cells from the time of the galaxy's infall also results in no noteworthy change in SFR.

exact method used to track these detached gas cells in Section A.1.2.

We contrast these three different measures of SFR as a function of galactic stellar mass for redshift $z = 0$ in Fig. A.1. It is apparent that the usage of different SFR measures does not greatly alter the overall global SFR of the galaxies from the jellyfish population. Star formation within $2 \times r_{1/2,*}$ (dots) already accounts for the majority of star formation in the galaxy. If one extends the measured SFR to that of all gravitationally bound gas (squares), this only results in a mild change of global SFR at best. Differences are only noticeable for jellyfish galaxies at the highest SFRs $> 10^{-2}\,\mathrm{M_\odot yr^{-1}}$.

When adding the SFR from gas cells that were bound to the galaxy at its time of infall, but have since become unbound (pentagons), one finds no further noticeable change in SFRs. We therefore conclude that this gas has no major impact on the global SFR of jellyfish galaxies. It mainly contributes to the jellyfish tails and shows

low star formation activity.

Most star formation in jellyfish galaxies in TNG50 therefore seems to take place within $2\times r_{1/2,*}$. Gas cells outside of this volume that are gravitationally bound contribute little to the overall SFR, gas cells unbound during the process of galactic infall into its host halo add no noteworthy star formation to the galaxy. As our interest includes jellyfish galaxies as a whole, including their bodies *and tails*, we decide to include SFR from all gravitationally bound gas in our analysis, instead of relying on the SFR within $2 \times r_{1/2,*}$. Otherwise we would underestimate the SFR of massive galaxies extending as far out, or even farther, than the stellar component. Whereas the addition of gas cells belonging to the galaxy at the time of infall draws a more complete picture of the jellyfish tail, we refrain from using this method, as we find no noticeable change in the SFR (compare squares and pentagons), and also not in the tails (compare dots and pentagons). Moreover, the adopted method for identification of additional gas cells presented in Section A.1.2 is not very rigorous, because in IllustrisTNG, gas cells can change their IDs.

A.1.2 Accounting for Gas Cells from the Time of Infall

In order to find gas cells that were bound to a galaxy at its time of infall, we first need to determine this infall time. This was done by Chua et al. (2017), who created the 'InfallCatalog' that contains the desired information. Merger trees connecting SUBFIND galaxies through the "SubLink_gal" algorithm of Rodriguez-Gomez et al. 2015 are provided in the IllustrisTNG simulations. These merger trees, however, do not contain information on the merger histories of the host FOF groups. To create the InfallCatalog, they instead trace back the central galaxy of each host halo and assume a direct link between the main branch of the host halo and the main branch of its central galaxy. Satellite galaxies are then traced back in time to the last snapshot in which their progenitors are not in the same FOF group as the progenitors of the central galaxy in their current host halo.

We thus obtain the progenitor of each jellyfish galaxy at its time of infall and query the IDs of their gas cells. We then track the same cell IDs at the current snapshot. Doing so, we assume that each gas cell keeps the same cell ID for all times, but this is not necessarily the case. However, in regions of low density and low star formation activity, sch as tails of jellyfish galaxies, this procedure can be

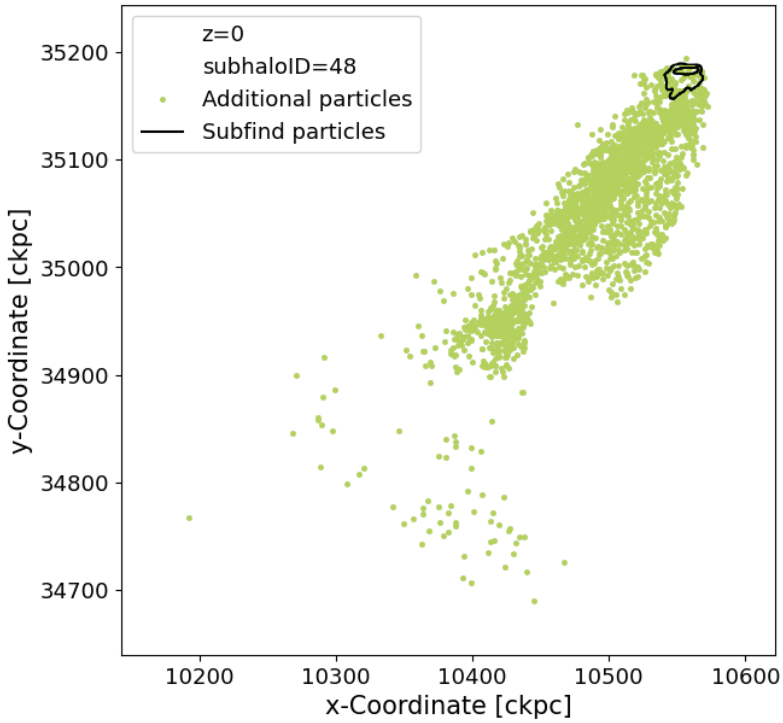

Figure A.2: Gas cells of galaxy 48 of TNG50 at $z = 0$. Black contours indicate the extent of gas bound to the galaxy identified by the SUBFIND algorithm. Green dots denote additional cells identified by the search for infall cells. The gaseous tail trailing the galaxy from additional cells ranges several hundreds of kpc wider than that identified by the SUBFIND algorithm.

justified, as processes changing cell IDs rarely occur there.

We present the result of this tracking of initial gas cells for an example galaxy in Fig. A.2. The gas cells traced from the infall time (green dots) form a low-density tail behind the galaxy identified by the SUBFIND algorithm (black contours) and extend it by several hundredth of kpc. We find this for many galaxies in our jellyfish sample. Potentially, these cells could alter global properties of the galaxies we study, however, as shown in the previous section, the inclusion of these cells has a negligible impact on the global SFRs and therefore do not affect the results we present in Chapter 3.

B Appendix to Chapter 4

This chapter is based on the appendix of Göller et al. (2025), submitted to Astronomy & Astrophysics. Junia Göller is the first author of this paper, conducted all the analysis presented there, wrote all the text and made all figures.

B.1 Outcome of Phase I

As mentioned in Section 2.3.2, before the phase we analyze in Chapter 4, an initial phase I takes place. During this phase, the galaxies evolve from the smooth gaseous density distribution set on initial conditions to a structured galaxy, which we start our simulation from.

These start and end points of phase I we show in Fig. B.1 in a projection along the y and z axis. The left panel depicts the smooth initial density distribution as it

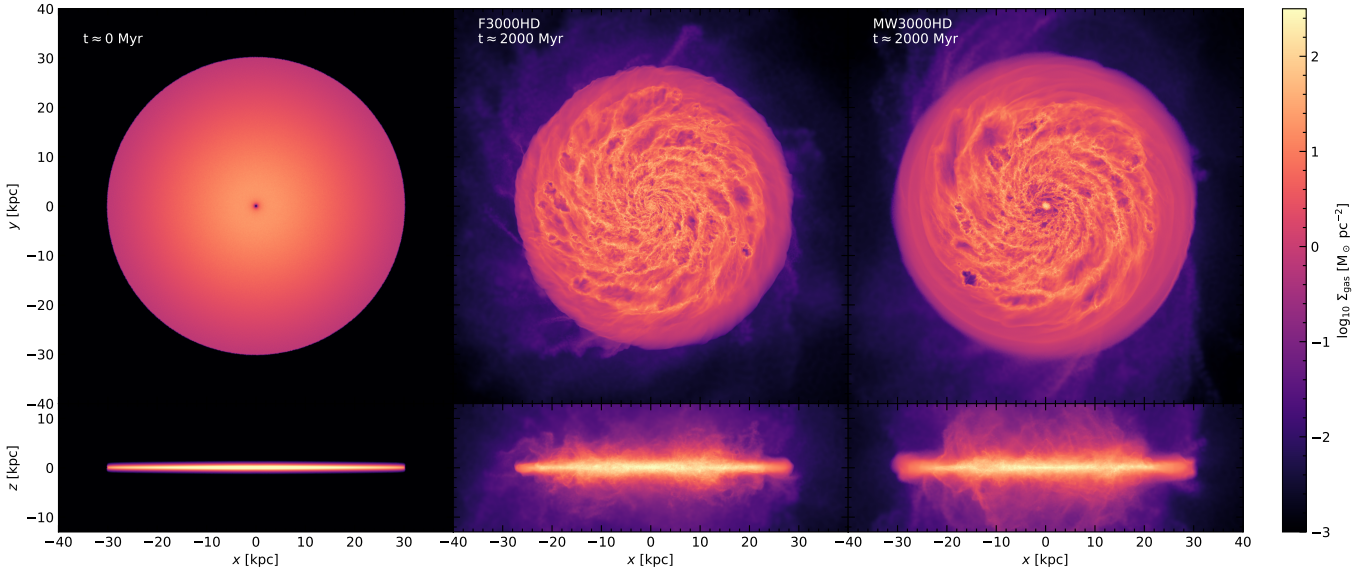

Figure B.1: Projected gas surface density at $t = 0$ Myr (initial conditions) and at the end of phase I for both simulations.

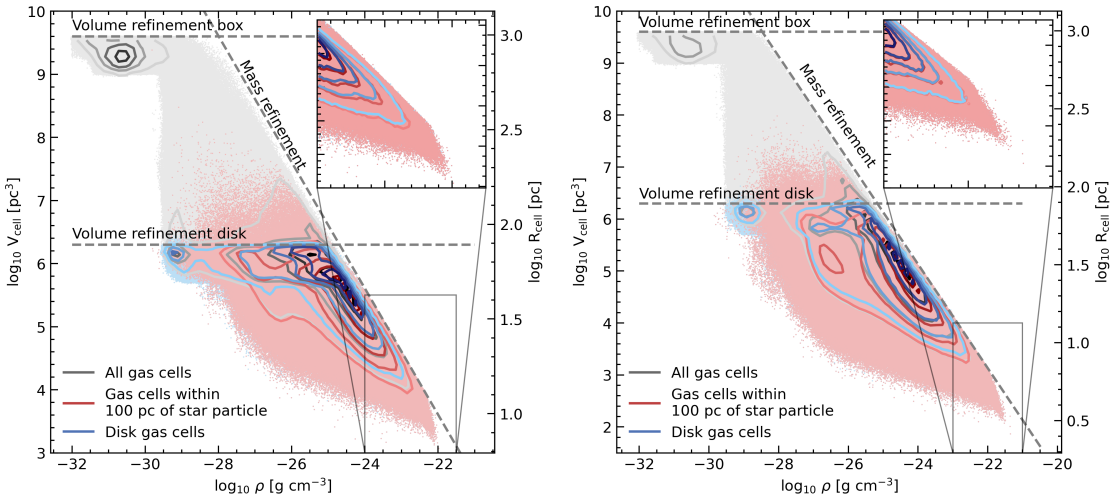

Figure B.2: Volume-density distribution of cells in F3000HD (left) and F1000HD (right) at a simulation time of about 2500 Myr. The shown contour levels enclose 10%, 30%, 50%, 70% and 90% of cells.

is set from Equation 2.16, the other two panels show the evolved state at the end of phase I for F3000HD (middle panel) and MW3000HD (right panel). At this time, we already see the general structure prevalent also in Fig. 4.2 and B.5.

During this phase, due to numerical limitations in the mesh refinement, we loose some SN that explode in regions of strongly diverging gas motion. In F3000HD, this applies to about 2 % of all SN, in MW3000HD about 6 % of SN are affected. During phase II, the phase analyzed in Chapter 4 and 5, this fraction lowers to about 0.6 % for both simulations.

B.2 Resolution Study

To test the convergence of our conducted simulations, we run both potentials also at a higher mass resolution of 1000 $M_\odot$, where we see very good agreement with our fiducial runs at 3000 $M_\odot$ resolution.

In Fig. B.2 we present the cell sizes within our simulation box as a function gas density for F3000HD (left) and F1000HD (right) at our fiducial analysis time in phase II. Due to the lower target mass in the higher resolution run, the gas cells reach lower sizes and higher densities (up to $\sim 10^{-21.4}$ g cm^{-3} compared to $\sim 10^{-22}$ g cm^{-3}), as expected.

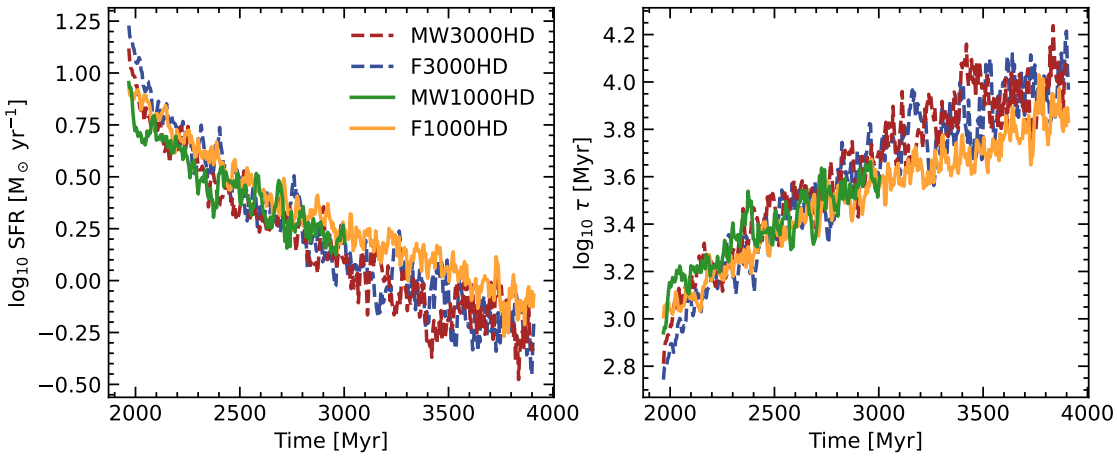

Figure B.3: SFR (left) and depletion time (right) as a function of simulation time for F3000HD (blue), MW3000HD (red), F1000HD (orange) and MW1000HD (green), limited to ±1 kpc above and below the Galactic plane. We find the simulations at 3000 $M_\odot$ and 1000 $M_\odot$ target mass to agree well.

We also show the SFR and depletion time τ as a function of simulation time for all simulations in Fig. B.3, i.e., the same as Fig. 4.7, but with the curves of F1000HD (orange) and MW1000HD (green) for comparison. Because running at higher resolution is more computationally costly, MW1000HD did just run up to about 3000 Myr, i.e., 1000 Myr into phase II. For the first 1000 Myr of phase II se see excellent agreement between the 3000 $M_\odot$ and 1000 $M_\odot$ realizations of the simulations. The depletion times agree as well. At later stages, the SFR tends to be slightly higher in the simulations with higher resolution. This is because of the increased ability of the gas to collapse to high densities and form stars. However, this effect is mild.

Also the temperature-density distribution of gas at higher resolution (Fig. B.4) agrees well with that at lower resolution (Fig. 4.3). No noticeable differences are present. As seen in Fig. B.2, gas reaches slightly higher densities and temperatures in the runs with lower target mass, but overall we see good convergence.

B.3 Additional Figures

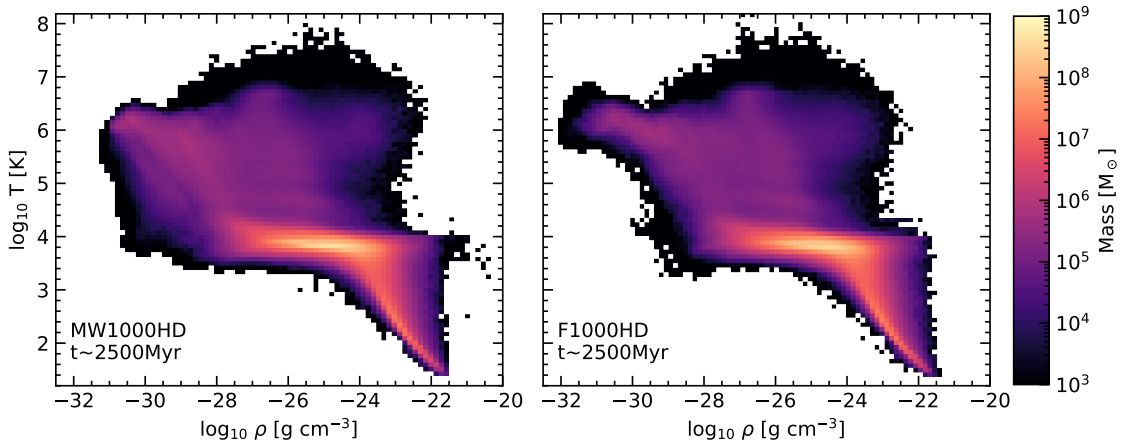

Figure B.4: Temperature-density plot for F1000HD and MW1000HD at 2500 Myr. Values agree well with Fig. 4.3.

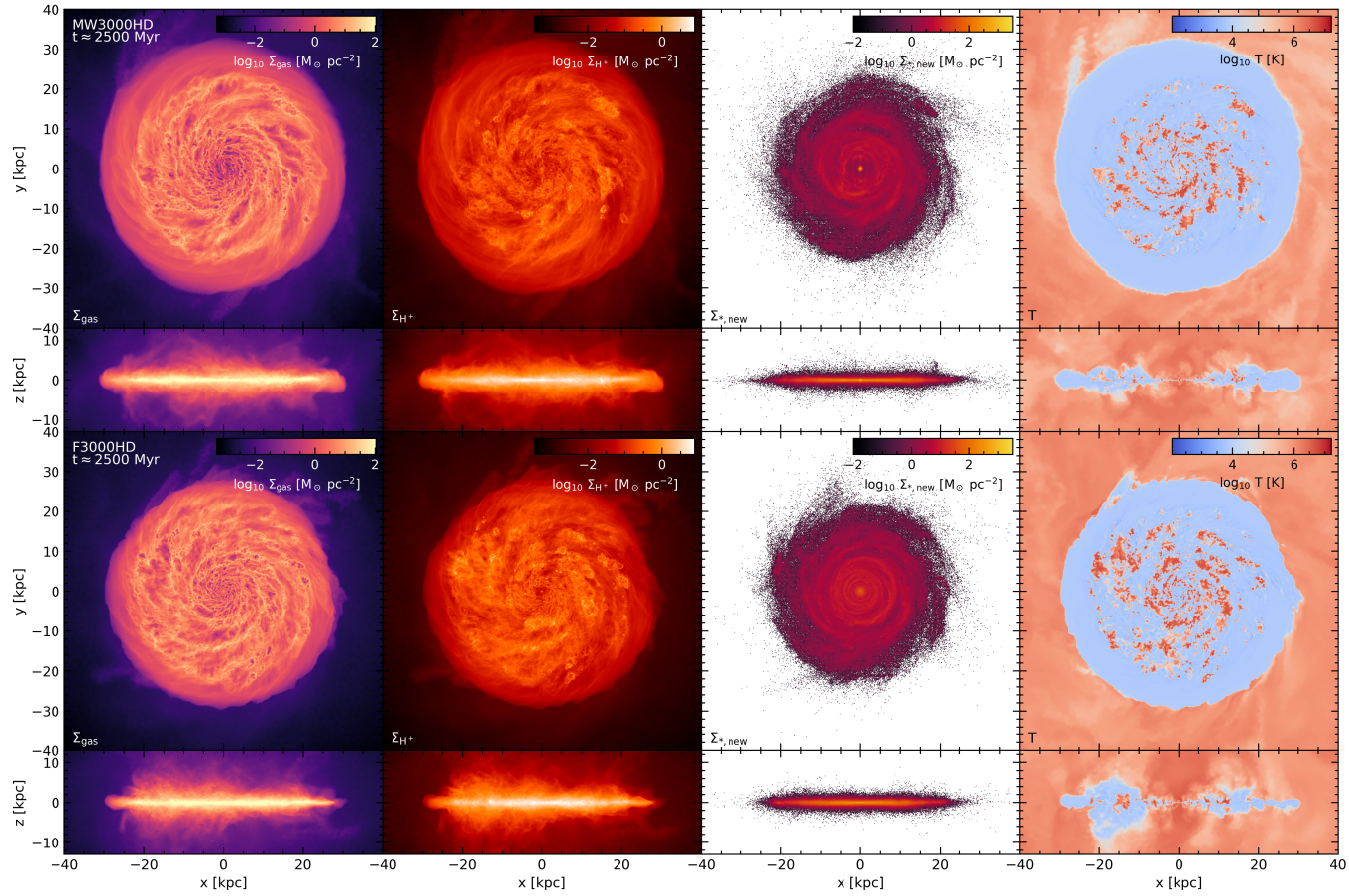

Figure B.5: Same as Fig. 4.2, but with a larger region of view to see the whole galactic disk and CGM.

C Appendix to Chapter 5

C.1 Migrator Definition

To convince us that the exact definition of migrators does not qualitatively influence the outcome of this study, we change the ΔR-threshold by ± 2 kpc and show the outcome in Fig. C.1. We find that a change in the threshold has very little influence on the galactocentric distance at which the stellar disk becomes dominated by migrators. Up to about 25 kpc (for both simulations), the fraction of migrators in the stellar population stays below 20 %, increases then abruptly to saturate at 100 % only a few kpc further out. An increase of the migration threshold to 7 kpc only sharpens this transition. When the threshold is lowered to 3 kpc, the overall behavior remains the same, but the migrator fraction in the inner stellar disk increase up to 40 %, especially between 10 and 25 kpc of galactocentric radius (further in, the migrator fraction remains low).

C.2 Orbital Eccentricity and Azimuthal Velocity

To quantify the effect of orbital eccentricities in azimuthal velocity distributions of star particles, we plot the mass weighted mean azimuthal velocity as a function of galactocentric distance measured for star particles in bins of mean orbital eccentricity in Fig. C.2. As expected, we find no kink in the distribution for stars of low orbital eccentricity (black) in MW3000HD. The distribution of F3000HD, however, shows a kink also for stars of low orbital eccentricity, but it is not correlated with the migrator dominated region as it already starts at about 20 kpc.

Is is striking that, at galactocentric distances $> R_{\rm kink}$, star particles with eccentricities between 0.1 and 0.2 experience a sharper decrease and lower azimuthal velocities than those of higher eccentricities. This is unexpected as from Fig. 5.6, we expect lower azimuthal velocities of star particles with higher eccentricities. Moreover, we

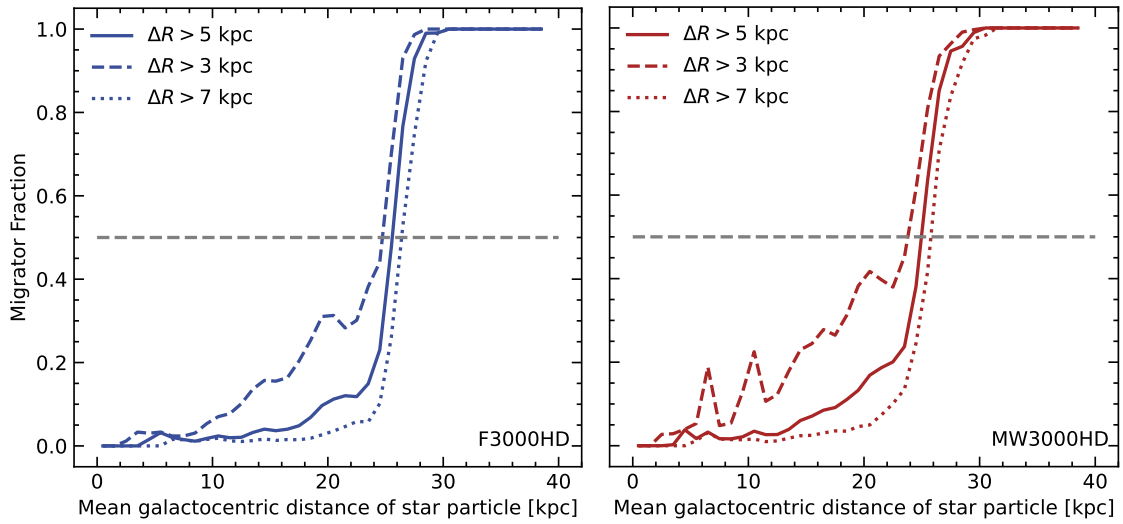

Figure C.1: Migrator mass fraction in F3000HD (left) and MW3000HD (right), in bins of the mean galactocentric distance of star particles. All star particles formed during phase II are taken into account here. The threshold for $\Delta R = |R_{\rm gal} - R_{\rm gal}^{\rm birth}|$ is varied by ± 2 kpc. The exact threshold choice has little influence on the transition to the migrator-dominated region.

see little differences between azimuthal velocity distributions of star particles of mean eccentricity larger than 0.2. At $R_{\rm gal} < R_{\rm kink}$ this is easily understandable, as in this region numerous stars orbit, averaging out slower v_φ of star particles moving out with higher v_φ of star particles moving in. However, from Fig. 5.3 we know that the majority of star particles observed at galactocentric distances $> R_{\rm kink}$ are born mostly within a 5 kpc region between 20 and 25 kpc galactocentric distance. They therefore inherit similar angular momenta, which result in similar angular velocities.

C.3 Radial Velocities

As the radial velocity component v_r is of great importance for the calculation of the rotation curve (Equation 5.5, second term), we present the radial distribution of the absolute radial velocity of migrators and non-migrators in Fig. C.3. In both simulations, migrators show a radial velocity component substantially higher than for their non-migrating counterparts. This again indicates the eccentric nature of their orbits, i.e., migrators are not moved to circular orbits with galactocentric radii different from their birth radius (which would result in a short period of high v_r, and

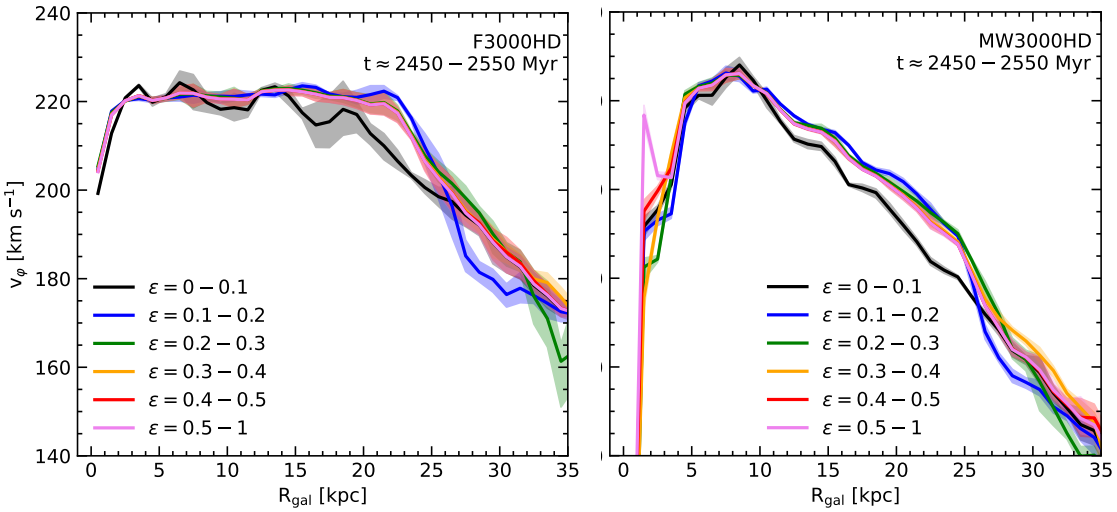

Figure C.2: Mass weighted mean azimuthal velocity as a function of galactocentric distance measured for star particles with mean orbital eccentricities in given bins only. Averaged from 2450 to 2550 Myr, shaded areas indicate 16th to 84th percentile. Star particles with lowest orbital eccentricities show little (F3000HD) to no (MW3000HD) decline in azimuthal velocity in the galactic outskirts.

a subsequent radial component close to 0), but are on elliptical orbits constantly changing their galactocentric distance. The higher radial velocity component also means that the second term of Equation 5.5 acts more strongly on migrators than on non-migrators and is therefore especially important for the rotation curve in the migrator dominated region beyond $R_{\rm kink}$.

The third term of Equation 5.5 moreover acts on the basis of the change of v_r with galactocentric distance. Such change is very low in non-migrators for both simulations, outside of the innermost 5 kpc. For migrators, on the other hand, this is not the case. For F3000HD, we find an increase of the average $|v_r|$ from 5 kpc up to about 20 kpc, with a subsequent moderate decrease, and finally an about constant average $|v_r|$ beyond 25 kpc. For MW3000HD we see an abrupt increase of the average $|v_r|$ from 20 km s^{-1} to about 40 km s^{-1} within only 5 kpc, followed by a moderate decrease up to $R_{\rm kink}$. Further out, the average radial velocity is again increasing. The third term of Equation 5.5 therefore acts more strongly on migrators as well. In the inner galaxy, at $R_{\rm gal} < 5$ kpc, radial velocities are large for both, migrators and non-migrators in both simulations, but more so in MW3000HD. This is in line with

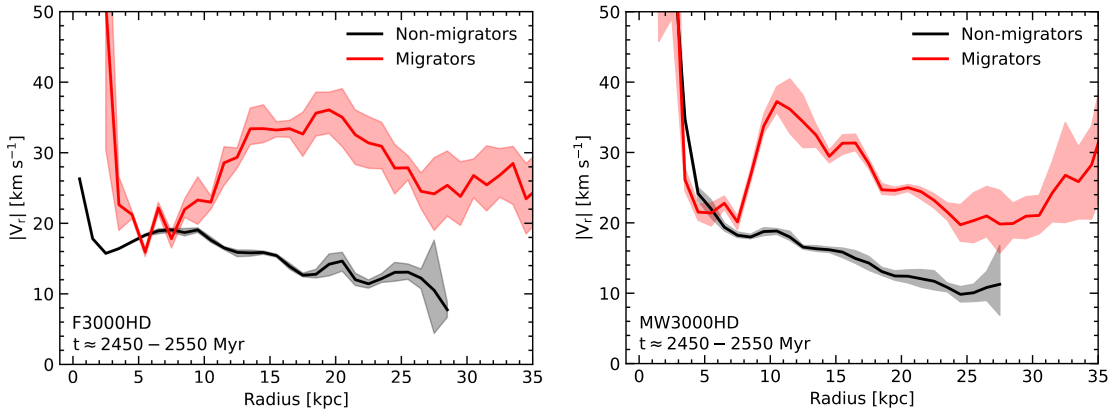

Figure C.3: Mass-weighted mean absolute radial velocity of migrators (red) and non-migrators (black) as a function of galactocentric distance for F3000HD (left) and MW3000HD (right), averaged from 2450 Myr to 2550 Myr. Shaded regions indicate 16th to 84th percentile. Migrating star particles clearly have a higher absolute radial velocity, as expected.

findings of Fig. 5.6, i.e., orbits in the galactic centers are less ordered than in the rest of the disk and affected by frequent gravitational interactions between star particles (F3000HD and MW3000HD) and the rotating bar potential (MW3000HD).

D Lists

D.1 List of Acronyms

AGB Asymptotic Giant Branch (stars)
AGN Active Galactic Nucleus
AMR Adaptive Mesh Refinement
BH Black Holes
CDM Cold Dark Matter
CNM Cold Neutral Medium
CR Cosmic Ray
DE Dark Energy
DM Dark Matter
FDM Finite Difference Method
FVM Finite Volume Method
FEM Finite Element Method
GMC Giant Molecular Cloud
HD Hydrodynamics
HIM Hot Ionized Medium
ICM Intracluster Medium
IMF Initial Mass Function
ISM Interstellar Medium
ISRF Interstellar Radiation Field
LOS Line Of Sight
MHD Magneto-Hydrodynamics
MW Milky Way
NSC Nuclear Stellar Cluster
NSD Nuclear Stellar Disk
PAH Polycyclic Aromatic Hydrocarbon

PM Particle Mesh (algorithm)
RPS Ram-Pressure Stripping
SED Spectral Energy Distribution
SF Star Formation
SFE Star Formation Efficiency
SFMS Star Forming Main Sequence
SFR Star Formation rate
SN Supernova
SPH Smoothed Particle Hydrodynamics
WIM Warm Ionized Medium
WNM Warm Neutral Medium

D.2 List of Figures

D.3 List of Tables